A NUMERICAL STUDY OF H_2/O_2 DETONATION WAVES AND THEIR INTERACTION WITH DIVERGING/CONVERGING CHAMBERS

QU QING

NATIONAL UNIVERSITY OF SINGAPORE

2008

A NUMERICAL STUDY OF H_2/O_2 DETONATION WAVES AND THEIR INTERACTION WITH DIVERGING/CONVERGING CHAMBERS

QU QING

(*B.ENG., Northwestern Polytechnic University, China*)

A THESIS SUBMITTED FOR THE DEGREE OF DOCTOR OF PHILOSOPHY DEPARTMENT OF MECHANICAL ENGINEERING NATIONAL UNIVERSITY OF SINGAPORE

2008

ACKNOWLEDGEMENTS

I would like to express my deepest gratitude to my supervisors, Prof. Khoo B.C. and for guiding me into the exciting field of detonation and giving me so many good suggestions that helped me a lot in my research work. Their enlightenment, supervision, patience, support, encouragement, as well as criticism, are really appreciated.

Sincere thanks also go to Dr. Dou H.S. (Temasek Laboratories, Singpapore) for many helpful and insightful discussions and suggestions. I appreciate his effort in reading and giving me with valuable suggestions on the earlier version of this thesis.

Moreover, I would like to express my sincere thanks to Prof. Hu X.Y. (Technical University Munich, Germany) for the original code and considerable assistance, to Tsai H.M.Dr. and Dr. Liu T.G. (Institute of High Performance Computation, Singapore) for guidance and helps, I also appreciate the financial support that the National University of Singapore provides by offering me a research scholarship and an opportunity to pursue my Ph.D. degree.

My sincere appreciation will go to my dear family. Their love, concern, support and continuous encouragement help me with tremendous confidence in solving the problems in my study and life.

Finally, I would like to thank all my friends who have helped me in one way or another during my entire Ph.D. study. Their friendships are my invaluable asset.

TABLE OF CONTENTS

SUMMARY

Due to its potential application to some high-thrust propulsion systems, the subject on detonation has been increasingly studied by many researchers from various quarters. The objective of this thesis is to study the cellular structure of H_2/O_2 detonation waves, which entails the formation, evolution and the dynamic characteristics of the cellular structure, as well as the influences of diverging/converging chambers on the detonation structure.

In this work, a detailed elementary chemical reaction model with 9 species and 19 elementary reactions is used for a stoichiometric H_2/O_2 mixture diluted with argon. The 3rd TVD Runge-Kutta method and the weighted essentially non-oscillatory (WENO) numerical scheme with high resolution grids are employed to discretize the temporal and convection terms in the governing equations, respectively, while the source terms are solved by the numerical package of CHEMEQ.

First, the one-dimensional Chapman-Jouguet (C-J) detonation wave was simulated. The one-dimensional results were then mapped to two-dimensional grids as the initial condition of the two-dimensional numerical computation in a straight tube. By introducing some artificial perturbation, the cellular structure of the two-dimensional detonation wave was successfully simulated. Furthermore, the obtained two-dimensional detonation wave was placed at the entrance of a two-dimensional varying cross-sectional chamber. By allowing the detonation wave to propagate

through the diverging/converging walls, we investigated the influence of the diverging/converging walls on the detonation wave and its cellular structure. For further understanding of these influences, axisymmetric diverging/converging chambers were introduced. A comparison on the simulation results between the axisymmetric chambers and the two-dimensional chambers was presented, followed by a detailed analysis.

NOMENCLATURE

a	Disturbance coefficient
a_{∞}^{*}	Initial sonic speed ahead of the leading shock wave
C_{cj}	Sonic speed at the C-J plane
Cp_i	Specific heat of the *i*th species
C_{xi}	Mole concentration of the *i*th species
D_{cj}	Detonation velocity at the C-J plane
d_r	Optimal weight coefficients
e	Static energy per unit volume
E	Total energy per unit volume
f	A random number distributed in [-1.0, 1.0]
$F_{i+1/2,j}$	Numerical flux at the *x* direction
$\frac{\partial F(U)}{\partial U}$	Jacobi Matrix of $F(U)$
$G_{i,j+1/2}$	Numerical flux at the *y* direction
$\frac{\partial G(U)}{\partial U}$	Jacobi Matrix of $G(U)$
h	Enthalpy per unit mass
h_i	Enthalpy per unit mass of the *i*th species
I	*N-1* by *N-1* identity matrix
$K_{f,k}$	Forward reaction rate constants in reaction k
$K_{b,k}$	Backward reaction rate constants in reaction k
l^{*}	Theoretic length of the reaction zone of 1-D gaseous detonation,

L_{const}	Length of the uniform region
ℓ_{ind}	Calculated induction zone length
ℓ_{rxn}	Calculated reaction zone length
$\overrightarrow{L^p}$	Left eigenvectors of the Jacobi Matrices
M_D	Mach number of detonation wave
M_∞	Mach number of the free stream
N	Number of species being considered
p	Pressure
p_0	Initial pressure
p_1, T_1, u_1, c_1, M_1	Pressure, Temperature, velocity, sound speed and Mach number of the unburnt gas
p_2, T_2, u_2, c_2, M_2	Pressure, Temperature, velocity, sound speed and Mach number of the burnt gas
p_3, T_3, u_3, c_3	Pressure, Temperature, Velocity and sound speed in the uniform region
p_{atm}	Atmospheric pressure
p_{cj}	Pressure at the C-J plane
p_{ign}	Pressure in the ignition area
$p_{\max}$	Maximum pressure at a certain location for some time period
p_{peak}	Peak pressure at the detonation front
q	Heat release per unit mass of reactants

r	Relaxation coefficient
R	Specific gas constant
R_i	Specific gas constant for the *i*th species
R_u	Universal gas constant
$\overrightarrow{R^p}$	Right eigenvectors of the Jacobi Matrices
S_i^0	Standard state entropy
T	Temperature
t_{char}	Characteristic time of cellular structures
T_∞^*	Initial temperature ahead of the leading shock wave
u	Velocity at the *x* direction
u_{cj}	Flow velocity at the C-J plane
u_D	Detonation wave velocity
v	Velocity at the *y* direction
$v_{ik}^{'}$	Forward chemical stoichiometric coefficients for the *i*th species in reaction k
$v_{ik}^{''}$	Backward chemical stoichiometric coefficients for the *i*th species in reaction k
$\lvert v \rvert_{\max}$	Absolute value of the maximum flow velocity at a certain location for some time period
W	Mean molecular weight of the mixture
W_i	Molecular weight of the *i*th species
X_i	Mole fraction of the *i*th species
Y_i	Mass fraction of the *i*th species

Δt	Time step
$\Delta x, \Delta y$	Mesh size

Greek Symbols

α	Monotone flux
α_{1i} □ α_{7i}	Thermal parameters
α_{ik}	Third body coefficients
β	Entrance angle of the detonation cellular structure
β_r	Smoothness measurement of the flux function
γ	Specific heat ratio
δ	The acute angle between the incident wave and the triple-point trajectory line
ε	A positive real small number
θ	Sloping angle of Diverging or converging channels
λ_i	Eigenvalues of the Jacobian matrix of $F(U)$
λ_j	Eigenvalues of the Jacobian matrix of $G(U)$
ρ	Density
ρ_∞^*	Initial density ahead of the leading shock wave
φ	Exit angle of the detonation cellular structure
ϕ	The acute angle between the Mach stem and the triple-point trajectory line
χ	Triple-point trajectory angle
ψ	The acute angle between the transverse wave and

	the incident wave
ω	Transverse track angle
$\dot{\omega}_i$	Mass production rate of the *i*th species
$\omega_r^+, \omega_r^-, \alpha_r^+, \alpha_r^-$	Numerical weight coefficients
Δ	The acute angle between the incident wave and the Mach stem

LIST OF FIGURES

LIST OF TABLES

Chapter 1 Introduction

1.1 Background

Combustion process is a vital mechanism in most propulsion systems. The combustion process can be characterized as either a deflagration or a detonation. The deflagration is mainly governed by mass and thermal diffusion and has a flame speed of several meters per second. Usually, a deflagration process produces a slight decrease in pressure and can be designed as a constant-pressure combustion process. Engines based on the deflagration process can be constructed to operate at steady state and are easily optimised with modular analyses of each subsystem. Most conventional engines, such as turbofans, turbojets, ramjets, and rocket engines, utilize a steady deflagration process.

In contrast to deflagration, the detonation process takes place much more rapidly and produces a supersonic combustion wave, or a detonation wave, which propagates at around two thousand meters per second toward the unburnt reactants. The detonation wave can be described as a strong shock wave coupled to a reaction zone. The leading part of a detonation front is a strong shock wave propagating into the unburnt fuel. The shock heats up the material by compressing it, thus triggering chemical reaction, and a balance is attained such that the chemical reaction supports the shock. In this process, material is consumed at O(100) times faster than a flame, making detonation easily distinguishable from other combustion processes. For example, a good solid explosive converts energy at a rate of 10^{10} watts per square centimeter of its

detonation front, which can be compared with the solar energy intercepted by the earth. A 400m^2 detonation wave operates at a power level roughly equals to all the power the earth receives from the sun (about 4×10^{16} watts). These virtues of detonation wave become the primary reason that has been driving people's interests in developing engines that employ detonation processes. Examples of these engine concepts include those employing standing detonation waves, such as the detonation thrusters, the detonation ramjet, and the oblique detonation wave engine (ODWE), or those employing intermittent traveling detonation waves, such as the pulse detonation engine (PDE).

The earlier studies on detonation have gone through various stages. First, the detonation phenomenon was independently discovered by Berthelot and Vielle (1882), Mallard and le Chatellier (1881). About 20 years later, the Chapman-Jouguet theory was used to evaluate some detonation parameters successfully. The simplest theory was proposed by Chapman (1899) and Jouguet (1905), usually referred to as the C-J theory. It treats the detonation wave as a discontinuity in one dimension. This theory can be used to predict the detonation wave velocity without the need to know the details of the chemical reaction and the detonation wave structure. A significant advancement in the understanding of the detonation wave structure was made independently by Zeldovich (1940) in Russia, von Neumann (1942) in the United States, and Döring (1943) in Germany. They considered the detonation wave as a leading planar shock wave with a chemical reaction zone behind the shock. Their treatment has come to be called the ZND model of detonation, and the corresponding

detonation wave structure is called the ZND detonation wave structure. Although all the experimentally observed detonation waves have much more complex cellular three-dimensional structures resulting from the strong nonlinear coupling between gas-dynamics and chemical kinetics (Glassman, 1996), the C-J theory and the ZND model, which assume a planar one-dimensional detonation wave, are still very useful. An overview of these theories is hence given in the following section to provide some basic knowledge on detonation physics. More detailed and extended discussions about detonation physics and phenomena can be found from several textbooks, such as Fickett and David (1979), Kuo (1986) and Glassman (1996).

1.1.1 C-J Theory

For a steady, planar, one-dimensional detonation wave, with both the reactants and products modeled as the same perfect gas and the detonation wave modeled as a discontinuity at which heat addition occurs, the conservations of mass, momentum, and energy in a coordinate system fixed at the wave front result in,

$$\rho_1 u_D = \rho_2 (u_D - u_2) \tag{1.1}$$

$$p_1 + \rho_1 u_D{}^2 = p_2 + \rho_2 (u_D - u_2)^2 \tag{1.2}$$

$$\frac{\gamma}{\gamma - 1}\frac{p_1}{\rho_1} + \frac{1}{2}u_D{}^2 + q = \frac{\gamma}{\gamma - 1}\frac{p_2}{\rho_2} + \frac{1}{2}(u_D - u_2)^2 \tag{1.3}$$

where u_D is the detonation wave velocity, q the heat release per unit mass of reactants due to chemical reaction, and γ ratio of the specific heat of the gas. ρ_1, p_1, and u_1 represent the density, pressure, and velocity of the unburnt gas, and ρ_2, p_2, and u_2 represent the density, pressure, and velocity of the burnt gas. Since there are only three equations, an additional equation is needed to solve for the four unknowns

p_2, ρ_2, u_2 and u_D. This additional equation will be obtained through the following analysis. Combining the mass and momentum conservation equations leads to the Rayleigh relation,

$$(p_2 - p_1)/(\frac{1}{\rho_2} - \frac{1}{\rho_1}) = -\rho_1^2 u_D^2 . \tag{1.4}$$

Manipulating Eqs. (1.1) − (1.3) results in the following Hugoniot relation,

$$\frac{\gamma}{\gamma - 1}(\frac{p_2}{\rho_2} - \frac{p_1}{\rho_1}) - \frac{1}{2}(p_2 - p_1)(\frac{1}{\rho_2} + \frac{1}{\rho_1}) = q . \tag{1.5}$$

Figure 1.1 shows the schematic of the Hugoniot curve and the Rayleigh line in the $p_2 \square 1/\rho_2$ plane. In this figure, the point corresponding to the unburnt gaseous state is denoted by A. Apparently, all the Rayleigh lines pass through this point A. The possible final states are defined by the points of intersection of the Rayleigh line and the Hugoniot curve. Among all the straight lines passing through point A, there are two lines which are tangential to the Hugoniot curve. The corresponding tangent points are defined as the C-J (Chapman-Jouguet) points, denoted in the figure by point U for the upper C-J point and L for the lower C-J point. The horizontal and vertical lines passing through point A correspond to a constant pressure and a constant-volume process, respectively. The Hugoniot curve is divided into five regions, namely regions I~V, by the two tangent lines and the horizontal and vertical lines. Region V is unphysical since the Rayleigh lines defined by Eq. (1.4) cannot have positive slope. Regions I and II are called detonation branch, within which the velocity of the wave front is supersonic; regions III and IV are called deflagration branch, within which the velocity of the wave front is subsonic. The upper C-J point

corresponds to a minimum detonation velocity, whereas the lower C-J point corresponds to a maximum deflagration velocity.

Through simple mathematical derivations, i.e., by equating the slope of the Hugoniot curve to that of the Rayleigh line, the following relation, usually referred to as the C-J condition, can be obtained at the C-J points,

$$u_2' = u_D - u_2 = \sqrt{\gamma p_2 / \rho_2} = c_2 \quad or \quad M_2' = u_2' / c_2 = 1 \tag{1.6}$$

where c_2 is the sound speed of the burnt gas, u_2' and M_2' the velocity and Mach number of the burnt gas relative to the wave front, respectively. The flow velocity relative to the wave front at the C-J points equaling to the local sound speed is one of the notable characteristics of the C-J points. At the upper C-J point, since $u_2 + c_2 = u_D$, any rarefaction waves arising behind the wave front will not overtake the detonation wave and thus a self-sustained steady detonation wave can be established.

Region I is called the strong-detonation region. In this region, the velocity of the burnt gas relative to the wave front is subsonic, i.e., $u_2 + c_2 > u_D$, thus, any rarefaction waves arising behind the wave front will overtake and weaken the detonation wave. As a matter of fact, a strong detonation, also called overdriven detonation, is not stable and is thus seldom observed experimentally. It may, however, appear during a transient process or be generated with a driving piston.

Region II is called the weak-detonation region. In this region, the velocity of the burnt gas relative to the wave front is supersonic, i.e., $u_2 + c_2 < u_D$. If the ZND

(Zeldovich-von Neumann-Döring) detonation wave structure is adopted, the detonation wave can be considered as a shock wave and a following heat addition zone. The gas velocity immediately behind the shock relative to the wave front is known to be subsonic from classical shock dynamics theory. On the other hand, it is also well known that for a steady flow in a constant-area tube, the fluid cannot be accelerated from subsonic to supersonic by heat addition. This means that the velocity of the burnt gas relative to the wave front cannot be supersonic. Thus, region II is physically impossible as long as the ZND detonation wave structure is assumed. Another discussion leading to the same conclusion can be found in the textbook of Glassman (1996).

Region III is called the weak-detonation region. The weak deflagration, or simply the deflagration, is often observed in experiments. A deflagration wave propagates toward the unburnt gas at a subsonic velocity. Across a deflagration wave, the velocity of the gas relative to the wave front is accelerated within the subsonic regime, and the pressure is reduced.

Region IV is called the strong-deflagration region. Across a strong deflagration wave, the gas velocity relative to the wave front accelerates from subsonic to supersonic. Similar to the discussion for region II, this contradicts with the known theory that for a steady flow in a constant-area tube, the fluid cannot accelerate from subsonic to supersonic by heat addition. Therefore, region IV is physically impossible, and a strong deflagration can never be observed experimentally. Based on the discussions

above, the upper C-J point is the only possible state for a self-sustained steady detonation wave. Thus, the C-J condition, Eq. (1.6), can be used as an additional equation to Eqs. (1.1) ~ (1.3) to solve for the four unknowns aforementioned, i.e., p_2, ρ_2, u_2 and u_D. It is convenient to find the detonation wave Mach number M_D first and then express the other unknowns with respect to it. It can be shown through algebraic manipulation that the unknowns as well as several other properties of the final state take the following forms,

$$M_D \equiv \frac{u_D}{c_1} = \sqrt{\frac{\gamma^2-1}{2\gamma}\frac{q}{RT_1}} + \sqrt{\frac{\gamma^2-1}{2\gamma}\frac{q}{RT_1}+1}\ , \tag{1.7}$$

$$u_D = M_D\sqrt{\gamma RT_1}\ , \tag{1.8}$$

$$u_2 = \frac{M_D{}^2-1}{(1+\gamma)M_D}\sqrt{\gamma RT_1}\ , \tag{1.9}$$

$$c_2 = \frac{1+\gamma M_D{}^2}{(1+\gamma)M_D}\sqrt{\gamma RT_1}\ , \tag{1.10}$$

$$M_2 = \frac{M_D{}^2-1}{\gamma M_D{}^2+1}\ , \tag{1.11}$$

$$\frac{p_2}{p_1} = \frac{1+\gamma M_D{}^2}{(1+\gamma)}\ , \tag{1.12}$$

$$\frac{\rho_2}{\rho_1} = \frac{(1+\gamma)M_D{}^2}{1+\gamma M_D{}^2}, \tag{1.13}$$

$$\frac{T_2}{T_1} = \frac{p_2/(R\rho_2)}{p_1/(R\rho_1)} = \left(\frac{1+\gamma M_D{}^2}{(1+\gamma)M_D}\right)^2, \tag{1.14}$$

where R is the gas constant; T_1, c_1, ρ_1, p_1 are the temperature, sound speed, density and pressure of the unburnt gas, respectively; T_2, ρ_2, p_2, c_2, u_2 and M_2, are the temperature, density, pressure, gas velocity, sound speed, and Mach number of the burnt gas, respectively.

For most cases, $M_D^2 >> 1$, and some of the expressions (1.7-1.14) can be approximately reduced to the following forms,

$$u_2 \cong \frac{1}{(1+\gamma)}, \tag{1.15}$$

$$c_2 \cong \frac{\gamma}{(1+\gamma)} u_D, \tag{1.16}$$

$$M_2 \cong \frac{1}{\gamma}, \tag{1.17}$$

$$\frac{p_2}{p_1} \cong \frac{\gamma}{1+\gamma} M_D^2, \tag{1.18}$$

$$\frac{\rho_2}{\rho_1} \cong \frac{1+\gamma}{\gamma}, \tag{1.19}$$

$$\frac{T_2}{T_1} \cong \left(\frac{\gamma M_D}{1+\gamma} \right)^2, \tag{1.20}$$

1.1.2 ZND Detonation Wave Structure

The C-J theory has been very successful in predicting the detonation wave velocity. However, it cannot tell the details of the detonation wave structure. In the early 1940s, Zeldovich (1940), von Neumann (1942), and Döring (1943) independently extended the C-J theory to consider the detonation wave structure that has become the well-known ZND detonation structure. Their treatment is referred to as the ZND model. According to them, the detonation wave is interpreted as a strong planar shock wave propagating at the C-J detonation velocity, with a chemical reaction region following and coupled to the shock wave. The shock wave compresses and heats the reactants to a temperature at which a reaction takes place at a rate high enough for ensuring the deflagration to propagate as fast as the shock wave. The shock wave

provides activation energy for igniting the reaction, whereas the energy released by the reaction keeps the shock moving. Their assumption that no reaction takes place in the shock wave region was based on the fact that the width of the shock wave is in the order of a few mean free paths of the gas molecules, whereas the width of the reaction region is in the order of one centimeter (Kuo, 1986).

Figure 1.2 shows schematically the variation of physical properties through a ZND detonation wave. Plane 1 denotes the state of unburnt gas. Plane 1' denotes the state immediately after the shock wave. Chemical reaction starts at plane 1' and finishes at plane 2, at which the C-J state reaches. If a single variable is used to represent the reaction progress or the degree of reaction, it will have a value of 0 at plane 1' and a value of 1 at plane 2. Following the Arrhenius law, the reaction rate increases with temperature. The chemical reaction region can be divided into an induction zone and a heat addition zone. The induction zone is directly behind the shock wave. In the induction zone, the temperature is not very high, and the reaction rate is relatively slow. As a result, the temperature, pressure, and density profiles are relatively flat. In the heat addition zone that is behind the induction zone, the reaction rate increases drastically to high values. A large amount of heat release from the reactions, and the gas properties change sharply.

The ZND detonation wave structure can be also interpreted by Hugoniot curves shown in Figure 1.3. There are many paths, such as those labeled by a, b, c, and d, through which a reacting mixture may pass through the detonation wave from the

unburnt state to the burnt state (Kuo, 1986). In the limit of zero chemical-energy release in the shock, a path will reach point s, the intersection of the shock Hugoniot curve and the Rayleigh line, and then the upper C-J point. The point s is referred to as the von Neumann spike. The von Neumann spike pressure can be determined from a normal shock relation:

$$\frac{p_s}{p_1} = \frac{2(1+\gamma M_D{}^2)}{1+\gamma} - 1 \tag{1.21}$$

Using Eq. (1.12), the relationship between von Neumann spike pressure and the C-J pressure can be shown as,

$$\frac{p_s}{p_1} = 2\frac{p_2}{p_1} - 1 \tag{1.22}$$

Eq. (1.22) shows that the von Neumann spike pressure is about twice of the C-J pressure.

The ZND model marks a great advancement from the C-J theory in recognizing the detonation wave structure. However, all the experimentally observed detonation waves exhibit much more complex cellular three-dimensional structures. The smoked-foil record of a detonation shown in Fig. 1.4 displays a typical cellular structure (Strehlow, 1968). More detailed discussions about these structures can be found in Kuo (1986) and Glassman (1996).

1.1.3 ZND Detonation Wave Propagation in a Tube

This subsection considers the ZND detonation propagation in a constant-area tube that is closed at one end and open at the other, shown schematically in Figure 1.5. The

tube is initially filled with a static premixed detonable mixture. Detonation is initiated at the closed end and propagates downstream toward the open end. Following the detonation wave is a centered rarefaction wave, known as the Taylor wave, emanating from the closed end to satisfy the stationary boundary condition there. After the passage of the Taylor wave, a uniform region forms. The corresponding wave form in the space-time plane is given in Figure 1.6. Figure 1.7 schematically shows the pressure profile within the tube. The width of the detonation wave is enlarged for visualization. The states 1, s, 2, and 3 denote the unburnt gas state, the von Neumann spike state, the C-J state, and the uniform region state, respectively. The von Neumann spike state and the C-J state can be readily determined using the equations derived in the previous subsection. The focus of this subsection is hence on the solution of the Taylor wave and uniform regions.

The properties of the uniform region can be obtained as follows. Applying the Riemann invariant relation along the characteristic line passing through the Taylor wave from state 2 to state 3, one obtains

$$u_3 - \frac{2}{\gamma - 1} c_3 = u_2 - \frac{2}{\gamma - 1} c_2 , \tag{1.23}$$

where u_3 and c_3 are the velocity and sound speed in the uniform region, respectively. Since u_3 = 0, the above equation yields

$$\frac{c_3}{c_2} = 1 - \frac{\gamma - 1}{2} \frac{u_2}{c_2} = 1 - \frac{\gamma - 1}{2} M_2 = 1 - \frac{\gamma - 1}{2} \frac{M_D{}^2 - 1}{\gamma M_D{}^2 + 1}, \tag{1.24}$$

where M_2 is the Mach number of the gas at state 2 expressed with Eq. (1.11).

Consequently, the temperature in the uniform region is

$$\frac{T_3}{T_2}=\left(1-\frac{\gamma-1}{2}\frac{{M_D}^2-1}{\gamma{M_D}^2+1}\right)^2. \tag{1.25}$$

Through an isentropic relation from state 2 to state 3, the pressure can be determined as:

$$\frac{p_3}{p_2}=\left(1-\frac{\gamma-1}{2}\frac{{M_D}^2-1}{\gamma{M_D}^2+1}\right)^{\frac{2\gamma}{\gamma-1}}. \tag{1.26}$$

The relation of the sound speed c_3 with the detonation wave velocity u_D can be obtained by combining Eqs. (1.24), (1.10), and (1.8):

$$\frac{c_3}{u_D}=\frac{{M_D}^2+1}{2{M_D}^2}. \tag{1.27}$$

Since the rear of the Taylor wave propagates at c_3, the length of the uniform region, L_{const}, can be calculated by the following expression,

$$L_{const}=c_3 t. \tag{1.28}$$

Similar to the previous subsection, considering that the square of the detonation wave Mach number, ${M_D}^2$, is much larger than 1, the above expressions, Eqs. (1.24) ~ (1.27) can be further simplified with approximation:

$$\frac{c_3}{c_2}\cong\frac{\gamma+1}{2\gamma}, \tag{1.29}$$

$$\frac{T_3}{T_2}\cong\left(\frac{\gamma+1}{2\gamma}\right)^2, \tag{1.30}$$

$$\frac{p_3}{p_2}\cong\left(\frac{\gamma+1}{2\gamma}\right)^{\frac{2\gamma}{\gamma-1}}, \tag{1.31}$$

$$\frac{c_3}{u_D}\cong\frac{1}{2}. \tag{1.32}$$

The length of the uniform region can thus be approximated as:

$$L_{const} = c_3 t \cong \frac{1}{2} u_D t \tag{1.33}$$

It indicates that the length of the uniform region is about halfway between the detonation wave front and the head end (Fickett and Davis, 1979).

The flow properties within the Taylor wave region, $c_3 t \le x \le u_D t$, can also be derived. The Riemann invariant relation along the characteristic line from state 3 to the point (x, t) gives:

$$0 - \frac{2}{\gamma - 1} c_3 = u - \frac{2}{\gamma - 1} c \tag{1.34}$$

where *u* and *c* are the velocity and sound speed at point (x, t). On the other hand, since the forward characteristic lines are straight, thus,

$$\frac{x}{t} = u + c\,. \tag{1.35}$$

Combining Eq. (1.34) with (1.35) leads to,

$$\frac{u}{c_3} = \frac{2}{\gamma + 1} \frac{x}{c_3 t} - \frac{2}{\gamma + 1} \tag{1.36}$$

$$\frac{c}{c_3} = \frac{\gamma - 1}{\gamma + 1} \frac{x}{c_3 t} + \frac{2}{\gamma + 1}. \tag{1.37}$$

$$\frac{T}{T_3} = \left(\frac{\gamma - 1}{\gamma + 1} \frac{x}{c_3 t} + \frac{2}{\gamma + 1} \right)^2 \tag{1.38}$$

$$\frac{p}{p_3} = \left(\frac{\gamma - 1}{\gamma + 1} \frac{x}{c_3 t} + \frac{2}{\gamma + 1} \right)^{\frac{2\gamma}{\gamma - 1}}. \tag{1.39}$$

1.2 Literature Review

Studies of detonation that have been conducted for about a century can be classified into experimental and numerical studies.

1.2.1 Experimental Studies

Experimentally, much effort has been expended in studying various important aspects of PDEs, including the detonation initiation, propagation and the blowdown processes etc. Some experiments can be used to determine the detonation initiation energy required for a given mixture or to measure the detonation wave properties. Both hydrogen and hydrocarbon fuels were involved in the experiments. The hydrocarbon fuels include both gaseous fuels such as ethylene (C_2H_4) and propane (C_3H_8) and liquid fuels such as JP10 ($C_{10}H_{16}$). Ethylene (C_2H_4) was selected by many researchers because of its well-documented detonation properties and as a common decomposition of some typical heavy hydrocarbon fuels.

Detonation initiation is one of the major challenges in the PDE design. A detonation can be initiated either directly through a large amount of energy deposition or indirectly through a low-energy deposition along with a deflagration-to-detonation (DDT) process. Typical values for direct initiation energy for hydrocarbon fuel/air mixtures are of the order of Kilo-Joules to Meg-Joules (Benedick et al., 1986). The deposition of such high initiation energies is impractical for repetitive initiations. Most PDE experiments have thus relied on a DDT process for detonation initiation.

According to the literature (Oppenheim, 1962; Lee and Moen, 1980; Kuo, 1986), a DDT process consists of the following sequence of events: 1) deflagration initiation – a deflagration combustion is initiated by a low-energy deposition; 2) shock wave formation – the energy released by the deflagration increases the volume of the

products and generates a train of weak compression waves that propagate into the reactants ahead of the flame and finally merge into a shock wave; 3) onset of "an explosion in an explosion" – the shock wave heats and compresses the reactants ahead of the flame, creates a turbulent reaction zone within the flame front, and eventually cause one or more explosive centers formed behind the shock front; 4) overdriven detonation formation – strong shock waves are produced by the explosions and coupled with the reaction zone to form a overdriven detonation; 5) stable detonation establishment – the overdriven detonation wave decreases to a steady speed at around the C-J detonation velocity.

The distance from the ignition to the detonation formation point is referred to as the DDT length, which is in general a function of the fuel and oxidizer, the tube diameter and geometry, the tube wall surface roughness, and the method used to ignite the mixture. Sinibaldi et al. (2000) investigated the dependence of the DDT length on the ignition energy, ignition location, and stoichiometric mixture for a $C_2H_4/O_2/N_2$ mixture. They found that ignition energies above 0.28 J had little effect on DDT length. The ignition location tests revealed that when the ignitor was placed 1.33 tube diameter from the head wall, the DDT length could be reduced by up to 32%. Their results also showed that the mixture equivalence ratio significantly affects the DDT length. The minimum DDT length of around 7.5 cm for the C_2H_4/O_2 mixture was obtained with an equivalence ratio of 1.2. A drastic increase in DDT length was observed when the equivalence ratio is less than 0.75.

In general, the DDT length could be large compared to the tube length used in PDE experiments. Hinkey et al. (1995) carried out a series of tests with H_2/O_2 mixtures of various equivalence ratios and found that the DDT lengths are on the order of 30 to 100 cm. They thus suggested using some DDT augmentation devices to enhance the DDT process and reduce the DDT length, which was adopted in most subsequent PDE experiments. In the early multi-cycle experimental work of Nicholls (1957) and Krzycki (1962), it is not clear whether full detonation waves were realized because a low-energy spark ignitor was used in their experiments and no DDT augmentation devices were implemented.

A classical approach for DDT enhancement is to place the Shchelkin spiral (Shchelkin, 1940), into the detonation tube. Hinkey et al. (1995) first applied this approach to their single-pulse PDE experiments with H_2/O_2 mixture and found that the Shchelkin spiral reduced the DDT length by a factor of about 3. Recently, New et al. (2006) performed experiments on a multi-cycle PDE, running on a propane-oxygen mixture using a rotary-valve injection system and a low energy ignition source to investigate the effectiveness of Shchelkin spiral parameters on DDT. Their results showed that only spiral with the highest blockage-ratio were able to achieve successful and sustained DDT in the shorter length configuration. In addition to the Shchelkin spirals, other internal obstacles such as half-disk protrusions (Broda et al., 1999), blockage plates and orifice plates (Cooper et al., 2002), and coannulus (Mayer et al., 2002) have also been used by various researchers. It should be noted, however, while enhancing the DDT processes, all these obstacles result in significant total pressure

loss and degrade the propulsive performance. Cooper et al. (2002) reported that the DDT lengths could be reduced by an average of 65% in various $C_3H_8/O_2/N_2$ and $C_2H_4/O_2/N_2$ mixtures using obstacles with a blockage ratio of 0.43, whereas the impulse was reduced by up to 25%.

Another traditional detonation initiation concept involves using a predetonator (Helman et al., 1986), which is in essence a detonation-to-detonation initiator. A detonation is initiated in a more easily detonable mixture called as the driver gas and then propagates into and initiates a detonation in the primary mixture. A simple example of this concept is to fill a fuel/oxygen mixture or the driver gas in an initiation section near the closed end of the detonation tube (Hinkey et al., 1995; Sanders et al., 2000). The minimum length of the initiation section is the DDT length of the driver gas. The aforementioned DDT augmentation devices can be further implemented within the initiation section to achieve more rapid initiation. A disadvantage of this concept is the need to carry an additional driver gas or oxygen generator, which increases the system weight. The additional driver gas also lowers the specific impulse since the weight flow rates of both the fuel and the driver gas should be taken into account in calculating the specific impulse. To mitigate this disadvantage, the amount of the driver gas or the volume of the driver gas region must be as small as possible. A practical way to reduce the volume of the driver gas region is to utilize an additional smaller tube for the driver gas. This additional tube, usually with a volume on the order of 1% of that of the main detonation tube, is called a predetonator. The detonation transmission from the predetonator to the main

detonation tube is thus a key issue in the predetonator applications (Sinibaldi et al., 2001; Santoro et al., 2003).

Diffraction of detonation from a small tube into an unconfined space has been extensively investigated in the past (Lee, 1984; Desbordes, 1988). According to the literature, a successful detonation transmission happens if the tube diameter is larger than the critical diameter. This critical diameter is usually expressed in terms of the detonation cell size of the mixture. It is now commonly accepted that the critical diameter is about thirteen times of the detonation cell size for smooth circular tubes. The detonation transmission from the predetonator to the main detonation tube has also been investigated recently (Sinibaldi et al., 2001; Santoro et al., 2003; Brophy et al., 2003). Successful detonation transmission from the predetonator to the main detonation tube could be achieved at predetonator tube diameters less than the critical diameter because of the confinement of the transition region and main detonation tube (Santoro et al., 2003).

Other techniques proposed for promptly achieving detonation initiation include hot jet initiation, detonation wave focusing, etc. Hot jet initiation was observed by Knystautas et al. (1979) for sensitive fuel-oxygen mixtures. Lieberman et al. (2002) recently demonstrated the possibility of using a hot jet to initiate a detonation in a short detonation tube filled with the $C_3H_8/O_2/N_2$ mixture. The idea of the detonation wave focusing is to initiate the detonation in the main detonation tube through the merging of the detonation waves coming from a bunch of small tubes (Jackson and

Shepherd, 2002).

Besides the above-mentioned works about DDT, detonation reflection and diffraction have also been investigated by some researchers experimentally. Guo et al (2001) described the Mach reflection processes of a detonation and revealed some characteristics by presenting some soot tracks formed by gaseous detonation waves diffracting around wedges with different wedge angles. The relationship between the trajectory angle of the triple point, wedge angle, and initial pressure in Mach reflection was also analyzed. Their results showed that the triple-point trajectory angle χ is dominantly dependent on wedge angle θ and is not sensitive to the initial pressure p_0. In addition, they also found that the triple-point trajectory could be detached from the wedge apex when the wedge angle is less than 30° in their experiments. For Mach-reflected detonations, the trajectory of the triple point was observed to be a curve line.

Khasainov et al (2005) reported an experimental study on the detonation diffraction from circular tubes to cones of various angles in stoichiometric C_2H_2/O_2 mixture, and they also proposed critical conditions for diffraction and investigated the mechanisms involved. Their research results showed that the critical transmission was due to a super-detonation that propagates transversally in shocked gas before the flame front. The critical conditions for diffraction were discussed, that is, at large cone angles (θ >40°), super-detonation originates at the axis of the flow and propagates tangentially to the cone wall, while at smaller angles (θ<40°), super-detonation

originates at the cone wall and propagates toward the axis.

By using the chambers with different shapes from those by Khasainov et al. (2005), Thomas and Williams (2002) experimentally analyzed the interaction of gaseous detonations with obliquely inclined surfaces, which involves a planar inclined wall, two-dimensional propagation in a curved channel and finally three-dimensional interaction with a bend in a cylindrical pipe. The role of detonation structure was also discussed as well as the magnitude and duration of potentially damaging overpressures. Their numerical results showed that the presence of transverse structure influenced the reflection process directly and the natural transverse structure participated actively in the wave reflection processes occurring near the wedge. Detonation structure was found to play a crucial role when expansions were present, as expansion could lead to local failure of the transverse structure and hence of the detonation process locally. That local overpressures peaks up to six times the incident peak C-J pressure could occur and they were very short lived ($< 10\mu s$).

1.2.2 Numerical Studies

In addition to experimental investigations, substantial attempts have been made to numerically study detonation wave and its cellular structure since the late 1970s when the development of computer technology made possible the numerical simulations of detonation, especially on some aspects that cannot be studied easily in experiments, like propagating mechanism of self-sustained detonation, deflagration to detonation transition and the detailed detonation structure etc. In contrast to experiments in which ethylene (C_2H_4) is often used as the fuel, most numerical studies use hydrogen

(H_2) as the fuel because of its relatively simpler chemical kinetics. Another significant difference between experiments and simulations is the detonation initiation. In experiments, as discussed above, the detonation is usually initiated indirectly through a low-energy deposition along with a DDT process since the direct initiation with high-energy deposition is not practical. In numerical simulations, however, a small spark region with high temperature and pressure is commonly implemented to directly initiate the detonation.

One of the early studies on one-dimensional detonation was attributed to Cambier and Adelman (1988). Quasi-one dimensional simulations with multi-step finite rate chemical kinetics were carried out for a 50-cm-long detonation tube attached to a 43-cm-long diverging nozzle with stoichiometric H_2/Air mixture. The detonation was initiated at the closed end by a 2-cm-long spark region with a temperature of 1500 K. The refilling process started when the head-end pressure fell to 3.5 atm. The fresh reactants moved at speeds up to 350 m/s. The engine reached steady cyclic operation by the third cycle with a cycle frequency of about 667 Hz. Specific impulses up to 6507 s were reported. These very high specific impulses may be due to the fact that their calculations were based on the gross thrust from the exit plane and that the contribution from the spark region on the impulse was not accounted for.

Sterling et al. (1995) also conducted one-dimensional simulations with H_2/air mixture. The detonation tube is 100 cm long. The spark region has a length of 0.5 cm with a temperature of 3000 K and a pressure of 50 atm. The refilling process began when the head-end pressure decayed to the atmospheric pressure. They calculated the specific

impulse for the sixth cycle based on the head-end pressure history and obtained a value of 5152 s, which is much smaller than that of Cambier and Adelman (1988).

Cambier and Tegner (1998) examined the effect of the spark region on the performance in their quasi-one-dimensional and two-dimensional simulations with H_2/air mixture for a 10-com-long detonation tube with various divergent nozzles. The spark region spans 0.4 cm, with a temperature of 2500 K and a pressure of 50 atm. They observed that the contribution from the spark region on the single-pulse peak impulse ranges from 17% to 27%. After subtracting this contribution, they obtained specific impulses of 3500 s ~ 4100 s based on the head-end pressure history of their quasi-one dimensional multi-cycle results.

In addition to the differences in the operation conditions and in the calculation methods for the specific impulse, the exit boundary condition plays another important factor that cause the differences in the reported specific impulses from one-dimensional simulations (Kailasanath et al., 1999). The choice of appropriate exit boundary conditions poses a major challenge in one-dimensional simulations for PDEs. In general, if the outflow is supersonic, extrapolation of the condition from the interior points of the computational domain can be used. However, for subsonic outflow, the flow inside the domain near the exit relates to the flow field outside the domain, which is unknown for the one-dimensional simulations. The situation is further compounded by the existence of the unsteady detonation waves and other associated waves. Strictly, there are no accurate exit boundary conditions for this kind

of complex unsteady subsonic outflow.

Most one-dimensional simulations have relied on a fixed-pressure boundary condition for the outflow (Cambier and Adelman, 1988; Starling, 1995). Ebrahimi et al. (2002) used the fixed-boundary condition as well as a varying-pressure condition based on corrections from two-dimensional simulations. They found that with the fixed pressure condition, the flow chokes as soon as the detonation wave arrives at the exit, whereas the varying-pressure result shows duration of a subsonic outflow before choking. Kailasanath et al. (1999) utilized a relaxing-pressure boundary condition. The pressure is set to reach the ambient value in a relaxation length from the end of the detonation tube. A larger value of the relaxation length implies a slower relaxation of pressure to ambient. Based on single-pulse operation, they observed that the specific impulse is larger for slower relation cases. They then concluded that the variations in specific impulses reported in the literature could be explained on the basis of exit boundary conditions used.

For two-dimensional simulations, early numerical research works have shown the effectiveness and significance of a reasonably high spatial resolution and detailed chemical reaction model.

Simple one- or two-step chemical reaction models were used to simulate an oxyhydrogen mixture by Taki and Fujiwara (1978). The calculation employed a plane C-J detonation as an initial condition. Two-dimensional disturbances were generated by artificially placing non-uniformities ahead of the detonation front. Regardless of

the given different initial disturbances, a fixed number of triple shock waves were generated for a fixed combination of mixture model and geometry ultimately. Their numerical result showed that for a given detonation tube geometry, any exothermic system had its own characteristic multidimensional structure.

High resolution numerical simulations with simple reaction models have also been used to study the detailed detonation structure (Quirk 1993; Lefebvre and Oran 1995; Gamezo et al 1999). Additionally, using the multi-step, detailed reaction model, Oran et al (1991, 1998) successfully presented the triple-wave configuration for a low pressure argon-diluted H_2/O_2 mixture. The energy-release pattern in a detonation cell showed that, in addition to the primary release of energy behind the Mach stem, there was a secondary energy release that started about two-thirds of the way through the cell. In addition, it was also found that after the triple point collision, the structure evolves from a single-Mach configuration to double-Mach and more complex configurations. Resolution tests showed that the number of triple points or transverse waves, as well as global and local energy release, converges ultimately.

However, relatively low resolution may lead to some disagreement, as shown by Sharpe (2001). Sharpe used a very high spatial resolution numerical simulation for the same mixture but with simple reaction models. The results showed that the structure has a double-Mach-like configuration of the strong type and there is no further change before and after the triple point collision. This observation may have led Sharpe to conclude that for simple kinetics, the failure to resolve accurately the structures as

predicted by steady analysis can induce qualitatively incorrect conclusions. Somewhat similar conclusions have also been reached for detonation diffraction problems that when the grid resolution is insufficient to capture the reaction zone and radius of curvature effects, large errors can arise (Wescott at al 2004; Arienti and Shepherd 2005).

By utilizing a high resolution of up to 0.025mm, detailed reaction model and high order numerical scheme, Hu et al. (2004) studied a low pressure argon-diluted H_2/O_2 mixture and resolved the structure configuration and its evolution. The numerical results showed some fine structure features as characterized by the complex chain-branching reaction process. Through the triple point collision, three regular collision processes were observed, followed by a quick change to the double-Mach-like configuration. In addition, three different tracks associated with different triple points or the kink on the transverse wave were found. Resolution study showed that the discrepancies concerning the structure type by the coarser grid could be resolved using a sufficient find mesh size of 0.05mm or below.

Besides the above-mentioned works and others, the interactions between detonation wave and a wedge or a sloping wall have been studied by some researchers numerically as well. Yu (1996) and Akbar (1997) performed some investigations of the interaction between a gaseous detonation and a wedge. Ohyagi et al (2000)'s numerical simulation of the detonation reflection processes on a wedge employed the flux corrected transport scheme and a two-step chemical reaction model for

stoichiometric H_2/O_2 mixture diluted with argon. Results showed that there exists a critical angle beyond which Mach reflection could not occur. When Mach reflection occurred, the cell sizes in Mach stem were smaller than those in the incident waves. In addition, it was also found that there was an initiating stage during which the cells in the Mach stem were created. The trajectory of the Mach reflection triple point was observed to be a curved line.

Regarding the work on oblique detonation waves, Li et al (1994) studied the two-dimensional, oblique detonations generated by wedge-induced shocks in $H_2/O_2/N_2$ mixture, and revealed that the basic structure of such an oblique detonation was found to consist of a non-reactive oblique shock, an induction region, a set of deflagration waves, and a reactive shock in which the shock front is closely coupled with the energy release. In addition, the detonation structure was found to be stable and very resilient to disturbances in the flow. The entire detonation structure was steady on the wedge when the flow behind the structure was completely supersonic, while if the flow somewhere behind the structure was subsonic, the structure might be detached from the wedge and move upstream continuously.

Papalexandris (2000) also investigated the wedge-induced oblique detonations. By using an unsplit algorithm which integrates the convective and reaction source terms simultaneously, Papalexandris discussed the evolution of the leading shock in two different geometrical configurations with various wedge angles, depending on whether the top corner would affect the structure of the reaction zone. The numerical

results showed that, for small wedge angles, the shock attached to the wedge would turn smoothly to an oblique ZND wave, while an explosion could occur at the front for high wedge angles. Studies of the effect of the wedge corner revealed that, when explosion occurred upstream of the corner, the expansion at the corner would not affect the evolution of the front. If explosion occurred downstream of the corner, the curvature of the front and the reaction process could be affected. It was also found that for wedge heights small enough, a detonation could not be established downstream, and the front decayed downstream to a Mach wave.

Recently, Fusina et al (2005) employed CFD to investigate the formation and stability of a standing oblique detonation wave (ODW) near the C-J point. Simulating the formation of a near C-J ODW indicated that it reached a non-oscillatory position. The C-J ODW was observed to be resilient to inhomogeneities in the oncoming fuel-air flow; after displacing upstream slightly, it returned to its original position. The change in the combustion-inducing shock caused by the inhomogeneities was determined to be the leading cause of the ODW displacement and to be the part of the ODW structure most sensitive to disturbances. The test of an under-driven ODW's stability showed that it displaced three times as much as its C-J counterpart. The study of the radical species formation in the induction region of the ODW revealed that HO_2 is the first radical to appear in the induction zone and that the other radicals appear subsequently.

In addition, Walter et al (2006) conducted work on the interaction between the leading oblique detonation wave and the expansion waves generated by a wedge surface. Their computational results showed that for intermediate wedge angles, a C-J oblique detonation wave was obtained, while for wedge angles near to a maximum angle, the oblique detonation wave was decoupled. They also found that when decoupling occurred, the ratio between the height of the ramp h and induction length l_i of the chemical process downstream from the leading OSW of the overdriven ODW is smaller than when a C-J ODW is obtained. For given values of the induction length and ODW angle, the ramp height controls the pressure gradient of the expansion fan downstream from the ODW.

1.3 Objectives of the Study

1.3.1 Motivation

As discussed above, some important topics like propagating mechanism of self-sustained detonations, deflagration to detonation transition, and detonation reflection and diffraction, to name a few, have not been well understood as yet (Oppenheim et al 1973, and Lee 1984). One of the key topics is the detonation reflection and diffraction associated with the shape or area change in the chambers considered. The importance of shape or area variation is intricately related to the different dimension chambers in an operating PDE (Wintenberger et al 2003). A typical air-breathing PDE consists of an inlet, a series of valves, one or multiple detonation tubes, and an exit nozzle. The different sections of the PDE invariably have different cross-sectional areas. For example, the pre-detonator PDE may be a

smaller size chamber and use more volatile fuel for ease of initiation of detonation and it expands into the larger size main detonation chamber filled with a different gaseous fuel. Besides the possibility that the detonation wave decays or dies in the expansion or contraction chambers, the overall performance of a PDE can also be strongly affected by the cross-sectional area variation in the PDE tube (Daniel 2003). Therefore, it is significant and even critical to study the detonation reflection or diffraction in a contraction or expansion chambers of various areas for a better understanding of the detonation transition. Although fairly extensive works have been carried out to investigate the reflection or diffraction of shocks in non-reactive gases by planar wedges, much less work has been done on the more complex reflection or diffraction of detonation.

As mentioned above, Thomas and Williams (2002) found that there exists a transition region from the irregular cell structure to the ultimate regular cell structure as a detonation wave passes through a variable cross-sectional chamber. Due to the limitation of experimental setup, they did not investigate the relationship between the length of the transition region and the oblique angle of the sloping wall quantatively. In order to explore this relationship, if any, we can impose an existing detonation wave in the diverging/converging chambers as the initial condition and then study the evolution of the detonation cellular structure by using the numerical simulation technology.

1.3.2 Objectives

The present research aims to study the detailed triple-wave configuration of a gaseous detonation wave, as well as the formation, evolution and the dynamic characteristics of the detonation cellular structure.

Another aim is to observe the evolution of detonation cellular structures in variable cross-sectional chambers, and examine the influences of the variable cross-sectional walls on the detonation wave and its cellular structure. These variable cross-sectional chambers are either two-dimensional diverging/converging chambers or axisymmetric diverging/converging chambers.

An extension to the study of the evolution of detonation cellular structure is the possibility of a relationship between the length of the transition region and the diverging or converging oblique angle. When the detonation wave passes through a diverging or converging sloping wall, its cellular structure would be distorted, until these detonation cells re-gain their regularity. The process can be viewed as a transition region, and its length is significant for the design of the industrial detonation propulsion systems.

Finally, the diffraction and reflection of detonation waves are also studied. A relationship between the triple-point trajectory angle of Mach reflection and the oblique angle of a converging sloping wall is discussed.

1.4 Organization of the Thesis

In Chapter 2, the physical conditions and a detailed chemical reaction model are

introduced. The multi-species Euler equations with the multi-step chemical reaction model are solved by the third order TVD (Total Variation Diminishing) Runge-Kutta time integration technique for temporal discretization, the fifth order WENO-LLF (Weighted Essentially Non-oscillatory –Local Lax-Friedrichs) scheme for spatial discretization and the numerical package of CHEMEQ for the source terms of the governing equations. The two-dimensional code is efficiently parallelized by implementing the message passing interface (MPI) library and a domain decomposition technique.

In Chapter 3, a variety of numerical experiments on shock wave are performed to validate the present code. The experiments include computation of shock waves in one-dimensional, two dimensional straight-duct, two-dimensional diverging /converging and axisymmetric diverging /converging channels.

In Chapter 4, the one-dimensional detonation wave initialized by a strong shock wave is simulated. The fundamental characteristics and parameters relating to the one-dimensional detonation wave, as well as the variation in concentration of species are investigated. In addition, a resolution study is also performed.

In Chapter 5, by introducing some artificial perturbation, the cellular structure of the two-dimensional detonation wave is simulated. The detailed triple-wave configuration, as well as the formation, evolution and the dynamic characteristics of the cellular structure are investigated, to be followed by a resolution study.

In Chapter 6, profiles of the two-dimensional detonation wave passing through the

diverging/converging chambers with various oblique angles are presented. The influence of the diverging/converging walls on the detonation wave and its cellular structure, as well as diffraction and reflection of the detonation wave are discussed.

In Chapter 7, profiles of the detonation wave passing through axisymmetric diverging/converging chambers with various oblique angles are presented. By comparison with the two-dimensional diverging/converging case, the influences of the axisymmetric diverging/converging walls on the detonation wave and its cellular structure, as well as diffraction and reflection of the detonation wave are discussed.

Finally, Chapter 8 summarizes the present work and provides several recommendations for the future work.

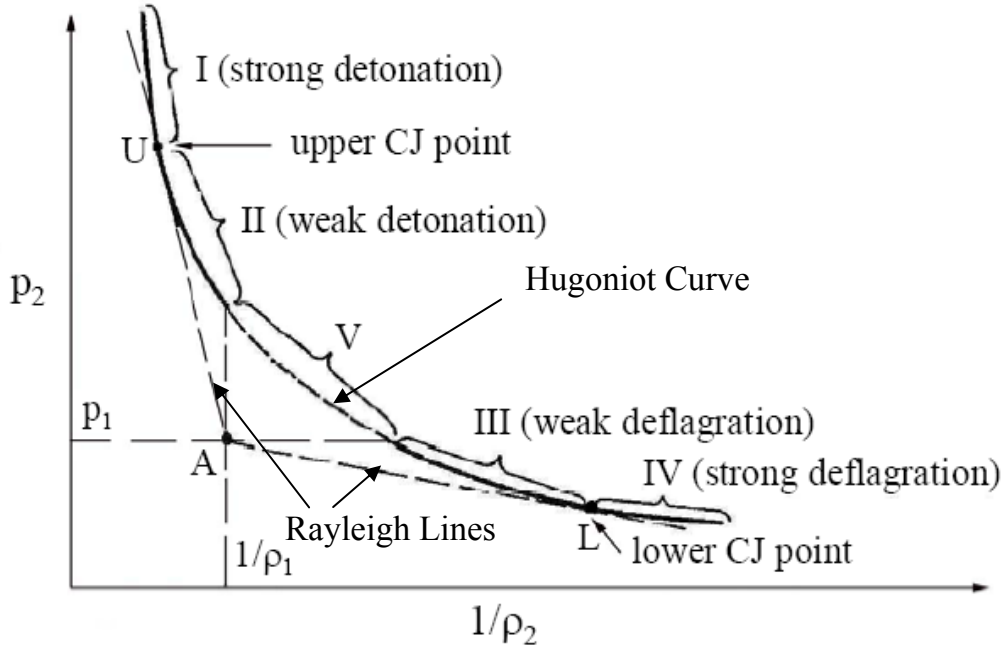

Figure 1.1 Schematic of Rayleigh lines and Hugoniot curve in $p_2 - 1/\rho_2$ plane (adapted from Kuo, 1986)

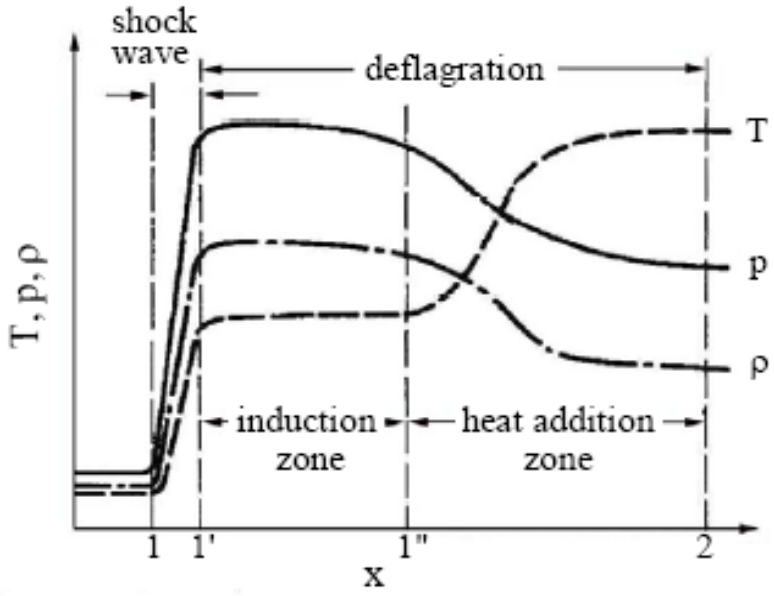

Figure 1.2 Variation of physical properties through a ZND detonation wave (adapted from Kuo, 1986)

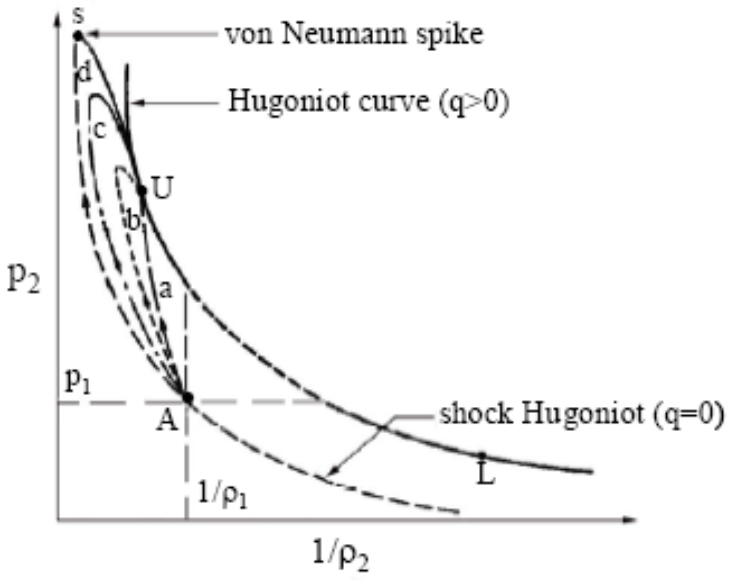

Figure 1.3 Schematic of ZND detonation structure

in $p_2 - 1/\rho_2$ plane (adapted from Kuo, 1986)

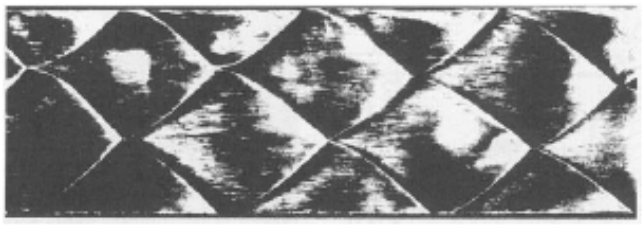

Figure 1.4 Smoked-foil record of a detonation (Strehlow, 1968)

Figure 1.5 ZND detonation propagation in a tube closed at one end

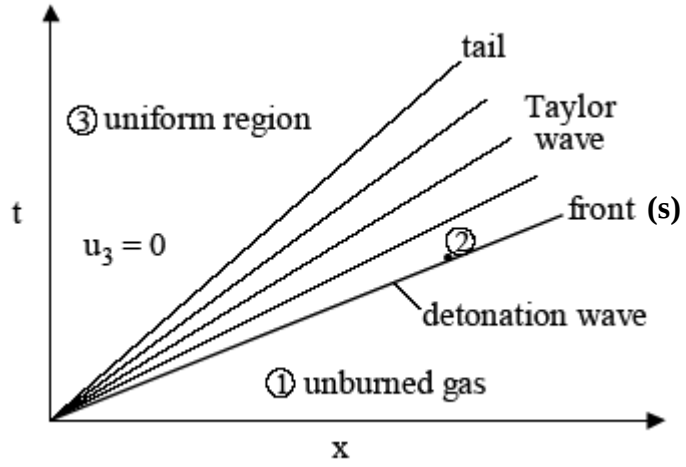

Figure 1.6 Space-time wave diagram for a ZND detonation wave propagation in a tube

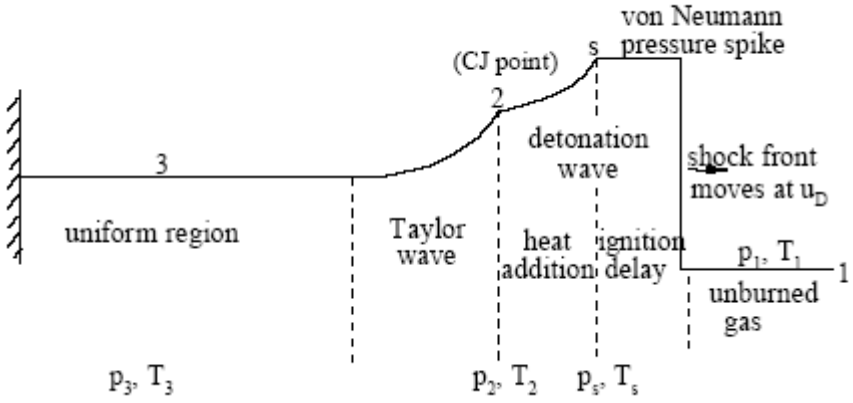

Figure 1.7 Schematic of pressure profile for a ZND detonation propagation in a tube closed at one end. (adapted from Bussing and Pappas, 1994)

Chapter 2 Physical and Mathematical Models

2.1 Physical Model and Assumptions

In the current research work, the fuel H_2 (Hydrogen) is mixed with O2 (Oxygen) stoichiometrically, and the mixture is placed in a chamber of various geometries, with the initial pressure of 6670Pa. For better cellular regularity, the mixture is diluted by 70% argon. For theoretical modeling of the detonation, viscosity, radiation and other dissipation effects are neglected. No heat exchange occurs between the fluid and the walls. All the gases involved are thermally perfect, and the equation of state for perfect gas is used. The chemical model we employ is 9 species (H_2, O_2, O, H, OH, HO_2, H_2O_2, H_2O, Ar) and 19 elementary reaction. All the species have different specific heats, same temperature.

2.2 Governing Equations

The governing equations for the idealized two-dimensional gaseous detonation with N species and a multi-step chemical reaction model are given as

$$U_t + [F(U)]_x + [G(U)]_y = S \tag{2.1}$$

where

$$U = \begin{pmatrix} \rho \\ \rho u \\ \rho v \\ E \\ \rho Y_1 \\ \vdots \\ \rho Y_{N-1} \end{pmatrix}, F(U) = \begin{pmatrix} \rho u \\ \rho u^2 + p \\ \rho uv \\ (E+p)u \\ \rho u Y_1 \\ \vdots \\ \rho u Y_{N-1} \end{pmatrix}, G(U) = \begin{pmatrix} \rho v \\ \rho uv \\ \rho v^2 + p \\ (E+p)v \\ \rho v Y_1 \\ \vdots \\ \rho v Y_{N-1} \end{pmatrix}, S = \begin{pmatrix} 0 \\ 0 \\ 0 \\ 0 \\ \dot{\omega}_1(T, P, Y_1, Y_2, \cdots, Y_{N-1}) \\ \vdots \\ \dot{\omega}_{N-1}(T, P, Y_1, Y_2, \cdots Y_{N-1}) \end{pmatrix} \tag{2.1a}$$

$$E=\rho e=-p+\frac{\rho(\mathrm{u}^2+\mathrm{v}^2)}{2}+\rho h\,.$$

(2.1b)

For the idealized axisymmetric detonation, the governing equations are given as

$$U_t+[F(U)]_x+[G(U)]_r=S\,, \tag{2.2}$$

where

$$U=\begin{pmatrix}\rho\\ \rho u\\ \rho v\\ E\\ \rho Y_1\\ \vdots\\ \rho Y_{N-1}\end{pmatrix},F(U)=\begin{pmatrix}\rho u\\ \rho u^2+p\\ \rho uv\\ (E+p)u\\ \rho uY_1\\ \vdots\\ \rho uY_{N-1}\end{pmatrix},G(U)=\begin{pmatrix}\rho v\\ \rho uv\\ \rho v^2+p\\ (E+p)v\\ \rho vY_1\\ \vdots\\ \rho vY_{N-1}\end{pmatrix},S=\begin{pmatrix}0\\ 0\\ 0\\ 0\\ \dot{\omega}_1\\ \vdots\\ \dot{\omega}_{N-1}\end{pmatrix}-\frac{1}{r}\begin{pmatrix}\rho v\\ \rho uv\\ \rho v^2\\ (E+p)v\\ \rho vY_1\\ \vdots\\ \rho vY_{N-1}\end{pmatrix} \tag{2.2a}$$

$$E=-p+\frac{\rho(\mathrm{u}^2+\mathrm{v}^2)}{2}+\rho h \tag{2.2b}$$

In our present numerical computations, the source term at the central line of the axisymmetric chamber (i.e. $r=0$) is modified as,

$$S=\begin{pmatrix}0\\ 0\\ 0\\ 0\\ \dot{\omega}_1\\ \vdots\\ \dot{\omega}_{N-1}\end{pmatrix} \tag{2.2c}$$

in which $Y_i=\rho_i/\rho$; $R_i=R_u/W_i$; $R=\sum_{i=1}^{N}Y_iR_i$; $Y_N=1-\sum_{i=1}^{N-1}Y_i$;

$$h_i=R_iT\times(\alpha_{1i}+\frac{\alpha_{2i}}{2}T+\frac{\alpha_{3i}}{3}T^2+\frac{\alpha_{4i}}{4}T^3+\frac{\alpha_{5i}}{5}T^4+\frac{\alpha_{6i}}{T})\,,\quad h=\sum_{i=1}^{N}Y_ih_i\,;$$

$$c_{pi} = R_i \times (\alpha_{1i} + \alpha_{2i}T + \alpha_{3i}T^2 + \alpha_{4i}T^3 + \alpha_{5i}T^4), \qquad c_p = \sum_{i=1}^{N} Y_i c_{pi};$$

$$S_i^0 = R_i(\alpha_{1i}\ln T + \alpha_{2i}T + \alpha_{3i}T^2/2 + \alpha_{4i}T^3/3 + \alpha_{5i}T^4/4 + \alpha_{7i});$$

$$H = h + 0.5(u^2 + v^2) = (E + p)/\rho; \qquad P = \sum_{i=1}^{N} \rho_i R_i T; \qquad \gamma = c_p/(c_p - R). \tag{2.2d}$$

The molecular weights of the species are listed in Table 2.1. The thermal parameters $\alpha_{1i} - \alpha_{7i}$ are shown in Table 2.2, which comes from the JANAF (Stull, 1971).

2.3 Numerical Methods

Now we consider solving the Eq. (2.1). In the Eq. (2.1), $[F(U)]_x$ and $[G(U)]_y$ are the convective (hyperbolic) terms, and S is the source terms for the chemical reactions. Because the reactions proceed rapidly once they are triggered, we expect that the source terms are stiff in time. Considering the stiffness of the source terms, we solve the Eq. (2.1) by using the Strang Splitting scheme.

2.3.1 Strang Splitting Scheme

Considering a linear ordinary equation,

$$y' = Ay + By \tag{2.3}$$

which we wish to solve by time splitting. We will use Strang Splitting (Oran and Boris, 1987), which is 2nd order accurate. The method consists of solving two separate ordinary differential equations,

$$y' = Ay \tag{2.4}$$

$$y' = By \tag{2.5}$$

To advance the solution one time step of size Δt, we solve (2.4) with the given initial

data of (2.3) and a time step of $\frac{\Delta t}{2}$. We use the result as initial data to solve for (2.5) with a time step of Δt. Then we use that result as initial data to solve (2.4) again with a time step of $\frac{\Delta t}{2}$.

When this scheme is applied over a series of time steps, we can combine the back-to-back evaluations of (2.4). Thus, we start to solve (2.4) with a time step of $\frac{\Delta t}{2}$. Then we alternate (2.5) and (2.4) with time steps of Δt. And we finish the series with an evaluation of (2.4) with a time step of $\frac{\Delta t}{2}$.

We can apply this methodology to Eq. (2.1) and (2.2). By Strang Splitting, the Eq. (2.1) can be broken into two separate equations,

$$U_t + [F(U)]_x + [G(U)]_y = 0 \tag{2.6}$$

$$U_t = S \tag{2.7}$$

where the first of these is the 2-D Euler equations for multi-species flow without chemical reactions, and the second is a purely reacting equation. In one step, we allow a non-reacting fluid to convect. In the other step, we allow a motionless fluid to react.

2.3.2 Spatial Discretization

In the current work, we use the 5th order WENO-LLF scheme (Jiang and Shu,1996) to compute the convective terms, which is based on the 3rd order ENO-LLF (Shu and Osher, 1988, 1989).

Consider the vector equation (2.6),

$$U_t + [F(U)]_x + [G(U)]_y = 0 .$$

The WENO scheme, which approximates $-F(U)_x$ and $-G(U)_y$ at $x_{i,j}$, will take the

conservative from

$$U_t = -\frac{1}{\Delta x}(F_{i+1/2,j} - F_{i-1/2,j}) - \frac{1}{\Delta y}(G_{i,j+1/2} - G_{i,j-1/2}) \tag{2.8}$$

The numerical flux $F_{i+1/2,j}$ can be computed by the following steps:

1) The generalized Roe's Approximate Riemann Solver is used to calculate the relevant variables which are needed to evaluate the eigenvalues and eigenvectors of the Jacobi matrix in the next step.

   The generalized Roe's Approximate Riemann Solver is the most common solver among the various approximate Riemann solvers, because of its simplicity and its ability to satisfy the jump conditions across discontinuities exactly. To obtain a generalization for a non-equilibrium flow, we use a different, but more direct approach, which has been used by Wada et al. (1989) and Liu et al. (1989). In the generalized Roe Approximate Riemann Solver, we define

$$D = \sqrt{\rho_R / \rho_L} \qquad \text{and} \qquad \Delta() = ()^R - ()^L ,$$

   then

$$Y_i = \frac{Y_i^L + DY_i^R}{1+D}, \quad u = \frac{u^L + Du^R}{1+D}, \quad v = \frac{v^L + Dv^R}{1+D}, \quad H = \frac{H^L + DH^R}{1+D},$$

$$\left(\frac{p}{\rho}\right) = \frac{(p^L/\rho^L) + D(p^R/\rho^R)}{1+D} + \frac{1}{2}\frac{D^2[(u_R - u_L)^2 + (v_R - v_L)^2]}{(1+D)^2},$$

$$p_\rho = p_{\rho R} - k\Delta\rho ,$$

$$p_E = p_{ER} + k[u\Delta(\rho u) + v\Delta(\rho v) - \Delta E] ,$$

$$p_{\rho i} = p_{\rho iR} - k\Delta\rho_i \tag{2.9}$$

where

$$p_{\rho R}=\frac{p_{\rho}^{L}+Dp_{\rho}^{R}}{1+D},\quad p_{ER}=\frac{p_{E}^{L}+Dp_{E}^{R}}{1+D},\quad p_{\rho iR}=\frac{p_{\rho i}^{L}+Dp_{\rho i}^{R}}{1+D},\ p_{E}^{L}=p_{E}^{R}=\gamma-1\ ,$$

$$p_{\rho}^{L}=(\gamma-1)\left(\frac{(u^{L})^{2}+(v^{L})^{2}}{2}-h_{N}^{L}+\frac{c_{p}R_{N}T^{L}}{R}\right),$$

$$p_{\rho}^{R}=(\gamma-1)\left(\frac{(u^{R})^{2}+(v^{R})^{2}}{2}-h_{N}^{R}+\frac{c_{p}R_{N}T^{R}}{R}\right),$$

$$p_{\rho i}^{L}=(\gamma-1)\left(-h_{i}^{L}+h_{N}^{L}+\frac{c_{p}(R_{i}-R_{N})T^{L}}{R}\right),\ p_{\rho i}^{R}=(\gamma-1)\left(-h_{i}^{R}+h_{N}^{R}+\frac{c_{p}(R_{i}-R_{N})T^{R}}{R}\right),$$

$$k=\frac{\overline{p_{\rho R}}\Delta\rho-\overline{p_{ER}}[\overline{u}\Delta(\rho u)+\overline{v}\Delta(\rho v)-\Delta E]+\sum_{j=1}^{N-1}(\overline{p_{\rho jR}}\Delta\rho_{j})-\Delta p}{(\Delta\rho)^{2}+[\overline{u}\Delta(\rho u)+\overline{v}\Delta(\rho v)-\Delta E]^{2}+\sum_{j=1}^{N-1}(\Delta\rho_{j})^{2}} \tag{2.10}$$

2) The eigenvalues and eigenvectors of the Jacobian Matrix of $F(U)$ at the point $x_{i+1/2,j}$ are then evaluated.

Based on the works by Fedkiw et al. (1997), the Jacobian Matrix of F(U), i.e. $\frac{\partial F(U)}{\partial U}$, can be written as $uI+JF+JB$ (2.11)

with,

$$JF=(\frac{dp}{d\rho}\overrightarrow{J_{f}}\ \ \frac{dp}{d(\rho u)}\overrightarrow{J_{f}}\ \ \frac{dp}{d(\rho v)}\overrightarrow{J_{f}}\ \ \frac{dp}{dE}\overrightarrow{J_{f}}\ \ \frac{dp}{d(\rho Y_{1})}\overrightarrow{J_{f}}\ ...\ \frac{dp}{d(\rho Y_{N-1})}\overrightarrow{J_{f}}) \tag{2.12}$$

$$JB=(1\overrightarrow{J_{b}}\ \ u\overrightarrow{J_{b}}\ \ v\overrightarrow{J_{b}}\ \ H\overrightarrow{J_{b}}\ \ Y_{1}\overrightarrow{J_{b}}\ ...\ Y_{N-1}\overrightarrow{J_{b}})^{T} \tag{2.13}$$

where *I* is the *N+3* by *N+3* identity matrix, and

$$\overrightarrow{J_f} = \begin{pmatrix} 0 \\ 1 \\ 0 \\ u \\ 0 \\ \vdots \\ 0 \end{pmatrix}, \quad \overrightarrow{J_b} = \begin{pmatrix} -u \\ 1 \\ 0 \\ 0 \\ 0 \\ \vdots \\ 0 \end{pmatrix} \tag{2.14}$$

The eigenvalues of this Jacobian matrix of F(U) are,

$$\lambda^1 = u - c$$

$$\lambda^2 = \cdots = \lambda^{N+2} = u$$

$$\lambda^{N+3} = u + c \tag{2.15}$$

The left eigenvectors, $\overrightarrow{L^p}$,are the rows of the following matrix.

$$\begin{pmatrix} \frac{b_2}{2} + \frac{u}{2c} + \frac{b_3}{2} & -\frac{b_1 u}{2} - \frac{1}{2c} & -\frac{b_1 v}{2} & \frac{b_1}{2} & -\frac{b_1 Z_1}{2} & \cdots & -\frac{b_1 Z_{N-1}}{2} \\ 1 - b_2 - b_3 & b_1 u & b_1 v & -b_1 & b_1 z_1 & \cdots & b_1 Z_{N-1} \\ v & 0 & -1 & 0 & 0 & \cdots & 0 \\ -Y_1 & 0 & 0 & 0 & & & \\ \vdots & \vdots & \vdots & \vdots & & I & \\ -Y_{N-1} & 0 & 0 & 0 & & & \\ \frac{b_2}{2} - \frac{u}{2c} + \frac{b_3}{2} & -\frac{b_1 u}{2} + \frac{1}{2c} & -\frac{b_1 v}{2} & \frac{b_1}{2} & -\frac{b_1 Z_1}{2} & \cdots & -\frac{b_1 Z_{N-1}}{2} \end{pmatrix} \tag{2.16}$$

The right eigenvectors, $\overrightarrow{R^p}$,are the columns of the following matrix.

$$\begin{pmatrix} 1 & 1 & 0 & 0 & \cdots & 0 & 1 \\ u - c & u & 0 & 0 & \cdots & 0 & u + c \\ v & v & -1 & 0 & \cdots & 0 & v \\ H - uc & H - \frac{1}{b_1} & -v & z_1 & \cdots & z_{N-1} & H + uc \\ Y_1 & Y_1 & 0 & & & & Y_1 \\ \vdots & \vdots & \vdots & & I & & \\ Y_{N-1} & Y_{N-1} & 0 & & & & Y_{N-1} \end{pmatrix} \tag{2.17}$$

Here ***I*** is the N-1 by N-1 identity matrix, and

$$q^2 = u^2 + v^2 \ , \qquad c^2 = \gamma \frac{p}{\rho} \ , \qquad b_1 = \frac{\gamma - 1}{c^2} \ , \qquad b_2 = 1 + b_1 q^2 - b_1 H \ ,$$

$$b_3 = b_1 \sum_{i=1}^{N-1} Y_i z_i \ , \qquad z_i = -\frac{p_{\rho i}}{p_E} \ . \tag{2.18}$$

3) Construct u' and $f(u')$ by using U, $F(U)$ and the left eigenvectors of the Jacob matrix of $F(U)$, which is given by,

$$u' = F\_L^{N+3}(U_{i+1/2,j})U \ , \quad f(u') = F\_L^{N+3}(U_{i+1/2,j})F(U) \tag{2.19}$$

4) Implement the local Lax-Friedrichs (LLF) flux splitting

$$f^+(u') = \frac{1}{2}(f(u') + \alpha u') \ , \quad f^-(u') = \frac{1}{2}(f(u') - \alpha u') \tag{2.20}$$

where the monotone flux $\alpha = \max\limits_{u_{i,j} \le u \le u_{i+1,j}} \left| f'(u') \right|$.

5) Compute $f^+_{i+1/2}$ and $f^-_{i+1/2}$ using WENO scheme, then $f_{i+1/2,j}$.

$$f^+_{i+1/2} = \sum_{r=0}^{2} \omega_r^+ f^{+(r)}_{i+1/2} \ , \quad f^-_{i+1/2} = \sum_{r=0}^{2} \omega_r^- f^{-(r)}_{i+1/2} \ , \quad f_{i+1/2,j} = f^+_{i+1/2} + f^-_{i+1/2} \tag{2.21}$$

where

$$\begin{aligned}
f^{+(0)}_{i+1/2} &= \frac{1}{3} f^+(u'_{i-2}) - \frac{7}{6} f^+(u'_{i-1}) + \frac{11}{6} f^+(u'_i) \\
f^{+(1)}_{i+1/2} &= -\frac{1}{6} f^+(u'_{i-1}) + \frac{5}{6} f^+(u'_i) + \frac{1}{3} f^+(u'_{i+1}) \\
f^{+(2)}_{i+1/2} &= \frac{1}{3} f^+(u'_i) + \frac{5}{6} f^+(u'_{i+1}) - \frac{1}{6} f^+(u'_{i+2}) \\
f^{-(0)}_{i+1/2} &= \frac{1}{3} f^-(u'_{i+2}) - \frac{7}{6} f^-(u'_{i+1}) + \frac{11}{6} f^-(u'_i) \\
f^{-(1)}_{i+1/2} &= -\frac{1}{6} f^-(u'_{i+1}) + \frac{5}{6} f^-(u'_i) + \frac{1}{3} f^-(u'_{i-1}) \\
f^{-(2)}_{i+1/2} &= \frac{1}{3} f^-(u'_i) + \frac{5}{6} f^-(u'_{i-1}) - \frac{1}{6} f^-(u'_{i-2}) \ .
\end{aligned}$$

The weights are $\omega_r^+ = \dfrac{\alpha_r^+}{\sum_{s=0}^{2} \alpha_s^+}$, $\omega_r^- = \dfrac{\alpha_r^-}{\sum_{s=0}^{2} \alpha_s^-}$

$$\alpha_r^+ = \frac{d_r}{(\varepsilon + \beta_r^+)^2} \ , \quad \alpha_r^- = \frac{d_r}{(\varepsilon + \beta_r^-)^2} \ , \quad r = 0,1,2 \ .$$

Here ε is a positive real number which is introduced to avoid the denominator

becoming zero (in the present work, we take ε =10^{-6}). The optimal weight coefficients d_r are chosen: $d_0 = \frac{1}{10}$, $d_1 = \frac{3}{5}$, $d_2 = \frac{3}{10}$. The smoothness measurement of the flux function β_r can be calculated by

$$\beta_0^+ = \frac{13}{12}(f^+(u'_{i-2}) - 2f^+(u'_{i-1}) + f^+(u'_i))^2 + \frac{1}{4}(f^+(u'_{i-2}) - 4f^+(u'_{i-1}) + 3f^+(u'_i))^2$$

$$\beta_1^+ = \frac{13}{12}(f^+(u'_{i-1}) - 2f^+(u'_i) + f^+(u'_{i+1}))^2 + \frac{1}{4}(f^+(u'_{i-1}) - f^+(u'_{i+1}))^2$$

$$\beta_2^+ = \frac{13}{12}(f^+(u'_i) - 2f^+(u'_{i+1}) + f^+(u'_{i+2}))^2 + \frac{1}{4}(3f^+(u'_i) - 4f^+(u'_{i+1}) + f^+(u'_{i+2}))^2$$

$$\beta_0^- = \frac{13}{12}(f^-(u'_i) - 2f^-(u'_{i+1}) + f^-(u'_{i+2}))^2 + \frac{1}{4}(3f^-(u'_i) - 4f^-(u'_{i+1}) + f^-(u'_{i+2}))^2$$

$$\beta_1^- = \frac{13}{12}(f^-(u'_{i+1}) - 2f^-(u'_i) + f^-(u'_{i-1}))^2 + \frac{1}{4}(f^-(u'_{i+1}) - f^-(u'_{i-1}))^2$$

$$\beta_2^- = \frac{13}{12}(f^-(u'_i) - 2f^-(u'_{i-1}) + f^-(u'_{i-2}))^2 + \frac{1}{4}(3f^-(u'_i) - 4f^-(u'_{i-1}) + f^-(u'_{i-2}))^2$$

6) Use the scalar numerical flux functions along with the right eigenvectors to reconstruct the vector numerical flux function $F_{i+1/2,j}$.

$$F_{i+1/2,j}^{N+3} = f_{i+1/2,j} F\_R^{N+3}(U_{i+1/2,j})$$

$$F_{i+1/2,j} = \sum_{N+3} F_{i+1/2,j}^{N+3} \tag{2.22}$$

Similarly, the numerical flux $G_{i,j+1/2}$ can be computed by the following steps:

1) Evaluate the eigenvalues and eigenvectors of the Jacobi Matrix of $G(U)$ at the point $y_{i,j+1/2}$.

Based on the works by Fedkiw et al. (1997), the Jacob matrix of G(U), i.e. $\frac{\partial G(U)}{\partial U}$, can be written as $uI + JF + JB$ (2.23)

with,

$$JF = (\frac{dp}{d\rho}\overrightarrow{J_f} \ \frac{dp}{d(\rho u)}\overrightarrow{J_f} \ \frac{dp}{d(\rho v)}\overrightarrow{J_f} \ \frac{dp}{dE}\overrightarrow{J_f} \ \frac{dp}{d(\rho Y_1)}\overrightarrow{J_f} \ldots \frac{dp}{d(\rho Y_{N-1})}\overrightarrow{J_f}) \tag{2.24}$$

$$JB = (1\overrightarrow{J_b} \ u\overrightarrow{J_b} \ v\overrightarrow{J_b} \ H\overrightarrow{J_b} \ Y_1\overrightarrow{J_b} \ldots Y_{N-1}\overrightarrow{J_b})^T \tag{2.25}$$

where I is the $N+3$ by $N+3$ identity matrix, and

$$\overrightarrow{J_f} = \begin{pmatrix} 0 \\ 0 \\ 1 \\ v \\ 0 \\ \vdots \\ 0 \end{pmatrix}, \quad \overrightarrow{J_b} = \begin{pmatrix} -v \\ 0 \\ 1 \\ 0 \\ 0 \\ \vdots \\ 0 \end{pmatrix} \tag{2.26}$$

The eigenvalues of this Jacobian matrix of G(U) are,

$$\lambda^1 = v - c$$

$$\lambda^2 = \cdots = \lambda^{N+2} = v$$

$$\lambda^{N+3} = v + c \tag{2.27}$$

The left eigenvectors, $\overrightarrow{L^p}$,are the rows of the following matrix.

$$\begin{pmatrix} \frac{b_2}{2}+\frac{v}{2c}+\frac{b_3}{2} & -\frac{b_1 u}{2} & -\frac{b_1 v}{2}-\frac{1}{2c} & \frac{b_1}{2} & -\frac{b_1 Z_1}{2} & \cdots & -\frac{b_1 Z_{N-1}}{2} \\ 1-b_2-b_3 & b_1 u & b_1 v & -b_1 & b_1 z_1 & \cdots & b_1 Z_{N-1} \\ -u & 1 & 0 & 0 & 0 & \cdots & 0 \\ -Y_1 & 0 & 0 & 0 & & & \\ \vdots & \vdots & \vdots & \vdots & & I & \\ -Y_{N-1} & 0 & 0 & 0 & & & \\ \frac{b_2}{2}-\frac{v}{2c}+\frac{b_3}{2} & -\frac{b_1 u}{2} & -\frac{b_1 v}{2}+\frac{1}{2c} & \frac{b_1}{2} & -\frac{b_1 Z_1}{2} & \cdots & -\frac{b_1 Z_{N-1}}{2} \end{pmatrix} \tag{2.28}$$

The right eigenvectors, $\overrightarrow{R^p}$,are the columns of the following matrix.

$$\begin{pmatrix} 1 & 1 & 0 & 0 & \cdots & 0 & 1 \\ u & u & 1 & 0 & \cdots & 0 & u \\ v-c & v & 0 & 0 & \cdots & 0 & v+c \\ H-vc & H-\frac{1}{b_1} & u & z_1 & \cdots & z_{N-1} & H+vc \\ Y_1 & Y_1 & 0 & & & & Y_1 \\ \vdots & \vdots & \vdots & & I & & \\ Y_{N-1} & Y_{N-1} & 0 & & & & Y_{N-1} \end{pmatrix} \tag{2.29}$$

Here ***I*** is the N-1 by N-1 identity matrix, and

$$q^2 = u^2 + v^2 \ , \qquad c^2 = \gamma \frac{p}{\rho} \ , \qquad b_1 = \frac{\gamma - 1}{c^2} \ , \qquad b_2 = 1 + b_1 q^2 - b_1 H \ ,$$

$$b_3 = b_1 \sum_{i=1}^{N-1} Y_i z_i \ , \qquad z_i = -\frac{p_{\rho i}}{p_E} \ . \tag{2.30}$$

2) Construct u' and $g(u')$ by using U, $G(U)$ and the left eigenvectors of the Jacob matrix of $G(U)$, which is given by,

$$u' = G\_L^{N+3}(U_{i+1/2,j})U \ , \quad g(u') = G\_L^{N+3}(U_{i+1/2,j})G(U) \tag{2.31}$$

3) Implement the local lax-Friedrichs (LLF) flux splitting

$$g^+(u') = \frac{1}{2}(g(u') + \alpha u') \ , \quad g^-(u') = \frac{1}{2}(g(u') - \alpha u') \tag{2.32}$$

where the monotone flux $\alpha = \max_{u_{i,j} \le u \le u_{i,j+1}} \left| g'(u') \right|$.

4) Compute $g^+_{j+1/2}$ and $g^-_{j+1/2}$ using WENO scheme, then $g_{i,j+1/2}$.

$$g^+_{j+1/2} = \sum_{r=0}^{2} \omega_r^+ g^{+(r)}_{j+1/2} \ , \quad g^-_{j+1/2} = \sum_{r=0}^{2} \omega_r^- g^{-(r)}_{j+1/2} \ , \quad g_{j+1/2,j} = g^+_{j+1/2} + g^-_{j+1/2} \tag{2.33}$$

where

$$g^{+(0)}_{j+1/2} = \frac{1}{3} g^+(u'_{j-2}) - \frac{7}{6} g^+(u'_{j-1}) + \frac{11}{6} g^+(u'_j)$$

$$g^{+(1)}_{j+1/2} = -\frac{1}{6} g^+(u'_{j-1}) + \frac{5}{6} g^+(u'_j) + \frac{1}{3} g^+(u'_{j+1})$$

$$g^{+(2)}_{j+1/2} = \frac{1}{3} g^+(u'_j) + \frac{5}{6} g^+(u'_{j+1}) - \frac{1}{6} g^+(u'_{j+2})$$

$$g^{-(0)}_{j+1/2} = \frac{1}{3} g^-(u'_{j+2}) - \frac{7}{6} g^-(u'_{j+1}) + \frac{11}{6} g^-(u'_j)$$

$$g^{-(1)}_{j+1/2} = -\frac{1}{6} g^-(u'_{j+1}) + \frac{5}{6} g^-(u'_j) + \frac{1}{3} g^-(u'_{j-1})$$

$$g^{-(2)}_{j+1/2} = \frac{1}{3} g^-(u'_j) + \frac{5}{6} g^-(u'_{j-1}) - \frac{1}{6} g^-(u'_{j-2})$$

The weights $\omega_r^+ = \dfrac{\alpha_r^+}{\sum_{s=0}^{2} \alpha_s^+}$, $\omega_r^- = \dfrac{\alpha_r^-}{\sum_{s=0}^{2} \alpha_s^-}$, $r = 0,1,2$,

$$\alpha_r^+ = \frac{d_r}{(\varepsilon + \beta_r^+)^2} \ , \quad \alpha_r^- = \frac{d_r}{(\varepsilon + \beta_r^-)^2} \ .$$

ε is a positive real number which is introduced to avoid the denominator

becoming zero (in the present work, we take ε =10^{-6}). The optimal weight coefficients d_r are chosen: $d_0 = \frac{1}{10}$, $d_1 = \frac{3}{5}$, $d_2 = \frac{3}{10}$. The smoothness measurement of the flux function β_r can be calculated by

$$\beta_0^+ = \frac{13}{12}(g^+(u'_{j-2}) - 2g^+(u'_{j-1}) + g^+(u'_j))^2 + \frac{1}{4}(g^+(u'_{j-2}) - 4g^+(u'_{j-1}) + 3g^+(u'_j))^2$$

$$\beta_1^+ = \frac{13}{12}(g^+(u'_{j-1}) - 2g^+(u'_j) + g^+(u'_{j+1}))^2 + \frac{1}{4}(g^+(u'_{j-1}) - g^+(u'_{j+1}))^2$$

$$\beta_2^+ = \frac{13}{12}(g^+(u'_j) - 2g^+(u'_{j+1}) + g^+(u'_{j+2}))^2 + \frac{1}{4}(3g^+(u'_j) - 4g^+(u'_{j+1}) + g^+(u'_{j+2}))^2$$

$$\beta_0^- = \frac{13}{12}(g^-(u'_j) - 2g^-(u'_{j+1}) + g^-(u'_{j+2}))^2 + \frac{1}{4}(3g^-(u'_j) - 4g^-(u'_{j+1}) + g^-(u'_{j+2}))^2$$

$$\beta_1^- = \frac{13}{12}(g^-(u'_{j+1}) - 2g^-(u'_j) + g^-(u'_{j-1}))^2 + \frac{1}{4}(g^-(u'_{j+1}) - g^-(u'_{j-1}))^2$$

$$\beta_2^- = \frac{13}{12}(g^-(u'_i) - 2g^-(u'_{i-1}) + g^-(u'_{i-2}))^2 + \frac{1}{4}(3g^-(u'_i) - 4g^-(u'_{i-1}) + g^-(u'_{i-2}))^2$$

5) Use the scalar numerical flux functions along with the right eigenvectors to reconstruct the vector numerical flux function $G_{i,j+1/2}$.

$$G_{i,j+1/2}^{N+3} = g_{i,j+1/2} G\_R^{N+3}(U_{i,j+1/2})$$

$$G_{i,j+1/2} = \sum_{N+3} G_{i,j+1/2}^{N+3} \tag{2.34}$$

2.3.3 Temporal Discretization

Eq. (2.8) can be expressed as

$$U_t = L(U) \tag{2.35}$$

The spatial operator $L(U)$ was already solved in Section 2.3.2.

An attractive way for advancing this equation in time is via TVD Runge-Kutta methods (Shu, 1988), which restricts the occurrence of non-physical oscillations in the solution. This is an extremely important property of a numerical scheme when considering compressible flow which may have shocks and/or contact discontinuities

present. Herein, we will consider the third order TVD Runge-Kutta method.

The third order TVD Runge-Kutta method is given by

$$\begin{aligned} U^{(1)} &= U^n + \Delta t L(U^n) \\ U^{(2)} &= \frac{3}{4}U^n + \frac{1}{4}U^{(1)} + \frac{1}{4}\Delta t L(U^{(1)}) \\ U^{n+1} &= \frac{1}{3}U^n + \frac{2}{3}U^{(2)} + \frac{2}{3}\Delta t L(U^{(2)}) \end{aligned} \tag{2.36}$$

The intermediate values of the variable $U^{(1)}$ and $U^{(2)}$ are used only for computational purpose. Note that this scheme is stable under the CFL restriction of,

$$(\Delta t)(\max|\lambda_i|, |\lambda_{i+1}|, |\lambda_j||\lambda_{j+1}|) \le 1.0 \tag{2.37}$$

where λ_i and λ_j are the eigenvalues of the Jacobian matrices of $F(U)$ and $G(U)$, respectively.

2.3.4 Chemical Kinetics

Now, we consider solving Eq. (2.7). For Eq. (2.7), the first four equations imply that $\rho_t = (\rho u)_t = (\rho v)_t = E_t = 0$. Thus, ρ, u, v and E are constants. Using the fact that ρ is constant, we see that solving Eq. (2.7) reduces to solving the following differential equations,

$$\begin{pmatrix} Y_1 \\ Y_2 \\ \vdots \\ Y_8 \end{pmatrix}_t = \begin{pmatrix} \dfrac{\dot{\omega}_1(T, \rho, Y_1, Y_2, \cdots Y_8)}{\rho} \\ \dfrac{\dot{\omega}_2(T, \rho, Y_1, Y_2, \cdots Y_8)}{\rho} \\ \vdots \\ \dfrac{\dot{\omega}_8(T, \rho, Y_1, Y_2, \cdots Y_8)}{\rho} \end{pmatrix} \tag{2.38}$$

where ρ is a constant. We solve this stiff system with the numerical package of CHEMEQ (Young, 1979), which uses the selected asymptotic integration method

(SAIM) to solve the chemical reaction equations. This one-step, 2nd order accuracy scheme can deal with the stiffness of the system well without the need of evaluating the Jacobian matrices. The method for calculating the finite production rate of each chemical species, $\dot{\omega}_i$, is shown in the next section.

2.3.5 Elementary Chemical Reactions

In this work, a chemical model of 9 species, 19 elementary reactions is used to simulate the hydrogen-oxygen hydrogen-oxygen combustion (Wilson and MacCormack, 1990), as shown in Table 2.3. The reacting species are H_2, O_2, O, H, OH, HO_2, H_2O_2, H_2O and dilute argon is added to the gas mixture. The chemical reactions can be uniformly expressed as:

$$\sum_{i=1}^{8} v_{ik}^{'} x_i \quad \underset{k_{b,k}}{\overset{k_{f,k}}{\rightleftharpoons}} \quad \sum_{i=1}^{8} v_{ik}^{"} x_i \qquad \text{k=1, 2,3…19} \tag{2.39}$$

where x_i denotes the *i*th species. The forward and backward reaction rate constants, $K_{f,k}, K_{b,k}$, are controlled by the Arrhenius law and chemical equilibrium conditions. They are given by

$$K_{f,k} = A_k T^{nk} \exp(-E_{ak}/RT) \quad \text{and} \quad K_{b,k} = K_{f,k}(RT/P_{atm})^{\sum_{i=1}^{9}(v_{ik}^{"}-v_{ik}^{'})} / K_{p,k}, \tag{2.41}$$

where $K_{p,k} = \exp\left[\sum_{i=1}^{9}\left\{\left(v_{ik}^{"} - v_{ik}^{'}\right)\left(S_i^0/R - h_i/R_iT\right)\right\}\right]$. Herein, the finite production rate of each chemical species, $\dot{\omega}_i$, is obtained by combining the elementary chemical reactions in the kinetic model so that

$$\dot{\omega}_i = W_i \sum_{k=1}^{K}(v_{ik}^{"} - v_{ik}^{'})\left\{\sum_{i=1}^{N}\alpha_{ik}C_{xi}\right\}\left\{K_{f,k}\prod_{i=1}^{N}(C_{xi})^{v_{ik}^{'}} - K_{b,k}\prod_{i=1}^{N}(C_{xi})^{v_{ik}^{"}}\right\}. \tag{2.42}$$

The third body coefficients α_{ik} are given as following: α_{1k} =2.5(H_2), α_{8k} =16.0

(H_2O), other α_{ik}=0;

Besides, the matrices of the forward and backward chemical stoichiometric coefficients v' and v'' are shown as following:

$$v' = \begin{Bmatrix} 0 & 1 & 0 & 1 & 0 & 0 & 0 & 0 & 0 \\ 1 & 0 & 1 & 0 & 0 & 0 & 0 & 0 & 0 \\ 1 & 0 & 0 & 0 & 1 & 0 & 0 & 0 & 0 \\ 0 & 0 & 1 & 0 & 0 & 0 & 0 & 1 & 0 \\ 1 & 0 & 0 & 0 & 0 & 0 & 0 & 1 & 0 \\ 0 & 0 & 2 & 0 & 0 & 0 & 0 & 0 & 1 \\ 0 & 0 & 1 & 0 & 0 & 0 & 0 & 0 & 1 \\ 0 & 0 & 0 & 1 & 1 & 0 & 0 & 0 & 1 \\ 0 & 1 & 0 & 1 & 0 & 0 & 0 & 0 & 1 \\ 0 & 0 & 0 & 1 & 0 & 1 & 0 & 0 & 0 \\ 0 & 0 & 0 & 1 & 0 & 1 & 0 & 0 & 0 \\ 0 & 0 & 1 & 0 & 0 & 1 & 0 & 0 & 0 \\ 0 & 0 & 0 & 0 & 1 & 1 & 0 & 0 & 0 \\ 0 & 0 & 0 & 0 & 0 & 2 & 0 & 0 & 0 \\ 0 & 0 & 0 & 0 & 0 & 0 & 1 & 0 & 1 \\ 0 & 0 & 0 & 1 & 0 & 0 & 1 & 0 & 0 \\ 0 & 0 & 0 & 1 & 0 & 0 & 1 & 0 & 0 \\ 0 & 0 & 1 & 0 & 0 & 0 & 1 & 0 & 0 \\ 0 & 0 & 0 & 0 & 1 & 0 & 1 & 0 & 0 \end{Bmatrix} \qquad v'' = \begin{Bmatrix} 0 & 0 & 1 & 0 & 1 & 0 & 0 & 0 & 0 \\ 0 & 0 & 0 & 1 & 1 & 0 & 0 & 0 & 0 \\ 0 & 0 & 0 & 1 & 0 & 0 & 0 & 1 & 0 \\ 0 & 0 & 0 & 0 & 2 & 0 & 0 & 0 & 0 \\ 0 & 0 & 0 & 2 & 0 & 0 & 0 & 0 & 1 \\ 0 & 1 & 0 & 0 & 0 & 0 & 0 & 0 & 1 \\ 0 & 0 & 0 & 0 & 1 & 0 & 0 & 0 & 1 \\ 0 & 0 & 0 & 0 & 0 & 0 & 0 & 1 & 1 \\ 0 & 0 & 0 & 0 & 0 & 1 & 0 & 0 & 1 \\ 1 & 1 & 0 & 0 & 0 & 0 & 0 & 0 & 0 \\ 0 & 0 & 0 & 0 & 2 & 0 & 0 & 0 & 0 \\ 0 & 1 & 0 & 0 & 1 & 0 & 0 & 0 & 0 \\ 0 & 1 & 0 & 0 & 0 & 0 & 0 & 1 & 0 \\ 0 & 1 & 0 & 0 & 0 & 0 & 1 & 0 & 0 \\ 0 & 0 & 0 & 0 & 2 & 0 & 0 & 0 & 1 \\ 0 & 0 & 0 & 0 & 1 & 0 & 0 & 1 & 0 \\ 1 & 0 & 0 & 0 & 0 & 1 & 0 & 0 & 0 \\ 0 & 0 & 0 & 0 & 1 & 1 & 0 & 0 & 0 \\ 0 & 0 & 0 & 0 & 0 & 1 & 0 & 1 & 0 \end{Bmatrix}$$

$v'_{k,9}$ stands for the third body $v''_{k,9}$ stands for the third body effect

$$v''- v' = \begin{Bmatrix} 0 & -1 & 1 & -1 & 1 & 0 & 0 & 0 & 0 \\ -1 & 0 & -1 & 1 & 1 & 0 & 0 & 0 & 0 \\ -1 & 0 & 0 & 1 & -1 & 0 & 0 & 1 & 0 \\ 0 & 0 & -1 & 0 & 2 & 0 & 0 & -1 & 0 \\ -1 & 0 & 0 & 2 & 0 & 0 & 0 & 0 & 1 \\ 0 & 1 & -2 & 0 & 0 & 0 & 0 & 0 & -1 \\ 0 & 0 & -1 & -1 & 1 & 0 & 0 & 0 & -1 \\ 0 & 0 & 0 & -1 & -1 & 0 & 0 & 1 & -1 \\ 0 & -1 & 0 & -1 & 0 & 1 & 0 & 0 & -1 \\ 1 & 1 & 0 & -1 & 0 & -1 & 0 & 0 & 0 \\ 0 & 0 & 0 & -1 & 2 & -1 & 0 & 0 & 0 \\ 0 & 1 & -1 & 0 & 1 & -1 & 0 & 0 & 0 \\ 0 & 1 & 0 & 0 & -1 & -1 & 0 & 1 & 0 \\ 0 & 1 & 0 & 0 & 0 & -2 & 1 & 0 & 0 \\ 0 & 0 & 0 & 0 & 2 & 0 & -1 & 0 & 1 \\ 0 & 0 & 0 & -1 & 1 & 0 & -1 & 1 & 0 \\ 1 & 0 & 0 & -1 & 0 & 1 & -1 & 0 & 0 \\ 0 & 0 & -1 & 0 & 1 & 1 & -1 & 0 & 0 \\ 0 & 0 & 0 & 0 & -1 & 1 & -1 & 1 & 0 \end{Bmatrix}$$

$$(v'' - v')_{k,9} = \sum_{i=1}^{8} (v''_{ik} - v'_{ik})$$

2.3.6 Solving for Temperature

In order to solve Eq. (2.38), we need to solve the temperature T first, which is a function of the mass fractions.

Based on (2.2c), we get,

$$h = \frac{1}{\rho}\sum_{i=1}^{N}\rho_i R_i(\alpha_{1i}T + \frac{\alpha_{2i}}{2}T^2 + \frac{\alpha_{3i}}{3}T^3 + \frac{\alpha_{4i}}{4}T^4 + \frac{\alpha_{5i}}{5}T^5 + \alpha_{6i}) \tag{2.43}$$

Substituting it to (2b) yields,

$$E = \sum_{i=1}^{N}\rho_i R_i\left\{(\alpha_{1i}-1)T + \frac{\alpha_{2i}}{2}T^2 + \frac{\alpha_{3i}}{3}T^3 + \frac{\alpha_{4i}}{4}T^4 + \frac{\alpha_{5i}}{5}T^5 + \alpha_{6i}\right\} + \frac{\rho u^2}{2} \tag{2.44}$$

Then we can use Newton-Rhapson method to solve for the temperature:

$$F(T) = \sum_{i=1}^{N}\rho_i R_i\left\{(\alpha_{1i}-1)T + \frac{\alpha_{2i}}{2}T^2 + \frac{\alpha_{3i}}{3}T^3 + \frac{\alpha_{4i}}{4}T^4 + \frac{\alpha_{5i}}{5}T^5 + \alpha_{6i}\right\} + \frac{\rho u^2}{2} - E$$

$$= b_0 + b_1 T + b_2 T^2 + b_3 T^3 + b_4 T^4 + b_5 T^5 \tag{2.45}$$

where $b_0 = \sum_{i=1}^{N}\rho_i R_i a_{6i} + \frac{\rho}{2}u^2 - E$, $b_1 = \sum_{i=1}^{N}\rho_i R_i(a_{1i}-1)$, $b_2 = \frac{1}{2}\sum_{i=1}^{N}\rho_i R_i a_{2i}$,

$b_3 = \frac{1}{3}\sum_{i=1}^{N}\rho_i R_i a_{3i}$, $b_4 = \frac{1}{4}\sum_{i=1}^{N}\rho_i R_i a_{4i}$, $b_5 = \frac{1}{5}\sum_{i=1}^{N}\rho_i R_i a_{5i}$

Also $F'(T) = b_1 + 2b_2 T + 3b_3 T^2 + 4b_4 T^3 + 5b_5 T^4$. (2.46)

Thus, the iteration formula can be expressed as:

$$T_{new} = T_{old} - \frac{F(T_{old})}{F'(T_{old})} \tag{2.47}$$

2.3.7 Normalization

In order to minimize the errors caused by extremely big or small values, non-dimensionalization serving as normalization is implemented. In our computation, four non-dimensional parameters are used:

1) l^* : the theoretical length of the reaction zone of 1-D gaseous detonation,

2) ρ_∞^* : the initial density ahead of the leading shock wave,

3) a_∞^* : the initial sonic speed ahead of the leading shock wave,

4) T_∞^* : the initial temperature ahead of the leading shock wave.

The parameters involved are non-dimensionalized as following,

$$x=\frac{x^*}{l^*},\ u=\frac{u^*}{a_\infty^*},\ P=\frac{P^*}{\rho_\infty^* a_\infty^{*2}},\ \rho=\frac{\rho^*}{\rho_\infty^*},\ T=\frac{T^*}{T_\infty^*},\ t=\frac{t^* a_\infty^*}{l^*}$$

$$e=\frac{e^*}{\rho_\infty^* a_\infty^{*2}},\ h=\frac{h^*}{a_\infty^{*2}},\ \dot{\omega}=\frac{\dot{\omega}^* l^*}{\rho_\infty^* a_\infty^*},\ \rho_i=\frac{\rho_i^*}{\rho_\infty^*},\ R_i=\frac{R_i^* a_\infty^*}{T_\infty^*}.$$

Note that for simplicity, the thermal parameters in terms of α (shown in Table 2.2) were not normalized in the present work, and we still use the unit system of (m-sec-mol-cal-K).

2.4 Message Passing Interface (MPI)

Due to the stiffness of the governing equations mentioned above, it takes a huge amount of CPU time to advance the equations in time. In order to improve the computational efficiency, we consider using parallel programming technology. In the present work, the Message Passing Interface (MPI) technology is employed to parallelize the computation job to multiple computers with distributed memory.

MPI, the Message Passing Interface, is a standardized and portable message passing system designed by a group of researchers from academia and industry to function on a wide variety of parallel computers. The standardization process, involving over 80 people from 40 organizations, began with the Workshop on Standards for Message

Passing in a Distributed Memory Environment in 1992. A preliminary draft proposal, known as MPI1, was put forward in 1992, and a revised version was completed in 1993.

An MPI program consists of autonomous processes, executing their own code, in a Multiple Instruction, Multiple Data (MIMD) style. In our current MPI design, the codes executed by each process are identical. The only difference among these processes is the initial conditions given to them. Using the initial conditions, each process executes its own code independently. After advancing for the first time step, each process exchanges its boundaries with its adjacent processes, and then continues advancing in time. The block partitioning with overlap and the communication pattern of the processes are shown in Figure 2.1.

In this pattern, a total of N processes are employed. After every time step, each process needs to communicate with its adjacent processes to obtain some of its boundary conditions. Besides, for Process 0, the left boundary is the physical boundary, and for Process N-1, the right boundary is the physical boundary.

Table 2.1 Molecular Weight of Each Species (g)

	H_2	O_2	O	H	OH	HO_2	H_2O_2	H_2O	Ar
W_i	2.0159	31.9988	15.9994	1.0079	17.0073	33.0067	34.0147	18.0153	39.9480

Table 2.2 Thermal Parameters (K) (Stull 1971)

	H_2	O_2	O
a_{1i}	0.30172281×10^{1}	0.32524882×10^{1}	0.28063958×10^{1}
a_{2i}	0.88727912×10^{-3}	0.13058732×10^{-2}	-0.55153963×10^{-3}
a_{3i}	-0.25767118×10^{-6}	-0.49629683×10^{-6}	0.32797643×10^{-6}
a_{4i}	0.53895544×10^{-10}	0.10165240×10^{-9}	$-0.78048938\times10^{-10}$
a_{5i}	$-0.45914741\times10^{-14}$	$-0.79663144\times10^{-14}$	0.66494386×10^{-14}
a_{6i}	-0.93687332×10^{3}	-0.10235836×10^{4}	0.29176829×10^{5}
a_{7i}	-0.17284120×10^{1}	0.57751164×10^{1}	0.35329500×10^{1}
	H	OH	HO_2
a_{1i}	0.25017076×10^{1}	0.37882016×10^{1}	0.34491550×10^{1}
a_{2i}	0.44689446×10^{-15}	-0.67413256×10^{3}	0.33062160×10^{-2}
a_{3i}	$-0.34801365\times10^{-18}$	0.79813467×10^{-6}	-0.12868533×10^{-5}
a_{4i}	0.98627573×10^{-22}	-0.22767644×10^{-9}	0.23032337×10^{-9}
a_{5i}	$-0.92216057\times10^{-26}$	0.20492525×10^{-13}	$-0.15522042\times10^{-13}$
a_{6i}	0.25489817×10^{5}	0.36435184×10^{4}	0.13534267×10^{4}
a_{7i}	-0.46008683	0.68024710	0.68028889×10^{1}
	H_2O_2	H_2O	Ar
a_{1i}	0.31958586×10^{1}	0.37199834×10^{1}	0.25000000×10^{1}
a_{2i}	0.75744334×10^{-2}	0.10936956×10^{-2}	0.0
a_{3i}	-0.21470192×10^{-5}	0.31652569×10^{-6}	0.0
a_{4i}	-0.21868401×10^{-8}	-0.16872305×10^{-9}	0.0
a_{5i}	0.11687370×10^{-11}	0.17920633×10^{-13}	0.0
a_{6i}	-0.17647714×10^{5}	-0.30265156×10^{5}	-0.74537502×10^{3}
a_{7i}	0.76737985×10^{1}	0.11801086×10^{1}	0.43660006×10^{1}

Table 2.3 Reaction Mechanism and the Related Parameters (cm^3-mole-sec-cal)

		A_k	n_k	E_{ak}
1)	$H+O_2 \rightleftharpoons O+OH$	6.00×10^{14}	0.	16790
2)	$O+H_2 \rightleftharpoons H+OH$	1.07×10^{4}	2.80	5921
3)	$OH+H_2 \rightleftharpoons H+H_2O$	7.00×10^{12}	0.	4400
4)	$O+H_2O \rightleftharpoons OH+OH$	1.50×10^{10}	1.14	17190
5)	$H_2+M \rightleftharpoons H+H+M$	2.90×10^{18}	-1.00	104330
6)	$O+O+M \rightleftharpoons O_2+M$	6.17×10^{15}	-0.50	0
7)	$O+H+M \rightleftharpoons OH+M$	1.00×10^{15}	0.	-497
8)	$H+OH+M \rightleftharpoons H_2O+M$	8.80×10^{21}	-2.00	0
9)	$H+O_2+M \rightleftharpoons HO_2+M$	6.76×10^{19}	-1.42	0
10)	$HO_2+H \rightleftharpoons H_2+O_2$	2.50×10^{13}	0.	693
11)	$HO_2+H \rightleftharpoons OH+OH$	2.51×10^{13}	0.	1910
12)	$HO_2+O \rightleftharpoons OH+O_2$	2.00×10^{13}	0.	0
13)	$HO_2+OH \rightleftharpoons H_2O+O_2$	1.20×10^{13}	0.	0
14)	$HO_2+HO_2 \rightleftharpoons H_2O_2+O_2$	1.82×10^{12}	0.	0
15)	$H_2O_2+M \rightleftharpoons OH+OH+M$	3.19×10^{17}	0.	47100
16)	$H_2O_2+H \rightleftharpoons H_2O+OH$	3.20×10^{14}	0.	9000
17)	$H_2O_2+H \rightleftharpoons H_2+HO_2$	4.79×10^{13}	0.	7950
18)	$H_2O_2+O \rightleftharpoons OH+HO_2$	9.54×10^{6}	2.00	3970
19)	$H_2O_2+OH \rightleftharpoons H_2O+HO_2$	1.00×10^{13}	0.	1800

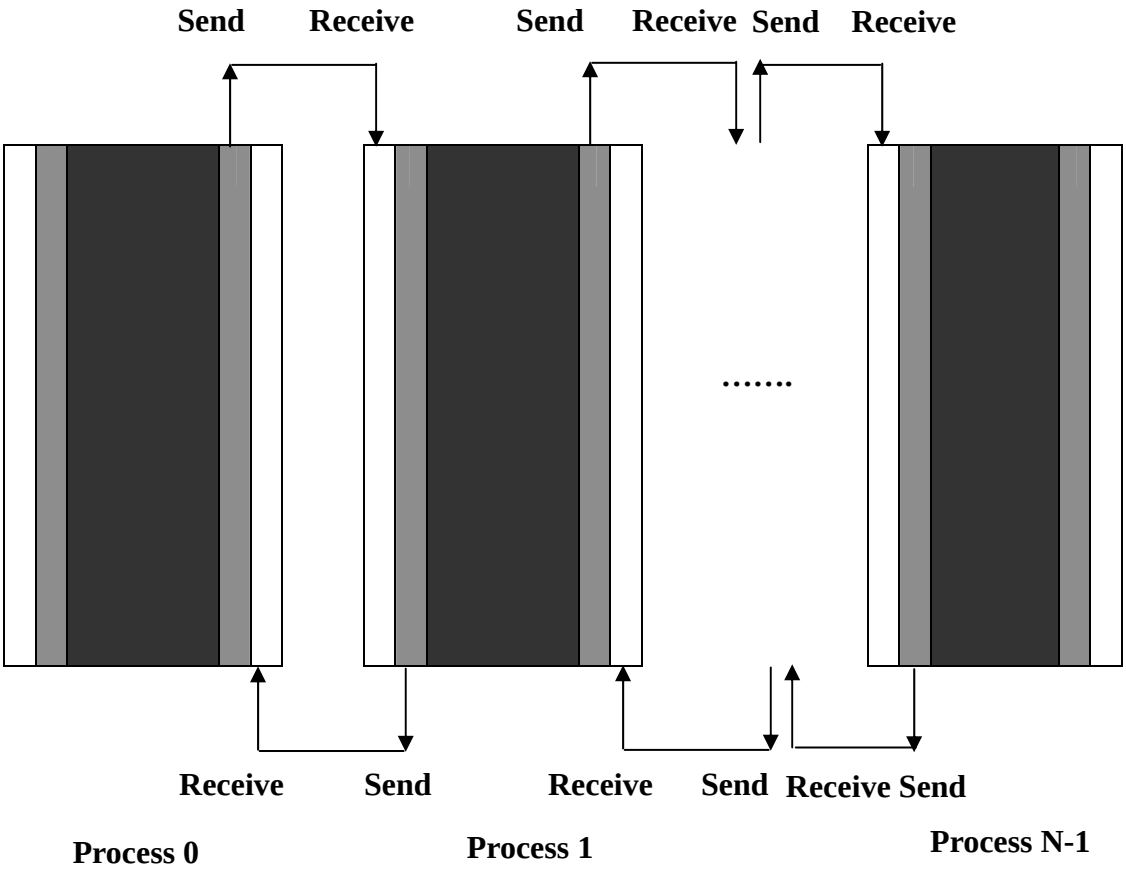

Figure 2.1 Block Partition with overlap and communication pattern

Chapter 3 Code Validation

Computational results for several test cases are presented in this section. In order to demonstrate the accuracy of the present numerical method, these computed results are compared with those obtained by other numerical methods, experiments or analytical solutions wherever possible. Test cases 1-6 are chosen to validate the pure flow part of the code without chemical reactions，in which a calorically perfect ideal gas is assumed with the specific heat ratio γ =1.4. Firstly, the one-dimensional problems are investigated, which include Sod's shock tube problem and Lax-Harten shock tube problem. Secondly, the two-dimensional problems are considered, involving the formation and reflection of an oblique shock wave, which include Steady two-dimensional oblique shock wave (test case 3) and Supersonic flow past a wedge (test case 4). Finally, two axisymmetric cases are employed to validate the code of the Euler equations in an axisymmetric geometry. Test case 5 is the shock wave reflection in a converging circular chamber with different oblique angles, while Test case 6 shows the formed oblique shock as the supersonic flow passes through a cone. For the two one-dimensional cases, a grid study was also made to evaluate the grid convergence and 'measure' the convergence rate. (In addition, in order to validate the code of the combined flow and chemical reactions, the one-dimensional detonation wave is simulated, which is presented in Chapter 4.) In the simulation of the one-dimensional detonation wave, a thermally perfect ideal gas is assumed and γ is calculated using the thermodynamics relation $\gamma = c_p/(c_p - R)$, where $c_p = \sum_{i=1}^{9} Y_i c_{pi}$

and $R = \sum_{i=1}^{9} Y_i R_i$. The effects of mesh sizes on the simulated detonation wave and the related detonation parameters were also studied.

3.1 One-dimensional Cases

Test case 1. Sod's shock tube problem

The classic Sod's shock tube problem is computed in this test case using 100 cells, and the computational domain is assumed to be unity. Both of the ends in this tube are closed, i.e. the boundary conditions imposed on the left-hand end and the right-hand end are both reflecting boundary conditions. The initial conditions in the present computation are given as follows:

$$\rho = 1.000, u = 0, p = 1.0, 0 \le x < 0.5,$$
$$\rho = 0.125, u = 0, p = 0.1, 0.5 \le x \le 1.$$

The initial data are those of the Riemann problem proposed by Sod as also can be found in Osher (1984), which has become a standard test problem for many other published works. The left-half side in the tube is the high-pressure, high-density zone, which is separated from the low-pressure, low-density zone on the right-half side by a membrane placed in the middle of the tube. After the membrane is ruptured, a shock wave, a contact discontinuity and some expansion waves will be observed. The shock wave moves rightwards, while the expansion waves move leftwards. Figure 3.1 compares the computed density, velocity, and pressure profiles with the exact solution at t=0.2, which depicts good concurrence.

Test case 2. Lax-Harten shock tube problem

This is another well known test case for the shock tube problem. We present calculations for the Riemann problem

$$\rho = 0.445, u = 0.7, p = 3.52773, 0 \le x < 0.5,$$
$$\rho = 0.500, u = 0.0, p = 0.57100, 0.5 \le x \le 1$$

used by Lax and Harten (Lax 1954; Harten 1983). The boundary conditions imposed on the left-hand end and the right-hand end in this tube are both reflecting boundary conditions. The computation is performed using only 100 cells in this test case, and the computational domain is assumed to be unity. The difference between the Lax-Harten shock problem and the Sod shock problem is that the former uses a moving high-pressure zone on the right-hand side, instead of a stationary high-pressure zone. Therefore, the Lax-Harten shock problem can be interpreted as a moving high-pressure flow colliding with a stationary low-pressure flow. Similarly, a shock wave, a contact discontinuity and some expansion waves will be observed. The shock wave moves rightwards, while the expansion waves move leftwards. Figure 3.2 compares the computed density, velocity, and pressure profiles with the exact solution at t=0.15. There is reasonable concurrence of the computed results with the exact solution.

3.2 Two-dimensional Cases

Test case 3. Steady two-dimensional oblique shock wave

A two-dimensional shock wave reflecting from a grid surface is considered in this test case. The computational domain is a rectangle of length 4.1 and height 1.0 units, with a uniform mesh size of 123×30. The following initial conditions are used:

$$(\rho, u, v, p)_{(x<2.0, y, 0)} = (1, 2.9, 0, 1/1.4)$$
$$(\rho, u, v, p)_{(x>=2.0, y, 0)} = (1.69997, 2.61934, -0.50632, 1.52819).$$

The boundary conditions are the reflecting surface along the bottom boundary, supersonic outflow along the right boundary, and prescribed fixed values on the other remaining two sides which are given as follows:

$$(\rho, u, v, p)_{(0, y, t)} = (1, 2.9, 0, 1/1.4)$$
$$(\rho, u, v, p)_{(x, 1, t)} = (1.69997, 2.61934, -0.50632, 1.52819).$$

The boundary conditions comprise an incident shock angle of 29º and the free stream Mach number M_∞ is 2.9. Figure 3.3(a) shows the computed density contours in the flow field for the shock reflection problem. The computed density distribution is compared with the exact solution at y=0.5 as shown in Figure 3.3(b). The comparison is reasonable considering that the present calculation was performed on a fairly coarse mesh; had a much finer mesh be employed, the resolution at the step change in the density plot (and others) would be even better.

Test case 4. Supersonic flow past a wedge

The case considered is the supersonic flow at M_∞=3.3806 past a 20º wedge. The Cartesian grid domain is a rectangle of length 4.0 and height 2.0 units, with a uniform mesh size of 100×50. The boundary conditions are the reflecting surface along the wedge surface, supersonic outflow along the right boundary, and fixed inflow values on other boundaries, which are given as:

$$(p, \rho, Mach, \alpha)_{boundaries} = (1.0, 1.0, 3.3806, 20°).$$

We use the boundary condition above as the initial values in the whole computational domain as well, i.e. $(p, \rho, Mach, \alpha)_{t=0} = (1.0, 1.0, 3.3806, 20°)$. The boundary conditions

produce an incident shock angle of 29º and the free stream Mach number M_∞ is 2.9. The computational domain and the computed pressure contours in the flow field are shown in Figure 3.4. One can clearly see the shock, which is obtained at an angle of β=35.30º, in excellent correlation with the analytical solution β=of 35.23º.

3.3 Axisymmetric Cases

Test case 5. Shock wave reflection in a converging circular chamber

In this case, a normal shock wave of M_∞=2.9 passes through a converging circular wall. The computational domain is shown in Figure 3.5, and the uniform mesh size is $\Delta x = \Delta r = 0.02$. The length of the computational domain ranges from 6.4 to 10, and the converging angle lies between 5° and 40°. The following initial conditions are used:

$$(\rho, u, v, p)_{(x<2.0, y, 0)} = (1, 2.9, 0, 1/1.4)$$
$$(\rho, u, v, p)_{(x>=2.0, y, 0)} = (1.69997, 2.61934, -0.50632, 1.52819).$$

The boundary conditions are the reflecting surface along the bottom boundary, supersonic outflow along the right boundary, and prescribed fixed values on the other remaining two sides which are given as follows:

$$(\rho, u, v, p)_{(0, y, t)} = (1, 2.9, 0, 1/1.4)$$
$$(\rho, u, v, p)_{(x, 1, t)} = (1.69997, 2.61934, -0.50632, 1.52819).$$

The converging oblique angle varies from 5º to 40º. As we can see in Figure 3.5, Mach reflection occurs at the oblique angle θ=5º to 30º. As the oblique angle θ increases, the angle between the circular wall and the triple-point trajectory line χ decreases, which agrees fairly well with the analytical results discussed in the subsequent chapters.

Test case 6. Supersonic flow past a cone

The case considered here is the supersonic flow at M_∞=3.3806 past a 20º cone, which apparently is the axisymmetric counterpart of the test case 4. The computational domain is shown in Figure 3.6, and the uniform mesh size employed is $\Delta x = \Delta r = 0.02$. The length of the computational domain depends on the converging angle. The boundary conditions are the reflecting surface along the wedge surface, supersonic outflow along the right boundary, and fixed inflow values on other boundaries, which are given as:

$$(p, \rho, Mach, \theta)_{boundaries} = (1.0, 1.0, 3.3806, 20°).$$

We use the boundary condition above as the initial values in the whole computational domain as well, i.e. $(p, \rho, Mach, \theta)_{t=0} = (1.0, 1.0, 3.3806, 20°)$. The boundary conditions produce an incident shock angle of 29º and the free stream Mach number M_∞ is 2.9. The computational domain and the computed pressure contours in the flow field are shown in Figure 3.6. One can clearly see the shock, which is obtained at an angle of β=35.26º, in good correlation with the analytical solution β=35.23º.

3.4 Grid Convergence Study

To investigate further the present numerical method, we take the test cases 1, 2 and 3 to study the grid convergence and "measure" the convergence rate. In the test cases 1 and 2, five different mesh sizes are employed: 0.02, 0.01, 0.005, 0.004 and 0.002. In the test case 3, the mesh sizes 0.1, 0.05, 0.033, 0.025, 0.02 and 0.01 are employed. Figures 3.7(a) - (c) show the log-log plots of error versus mesh size for the test case 1, 2 and 3, respectively. Herein, for the test cases 1 and 2, the error is defined

as $\sqrt{\frac{\sum_{i=1}^{N}(p_{num,i}-p_{exact,i})^2}{N}}$, where $p_{num,i}$ is the computed pressure at the node 'i', while $p_{exact,i}$ is the analytical solution at this node. For the test case 3, the error is defined as $\sqrt{\frac{\sum_{i=1}^{N}(\rho_{num,i}-\rho_{exact,i})^2}{N}}$ at y=0.5, where $\rho_{num,i}$ is the computed density at the node 'i' at y=0.5, while $\rho_{exact,i}$ is the analytical solution at this node. N is the number of nodes. As measured, the convergence rates for the test cases 1, 2 and 3 are 0.74, 0.74 and 0.79, respectively, which is less than 1. This means that the WENO_LF method employed in our computation converges at less than first order for problems with embedded discontinuities (contributed in a large part in the locality of discontinuity), which agrees with the conclusion by Henrick et al (2005).

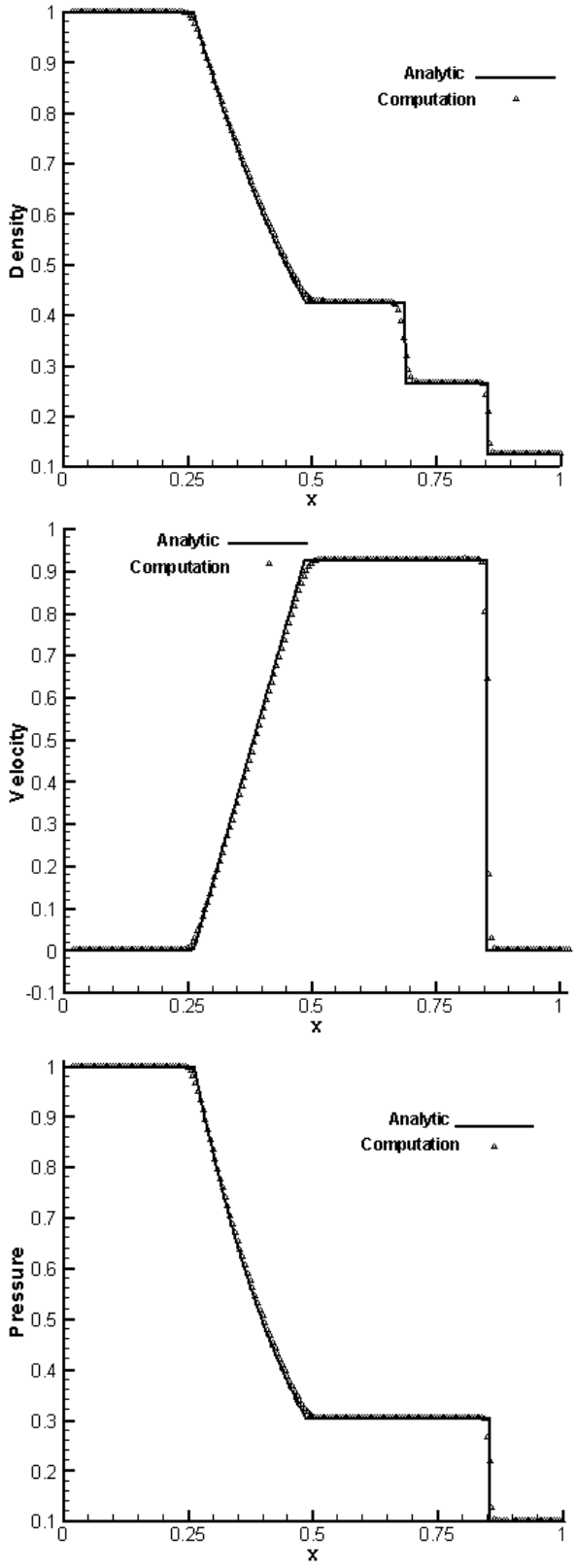

Figure 3.1 Comparison of the computed solution with the analytic solution for Sod shock problem at t=0.2 (Test case 1)

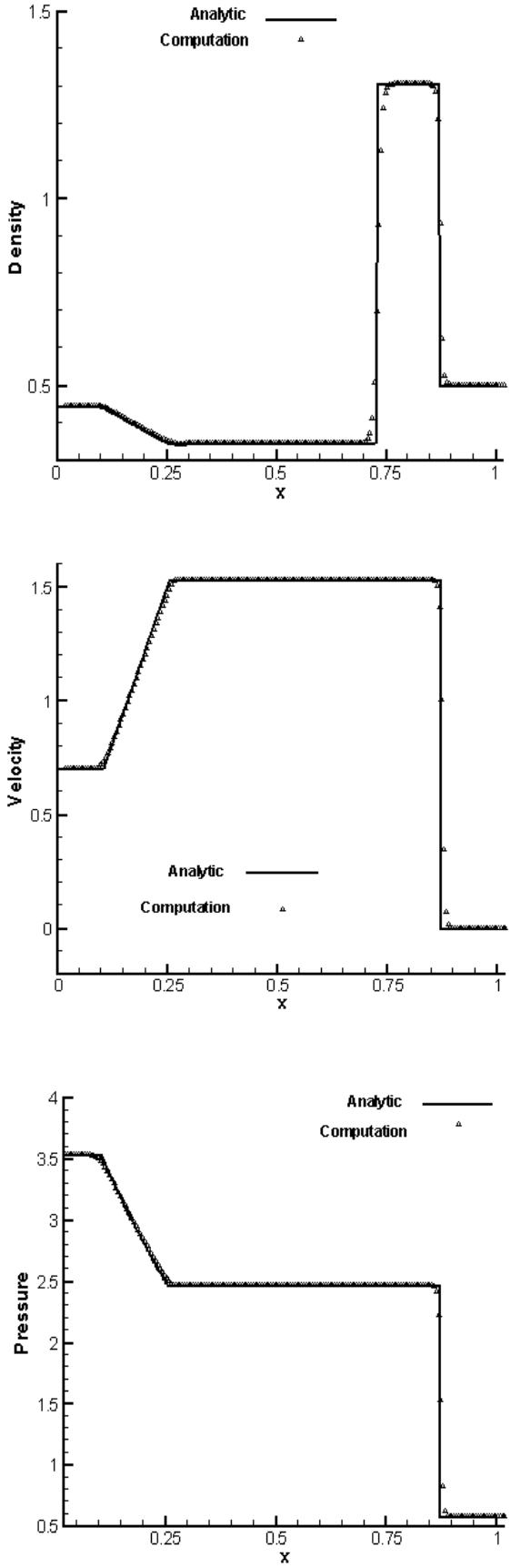

Figure 3.2 Comparison of the computed solution with the analytic solution for Lax-Harten shock tube problem at t=0.15 (Test case 2)

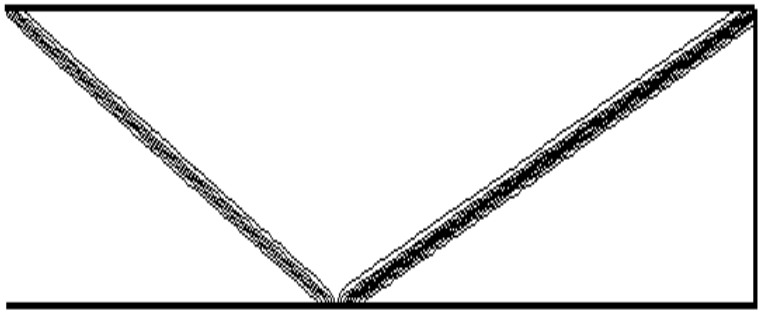

(a) Density Contour

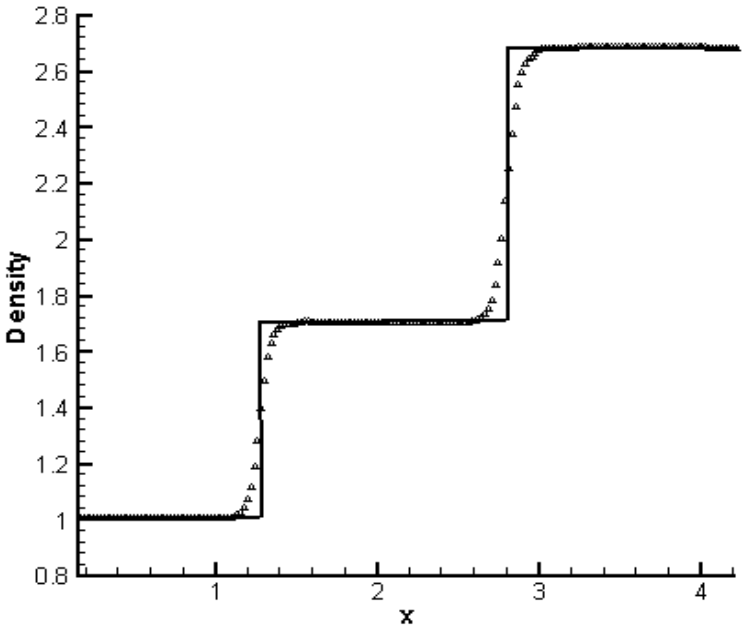

(b) Density Distribution at y=0.5

Figure 3.3 Computed density contours in the flow field
for stationary shock reflection problem (Test case 3)

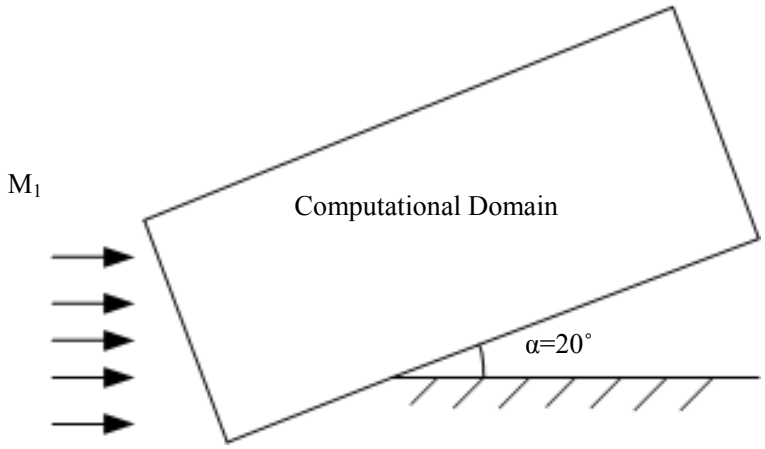

(a) Computation Domain

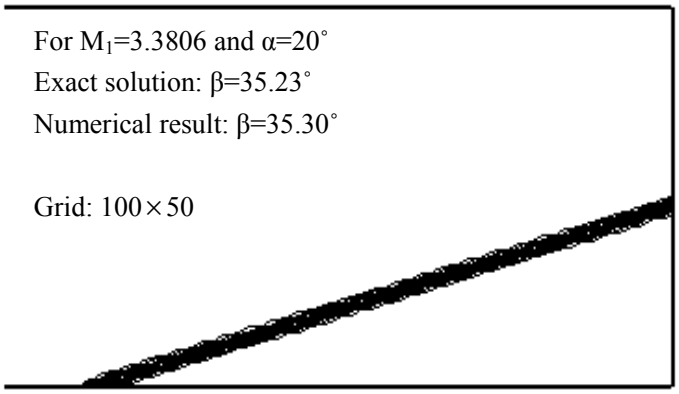

(b) Pressure Contour

Figure 3.4 Computed pressure contours in the flow field for supersonic flow past a 20º wedge (Test 4)

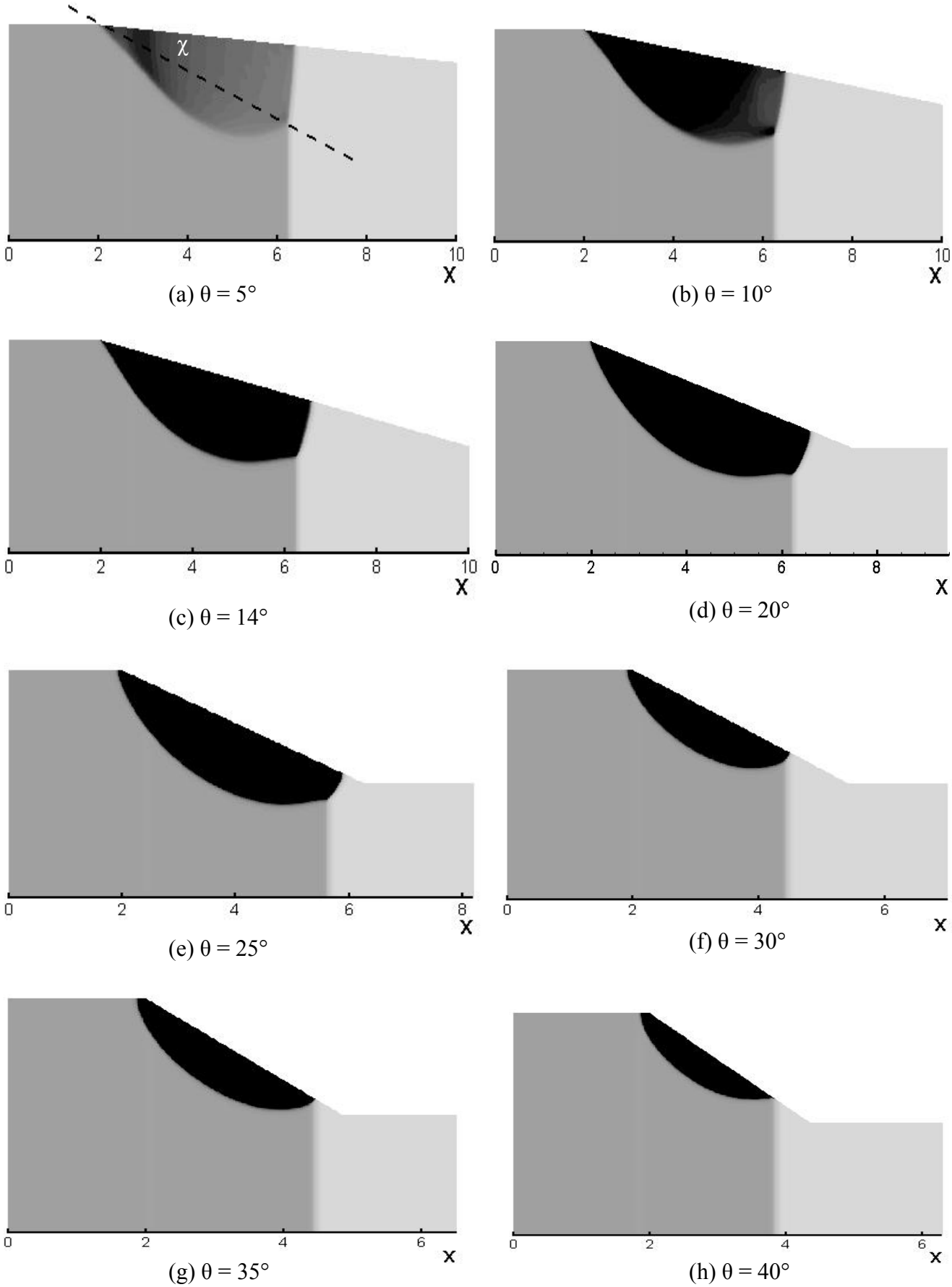

(a) θ = 5° (b) θ = 10°

(c) θ = 14° (d) θ = 20°

(e) θ = 25° (f) θ = 30°

(g) θ = 35° (h) θ = 40°

Figure 3.5 Mach reflection in the axisymmetric converging chamber (Test 5)

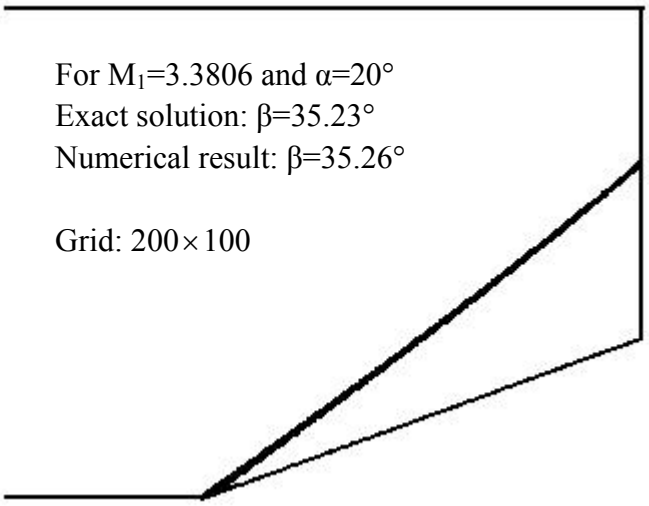

Figure 3.6 Computed pressure contours for supersonic flow past an axisymmetric 20º wedge (Test 6)

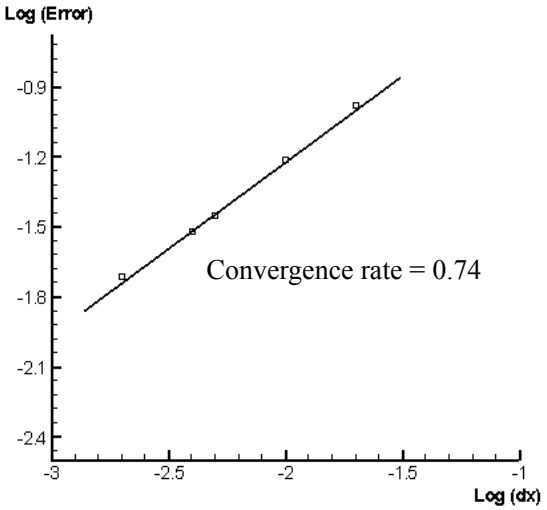

(a) Sod shock problem (Test case 1)

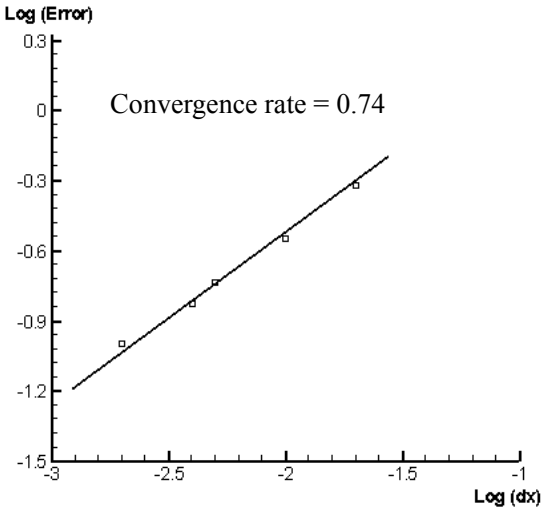

(b) Lax-Harten shock tube problem (Test case 2)

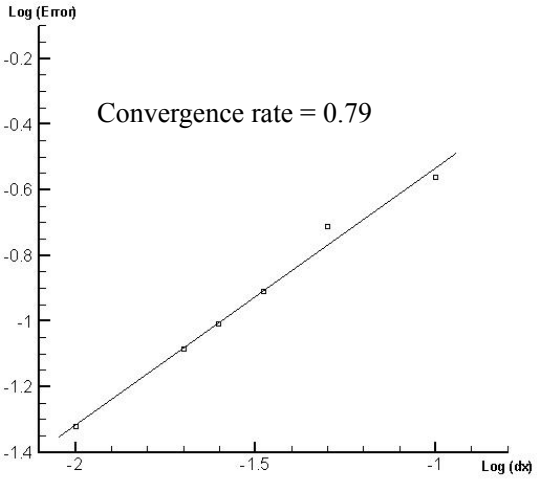

(c) Steady two-dimensional oblique shock wave (Test case 3)

Figure 3.7 Grid convergence study

Chapter 4 Numerical Results of One-dimensional Detonation Wave

4.1 Initialization

In the present study, the mixture is made up of three thermally perfect gases, H_2-O_2-Ar, and these are mixed at the molar ratio of 2:1:7. The initial pressure and temperature are 6670Pa and 298K, respectively. On the left end of the one-dimensional tube, a high-pressure area is used to yield a strong shock, which in turn heats the mixed gas to a high temperature, thereby igniting the reactions and the associated heat released in turn drives the shock. A steady detonation wave will be produced finally, and travel at a constant detonation speed. In the present computation, the pressure in the ignition area is $P_{ign} = 28*P_0$. The temperature and density in the ignition area can be obtained by the Rankie-Hugoniot equation and the gas relationship. The computational domain is set as 0.6 m, and 24,000 grids are distributed in it uniformly, i.e. $\Delta x = 2.5 \times 10^{-5}$m.

4.2 Boundary Conditions

The tube is closed on its left end, while open on its right end. Therefore, the left end employs the non-reflective boundary conditions, and the right end is the specified initial inflow. The detailed boundary conditions (4 boundary points) are given:

Left boundary: $(U_1)_i = \rho_i = \rho_4$, $i = 0,1,2,3$;

$(U_2)_i = (\rho u)_i = 0$, $i = 0,1,2,3$;

$(U_3)_i = (\rho e)_i = (\rho e)_4$, $i = 0,1,2,3$;

$(U_{3+k})_i = (\rho Y_k)_i = (\rho Y_k)_4$, $i = 0,1,2,3$; $k = 1,...,8$;

Right boundary: $(U_k)_{N+i} = (U_k)_N$, $\quad i = 1,2,3,4$; $\quad k = 1,...,11$;

4.3 Results and Discussions

4.3.1 Fundamental Characteristics and Parameters

Figures 4.1-4.4 show the profiles of pressure, velocity, temperature and density at time=360 μs as the steady detonation wave propagates from left to right, respectively. It is found that the leading shock wave and the subsequent chemical reaction zone make up the detonation front, and then the rarefaction wave zone follows. The flow velocity decreases gradually in the rarefaction wave zone till the steady zone is reached at about 1/2 of the detonation distance (distance from the left boundary to the front). In the steady zone, both the flow velocity and the pressure remain constant, which agrees with the self-similar solution of the Chapman-Jouguet (C-J) model well. More importantly, the present numerical result shows the structure of the detonation wave that the C-J model cannot resolve, i.e. the profile of the leading shock wave and the subsequent chemical reaction zone.

Figure 4.5 shows the details of the detonation parameters, as compared with those reported in other works. The mean one-dimensional detonation velocity obtained from the profile of the detonation wave is about 1625m/s, which is quite close to theoretical value of C-J (1618m/s) calculated by Gordon and McBride (1971). By using the C-J condition $D_{cj} = u_{cj} + c_{cj}$, one can determine the location of C-J plane and measure the C-J pressure $p_{cj} = 93600 Pa$, which is very close to the experimental result (94000 Pa) measured by Lefebvre (1995). The calculated von-Neumann peak pressure of the

leading shock is about 1.79 p_{cj}, slightly smaller than the analytical value from the ZND model (1.86 p_{cj}). If the reaction zone is defined as the distance from the leading shock to the C-J plane, the length of the reaction zone obtained in the present numerical simulation is about 0.011m, which agrees well with the calculated value (0.012m) through the steady solution by Oran et al (1998). The induction zone length (which is defined as the distance from the shock front to the maximum heat release location) obtained in our present computations is 0.16 cm, which is slightly larger than the result (0.147cm) by Joseph et al. (2005).

4.3.2 Changes in Concentration of the Species

Besides the profiles of the pressure, temperature, density and velocity behind the leading shock, the detailed elementary reactions model can also tell us clearly how the concentration of each species changes in the chemical reaction, i.e. the process of the chemical energy release.

Figures 4.6-4.8 are the molecular concentrations of each species at time=360 μs. It is found that the chemical reactions mainly occur in the zone from the leading shock to the C-J plane. Nonetheless, the chemical reactions do not stop completely after the C-J plane. The slight decrease of the temperature in the rarefaction zone helps break the chemical equilibrium by producing more H_2O, and some chemical energy is released. This energy cannot be transmitted to the detonation wave. Therefore, when using the detailed elementary reactions model, one should mainly calculate the energy released from the leading shock to the C-J plane, which is obviously smaller than that in the C-J model or ZND model.

As shown in Figures 4.6-4.8, the species involved, according to the magnitude of concentration change, can be classified into three groups. The first group includes H_2, O_2 and H_2O. Their concentrations change most dramatically, which is in the order of $10^{-1} mol/m^3$. The reactants, H_2 and O_2 are consumed rapidly in the reaction zone, and then change slowly in the rarefaction zone. The second group comprises OH, O and H, which change in the order of $10^{-2} mol/m^3$. After reaching their peak values rapidly, these attenuate quickly in the reaction zone, and slowly in the rarefaction until a steady value is obtained. The last group consists of H_2O_2 and HO_2, which exhibits the least changes. Although the change in the concentration of HO_2 is similar to that of the second group, its concentration peak is only about $10^{-5} mol/m^3$, and it reduces quickly. The concentration peak of H_2O_2 is about $10^{-4} mol/m^3$, and higher than HO_2, but attenuates faster than that of HO_2 too. In summary, these species involved have different characteristics and play different roles in the chemical reactions, which might be useful when we try to simplify the chemical reactions model to numerically simulate the structure of detonation waves better.

4.4 Resolution Study

In order to study the effect of mesh size on the fundamental detonation structure and the related parameters, we repeated the present one-dimensional detonation computation using 5 different mesh sizes: 2.0×10^{-3}, 1.0×10^{-3}, 5.0×10^{-4}, 2.0×10^{-4} and 1.0×10^{-4} m. All the computations employ the same initial and boundary conditions, which were presented in Sections 4.1 and 4.2.

The numerical computation shows that the mesh size has negligible influence on some detonation parameters, but pronounced influence on others. Table 4.1 lists the related detonation parameters for various mesh sizes. Figure 4.9 shows the von-Neumann peak pressure and the length of the reaction zone at different mesh sizes. What is clear is that the integrated variables like detonation velocity, C-J pressure and wall pressure are fairly insensitive to mesh size. Reaction zone length varies when the mesh size is larger than 0.1mm, i.e. reaction zone length is convergent at mesh size = 0.1mm. On the contrary, the von-Neumann pressure and the induction zone length, show some variations as the mesh size reduces to 0.025mm. The variations between the two smallest mesh sizes are, however, fairly limited. One may note that at the mesh size $\Delta x \geq 0.5\,\text{mm}$, the induction zone cannot be resolved. The possible reason is that the calculated shock front is comparable to the induction zone in thickness, so that they are indistinguishable from each other. At the mesh size $\Delta x \leq 0.2\,\text{mm}$, the calculated induction zone length reduces with the mesh size. The minimum induction zone length obtained in our present computations is 0.16 cm, which is slightly larger than the result (0.147cm) by Joseph et al. (2005) and much larger than the reported value (2.0×10^{-3} cm) by Oran et al. (1998). As Joseph et al. (2005) mentioned, it is believed that the value reported in the work of Oran et al. (1998) is a typographical error because agreement is obtained with other reported values from it.

Table 4.1 Detonation Parameters vs Mesh Size

Mesh size (mm)	Detonation Velocity (m/s)	C-J Pressure (Pa)	Wall pressure (Pa)	von Neumann pressure (Pa)	Reaction zone length (cm)	Induction zone length (cm)
2	1625	93600	32800	130000	3.8	----
1	1625	93600	32800	144000	2.2	----
0.5	1625	93600	32800	154000	1.8	----
0.2	1625	93600	32800	161000	1.3	0.21
0.1	1625	93600	32800	165000	1.1	0.17
0.025	1625	93600	32800	168000	1.1	0.16

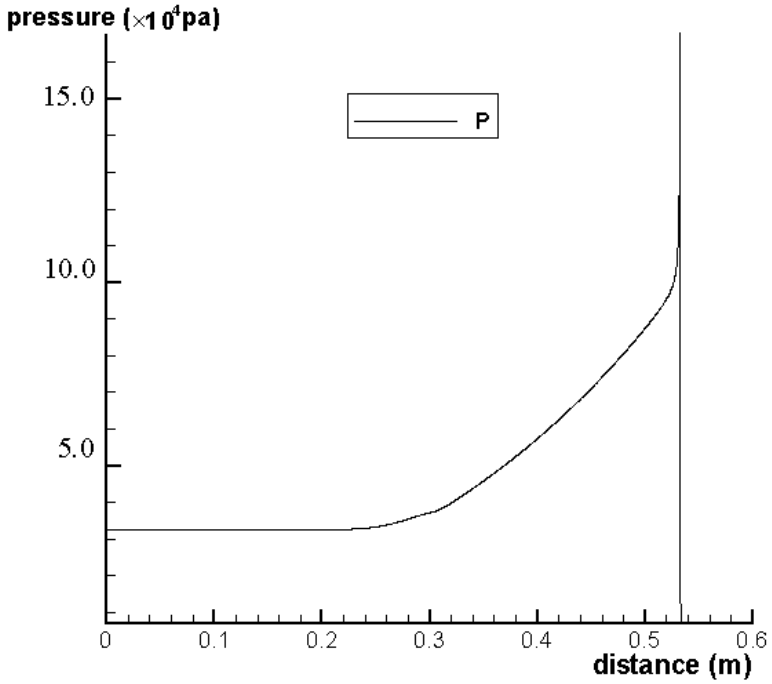

Figure 4.1 Profile of pressure at time = 320 μs

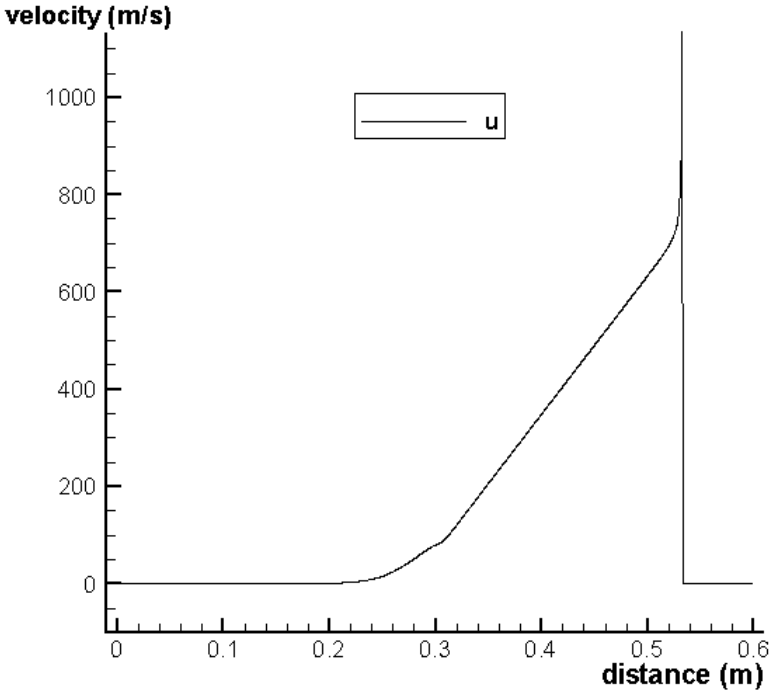

Figure 4.2 Profile of flow velocity at time = 320 μs

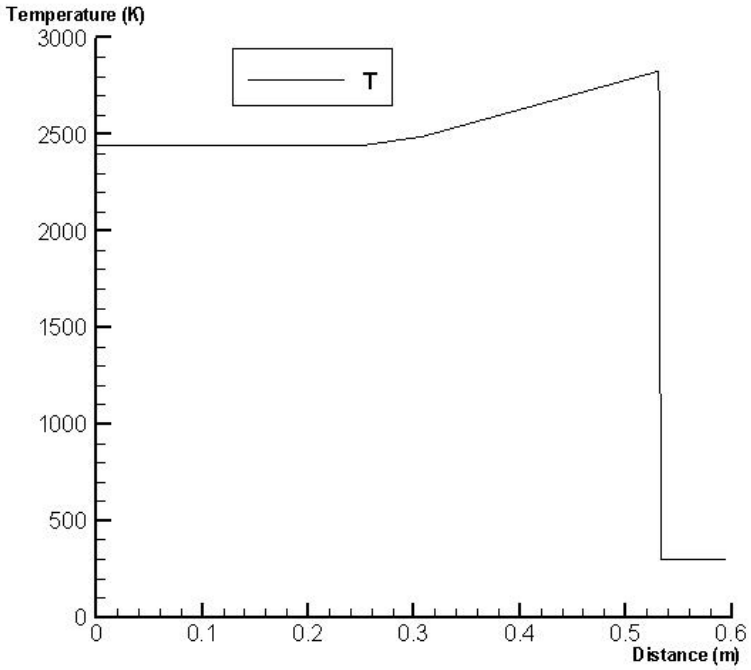

Figure 4.3 Profile of temperature at time = 320 μs

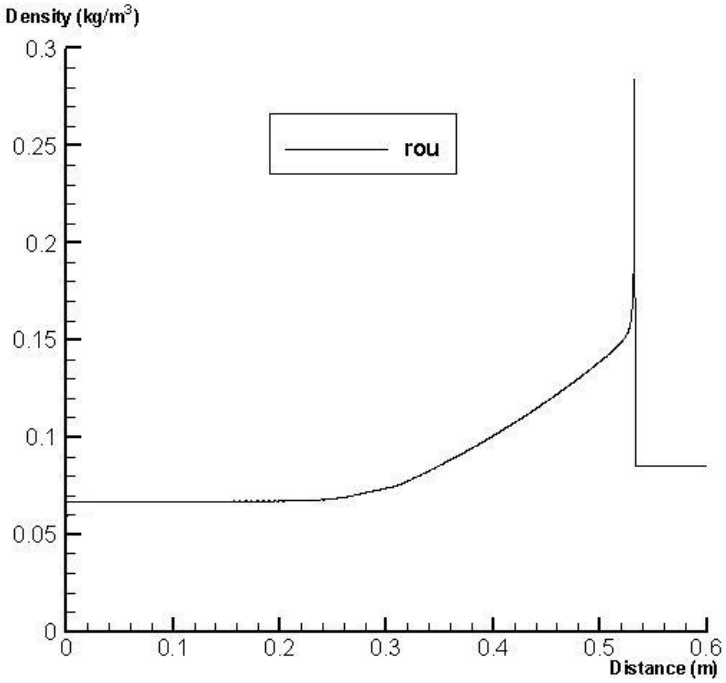

Figure 4.4 Profile of density at time = 320 μs

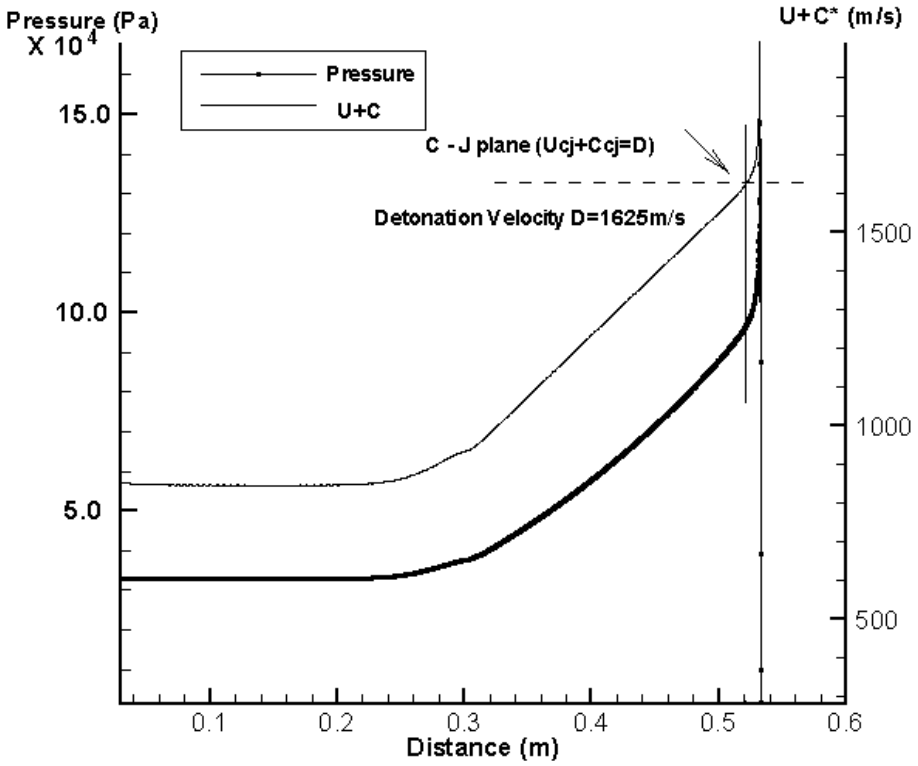

Calculated detonation velocity D_{CJ}=1625m/s versus
D_{CJ} value=1618m/s given by Gordon and McBride (1971);

Calculated induction zone length of ℓ_{ind}=1.6×10^{-3} m versus

1.47×10^{-3} m, given by Joseph et al (2005), and
2.0×10^{-5} m, given by Oran et al (1998);

Calculated reaction zone length of ℓ_{rxn}=1.1×10^{-2} m versus

1.2×10^{-2} m given by Oran et al (1998);
Calculated P_{peak}=1.79 P_{CJ} versus
1.86 P_{CJ} for the ZND model.

Here U and C denote the particle speed and the sonic speed, respectively, P_{peak} denotes the peak pressure on the front and P_{CJ} is the pressure on the CJ plane.

Figure 4.5 Comparison of the computed solution with other works

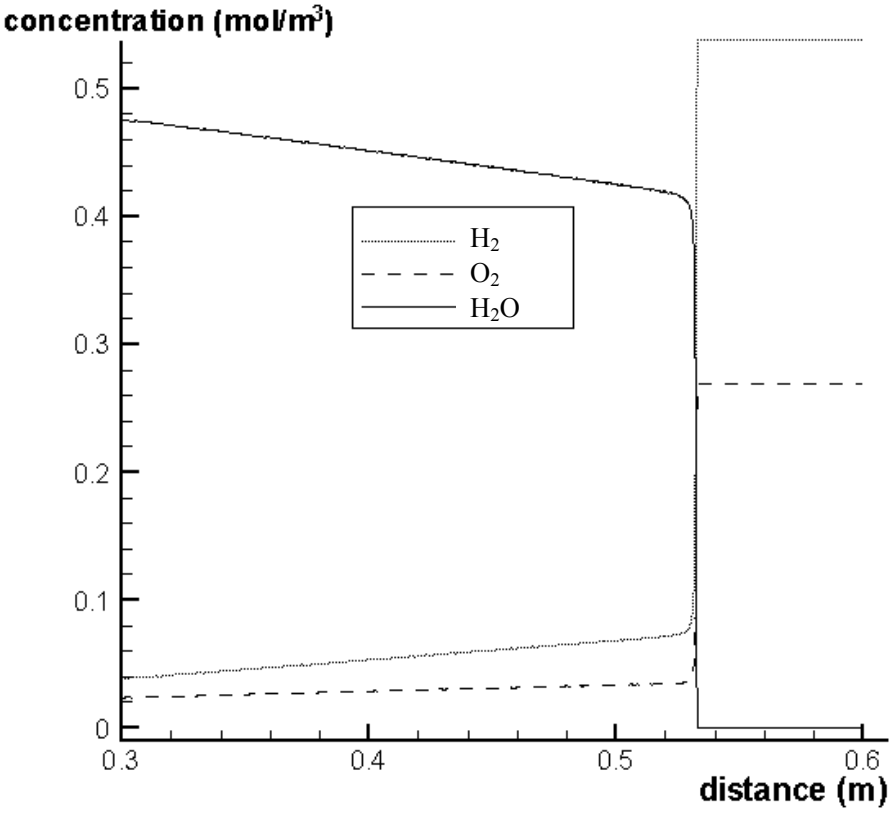

Figure 4.6 Molecular concentration of H_2, O_2 and H_2O at time = 320 μs

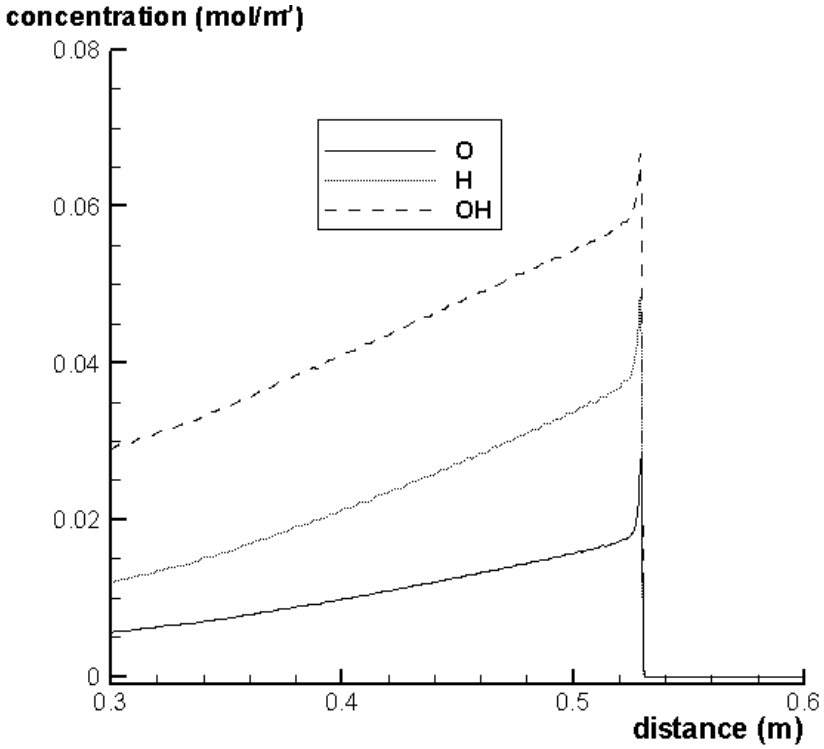

Figure 4.7 Molecular concentration of O, H and OH at time = 320 μs

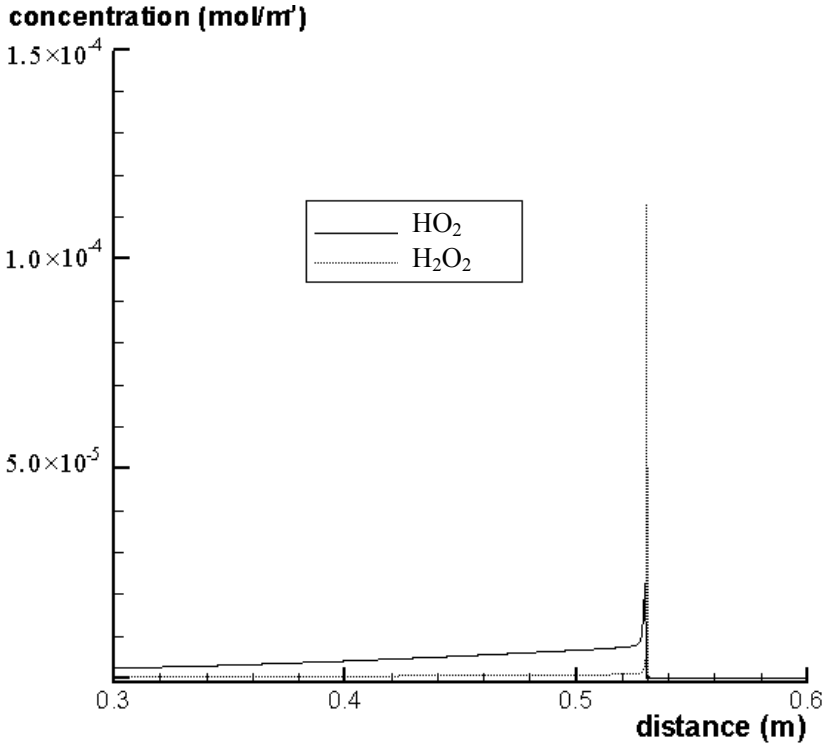

Figure 4.8 Molecular concentration of HO_2 and H_2O_2 at time = 320 μs

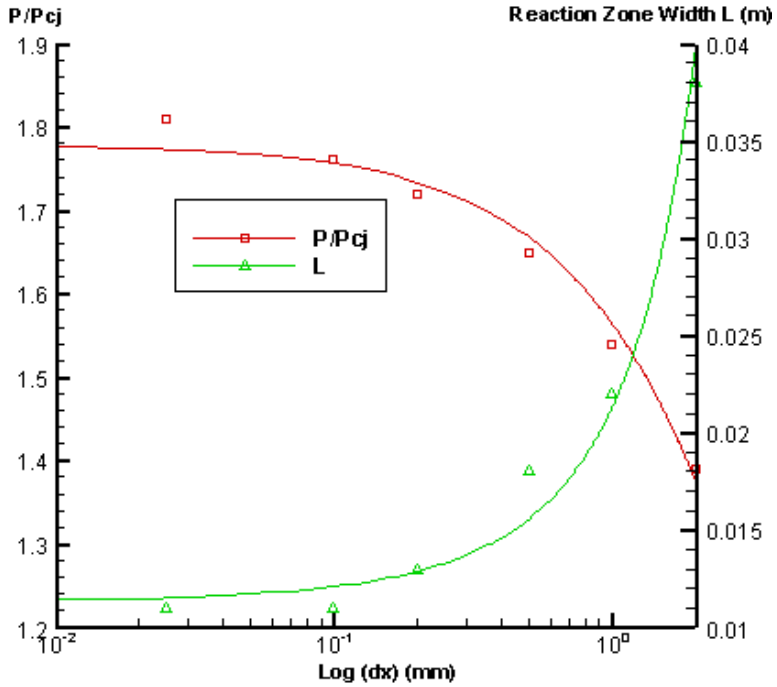

Figure 4.9 Peak pressure and reaction zone width vs mesh size

Chapter 5 Numerical Simulation of Two-dimensional Detonation in a Straight Duct

5.1 Initial and Boundary Conditions

In this work, we are studying the detonation of hydrogen-oxygen system in a straight tube. Hydrogen and oxygen are mixed at the ratio of 2:1, diluted by 70% of argon. The initial pressure and temperature are 6670Pa and 298K, respectively, which are same as those in the one-dimensional computation. A strong shock wave ($2\,p_{cj}$) is imposed on a one-dimensional domain to obtain an overdriven detonation wave. After a while, the overdriven detonation wave will evolve to be a steady detonation wave. Then, we put the steady one-dimensional detonation wave on a two-dimensional domain, serving as the initial condition for the two-dimensional computation. The initial detonation wave on the two-dimensional domain is shown in Figure 5.1. The computational domain is $20mm \times 20mm$, and 200×200 Cartesian grids are distributed uniformly, i.e. $\Delta x = \Delta y$ =0.1mm.

The boundary conditions (4 boundary points at each boundary) are given as below,

Left boundary: Extrapolation outflow, defined for all the variables,

$$B_b(B = \rho, u, v, E, P, Y_i) = B_1(1-\gamma) + B_N\gamma$$

where γ is the relaxation coefficient, B_1 is the current value of the first cell near the boundary, and B_N is the extrapolation limit. In our computation, we use γ =0.05 and B_N equals to the ambient fluid parameters.

Right boundary: The unreacted inflow with specified initial parameters, i.e.,

$$(U_k)_{N_x+i} = (U_k)_{t=0},\quad i = 1,2,3,4;\quad k = 1,2,..,12$$

Upper boundary: Inviscid Solid wall (Reflective boundary condition), i.e.,

$(U_k)_{N_y+j} = (U_k)_{N_y-j}$, $(U_3)_{N_y+j} = -(U_3)_{N_y-j}$, $j = 1,2,3,4$; $k = 1,2,4,5..,12$.

Lower boundary: Inviscid Solid wall (Reflective boundary condition), i.e.,

$(U_k)_j = (U_k)_4$, $(U_3)_j = -(U_3)_4$, $j = 0,1,2,3$; $k = 1,2,4,5..,12$,

where $(U_k) = (\rho, \rho u, \rho v, \rho e, \rho Y_1, ..., \rho Y_8)$, and N_x is the last non-boundary cell on the right side; N_y is the last non-boundary cell on the upper end.

Due to stiffness of the chemical reaction equations, the time step for the part of chemical kinetics must be very small, which implies expensive CPU cost in a given computational domain, especially for the two-dimensional case. Therefore, the present small computational domain is employed to reduce the cost. In order to keep the detonation front within the computational domain all the time, we use moving mesh in the two-dimensional straight-duct computation. The grids are set to move at the one dimensional steady detonation velocity in the positive x-direction, i.e. the reference frame is attached to the detonation front so that the relative position of the front remains essentially unchanged in the computational domain. Thus, the flux $F(U)$ in the governing equations should be modified as:

$$F(U) = \begin{pmatrix} \rho u - \rho D_{cj} \\ \rho u^2 + P - \rho u D_{cj} \\ \rho uv - \rho v D_{cj} \\ (E+P)u - E D_{cj} \\ \rho u Y_1 - \rho Y_1 D_{cj} \\ \vdots \\ \rho u Y_{N-1} - \rho Y_{N-1} D_{cj} \end{pmatrix}$$

where D_{cj} is the calculated one-dimensional C-J detonation velocity.

5.2 Artificial Perturbation

In order to study the cellular structure of a detonation wave, we introduce random perturbations to the initial flow field. These artificial perturbations are used to simulate the real situation where a detonation wave develops into cellular structures with the existence of small disturbances. It has been known that without the initial perturbations, a planar detonation wave would not develop into cellular structures. In the present research, the numerical perturbations are imposed on the entire computation domain for the first time step in terms of $e^* = e + \alpha e f$, where f is a random number distributed in [-1.0, 1.0], and α is a fluctuation coefficient, ranging from 0 to 1. By adjusting the value of α, we can control the intensity of the initial perturbations. These artificial disturbances imposed on the elementary reactions will affect the pressure and temperature in the flow field too. This means of introducing artificial perturbations is similar to that used by Gamezo et al. (1999), and the latter's work is based on the simple one-step ZND model. Figure 5.2 shows the pressure contour with initial perturbations. The effect of the artificial perturbations on the flow field is hardly discernible.

There are also some other means of introducing initial perturbations, such as initial non-uniform region or adding unreacted gas pocket behind the ZND detonation wave. By comparison, these methods require stronger artificial perturbations. In real circumstances, small disturbances are likely to be enough for a detonation wave to develop into cellular structures. As mentioned in the subsequent chapter, when using the present method to introduce artificial perturbations, the formation process of the

calculated cellular structures is similar to that observed in the experiment of shock reflection, and therefore, the present method is possibly more suitable for the simulation of detonation cellular structures.

5.3 Formation and Evolution of the Cellular Structure

The numerical simulation shows that the formation of cellular structures can be divided into two stages. Stage 1 is the formation of the triple wave configuration, while Stage 2 is the formation of the cellular structures with a constant number of transverse waves. The second stage requires much longer time than the first stage.

Figure 5.3 shows the evolution of the pressure contours. It is found that the initial perturbations, with a=0.35, are very small and one can hardly tell the difference from the pressure contours calculated without the imposition of any numerical perturbations (see Figure 5.3(a), and 5.3(b)). However, as the detonation propagates, the effect of these perturbations is enhanced and many non-uniform regions are produced behind the leading detonation front. While the detonation front starts distorting, these non-uniform regions move in the transverse direction and become stronger, but the number of these regions declines. These non-uniform regions gradually develop into some transverse waves, traveling at about the sonic speed. There are many transverse waves at the beginning, but while these are enhanced in strength, the number decreases. The leading front also becomes more distorted. Thus, two regions with different strengths are observed, which, along with the transverse waves, gradually develop into the typical triple wave configuration (see Figure 5.3(f)),

i.e., transverse wave, Mach stem and incident wave. The transverse waves are traveling at supersonic speed.

The Mach stem and the incident wave interchange their roles via the Mach/triple point collision as the detonation wave proceeds forward. These triple wave configurations move and collide irregularly in the transverse direction. Initially, the transverse waves are neither uniformly distributed, nor necessarily in pairs. Two adjacent transverse waves move in the same or opposite direction, and therefore they either collide or catch up with each other. The latter usually results in the merging of the two triple-wave configurations. Furthermore, because of the instability of triple wave configurations, new transverse waves might be produced at the triple-wave point, but overall, the number of transverse waves tends to decrease gradually till a certain number of transverse waves are obtained. Figure 5.4 shows the ultimate steady detonation structure at time=871 μs .Our numerical results show that the evolution from the initial unsteady detonation structure to the steady detonation structure is a slow process, which requires several hundred of microseconds to one millisecond of physical time, and even more as the cross-sectional area of the duct increases. This agrees with the real gaseous detonation. Some experimental results have shown that when the width of the detonation duct is much larger than the width of the transverse wave, it is very difficult to obtain a steady detonation structure. Therefore, in the present numerical computation, a 20mm-high detonation duct is chosen. The number of the transverse waves is found to be 5.

Figure 5.5 are some continuous snapshots of pressure contours after the steady detonation structure is obtained, which shows that the same cellular structure occurs at about every 9.0us, called characteristic time of the detonation cell. In addition, it is also found that the average detonation velocity at the front is about 1625m/s, which is the same as that obtained in the one-dimensional computation.

5.4 Structure Tracks

The numerical smoke foil technique was widely used to study the tracks of the structure. Usually, a high speed flow can remove more soot than the lower speed counterpart, and so the tangential velocity discontinuity on the slip line is recorded dividing the regions behind the Mach stem and the transverse wave in a triple-wave configuration. Similarly, in the present work, the maximum flow velocity, $|v|_{\max}$, at all grid nodes in the time history are recorded to simulate the smoke foil tracks. That is,

$$|v|_{\max,i,j} = \left[(\sqrt{u^2 + v^2}_{i,j}) \right]_{\max}, t = 0, t_{end}$$

Figure 5.6 shows the numerical detonation cells as an analogue of smoke foil tracks and how the tracks are left after the sweeping of the structure, respectively. The cellular structure from the present numerical result agrees very well with that from the experiment (Fickett, 1979). The cellular structure has two convex curvature tracks in the first half cell and two concave tracks in the second half. Through comparison with the pressure contours at different times, we can find that these tracks are actually the trajectory of the triple-wave points. The jet near the starting point of a detonation cell is also recorded in the numerical detonation cell. Based on Figure 5.6, the cell size in our present computation is 0.008m (cell width)×0.015m (cell length), which is

smaller than that by Oran et al (1998). By comparison with Oran et al's computation, it is found that the present calculated C-J detonation speed, along with the shape of the cellular structures, are about the same as the latter. The only difference is that we use different chemical reaction models. Therefore, it is possible that the chemical reaction model has fair influence on the numerical cell size. More importantly, both of our numerical cell sizes are much less than the value from the experiment (0.17m) (Hanana et al., 2000). Although the numerical detonation cell size is different from the experimental value, the shape is very similar. The details of comparisons between the numerical simulation and experiments (Strehlow et al., 1968) are given in Table 5.1. Figure 5.7 shows the geometric relationship of a numerical cellular structure. As measured in the figure, the cell width/length ratio is about 0.55, which is in the range of the experimental result. When the Mach stem evolves into an incident wave, the angle change Δ is about 30°. In addition, it is found that the entrance angle β and the exit angle φ follow the approximate relationship $\varphi = \beta - \Delta$. The transverse track angle ω is about 28°, similar to the experimental result.

In our computation, it is observed that there are more transverse waves with good regularity at the early stage of the formation of the cellular structures, as shown in Figure 5.8 (a). As the detonation wave propagates forward, these transverse waves are not stable, and the cellular structures become irregular and the number of the transverse waves quantity decreases quickly (see Figure 5.8 (b)). After a long period of time which lasts about 500 microseconds, these irregular structures gradually become regular again and then sustain, as shown in Figure 5.8 (c).

5.5 Basic Characteristics of Cellular Structure

Figures 5.9 – 5.11 show the computed pressure, density and temperature contours after regular cell structures are formed. The typical cell structures are made up of multiple triple-wave configurations, each of which is the combination of Mach stem (M), incident wave (I) and transverse wave (T). The discontinuity of density or temperature can be used to locate the slip line between the transverse wave and the Mach stem. As shown in the figures, the region around the triple-wave point has the highest pressure, density and temperature. The incident wave is much flatter and weaker than the Mach stem. The density and temperature gradients behind the incident wave are also smaller than those behind the Mach stem, which suggests that the reaction front around the incident wave lags behind that around the Mach stem. The plot of the computed pressure contours around the Mach stem front show that the pressure in the middle of the Mach stem is lowest, and increases towards the triple-wave points. The pressure peak is reached somewhere around the triple-wave point. The pressure around the incident wave, however, is much more uniformly distributed. A transverse wave is the shock wave traveling in the transverse direction, which is not very strong. The regions behind the transverse wave and the Mach stem are separated by a contact discontinuity. As we can see in Figure 5.11, there exists a low-pressure region behind the transverse wave where the density and pressure match with those behind the incident wave. Two adjacent transverse waves collide and the reflected waves are deflected against the wall. As a result, the reflected waves propagate in the direction nearly vertical to the wall, and therefore they are called

“transverse waves”.

As far as a two-dimensional detonation is concerned, the cellular structure moves in a two-dimensional planar mode. Figure 5.12 shows the pressure contours for 6 consecutive moments. As we can clearly see, the leading shock wave of the present gaseous detonation involve incident wave and Mach stems laid out alternately. The two transverse waves intersecting on the same Mach stem move further apart, while the transverse waves intersecting on the same incident wave are approaching one another. On the leading front, the incident wave keeps exchanging its role with the Mach stem, while the adjacent triple-wave configurations collide with each other. As shown in Figure 5.12, when the leading front moves from 875.0μs to 875.4μs, the two transverse waves intersecting on the same incident wave get closer to each other, thereby causing the shrinking of the incident wave. At time = 875.4μs, these two transverse waves collide, and the triple-wave configurations continue to move close until at time = 876.6μs, they bump face to face on each other. Then a new Mach stem is generated somewhere around the corresponding incident wave. Meanwhile, the two triple-wave configurations and the two transverse waves intersecting on the same Mach stem move apart from each other, and the Mach stem gradually shrinks. After the collision of the adjacent triple-wave configurations, the old Mach stem area is replaced by a new incident wave. As the detonation wave propagates, the incident waves exchange their roles with the Mach stems alternately, accompanied with the collisions of the triple-wave configurations.

5.6 Details of Cellular Structures

5.6.1 Triple-wave Configuration

One typical characteristic of detonation cellular structures is that the detonation front is always made up of one or more triple-wave configurations, and Mach stems exchange their roles with incident waves through collisions of the triple-wave configurations. Figure 5.13 shows the close-up view of the pressure contours at 4 consecutive moments. As we can see, the triple-wave configuration at time = 875.0μs is a single-Mach structure, i.e. Weak Structure. The highest pressure in the cellular structure is located somewhere around the triple-wave point and on inner side of the Mach stem. Further away from the triple-wave point, the pressure declines. By comparison with the von-Neumann peak pressure, it is found that the peak pressure of Mach stem is higher than the von-Neumann pressure, while that of incident wave is lower than the von-Neumann pressure. Therefore, the detonation at Mach stem is overdriven, which is different from the sub-driven detonation at incident wave. As shown at time = 875.4μs, before these two triple-wave configurations collide, they have gradually evolved into more complex structures, called “Strong Structure”; that is, the original transverse wave (AB at time = 875.8μs) deflects near the triple-wave point and a new transverse wave is generated (AC at time = 875.8μs). The acute angle between the new transverse wave and the central line of the cellular structure is very small. As the adjacent triple-wave configurations move towards each other, the new transverse wave is strengthened.

Before the triple-wave configurations collide, the adjacent transverse waves start to

collide at about half way of the cellular structure, giving rise to a high-pressure area where collision just happened. As shown at time = 876.2μs, the incident wave has been very weak, and the pressure of the leading shock is only about 100,000Pa, much lower than the von-Neumann pressure. The area behind the incident wave is a low-temperature unreacted area. These two transverse waves at the strong structure collide in an approximate face-to-face direction, bringing about a converging structure in the vicinity of collision. The so-called converging effect enhances the energy at the converging point dramatically, which can be considered as a blast wave. As calculated, the pressure of the blast wave is about 510,000 Pa, more than 5 times of the C-J detonation pressure (96,000 Pa). Figure 5.14 shows the pressure contours as the blast –like wave is formed and developed. It is observed that the blast wave gives rise to a new Mach stem by interacting with the incident wave, and the transverse segments of the blast-like wave develop into new transverse waves. Due to expansion effect of the blast-like wave, a rounded low-pressure region is formed around the collision point. In essence, colliding of two triple-wave configurations is a very complex process, which is very different from the collision of two shock waves. The converging effect plays an important role in the collision of the triple-wave configurations.

5.6.2 Chemical Reactions in a Cellular Structure

The change of concentration around the leading shock front can be used to study the process of the chemical reactions. Figure 5.15 shows the computed concentration contour of H_2O at the vicinity of the reaction fronts. After a small white area behind the leading shock, there appears a concentration discontinuity, called “Reaction Front”.

The chemical reactions are nearly complete on the reaction front, and the concentration of species hardly changes in the subsequent broad area, called "Reaction Equilibrium Zone". In the reaction equilibrium zone, very little chemical energy is released. In addition, it is observed in Figure 5.15 that there exists a reaction induction zone between the reaction front and the leading shock, i.e. the white area behind the leading shock. The chemical reactions behind the Mach stem are different from those behind the incident wave, in that the lagged time behind the Mach stem is very short while the lagged time behind the incident wave is much larger, especially at the ending part of the cellular structure. Due to the weaker or less intense incident wave, the lagged time and the reaction induction zone behind the incident wave are longer and wider. Therefore, in the concentration contour, the reaction front behind the incident wave is further back than that behind the Mach stem. Figure 5.16 shows the close-up view of the chemical reaction front with incident wave. It is found that the reaction front behind the incident wave is quite flat and parallel to the incident wave. However, due to the motion of the transverse waves across the associated incident wave, the flow field right behind the incident wave is secondarily compressed, thus causing the reaction to complete earlier. As the transverse waves move towards each other, more flow field behind the incident wave is secondarily compressed, and therefore, the reaction front takes on a concave shape, as shown in Figure 5.15.

Based on the analysis above, a cellular structure can be classified into 5 regions in terms of characteristics of the chemical reactions, which are shown in Figure 5.17.

Region 1 is ignited by Mach stem, taking about 40% of the total area. Region 2 is ignited by incident wave, assuming about 25% or so of the area. Region 3 is secondarily compressed and ignited by transverse wave, which takes another 25% of the total area. The ignition occurs before the reaction front of the incident wave. Region 4 is enhanced by the collision of the transverse waves, which is about 7% of the entire cellular structure. Because the transverse waves collide behind the reaction front of the incident wave, the collision does not make big difference to the reaction front. The rest 3% is ignited by the collision of triple-wave configurations.

A further analysis reveals that in the area where the triple-wave configurations collide, the chemical reactions are very complex. Figure 5.18 shows the H_2O concentration before and after collision of the triple-wave configurations. As we can see, before the triple-wave configurations collide, the low-temperature un-reacted area behind the incident wave is surrounded, giving rise to an un-reacted gas pocket. Moreover, the transverse waves collide before the reaction front of the incident wave, thus igniting and accelerating the overdriven detonation reaction front. This overdriven reaction front instantly breaks the un-reacted pocket behind the incident wave into two parts. They collide with the two reaction fronts near the colliding triple-wave configurations. The collision among these three reaction fronts again accelerates the reaction fronts, making the detonation wave moves even faster.

It has been mentioned in Chapter 4 that by investigating the variation of the concentration of each species in the process of chemical reactions, we can determine

its significance in the entire chemical reactions. As shown in Figure 5.19 and 5.20, the concentration of each species has different characteristics. The species H_2O_2 and H_2O are consumed or produced rapidly in the reaction zone, and then change slowly in the reaction equilibrium zone. The equilibrium values for H_2, O_2 and H_2O are 0.05 mol/m^3, 0.025 mol/m^3 and 0.46 mol/m^3, respectively. The species HO_2 and H_2O_2 reach their peak values near the reaction front and then reduce to their equilibrium values rapidly. Their peak values are 4.8×10^{-5} mol/m^3 and 1.2×10^{-3} mol/m^3. Their equilibrium values are 5.0×10^{-6} mol/m^3 and 6.0×10^{-7} mol/m^3, respectively. The species OH, H, and O also reach their peak values near the reaction front, but their peak values, however, vary at different locations of the reaction front. There exist more fluctuations in the chemical equilibrium zone, and the amplitude of the fluctuations is much bigger than that in the one-dimensional detonation. The peak values for O, H, and OH are 0.04 mol/m^3, 0.082 mol/m^3 and 0.086 mol/m^3, respectively. Their equilibrium values are, O: 5.0×10^{-3} mol/m^3, H: 1.5×10^{-2} mol/m^3, OH: 2.8×10^{-2} mol/m^3.

In descending order of concentration, the species are listed as H_2, O_2, H_2O, Ar, OH, H, O, H_2O_2 and HO_2. Based on the concentration values, these species fall into 3 categories. Category 1 has the highest order of concentration, which includes Ar, H_2, O_2 and H_2O, followed by OH, H and O (Category 2). H_2O_2 and HO_2 belong to Category 3, which has the lowest order of concentration. In descending order of the variation of concentration in the chemical equilibrium zone, these species, however, are listed as H, O, OH, Ar, H_2O, O_2, H_2, HO_2 and H_2O_2. In addition, one may have

noticed that the species H_2O_2 only exists for a very short time, while other species exist in the entire flow field. The species HO_2 diminishes very quickly, and its concentration in the chemical equilibrium zone is only in the order of 10^{-7}mol/m^3.

By comparison with the pressure and temperature contours at the same time, one may find that the chemical reactions are insensitive to the change of pressure, but very sensitive to the change of temperature. The change of temperature in the chemical equilibrium zone behind the shock is very limited, but the change of concentration is considerable. The sensitivity of these species to the change of temperature in the flow field varies. O, H and OH have the highest sensitivity to temperature variation.

5.7 Variation of Detonation parameters in a Cellular Structure

5.7.1 Detonation Velocity

Figure 5.21 shows the trajectory of the leading front on the central line after the regular cellular structure is formed. The trajectory line is approximately a straight line, and there exists periodical fluctuations. The mean detonation velocity, as calculated, is about 1625 m/s, which is a little larger than the theoretical C-J detonation velocity 1618 m/s (Gordon, 1971). In addition, the instantaneous detonation velocity of the leading front on the central line of the cellular structure can also be obtained from the trajectory line. Figure 5.22 shows the instantaneous detonation velocity as time progresses, which demonstrates good periodicity relating to the cellular structure. A fluctuation period is just equal to the time when the leading shock propagates through a cellular structure, i.e. characteristic time of cellular structures, t_{char}. As shown in

Figure 5.22, in one period, the variation of the detonation velocity presents two stages: acceleration stage and deceleration stage. The acceleration stage involves the process where sub-driven detonation accelerates to overdriven detonation. The acceleration stage lasts about $0.15\,t_{char}$, and the sub-driven detonation accelerates to C-J detonation velocity at around $0.018\,t_{char}$. The peak velocity of the overdriven detonation is reached after the acceleration stage. The peak values for a few consecutive periods are normally quite close to each other, which is about $1.34\,D_{cj}$. Then the period with a rather different peak value follows. The maximum peak velocity is up to $1.75\,D_{cj}$. The deceleration stage involves the process where overdriven detonation decelerates to sub-driven. Based on the deceleration rate, the deceleration stage can be recognized as two parts. The deceleration in the first part is much faster than the second part. The turning point is normally located at around $0.37\,t_{char}$, which is just the moment when the overdriven detonation decelerates to C-J detonation. The deceleration in the second part is unstable and sometimes it entails some oscillations, with the minimum value of $0.7\,D_{cj}$. The peak velocity of the sub-driven detonation does not vary much in each period, which is around $0.8\,D_{cj}$.

Figure 5.23 shows the details relating to the different stages of the instantaneous detonation velocity on the center line of the cellular structure. One may find that the acceleration stage actually starts from the ending part of the last cellular structure. The maximum overdriven detonation velocity is reached somewhere right behind the apex of the cellular structure. The overdriven detonation then decelerates rapidly to the sub-driven detonation at about $0.3\,l$, followed by a long and slow deceleration process

until at the ending part of the cellular structure where the minimum sub-driven detonation velocity is reached. Therefore, in a cellular structure, sub-driven detonation occupies much more spatial extent than overdriven detonation.

The variation of detonation velocity in the rest of a cellular structure is different from that on the center line. In the first half cell, the leading front is Mach stem, and it keeps spreading out. The detonation velocity on both sides of the central line decelerates in a slower rate. The deceleration rate near the triple-wave configuration is slowest, and the overdriven detonation sustain until the colliding of the triple-wave configurations. On the contrary, in the second half cell, the detonation front is associated with the incident wave that keeps contracting. The detonation velocity on both sides of the cellular structure is not much different from that on the central line. They are all sub-driven detonation. Therefore, the overdriven detonation in the rest of the cellular structure occupies a smaller spatial region, which is similar to the case on the central line.

5.7.2 Pressure

Figure 5.24 shows the pressure distribution on the central line of a detonation cellular structure. As we can see, the pressure varies in the same way as the detonation velocity does. In the first 1/5 of the dimensional length of the cellular structure, the effect of rarefaction waves is strong, but get weaker as the detonation approaches C-J detonation. After the C-J detonation, the pressure profile becomes flat. When the detonation wave moves to the location of 1/10 of the length, there appear new pressure peaks somewhere far behind the leading front, which can be attributed to the

colliding of transverse waves. These new pressure peaks 'chase' after the leading shock, thus weakening the rarefaction effect behind the leading shock. These results agree well with the experimental result (Hanana et al., 2000).

The change of pressure in the rest part of the leading front is similar to the change of detonation velocity. The change of pressure around the Mach stem is milder on both sides than that on the central line. Around the incident wave, however, the change of pressure on both sides is nearly same as that on the central line. Near the apex of the cellular structure, the pressure peak is on the central line. In the subsequent half cell, the pressure peak takes on the quantity on the side of Mach stem near the triple-wave point. This peak value is much higher than the von-Neumann pressure, but it changes very mildly. In the second half cell, the pressure peak is in the vicinity where transverse waves collide, instead of where the leading front is.

5.7.3 Triple-wave Configuration

Except in the proximity of the end point of a cellular structure where a complex strong structure may occur, the triple-wave configuration always shows a single Mach structure, which involves transverse wave, incident wave and Mach stem. By calculation, the pressure ratio of one side of the transverse wave to the other remains about 2.2. The pressure ratio measured by experiments (Edwards and Jones, 1978) is about 1.5, smaller than the present numerical result. A possible reason is that the sensor is too large to measure precisely the strength of the transverse wave near the Mach stem. Figure 5.25 shows a typical triple-wave configuration obtained by numerical simulation. The acute angle ψ between the transverse wave and the

incident wave is about 65°. The acute angle Δ between the incident wave and the Mach stem is 30° or so. The acute angle δ between the incident wave and the triple-point trajectory line is around 50°, and the acute angle ϕ between the Mach stem and the triple-point trajectory line is about 90°. Through numerical analysis, it is found that the angles above are relatively constant as the detonation front propagates. When moving along the triple-point trajectory, the triple-wave configuration is like rotating along the triple-point trajectory. The rotational angle is about half of the difference between the entrance angle and the exit angle, i.e. $\beta - \varphi$.

5.8 Resolution Study

On the grid convergence for the two-dimensional detonation simulations, we repeated the two-dimensional straight-duct computation with the mesh sizes 0.2mm and 0.05mm. We compare them with the result at mesh size of 0.025mm by Hu et al. (2004). Figure 5.26 shows the comparison among the pressure contours computed with mesh sizes of 0.2mm, 0.1mm, 0.05mm. Figures 5.27 show the close-up view of the pressure, density and temperature contours at time t=871 μs obtained using mesh size 0.1mm depicting the structure within one transverse wave for a detailed comparison to the counterparts obtained using mesh size 0.2mm, 0.05mm and 0.025mm (Hu et al., 2004) shown in Figures 5.28-5.30. By comparison, it is clear that mesh size has a fair influence on the numerical simulation of the cellular structure. For the result with mesh size 0.2mm, the triple-wave configuration is only shown very vaguely. The detailed features around the triple point, however, are not at all resolved. The position of the triple point is not precisely defined. More importantly, till at time

t=3ms, the number of the transverse waves is still about 7, which is believed to be unstable. For the results with 0.1mm, 0.05mm and 0.025mm, the cellular structures have become steady and regular early at about 800us. In additional, a finer mesh size can resolve the structure details well. The numerical results based on the mesh size of 0.1mm present much more information than that of 0.2mm. In Figure 5.27, there seems to be the presence of a slip line dividing the regions behind the Mach stem and the transverse wave, and the features are more clearly defined in Figures 5.29 and 5.30. Strictly, a transverse wave can be divided into two parts: one is the part connected to the triple-wave point called the main transverse wave; the other part extends from the main transverse wave and is called the extending transverse wave. There should be a turning point between these two parts. However, in Figure 5.28, the transverse wave seems to be extended from the triple-wave points smoothly, and there is no distinct turning point, and therefore the configuration may look like a single-Mach configuration, which is one of the hallmarks of a weak structure. Figures 5.29 and 5.30, based on the mesh size of 0.05mm and 0.025mm, respectively, shows the detailed cellular structure and clear features around the triple point, and therefore is more satisfactory. Some selected features of the cellular structure with different mesh sizes are given in Table 5.2. In short, the results with mesh size 0.1mm, 0.05mm and 0.025 show similar resolution of the basic cellular structure. The mesh size of 0.05mm and 0.025mm can resolve more and finer features of the structure, such as more slip lines and additional shock wave, which was the focus of Hu et al. (2004), but not the intent of the present work. In addition, using finer mesh size like 0.05mm

or 0.025mm requires much more CPU resources. This is one reason why the mesh size of 0.1mm is used as the standard resolution for computation and analysis in the present work.

5.9 Experiment with Artificial Perturbations

In order to study the effect of the artificial perturbations on the present numerical computation, we repeated the two-dimensional straight-duct computation with the disturbance coefficient α =1.0. Figures 5.31 and 5.32 show the pressure contours of the structure with the disturbance coefficient α =0.35 and 1.0, respectively. The latter disturbance amplitude is much larger than the former. A comparison between Figure 5.31 and Figure 5.32 shows that increasing the intensity of initial perturbation by a higher value of a can shorten the time for the initial formation of the triple wave configuration (15us versus 25us). However, the same mode regular structure (including the structure regularity and cell size) is reached at almost the same time provided the channel height is kept constant. This numerical perturbation experiment suggests that the final cellular structure is fairly independent of the initial conditions.

Table 5.1 Comparison of cell geometries between the current simulation and experiments

Cell geometries	Current results	Experiments*
Width/length (d/l)	0.55	0.5-0.6
Exit angle (φ)	8°	5°-10°
Entrance angle (β)	38°	32°-40°
Transverse Track angle (ω)	28°	~30°

* From Strehlow (1968)

Table 5.2 Properties of the structures in a straight duct at different resolutions

Mesh size (mm)	Number of Detonation Cells	Number of Slip lines around one transverse wave	Number of triple-wave points around one transverse wave	Additional shock waves
0.2				
0.1	2.5	1	2	No
0.05	2.5	2	2	Yes
0.025*	2.5	2	2	Yes

* From Hu et al. (2004)

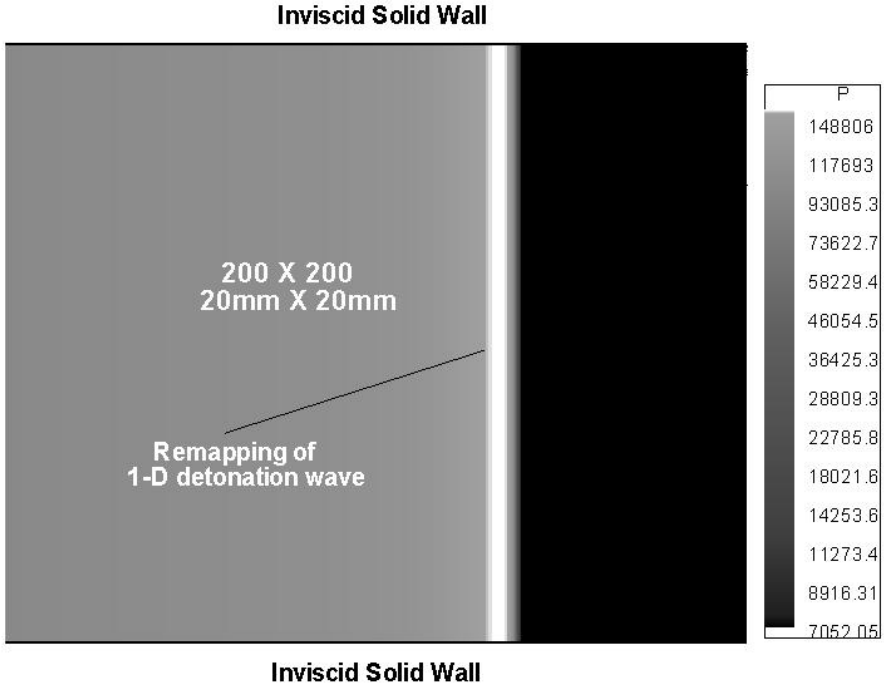

Figure 5.1 The computational domain and initial shock

wave for the 2-D detonation computation

Figure 5.2 The initial pressure contour with artificial perturbations

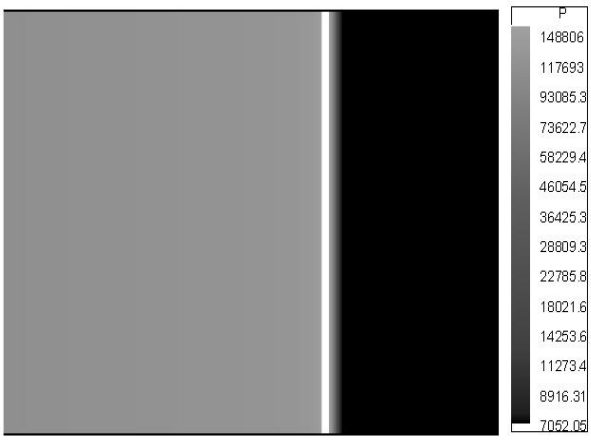

(a) Time = 0μs

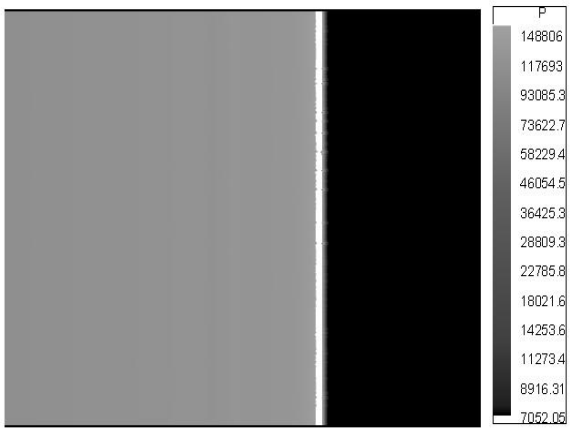

(b) Time = 5μs

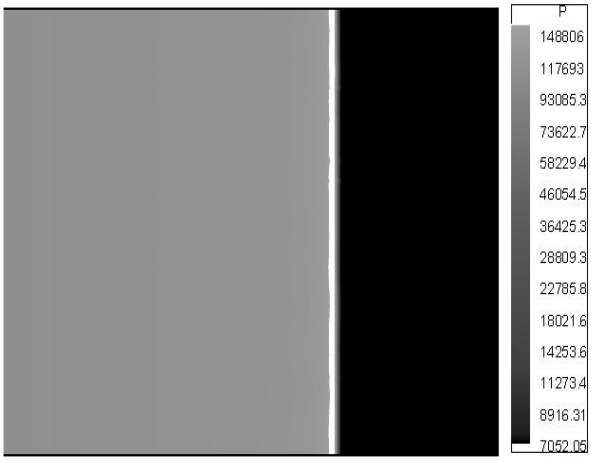

(c) Time = 10μs

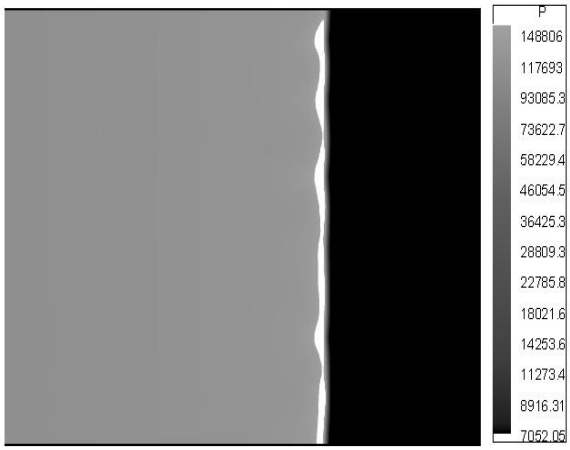

(d) Time = 15μs

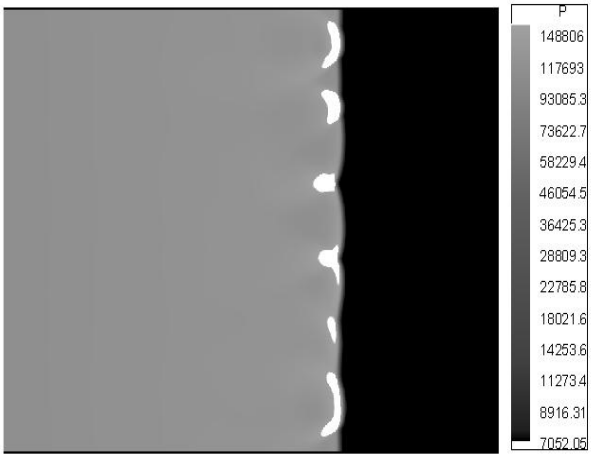

(e) Time = 20μs

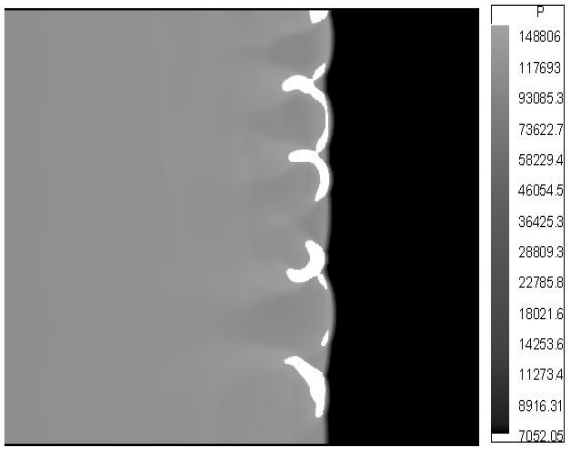

(f) Time = 25μs

Figure 5.3 Formation and evolution of the triple-wave configuration

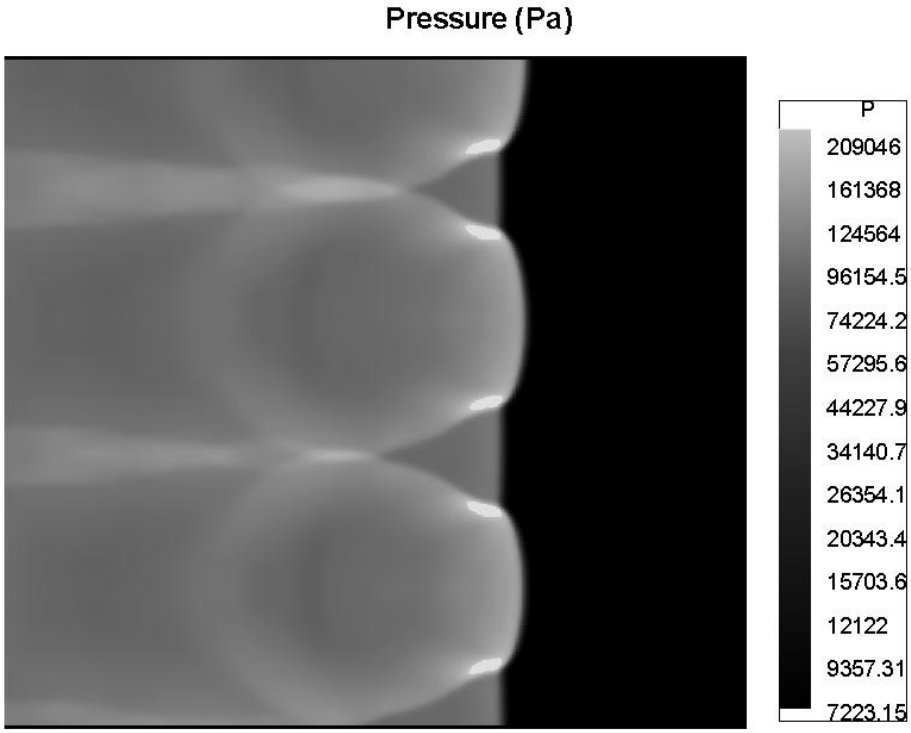

Figure 5.4 The regular triple-wave configuration at time = 871μs

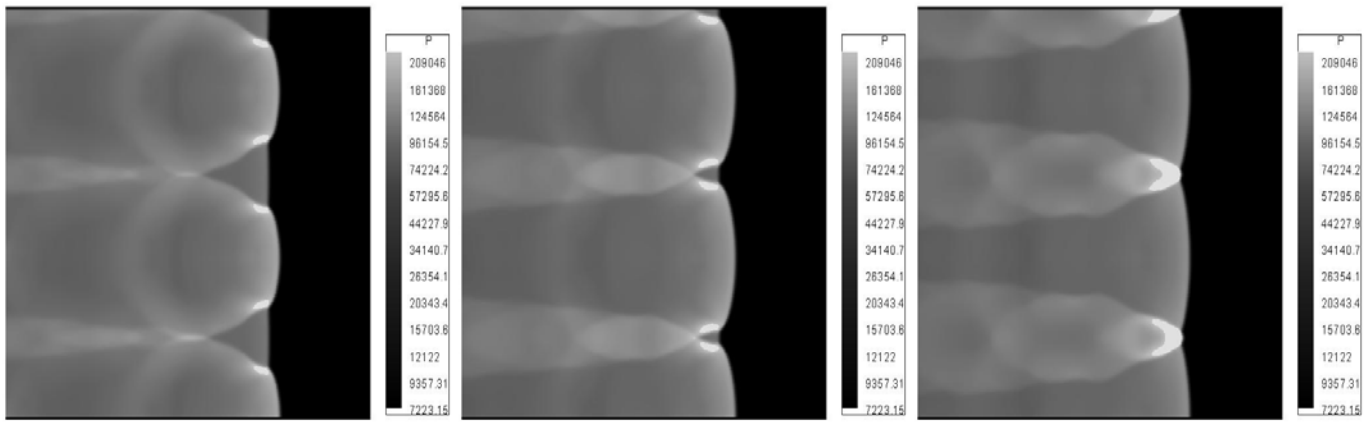

Time = 875μs Time = 876μs Time = 877μs

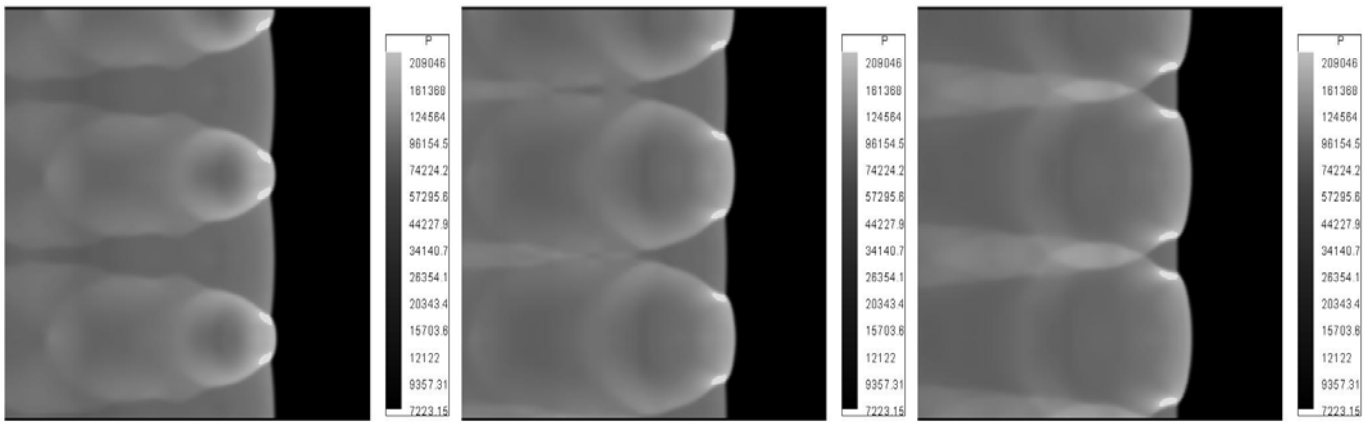

Time = 878μs Time = 879μs Time = 880μs

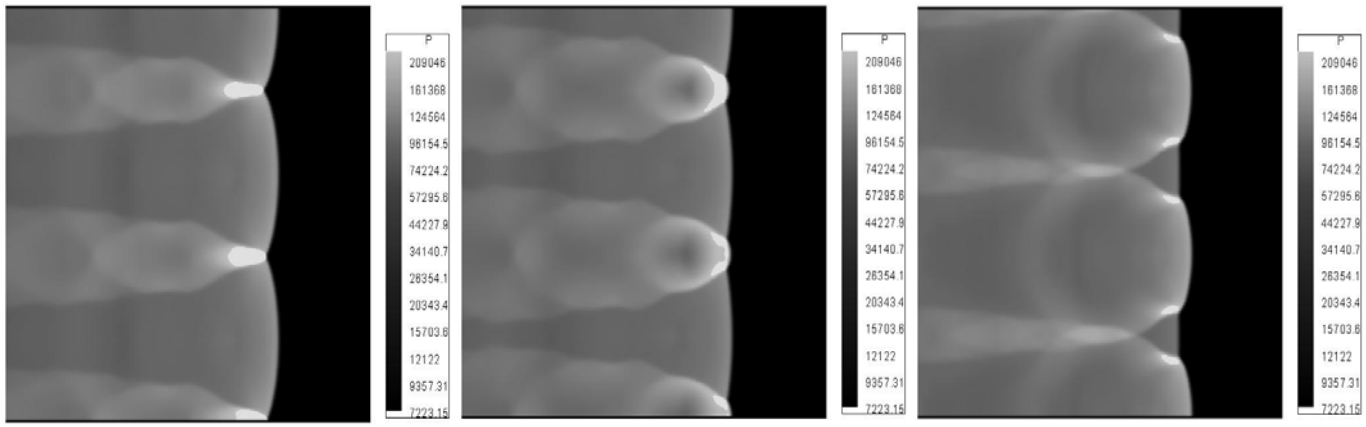

Time = 881μs Time = 882μs Time = 884μs

Figure 5.5 Periodical evolution of triple-wave configuration

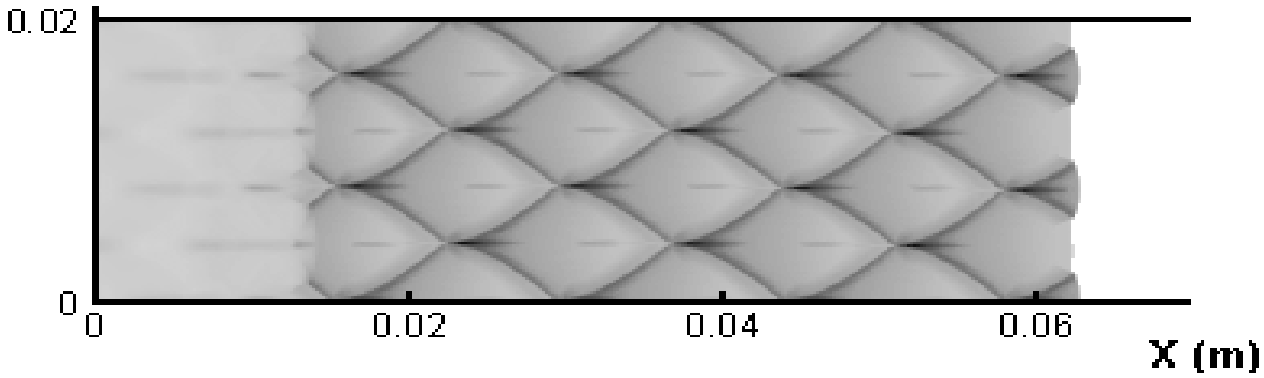

Figure 5.6 Numerical cellular structures obtained in the 2-D detonation simulation

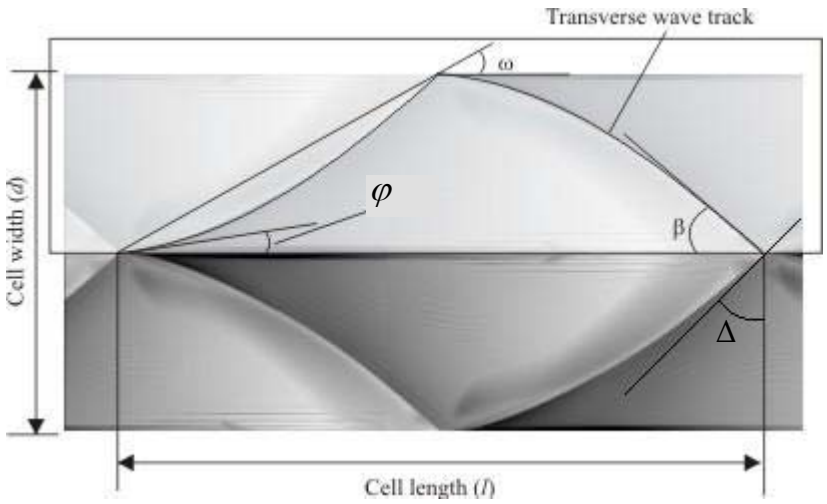

Figure 5.7 Numerical detonation cell and its geometry parameters

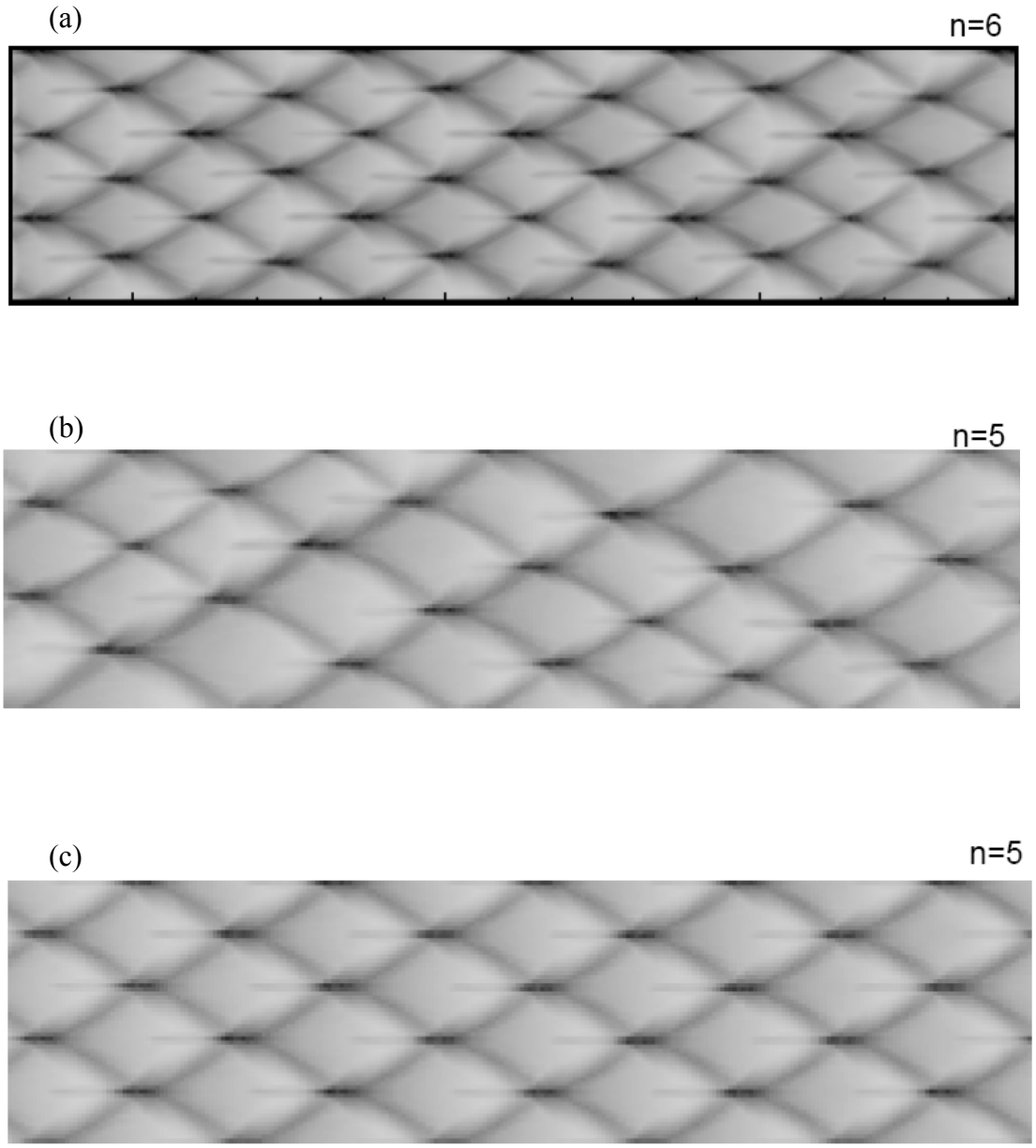

Figure 5.8 Evolution of the cellular structures with time

(a: 200-250μs, b: 500-550μs, c: 1000-1050μs)

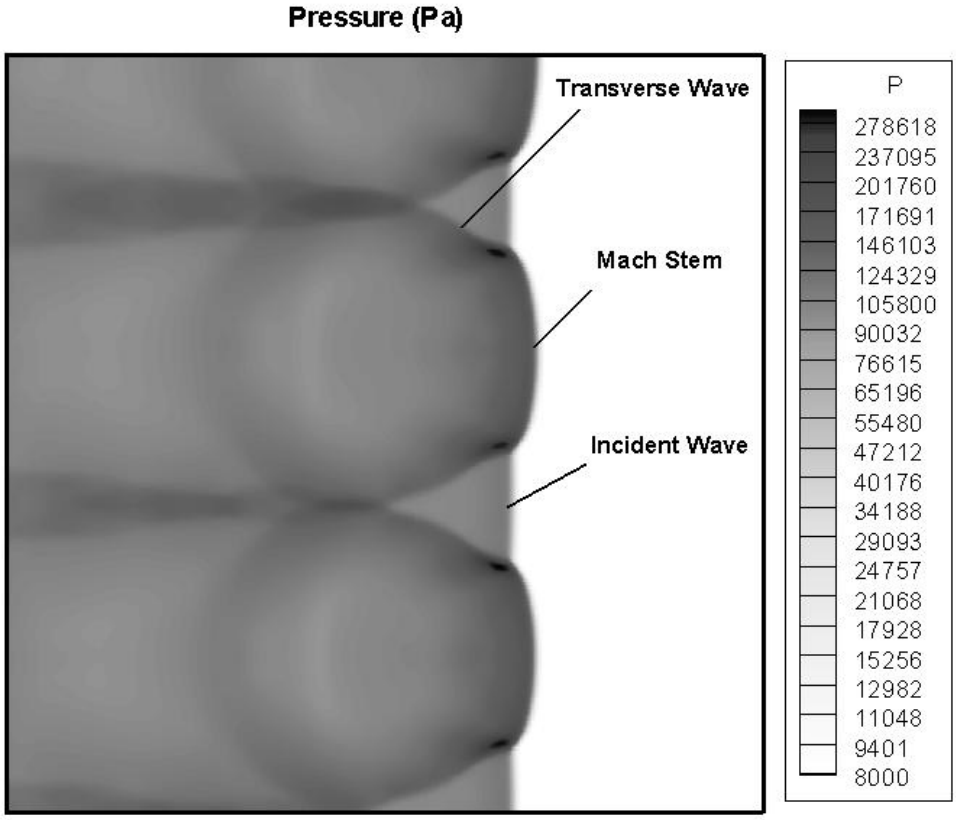

Figure 5.9 Pressure contours at time = 871μs

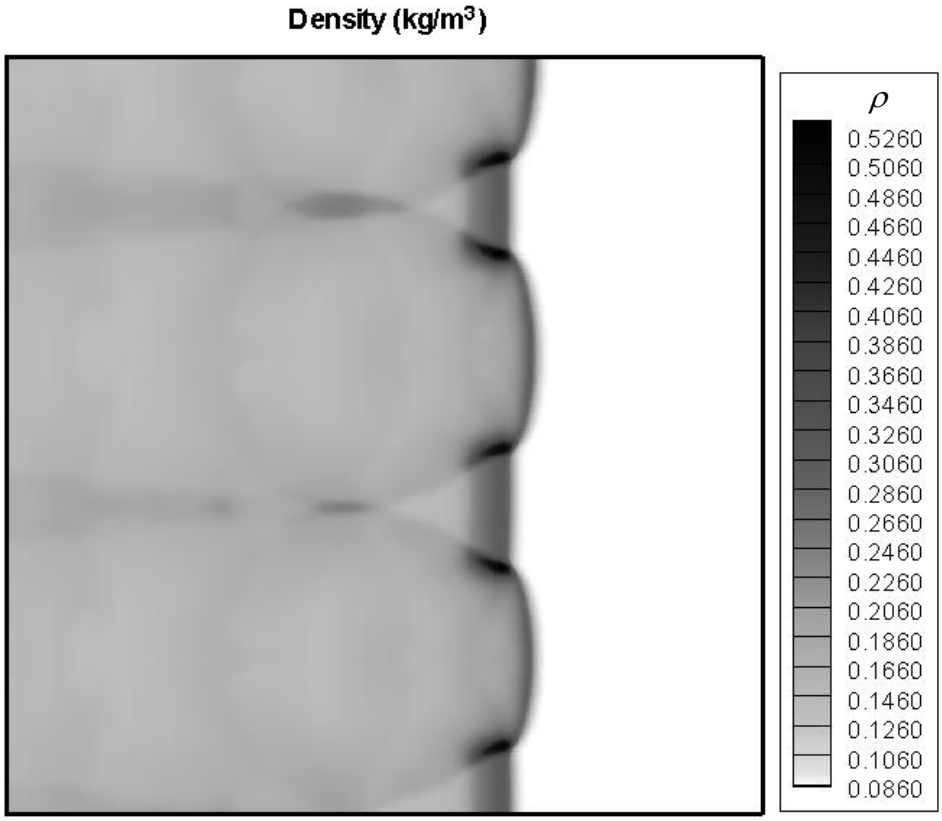

Figure 5.10 Density contours at time = 871μs

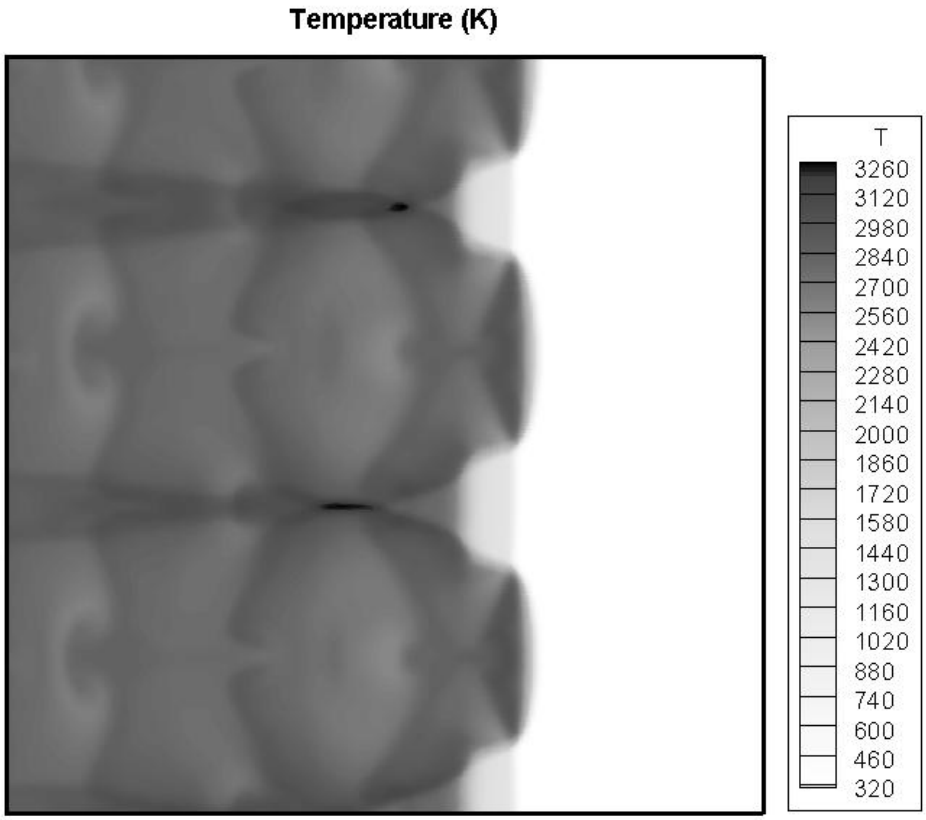

Figure 5.11 Temperature contours at time = 871μs

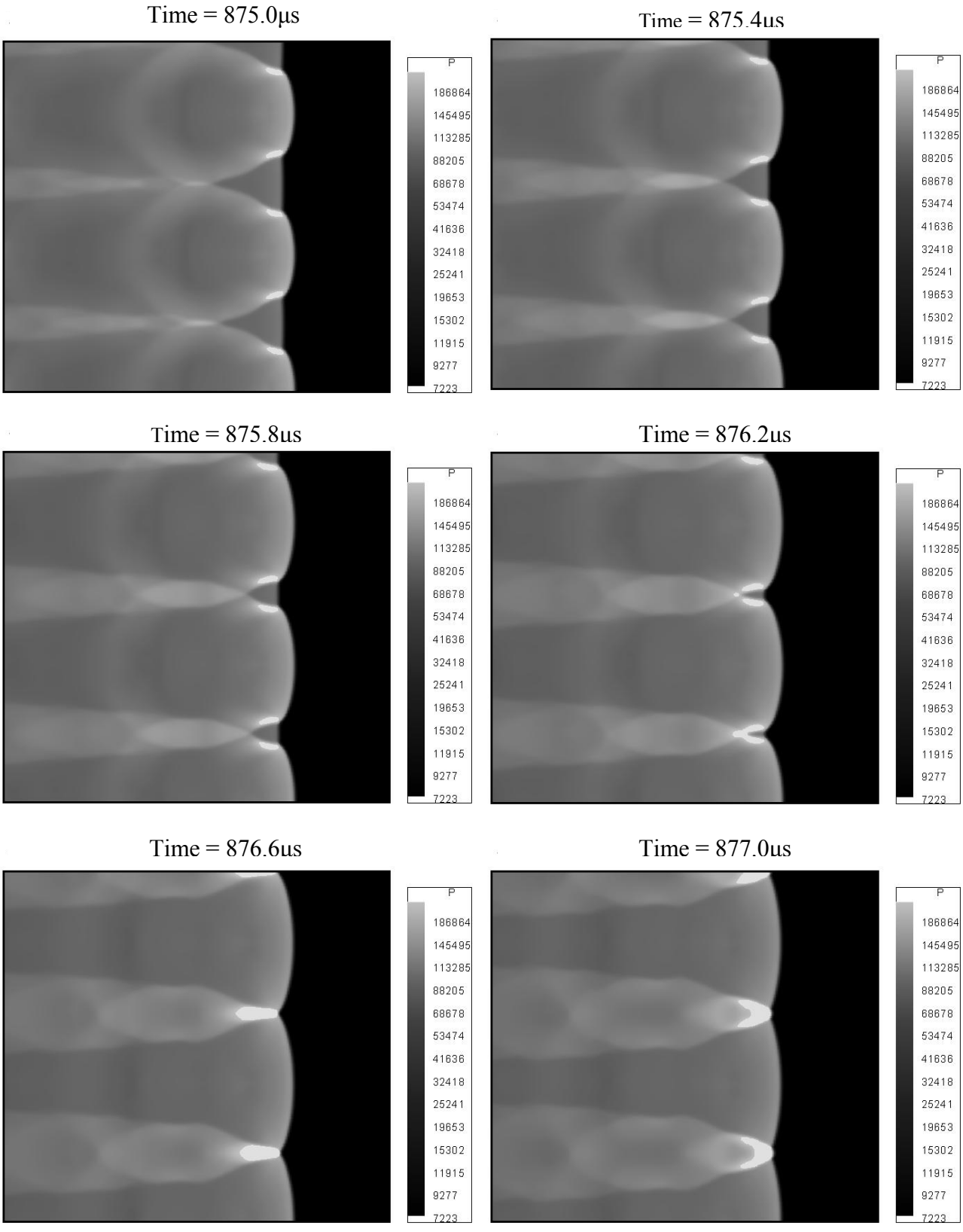

Figure 5.12 Pressure contours at 6 consecutive moments

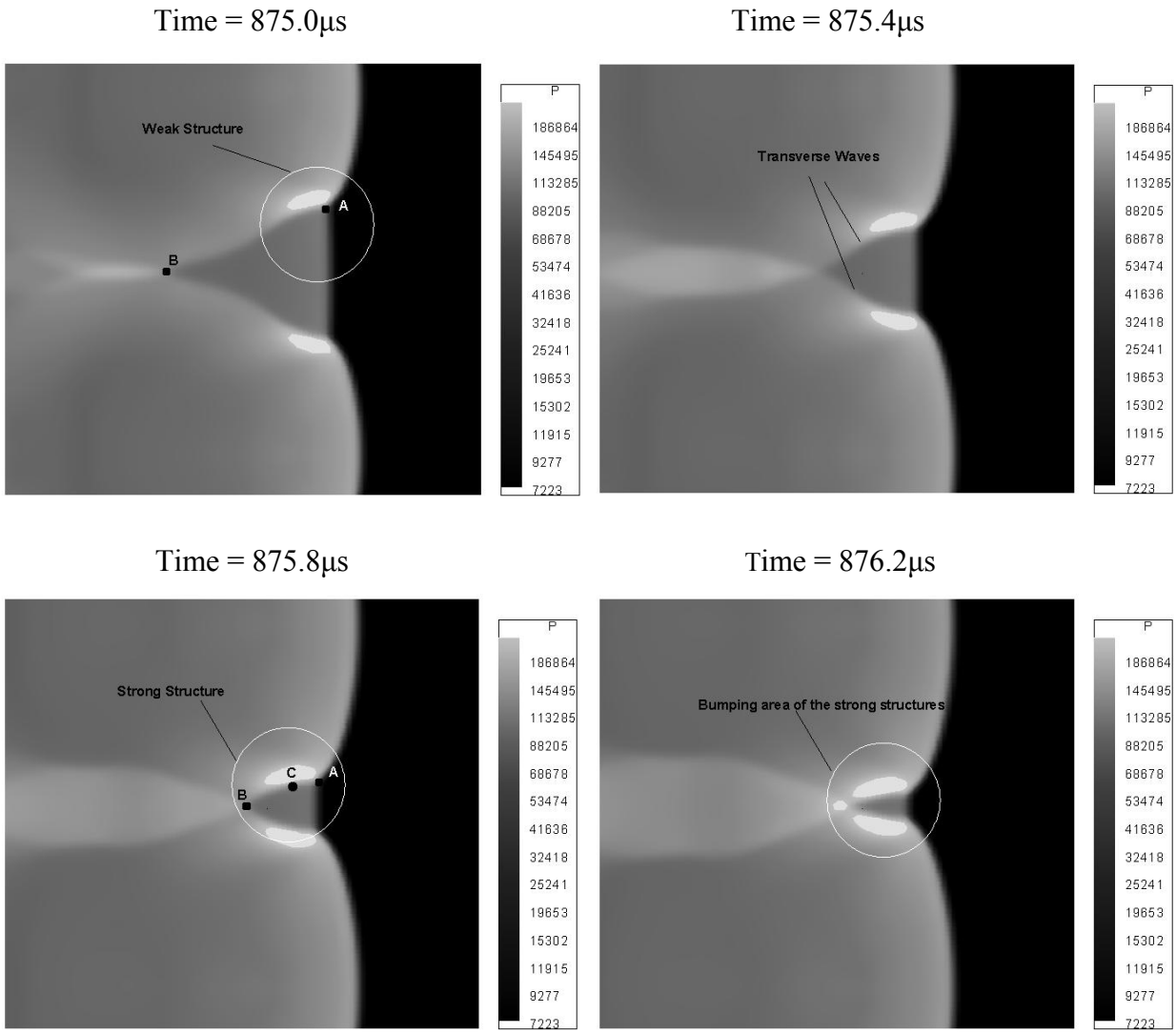

Figure 5.13 Close-up view of the pressure contours at 4 consecutive moments

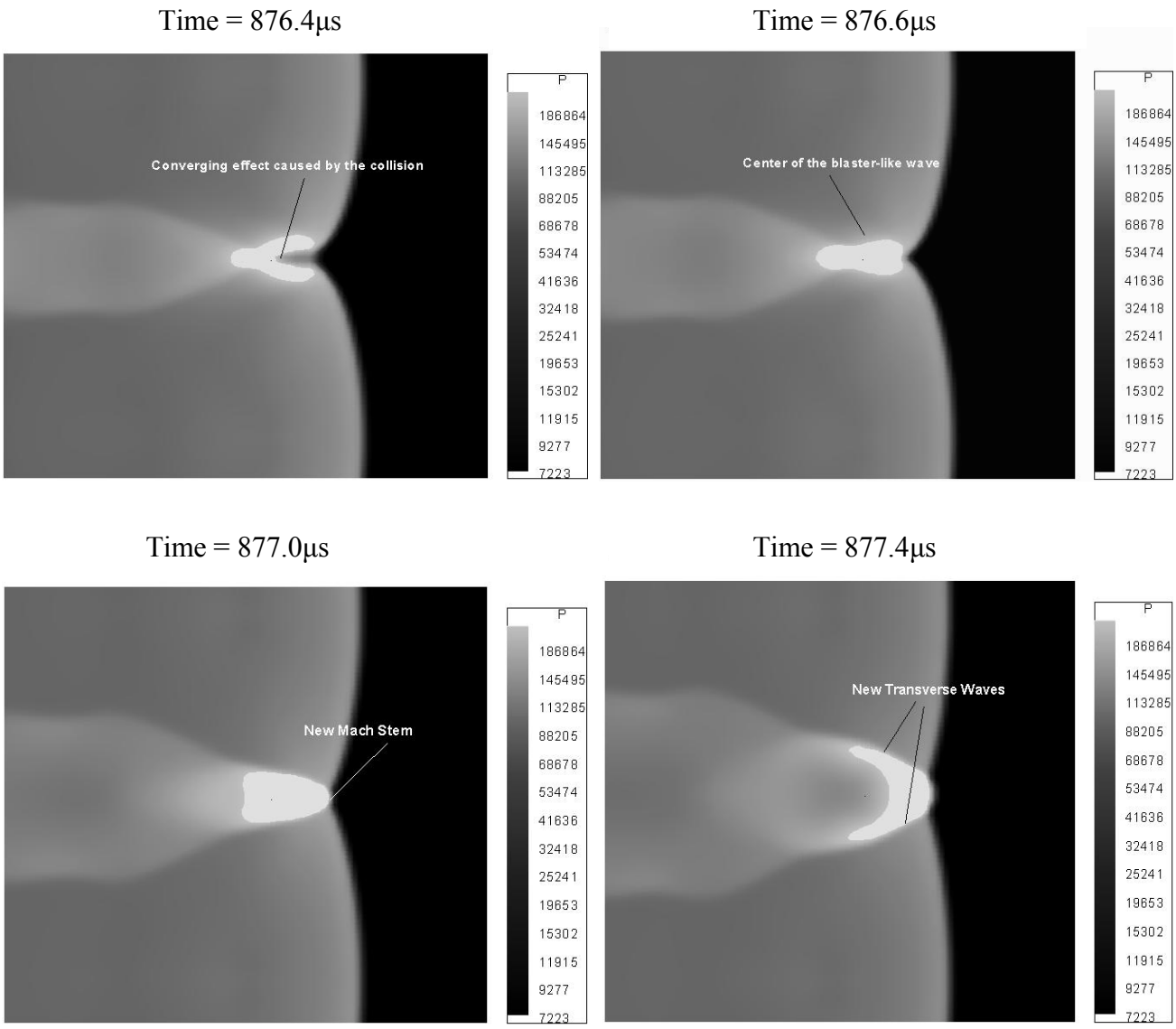

Figure 5.14 Pressure contours as the blaster-like wave is formed

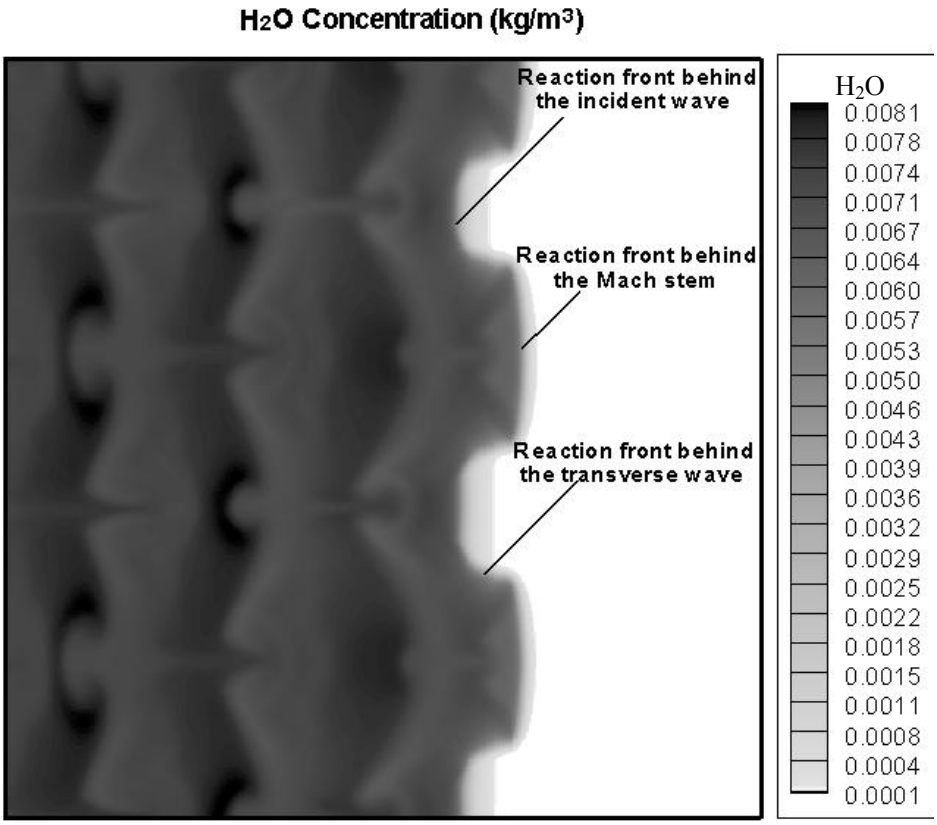

Figure 5.15 Concentration contour of H_2O with the reaction fronts at time = 871μs

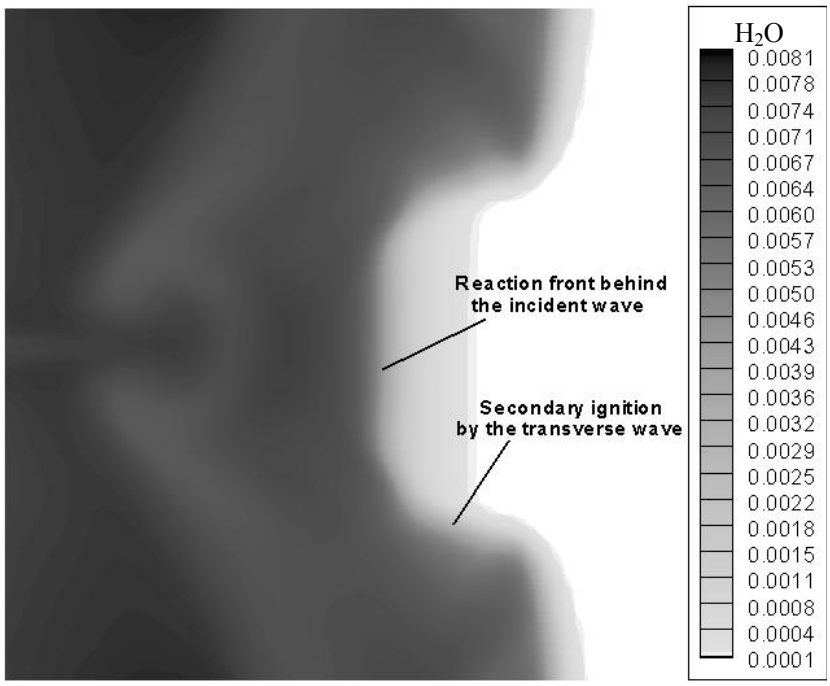

Figure 5.16 Close-up view of the reaction front

behind the incident wave at time = 871μs

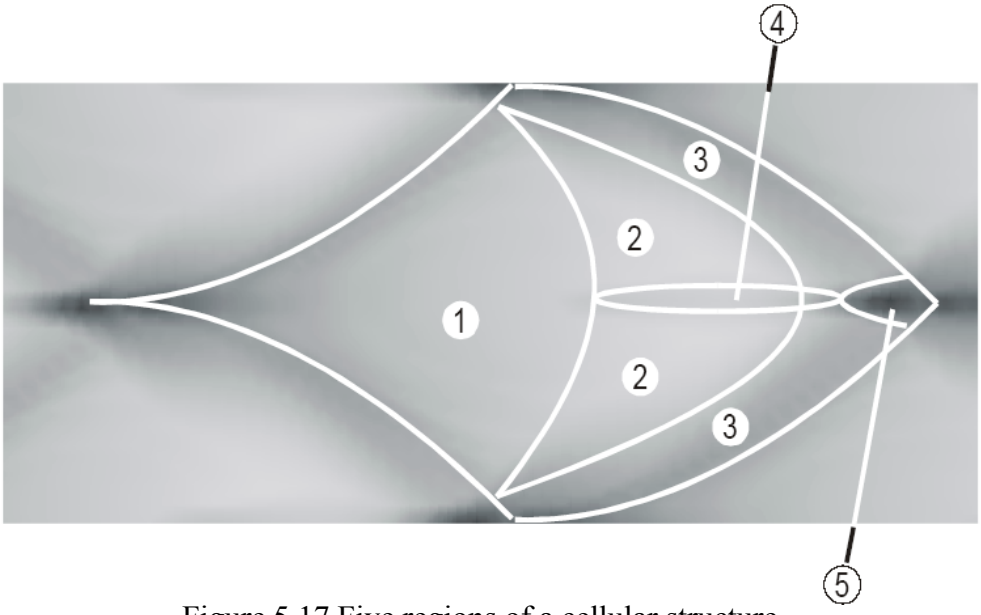

Figure 5.17 Five regions of a cellular structure

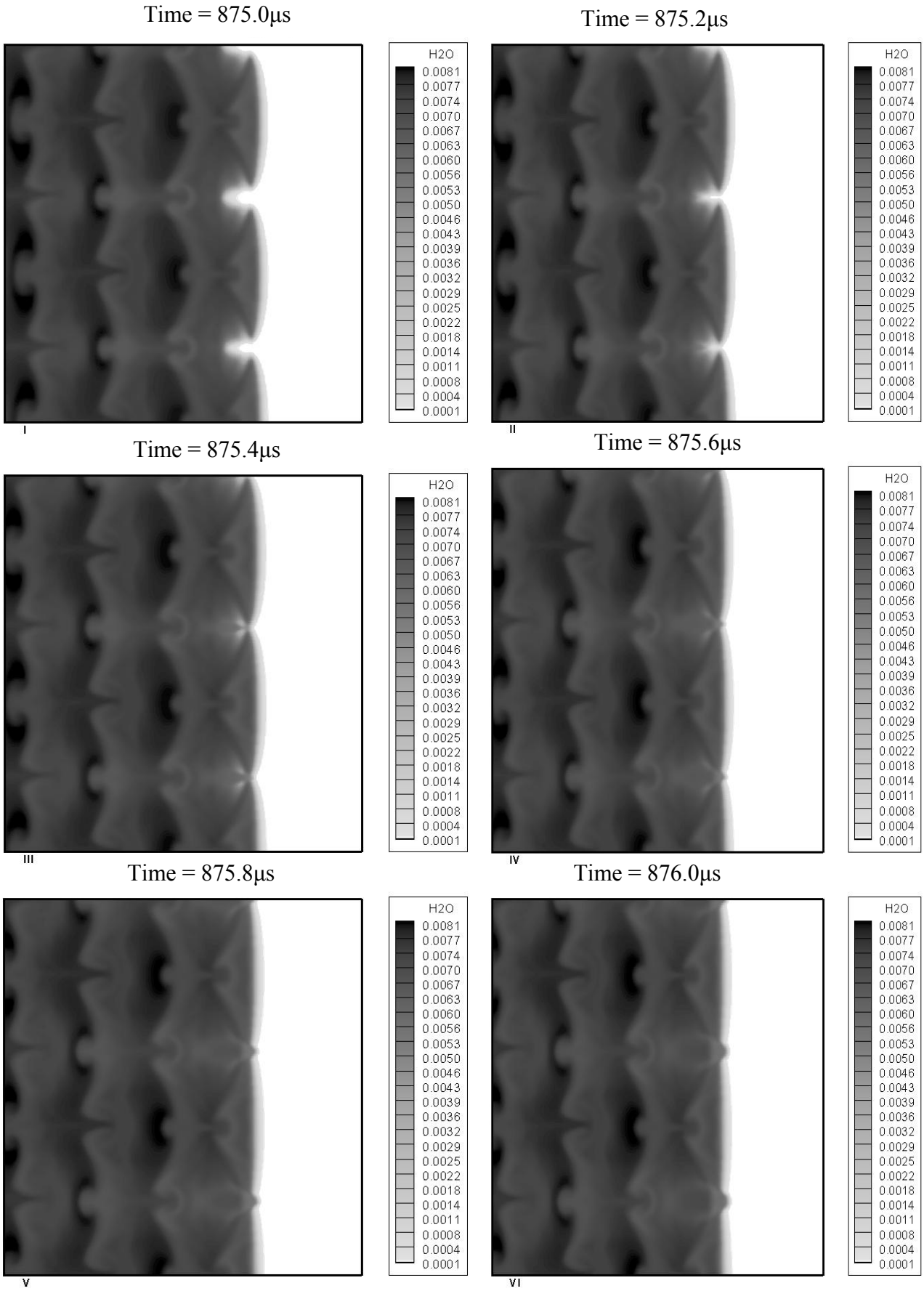

Figure 5.18 H_2O concentration at 6 consecutive moments

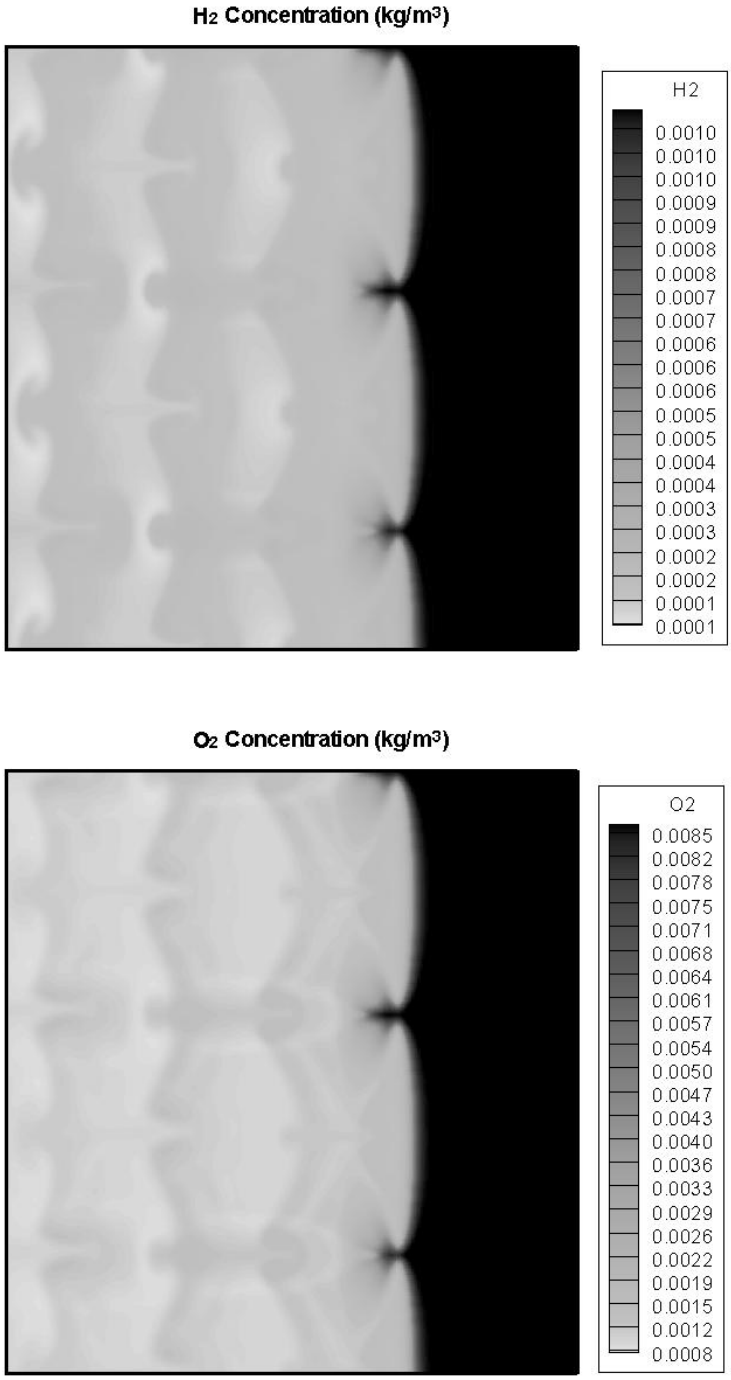

Figure 5.19 Concentration contours of H_2 and O_2 at time = 875μs

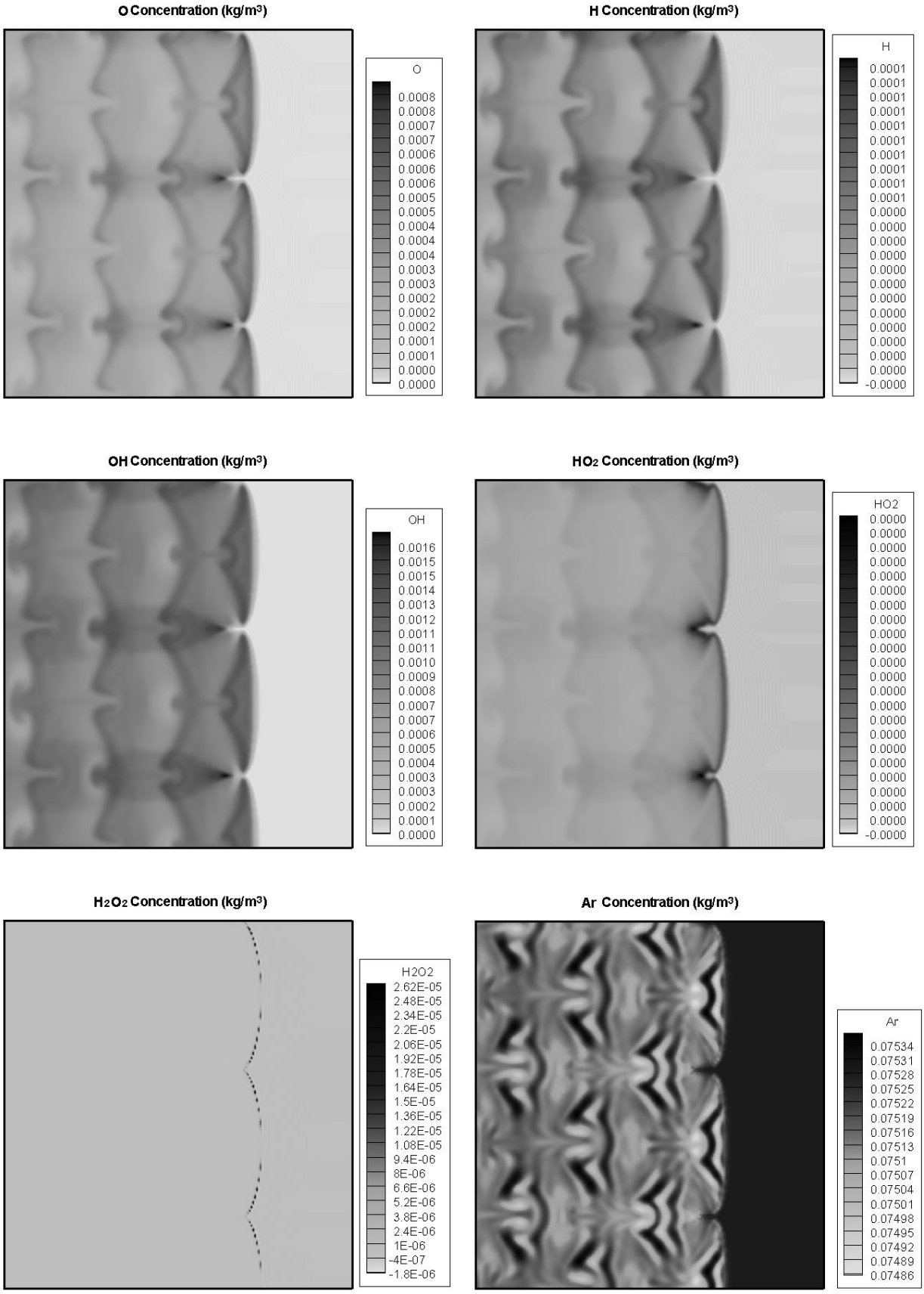

Figure 5.20 Concentration Contours of O, H, OH, HO_2, H_2O_2 and Ar at time = 875μs

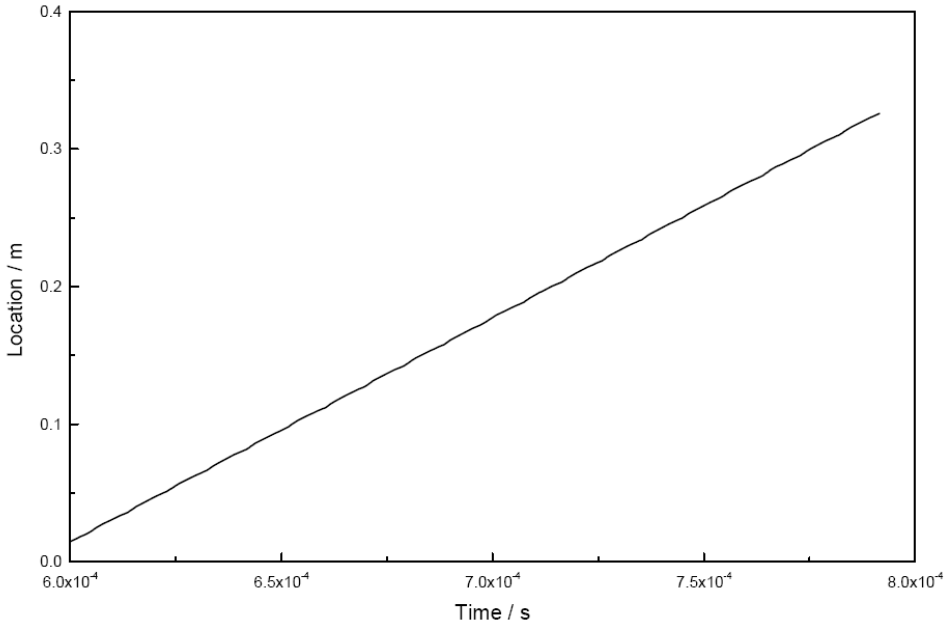

Figure 5.21 Location of the detonation front vs time

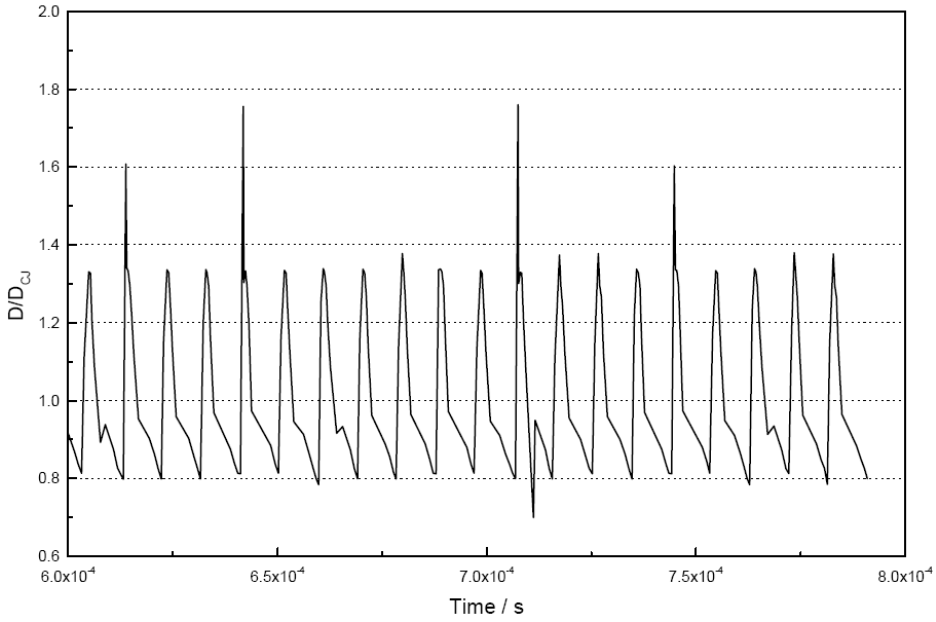

Figure 5.22 Instantaneous detonation speed vs time

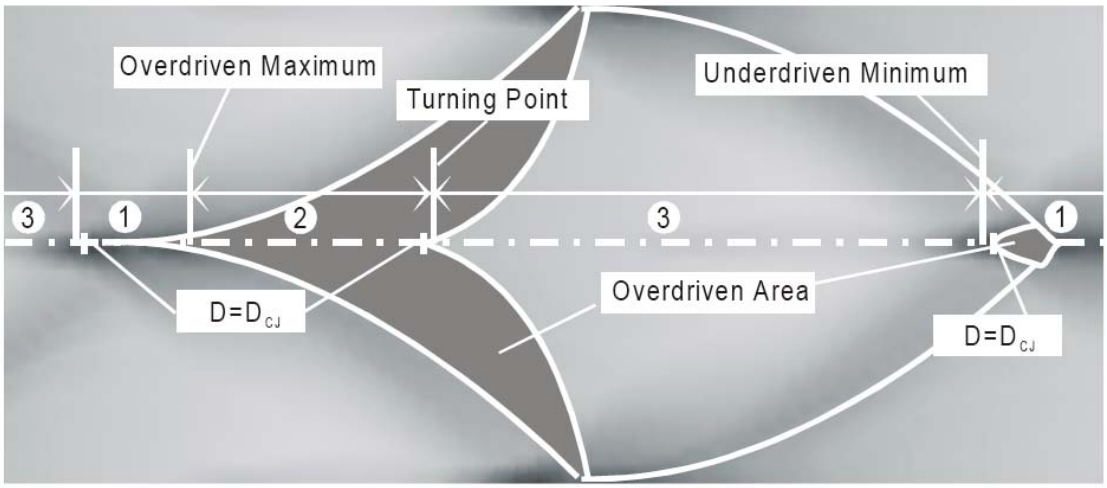

Figure 5.23 Distribution of the instantaneous detonation speed on a cellular structure

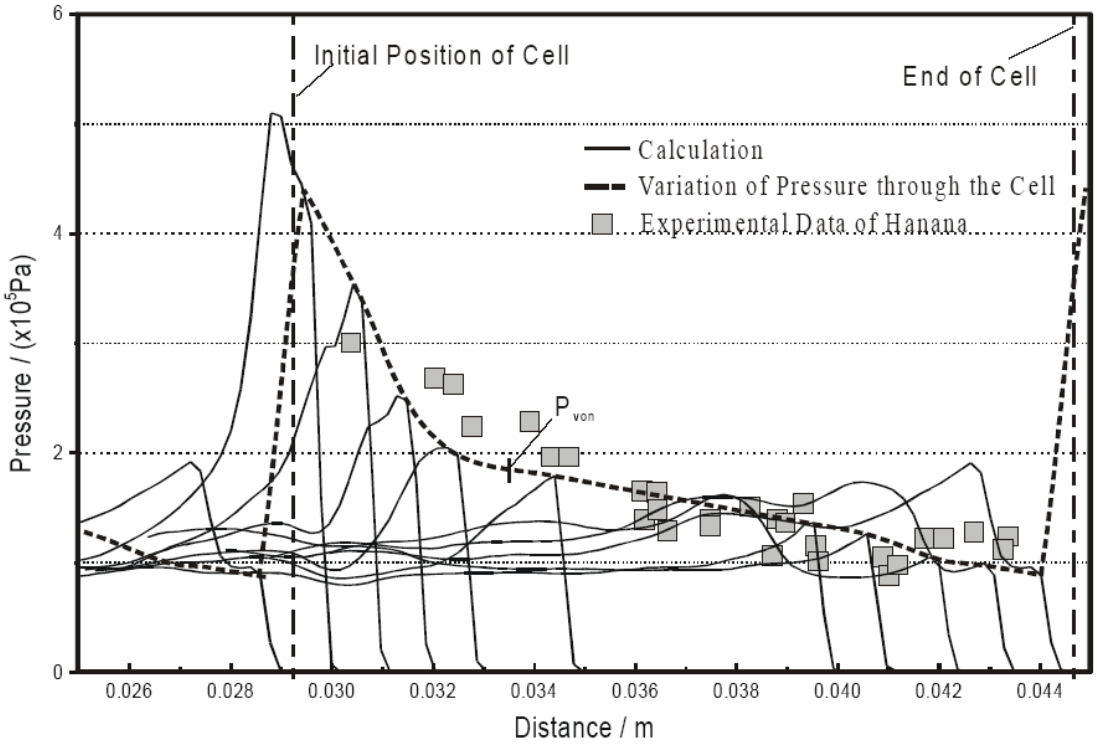

Figure 5.24 Pressure distribution on the central line of a cellular structure

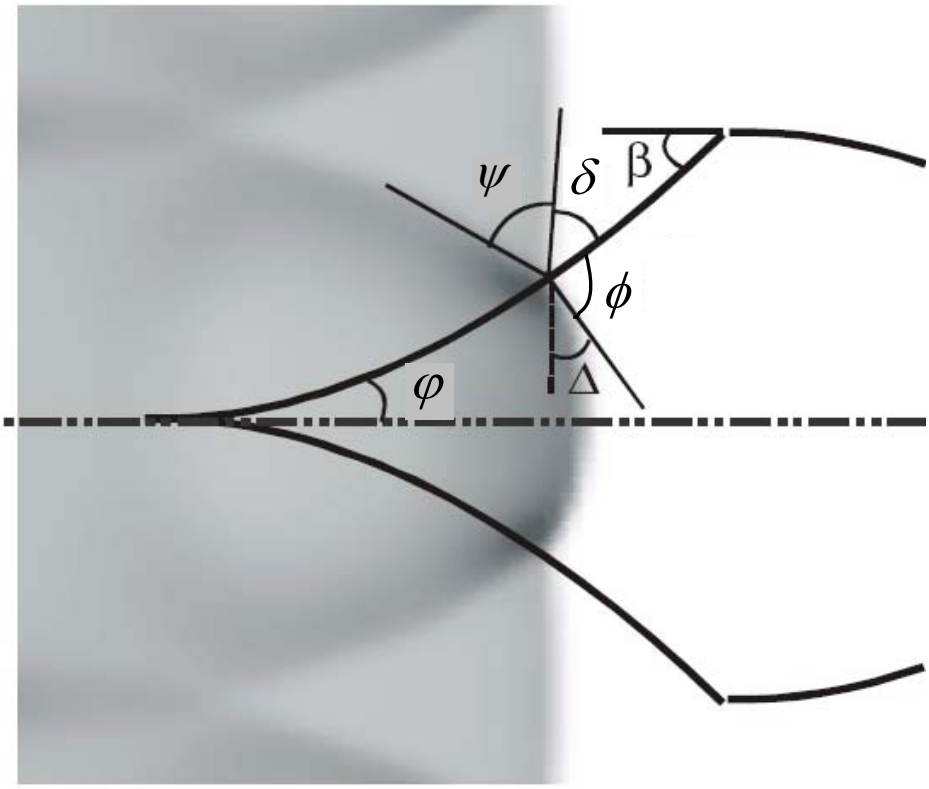

Figure 5.25 Geometric relationship of a numerical triple-wave configuration

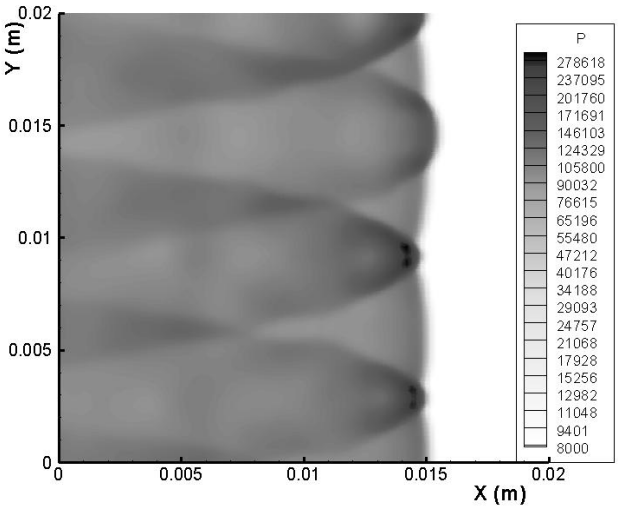

(a) Mesh size = 0.2mm

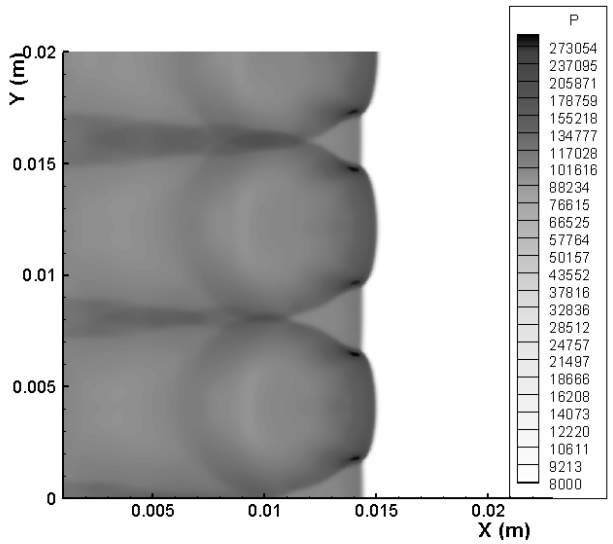

(b) Mesh size = 0.1mm

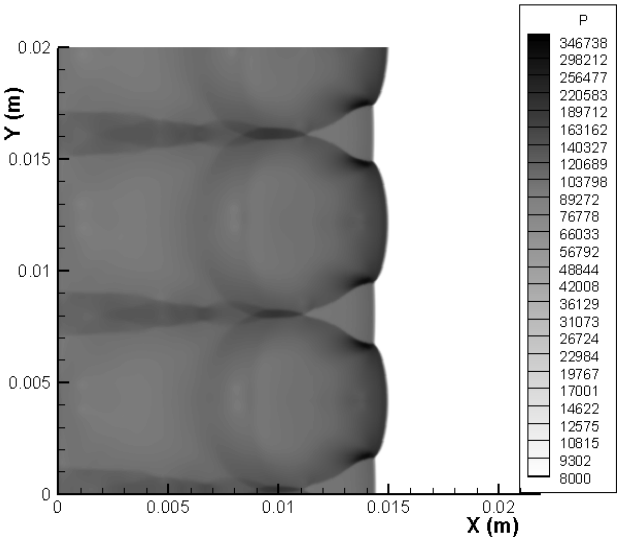

(c) Mesh size = 0.05mm

Figure 5.26 Comparison of the Pressure contours with different mesh size at time = 871μs

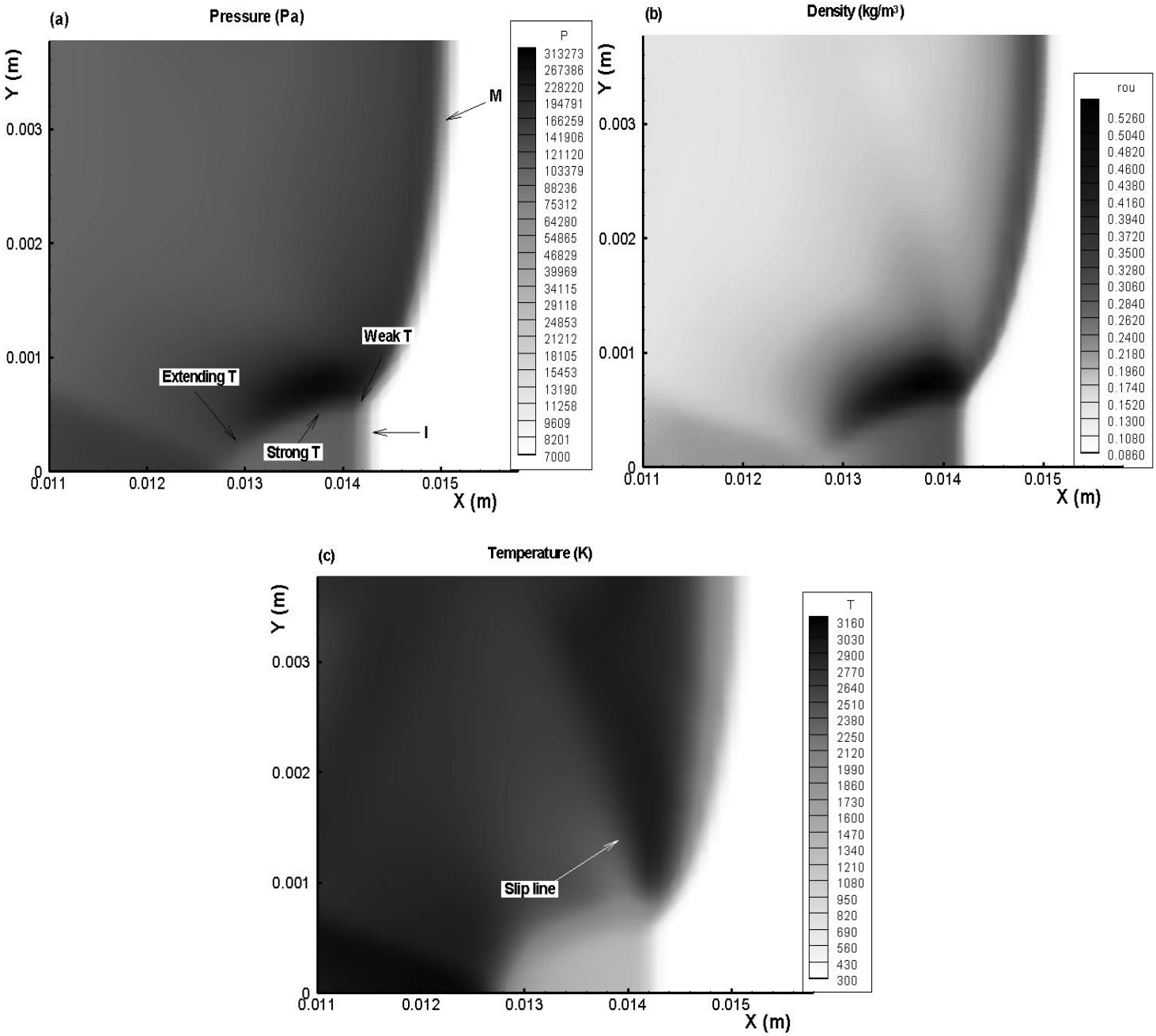

Figure 5.27 Structure with one transverse wave with the mesh size of 0.1 mm

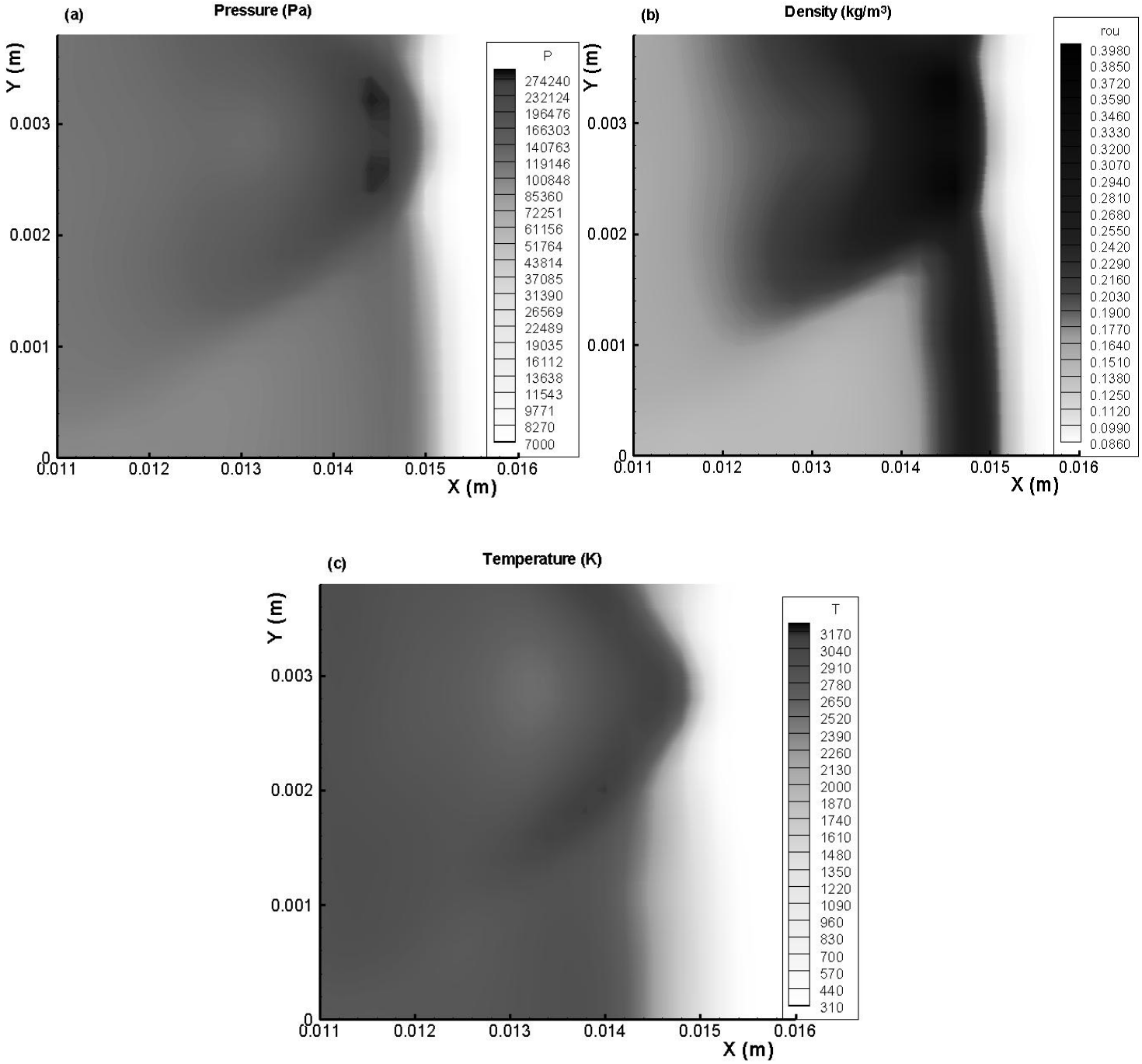

Figure 5.28 Structure with one transverse wave with the mesh size of 0.2mm

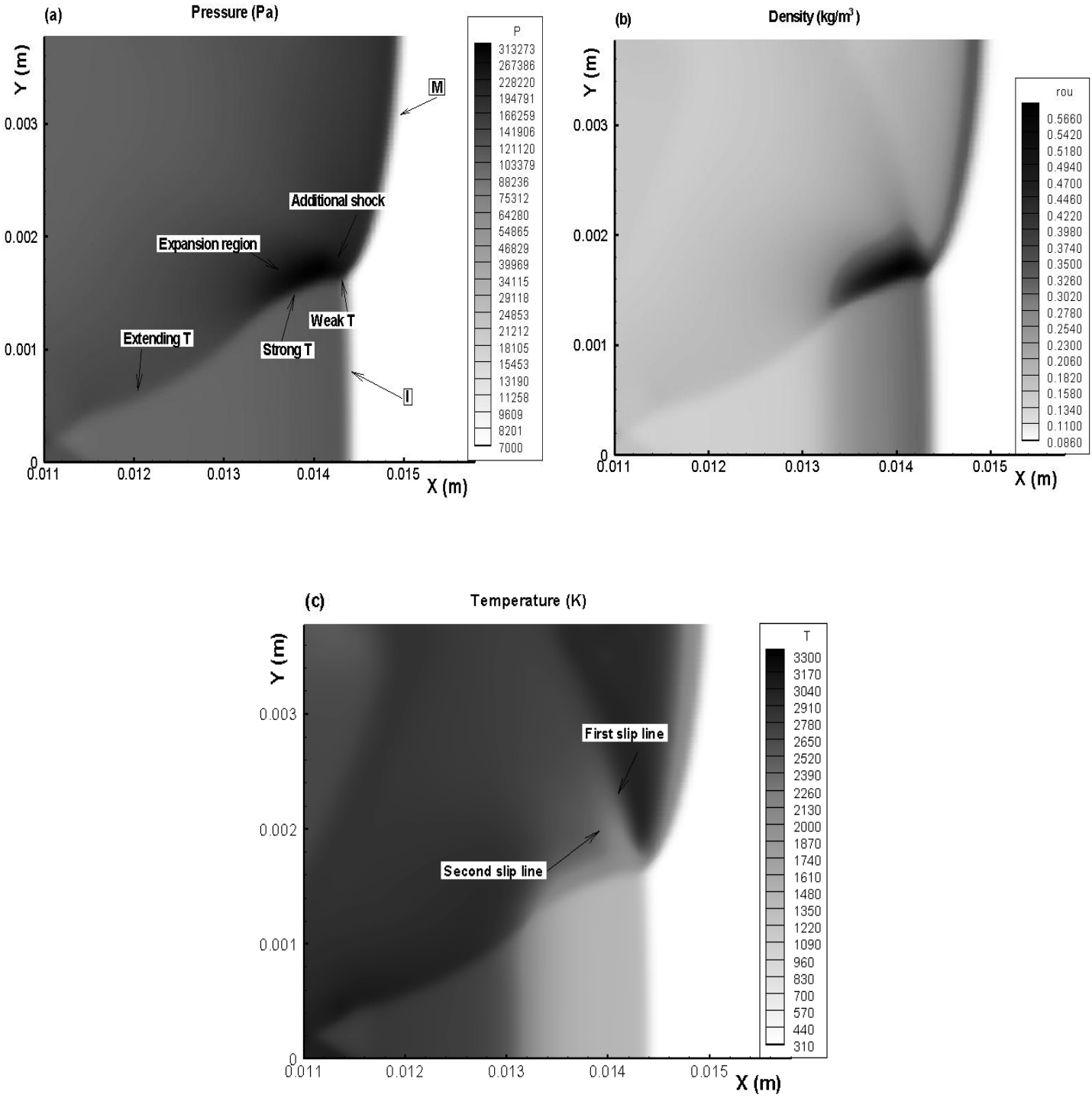

Figure 5.29 Structure with one transverse wave with the mesh size of 0.05mm

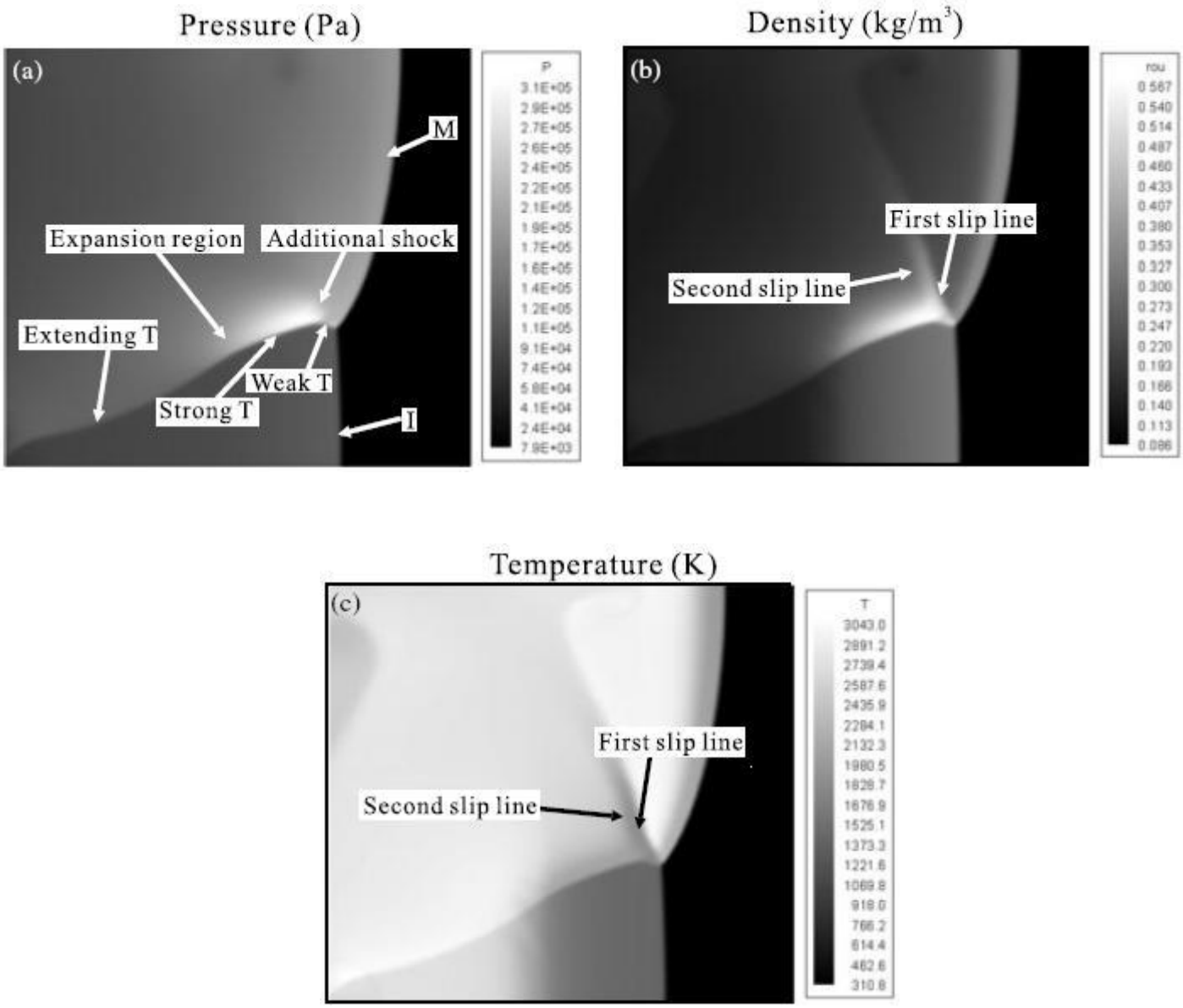

Figure 5.30 Structures with One Transverse Wave with the mesh size of 0.025mm (Hu et al., 2004)

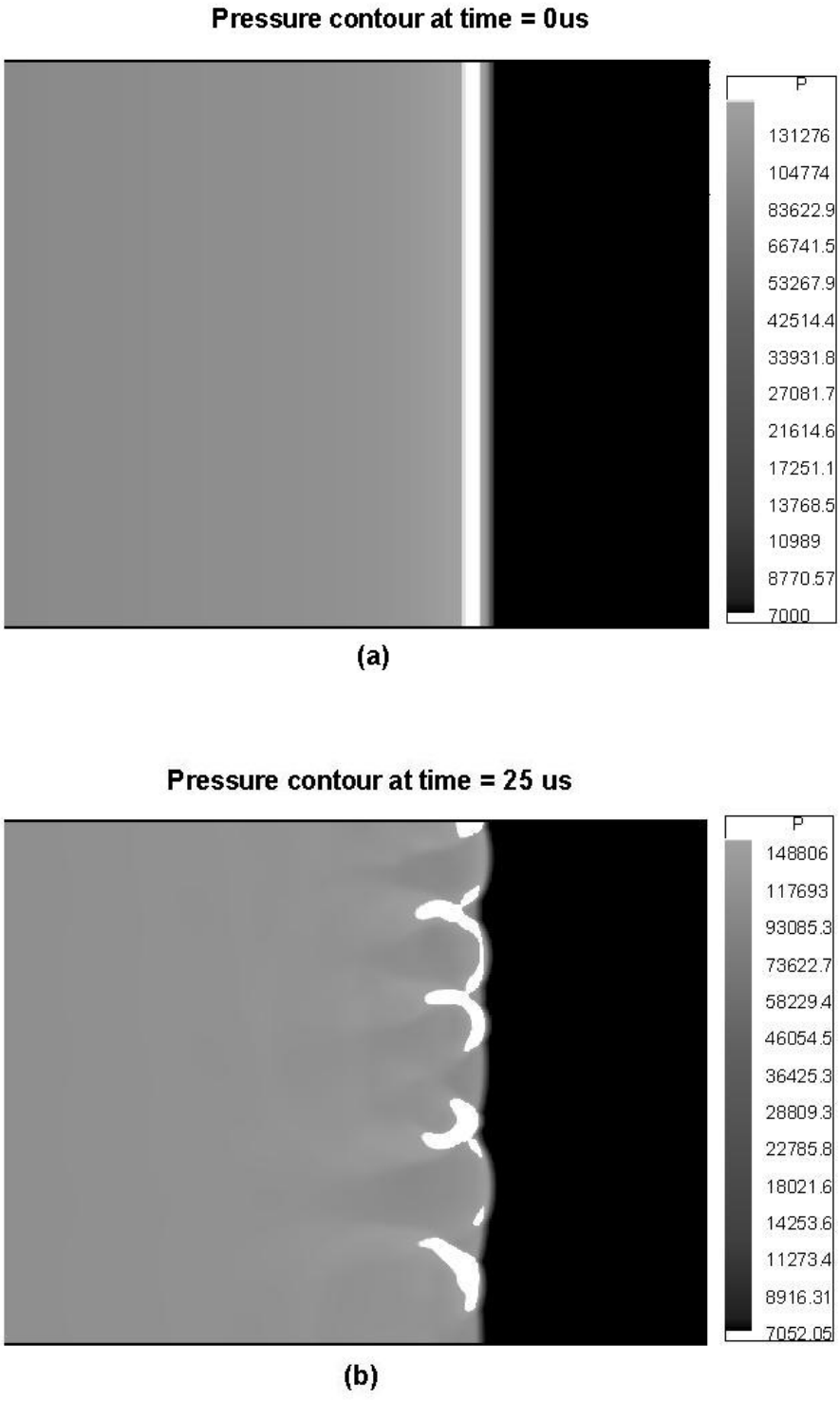

Figure 5.31 Formation of Triple-wave Configuration

with the disturbance coefficient α =0.35

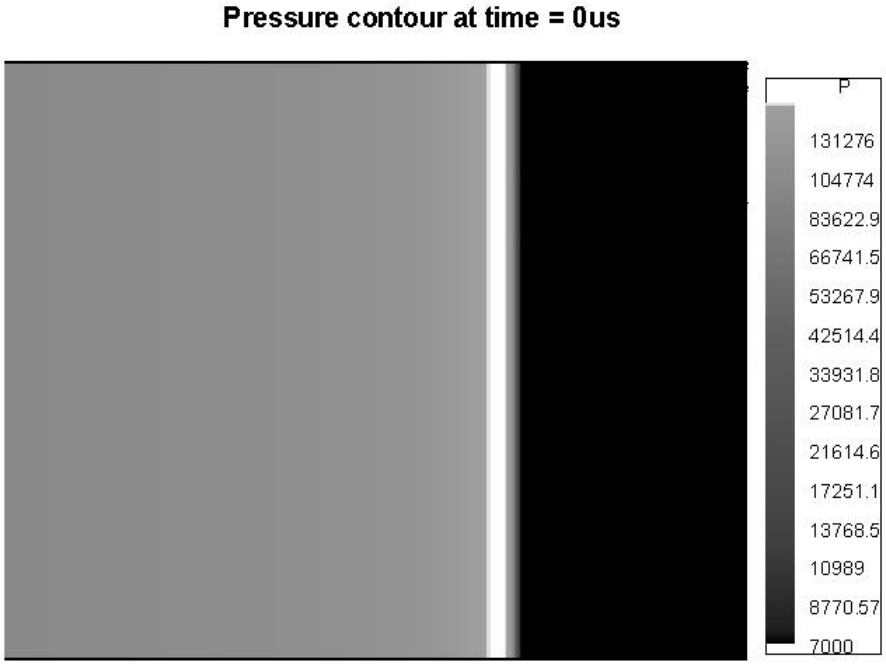

Figure 5.32 Formation of Triple-wave Configuration

with the disturbance coefficient α =1.0

Chapter 6 Two-dimensional Detonation Wave in a Diverging /Converging Chamber

6.1 Computational Setup

In this chapter, the numerical simulation models a detonation propagating from left to right in a two-dimensional converging/diverging chamber with a stoichiometric H_2/O_2 mixture diluted with 70% argon at an initial pressure and temperature of 6.67kPa and 298K, respectively. Figure 6.1 (a, b) shows the schematic of the two chambers considered for the present computation for the converging and diverging case. Each case consists of a short 2-D straight duct, followed by a converging/diverging duct with a wedge angle θ. The wedge angle θ is varied from 14 to 46 degree while the rest of the dimensions are provided in the figure. Cartesian coordinate system is employed in the present work. The mesh size is fixed at 0.1mm, i.e. $\Delta x = \Delta y = 0.1mm$. The number of grids in the *y* direction is defined as below,

$$Diverging\ \ Case: \begin{cases} N_y = 200, & if\ \ x <= 0.02m; \\ N_y = \text{int}((x-0.02)\tan\theta/\Delta y) + 200, & if\ \ x > 0.02m; \end{cases}$$

$$Converging\ \ Case: \begin{cases} N_y = 200, & if\ \ x <= 0.02m; \\ N_y = 200 - \text{int}((x-0.02)\tan\theta/\Delta y), & if\ \ x > 0.02m; \end{cases}$$

Figure 6.1(c) shows the sketch of the computational grids employed for the diverging case.

6.2 Initial and Boundary Conditions

In order to study the influences of geometry on the cellular structure and the detonation velocity of an existing detonation wave, we place the 2-D straight-tube

results obtained in Chapter 5 on this converging/diverging computational domain, serving as the initial condition, that is, the governing equations described in Section 2.2 are solved with an initial distribution of a stable 2-D detonation triple-shock structure. The initial pressure distributions are shown in Figure 6.2 for both the converging and diverging duct.

In the CJ detonation wave, the state behind the CJ plane is supersonic, and therefore could not affect the upstream state. As such, extrapolation is used for the inlet boundary condition. Neumann boundary condition is imposed on the outlet. The upper and lower walls use the reflected boundary conditions. The detailed boundary conditions (4 boundary points) are given as below,

Left boundary: Extrapolation outflow, defined for all the variables,

$$B_b(B = \rho, u, v, \rho e, P, Y_i) = B_1(1-\gamma) + B_N\gamma$$

where γ is the relaxation coefficient, B_1 is the current value of the first cell near the boundary, and B_N is the extrapolation limit. In our computation, we use γ =0.05 and B_N equals to the ambient fluid parameters.

Right boundary: The unreacted inflow with specified initial parameters, i.e.,

$$(U_k)_{N_x+i} = (U_k)_{t=0}, \quad i = 1,2,3,4; \quad k = 1,2,..,12$$

Upper boundary: Inviscid solid wall (Reflected boundary condition)

The details for the upper boundary are shown in Figure 6.1 (c). In Figure 6.1 (c), BP1, BP2, BP3 and BP4 are the boundary points. P1, P2, P3 and P4 are the points inside the computational domain.

Lower boundary: Central line (Reflected boundary condition), i.e.,

$(U_k)_j = (U_k)_4$, $(U_3)_j = -(U_3)_4$, $j = 0,1,2,3$; $k = 1,2,4,5..,12$

where $(U_k) = (\rho, \rho u, \rho v, \rho e, \rho Y_1, ..., \rho Y_8)$, and N_x is the last non-boundary cell on the right side;

6.3 Results and Discussions

6.3.1 Diverging Chamber

The development of the detonation is illustrated in Figure 6.3 in the form of the grey-scale contours of the maximum pressure, $p_{\max}$, reached at each point in space. We refer to these figures as calculated smoke-foil records because they look similar to experimental patterns produced by a detonation wave on a coated surface. One may find that in Chapter 5, the contour of the maximum flow velocity, $|v|_{\max}$, was employed as analogue of the smoke foil tracks used widely in experiments. Herein, we do not use the maximum flow velocity because the expansion effect caused at the diverging corner will accelerate the present supersonic flow, thus affecting the recording of the original cellular structure. Figure 6.3(a)-I shows the typical detonation cells pattern when the detonation wave propagates through the diverging chamber set at the sloping angle of θ=45º. From left to right, three regions are broadly identified, demarcated by A, B and C. The detonation cells in region A have good regularity and these are not affected by the diverging oblique wall. As the detonation wave moves through B, the initial regular cells becomes bigger and irregular by distorting upwards, until one of the cells nearly takes up the entire height of the tube. Due to the expansion effect at the diverging turning point, the detonation wave in region B is weaker than that in the region A. Then these big cells begin to split into more small

cells, which are shown in region C. These cells vary in size at the beginning. After complicated triple-point collisions and interactions, these cells tend to re-obtain their regularity and become uniform in size, which is shown in Figure 6.3(a)-II for $x \geq 0.64m$. Figure 6.3(a)-II can be viewed as the fourth region (demarcated by D). From this point of view, region B and C can be construed as a transition to the ultimate regular detonation structure of region D. The transition region is therefore defined as the combination of regions B and C. One may note the division or demarcation between region B and C is to some extent qualitative with the reiteration that region B is dominated by expanding/growing cell structure while region C is characterized by contracting cell structure. In addition, it is easily found that, the cell size in D is about 13.9mm long (x-direction), 7.72mm wide (y-direction), fairly similar to that found in region A (14.0mm long, 7.8mm wide).

Figures 6.3(b)-(d) show the other three cases with various diverging angles. As we can see, as the diverging angle increases, the detonation cells in region B are larger, and then more new cells arise in region C. Table 6.1 shows the length of transition region, the ultimate cell size and the width/length ratio at various oblique angles. Figure 6.4 shows the change of the transition length with the diverging angle graphically. It is easily discerned that as the diverging angle increases, the length of transition region gets shorter and the ultimate cell size becomes bigger, until at the diverging angle of 45º, the ultimate cells approximate their initial size found in region A. Although the ultimate cell size is considerably affected by the diverging angle, the width/length ratio tends to be approximately constant, i.e. the shape of the detonation cells remains

the same. In another word, when a fully-developed detonation wave propagates through a diverging surface to a straight tube, the detonation cells become distorted and irregular before they re-obtain their regularity. The ultimate regular cell size and the length of the transition region are noticeably affected by the oblique angle of the diverging surface, while the width/length ratio of the cells is nearly independent of it. From the point of view of engineering, a larger oblique angle can shorten the transition process. Thus, in order to re-obtain a regular cellular structure after the diverging surface, one will need a shorter straight tube.

Shown in Figure 6.5 is a series of pressure contour plots with time around the first corner turning point P1 for the case of diverging angle of 30º. Detonation diffraction occurs as the front enters the diverging section. An expansion region can be clearly identified, marked by ER in Fig. 6.5(b), in which the pressure is decreased due to a series of expansion waves. As time progresses, the expansion region grows by spreading downstream. Additionally, there exists a shock wave, marked by S, at the edge of the expansion region, which can be found in the diffraction of a non-reactive shock wave as well. The possible reason is that, as the detonation front moves downstream, the gases expand freely into the diverging tube at a higher rate than can be accommodated by the pressure and density drops behind the detonation wave. Inward facing compression waves hence coalesce and form inward facing shocks. Due to the expansion of the surface area of the front, the detonation cell becomes bigger in width while the number of triple points on the front remains constant. The expansion effect of shock reduces the ensuing pressure reduce, thus possibly allowing

the detonation cells to grow bigger, which can also account for what we have seen for the typical region B as depicted in Fig. 6.3.

Figures 6.6 and 6.7 follow the time series of Fig. 6.5 and show the pressure and temperature contours around the second corner turning point P2, respectively. As we can see in Figure 6.6, when propagating through this turning point, the detonation wave is compressed, and wave reflection occurs. Opposite to the situation around the first corner turning point P1, the effect of compression around P2 can cause the local pressure to increase and the detonation cells therefore become smaller and some new cells are created, which can be seen at the typical region C or the corresponding regions in Fig. 6.3. In Figure 6.6(b), we can see the Mach reflection clearly; the presence of the incident wave, regular reflection and Mach reflection are marked by I, R and M, respectively. Due to the compression effect, the pressure behind the Mach reflection wave is increased. At this moment, four transverse waves are identified, marked by TW1-4. In Figure 6.6(c), TW1 is bounced off the upper wall, and the pressure in the reflected TW1 is increased further. As time goes on, TW2 moves upward and collides with the reflected TW1 and the initial R before itself being reflected off the upper wall. The reflected TW1, TW2, and R interact with each other and the pressure and temperature are intensified greatly. Thus, as shown in Figure 6.6(d), a blast wave from a strong localized explosion occurs, which originates from this collision region. The localized explosion in turn increases the strength of the detonation wave ahead, which is similar to the localized explosion observed in the work of Khokhlov et al (2004).

As the detonation front moves through the turning point P2, due to the localized explosion and the detonation reflection, the pressure behind the detonation front increases, and the detonation cells therefore becomes once again smaller, which can account for what we have seen for the subsequent typical region C or the corresponding regions found in Fig. 6.3. As described above, when the detonation wave moves through the turning points P1 and P2, the shock wave S and the reflection wave R were formed respectively. The shock wave S propagates downstream, while the reflection wave R moves upstream. They will collide in the transition region and R is bounced off the central line, thus dividing the local flow domain into three different pressure regions, as shown in Figure 6.8. Figure 6.8 traces clearly the evolution of the collision of waves.

In summary, when passing through the turning points P1 and P2, the detonation wave is expanded and compressed, respectively. The detonation cells are enlarged by the expansion waves after P1. Due to compression around P2, the size of the detonation cells starts to reduce again. Ultimately, these detonation cells tends to become smaller than their original size shown in the typical region A or the corresponding regions of Fig. 6.3, but the width/length ratio of the ultimate cells keeps constant and it is hardly affected by the oblique angle. The mean detonation velocity at the front declines because of the expansion effect caused by the diverging chamber.

6.3.2 Converging Chamber

The development of the detonation in the converging chamber is illustrated in Figure

6.9 in the form of the grey-scale contours of the maximum velocity, $|v|_{max}$, reached at each point in space. The contour of the maximum flow velocity is employed as analogue of the smoke foil tracks used widely in experiments. Figure 6.9(a) shows the detonation cells pattern as the detonation wave propagates through the converging chamber of 46°. From left to right, four regions are identified, marked by regions A, B, C and D, which is similar to that for the diverging configuration. The detonation cells in region A have good regularity and they are not affected by the converging oblique wall. The detonation cells formed by the Mach stem are shown in region B. Region A is separated from region B by a triple-point trajectory line, which involves incident wave, reflection wave and Mach stem. Those cells in B lose their regularity and they are much smaller than those in A, which results from the effect of the compression wave. As the detonation wave moves to region C, the cells become bigger and they vary in size at the initial stage. After some triple-point collisions and interactions, these cells tend to be uniform in size and finally they re-obtain their regularity in region D. Similarly to the discussion in the diverging case above, region B and C can be construed as a transition to the ultimate regular detonation structure of region D. The transition region is therefore defined as the combination of regions B and C. The division or demarcation between region B and C is to some extent qualitative with the reiteration that region B is dominated by contracting cell structure while region C is characterized by expanding/growing cell structure, which is just opposite to that in the diverging case.

Figures 6.9(b)-(d) show the other three cases with various converging angles. Table

6.2 shows the length of transition region, the ultimate cell size and the width/length ratio at various oblique angles. Figure 6.10 shows the change of the transition length with the converging angle graphically. It is found that as the converging angle increases, the length of transition region gets shorter and the ultimate cell size in region D becomes bigger and also increasingly closer to the initial cell size found in region A, which are similar to the trend found for the diverging wall case. Although the ultimate cell size is considerably affected by the converging angle, the width/length ratio tends to be constant approximately. In another word, when a steady detonation wave propagates through a converging surface to a straight tube, the detonation cells become distorted and irregular before they re-obtain their regularity. The ultimate regular cell size and the length of the transition region are noticeably affected by the oblique angle of the converging surface, while the width/length ratio of the cells is nearly independent of it. From the point of view of engineering, a larger oblique angle can shorten the transition process. Thus, in order to re-obtain a regular cellular structure after the converging surface, one will need a shorter straight tube.

Figure 6.11 shows the pressure contours around the first turning point P1 with the converging oblique angle of 25°. Five transverse waves are identified in Figure 6.11(a), marked by TW1-TW5. When propagating through the turning point P1, the detonation wave is compressed and wave reflection occurs. Meanwhile, TW1 is bounced off the converging surface and interacts with the incident wave and the reflection wave. Shown in Figure 6.11(b) is the interacting Mach reflection configuration comprising the incident wave, regular reflection and Mach reflection

(which are marked by “I”, “R”, and “M”, respectively). In Figure 6.11(c), TW2 is bounced off the sloping surface, which creates a local high-pressure region in its interacting with the Mach reflection configuration, marked by “LH1”. As time goes on, the reflected TW2 moves downstream and collides with TW3. Another local high-pressure region, marked by “LH2” is created.

Physically, in the region B, due to the reduction of the surface area of the front, the detonation cell becomes smaller in width while the number of triple points on the front still remains constant. The compression effect of shock causes the pressure to rise, thus possibly allowing the detonation cells to shrink, which is observed for the typical cellular structure in the corresponding regions as depicted in Fig. 6.9. Figure 6.12 shows the close-up of detonation cells near the converging surface at various angles. As we can see in Figure 6.12, there exists a line that separates the undisturbed area (i.e. the area behind the incident detonation wave) from the Mach reflection area (i.e. the area behind the Mach reflection). This line is usually referred to as the trajectory of the triple point caused by Mach reflection. It is easily found that as the converging angle increases, the trajectory angle χ decreases. When the converging angle reaches at about 46°, the trajectory angle tends towards to 0°, i.e. no Mach reflection occurs. This finding agrees reasonably with Guo et al (2001) experiments. Table 6.3 lists the details of the triple-point trajectory. Strictly speaking, the triple-point trajectory is not straight, which may be attributed to the interaction between the transverse waves and the converging wall, i.e. the trajectory of the triple point is affected by both Mach reflection and the transverse waves. However, for inert

shock waves, the triple point trajectory is only a function of the incident Mach number and the wedge angle, and therefore it is a straight line. This is an essential difference between the Mach-reflected shock waves in non-reactive air and Mach-reflected detonation waves in combustible gas mixture. In order to measure the trajectory angle of the Mach-reflected detonation waves, one has to make a best linear fit to the irregular line to measure the trajectory angle. The dashed line in Figure 6.12(a) is the linearly-fitted trajectory. When the converging angle is larger than 14°, the triple-point trajectory is very clear and it cuts through some of the detonation cells in the undisturbed area.

In addition, it is observed that both the size and the shape of the detonation cells have changed after Mach reflection. The cell size behind the Mach stem is smaller, which conforms to the fact that Mach stem is overdriven detonation. The cellular structure behind Mach stem is not as clear as that behind the incident detonation wave. The deflection angle caused by the colliding of transverse waves is smaller, which suggests that the cellular structures behind Mach stem are weaker. As the converging angle increases, the cellular structures behind Mach stem are even more difficult to distinguish. When the converging angle is 25° or above, the cellular structures behind Mach stem disappear for while before they come out again. When the converging angle is larger than 30°, the cellular structures behind Mach stem disappear completely.

Figure 6.13 shows the pressure contours around the second turning point P2 with the

converging angle of 25°. The detonation wave diffracts when it passes through the turning point, and an expansion region, marked by “ER”, is created. The pressure in the expansion region is decreased by a series of expansion waves. At the edge of the expansion region, there exists a shock wave “S”, which is formed because the gases expand at a higher rate than can be accommodated by the pressure and density drops behind the detonation wave. Due to the expansion effect caused by detonation diffraction as the detonation front moves through the turning point P2, the pressure behind the detonation front decreases, and the detonation cells therefore become bigger again, which can account for what we have seen for the typical region C also depicted in Fig. 6.9.

In summary, when passing through the turning points P1 and P2, the detonation wave is compressed and expanded, respectively. Due to the compression effect around P1, the detonation cells shrink. However, after the turning point P2, the size of the detonation cells is enlarged again, which results from the expansion waves arising around P2. Ultimately, these detonation cells tends to become smaller than their original size shown in the typical region A or the corresponding regions of Fig. 6.9, but the width/length ratio of the ultimate cells keeps constant and it is hardly affected by the oblique angle. The mean detonation velocity at the front increases because of the compression effect caused by the converging chamber.

Lastly, it may be noted to continue where we left off in Section 2.6 to further investigate the effect of mesh size on our present variable cross-sectional detonation

simulations, we repeated the simulation for the converging configuration with the mesh size of 0.05mm. The 25° converging case is taken as an example for the resolution study. Figure 6.14 shows the detonation cell pattern (similar to the analogue of smoke foil tracks) based on mesh size 0.1mm and 0.05mm as the detonation wave propagates through the converging chamber around the two corners. The cell structure and its evolution for both of the mesh sizes are almost identical. Figure 6.15 and 6.16 depict the close-up of the pressure contours around the two turning points calculated with the mesh size of 0.05mm. Comparison to the counterparts on Figures 6.11(c) and 6.13(a) based on the mesh size of 0.1mm shows good agreements in the main features of the transverse waves and the reflected waves. Figures 6.17 shows the close-up view of the pressure and temperature contours obtained using mesh size 0.1mm depicting the structure near the sloping wall for a detailed comparison to the counterparts calculated with mesh size 0.05mm shown in Figures 6.18. It is found that the results with mesh size 0.1mm and 0.05mm show similar resolution of the basic cellular structure. The mesh size of 0.05mm can resolve more and finer features of the structure, such as additional shock wave and local high-temperature region, which is not the primary intent of the present work. Quantitative comparison of the specific geometric parameters of the structure gives an almost identical trajectory angle χ = 10° for both mesh sizes, and a transition length of 0.29m for the mesh size of 0.05mm versus 0.285m based on the mesh size of 0.1mm. The ultimate width/length ratio of the detonation cell measures 1.807 based on the mesh size of 0.05mm which is almost identical to that found on Table 6.2 for the larger mesh size of 0.1mm and different

converging oblique angles.

Through the above resolution analysis (and those in Section 2.6) and considering that one objective of our present work is to study the "broad dimension" of the detonation cellular structures, including the evolution of the detonation cells in the diverging/converging chambers, and how the length of the transition region changes with the diverging/converging angles, as opposed to the investigation of very fine and detailed structures/sub-structures around the detonation triple-wave configurations, we reckon the employment of mesh size 0.1mm in the present work shows faithfully the evolution of the transverse waves and main features of the detonation cell structures in response to the different sloping chamber wall imposed. The computed results obtained can certainly be compared to (future) experiments of smoke foil tracks. (Of course much finer cellular structure especially at the detonation front may not be captured clearly and explicitly as shown in Hu et al. (2004) for the straight-duct configuration based on their mesh size as fine as 0.025mm; this will be our future work.)

Table 6.1 Transition region and ultimate cell size at various diverging angles

Diverging Angle	Length of Transition Region	Ultimate Cell Size in Region D (Width, length)	width/length ratio
14º	0.752 m	6.15mm, 11.11mm	1.806
25º	0.674 m	6.70mm, 12.12mm	1.808
30º	0.641 m	7.30mm, 13.19mm	1.806
45º	0.593 m	7.72mm, 13.90mm	1.801

Table 6.2 Transition region and ultimate cell size at various converging angles

Converging Oblique Angle	Length of Transition Region	Ultimate Cell Size (Width, length)	width/length ratio
14º	0.330 m	4.10mm, 7.40mm	1.806
25º	0.285 m	5.60mm, 10.12mm	1.807
30º	0.260 m	5.70mm, 10.30mm	1.807
45º	0.250 m	6.40mm, 11.56mm	1.806

Table 6.3 Details of the triple-point trajectory

Converging Angle, θ	10º	14º	20º	25º	30º	35º	46º
Trajectory Angle, χ	20º	18º	14º	10º	6º	5º	0º

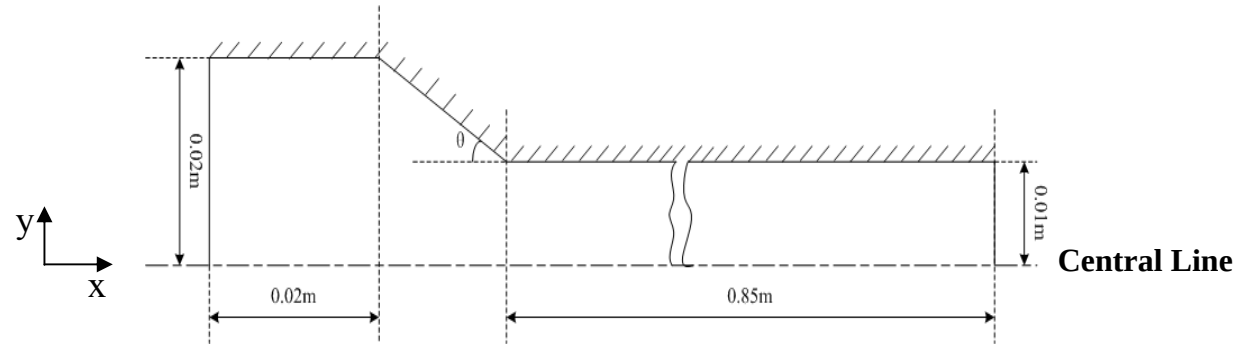

(a) Computational Domain of converging case (not to scale)

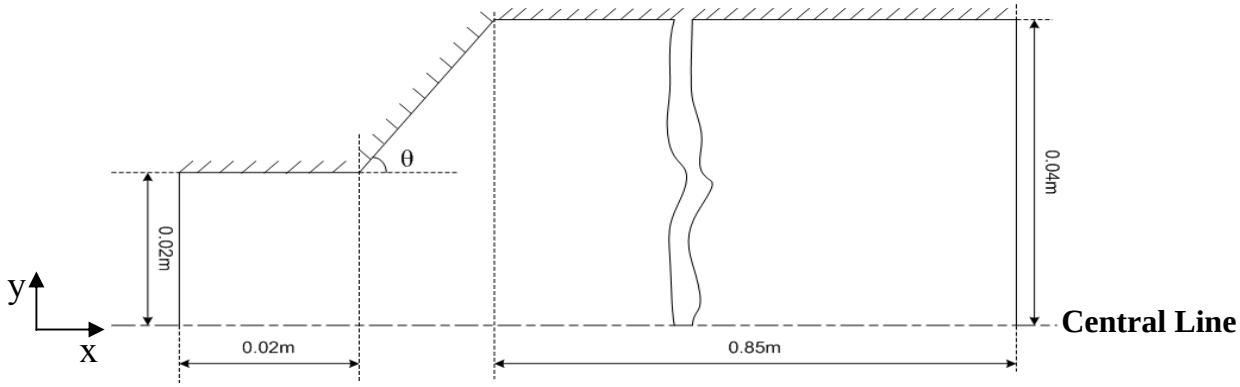

(b) Computational domain of diverging case (not to scale)

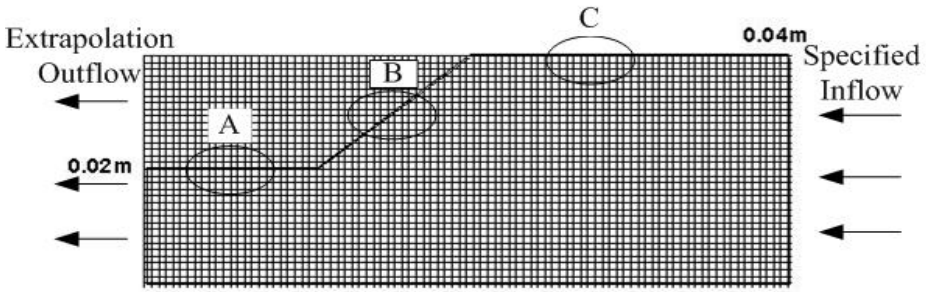

Central Line (Reflected boundary conditions)

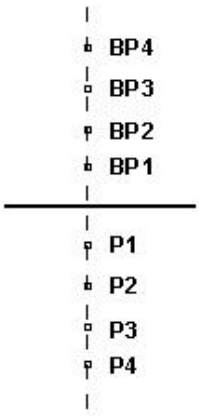

Close-up view of A and C

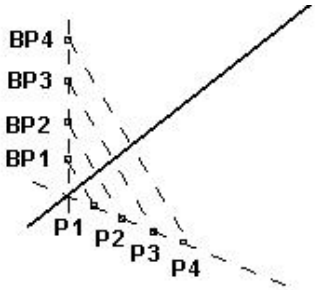

Close-up View of B

In A and C, the boundary conditions are:

$$(U_k)_{BPi} = (U_k)_{Pi}, \quad (U_3)_{BPi} = -(U_3)_{Pi},$$

where $i = 1,2,3,4$; $k = 1,2,4,5..,12$

In B, the boundary conditions are:

$$(U_k)_{BPi} = (U_k)_{Pi}$$
$$(U_2)_{BPi} = (U_2)_{Pi}(\cos^2\theta - \sin^2\theta) + 2(U_3)_{Pi}\sin\theta\cos\theta$$
$$(U_3)_{BPi} = (U_3)_{Pi}(\sin^2\theta - \cos^2\theta) + 2(U_2)_{Pi}\sin\theta\cos\theta,$$

where $i = 1,2,3,4$; $k = 1,4,5,6,..,12$

Note: the values of $(U)_{Pi}$ are obtained by interpolation of the values of the 4 node points surrounding the point *Pi*.

(c) Sketch of the boundary conditions

Figure 6.1 Computational domains and boundary conditions

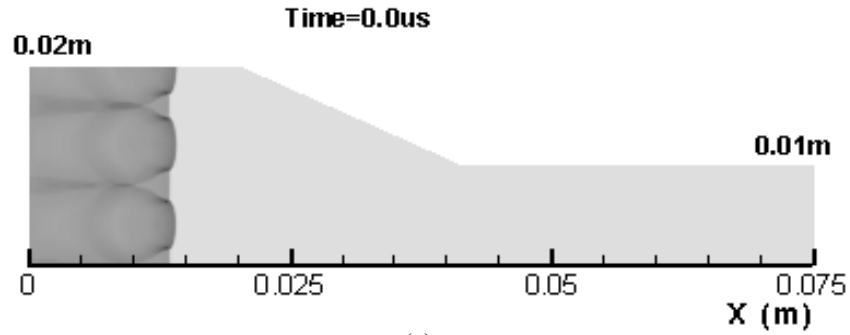

(a)

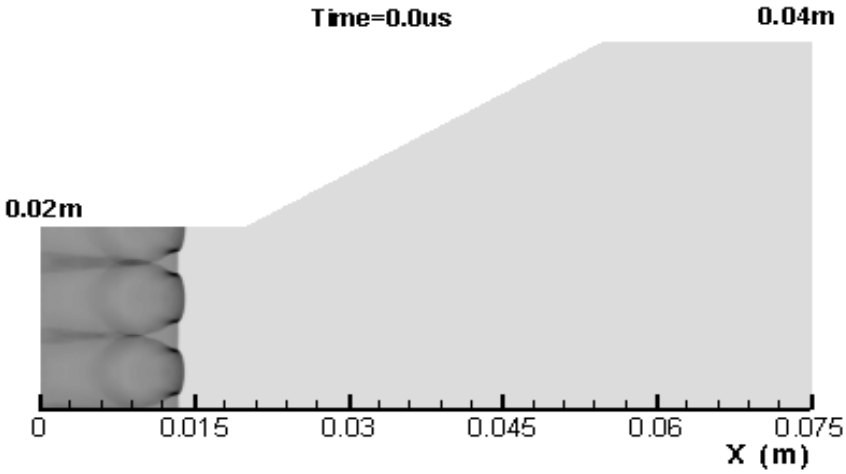

(b)

Figure 6.2 Initial pressure distributions

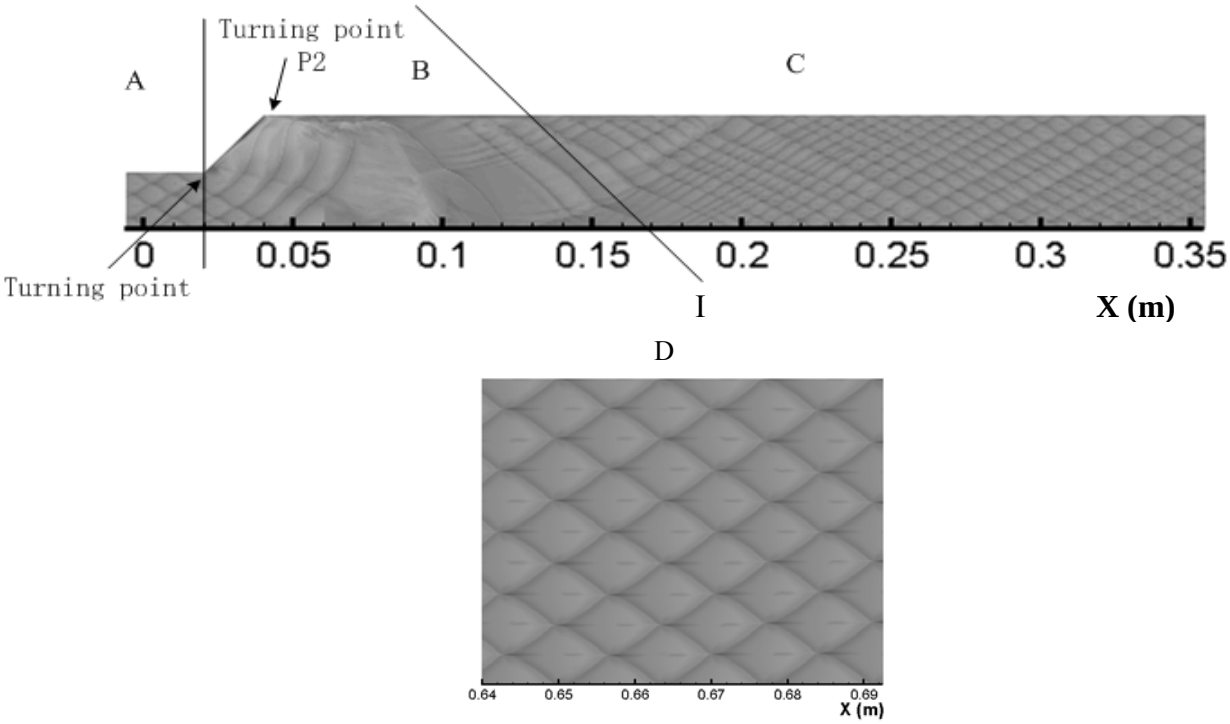

II (Close-up view of region D)

(a) $\theta = 45°$

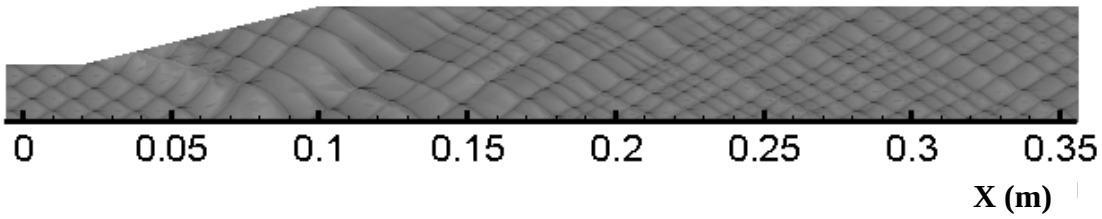

(b) $\theta = 14°$

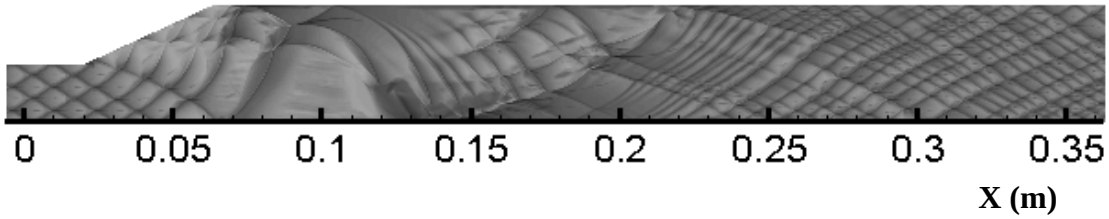

(c) $\theta = 25°$

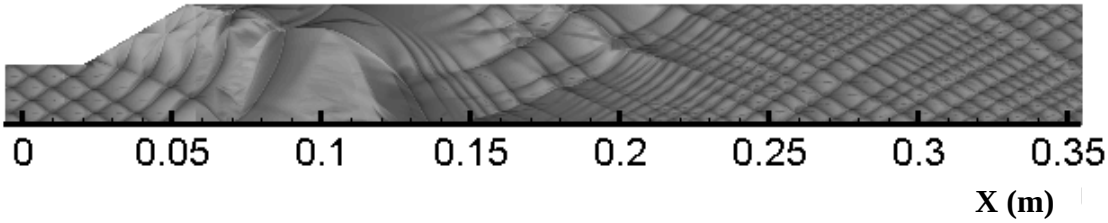

(d) $\theta = 30°$

Figure 6.3 Detonation cells pattern at various diverging angles

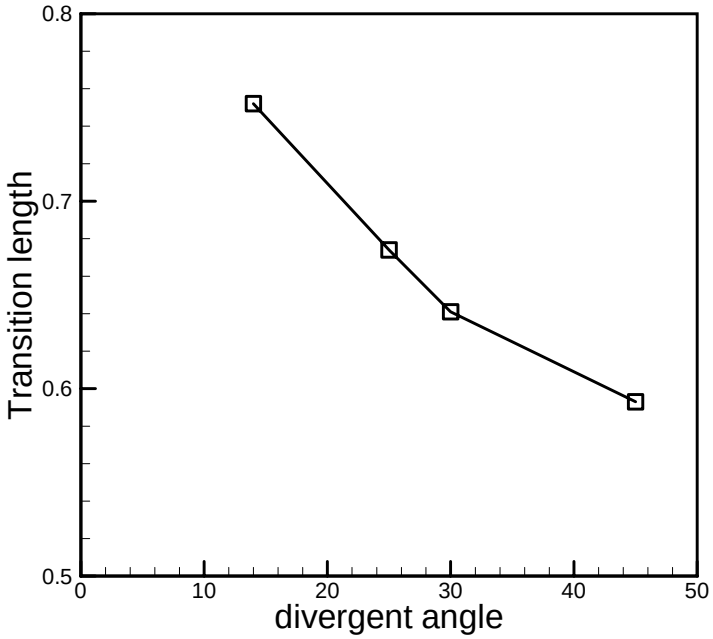

Figure 6.4 Transition length versus the diverging angle

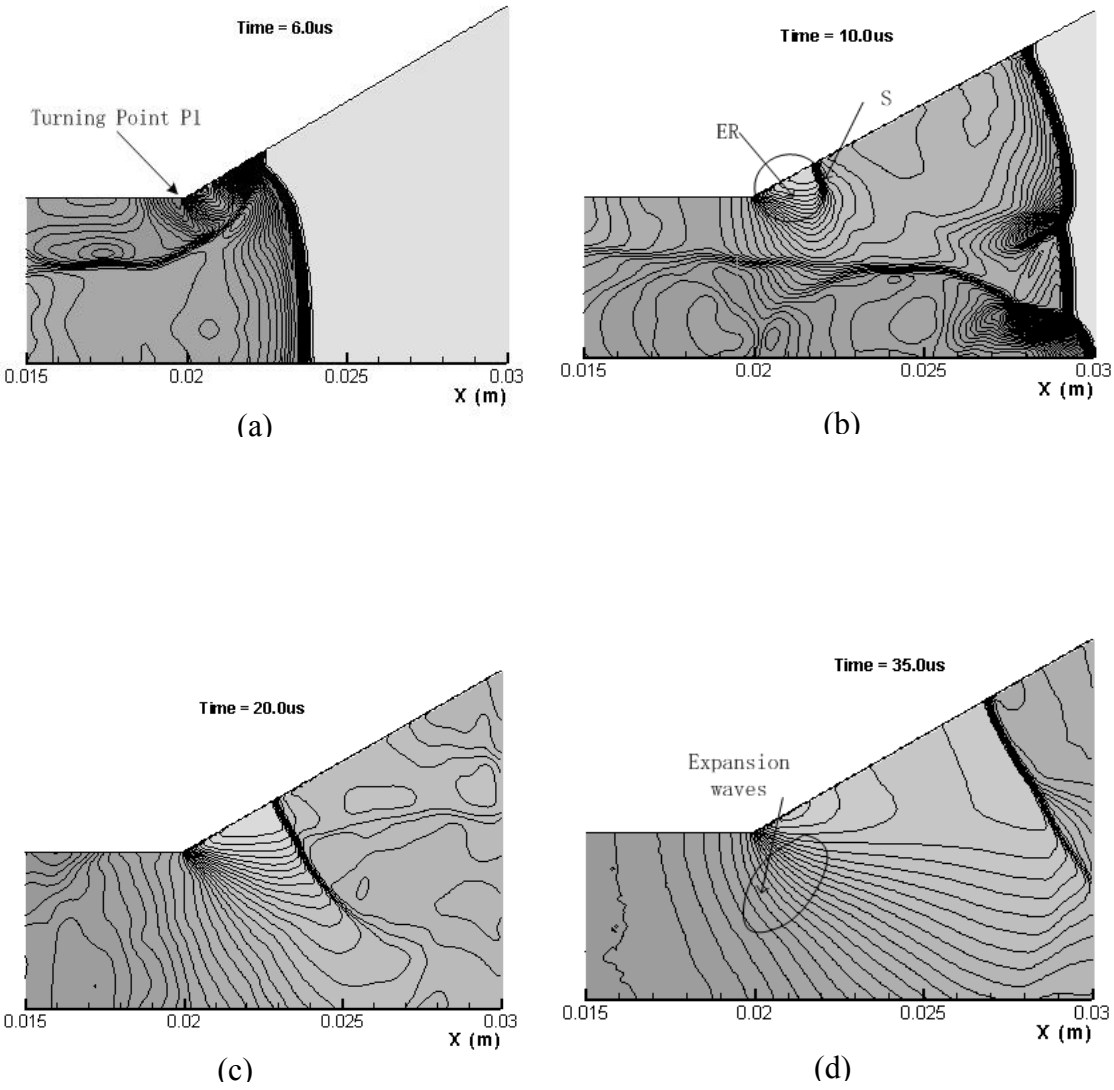

Figure 6.5 Pressure contours around the turning point P1

for configuration of diverging angle 30°

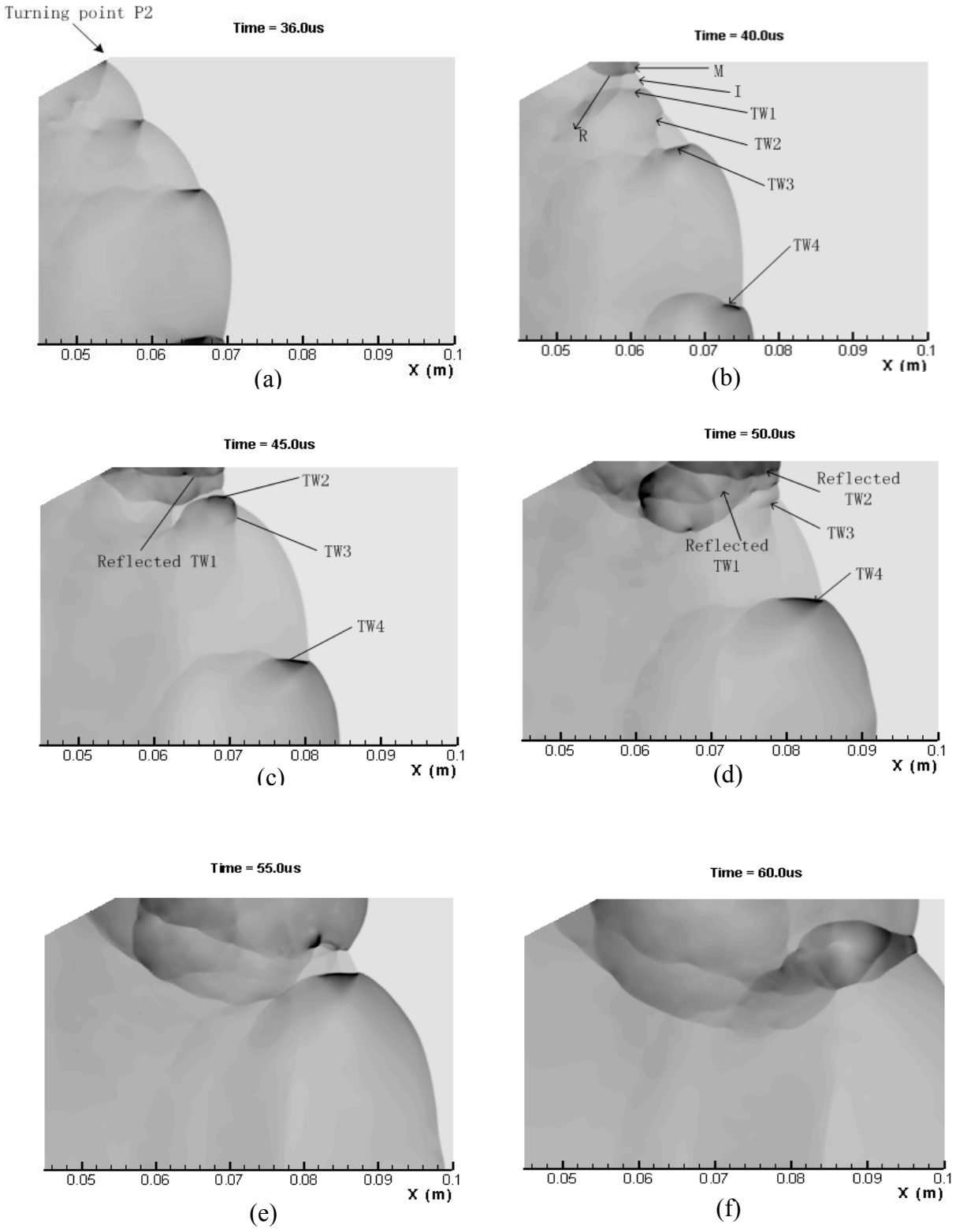

Figure 6.6 Pressure contour around the turning point P2

for configuration of diverging angle 30°

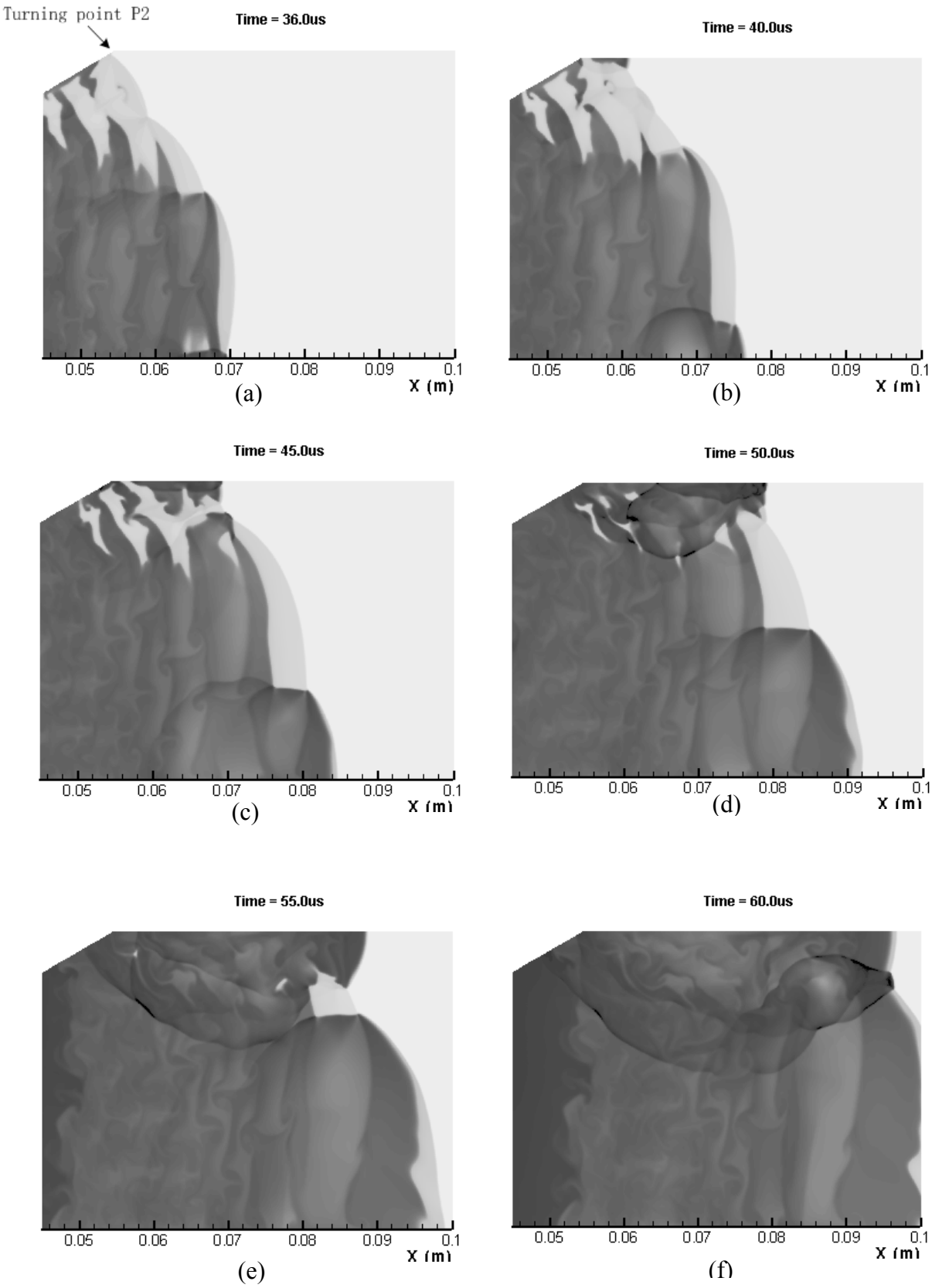

Figure 6.7 Temperature contour around the turning point P2

for configuration of diverging angle 30°

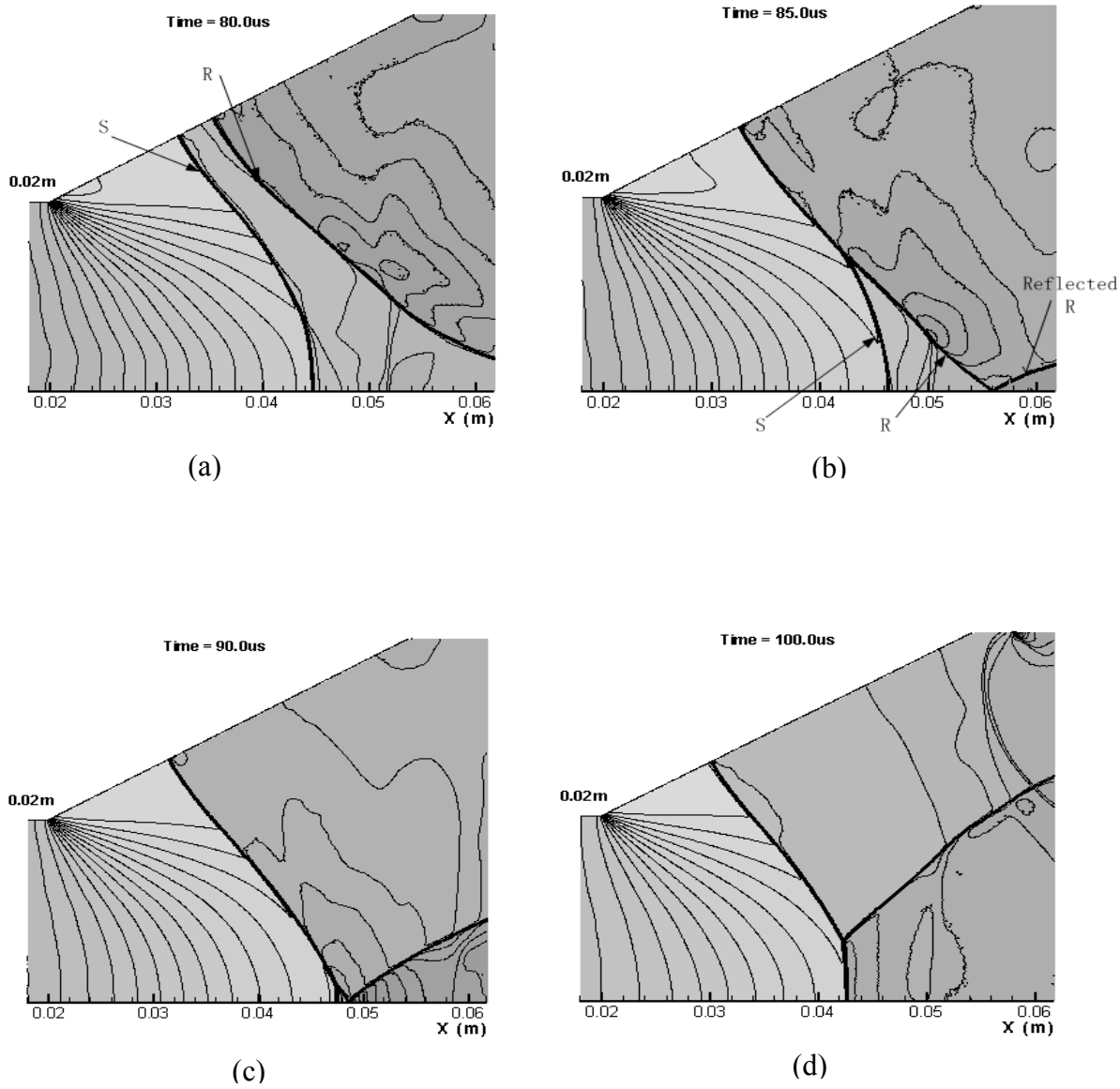

Figure 6.8 Collision of R and S for configuration of diverging angle 30°

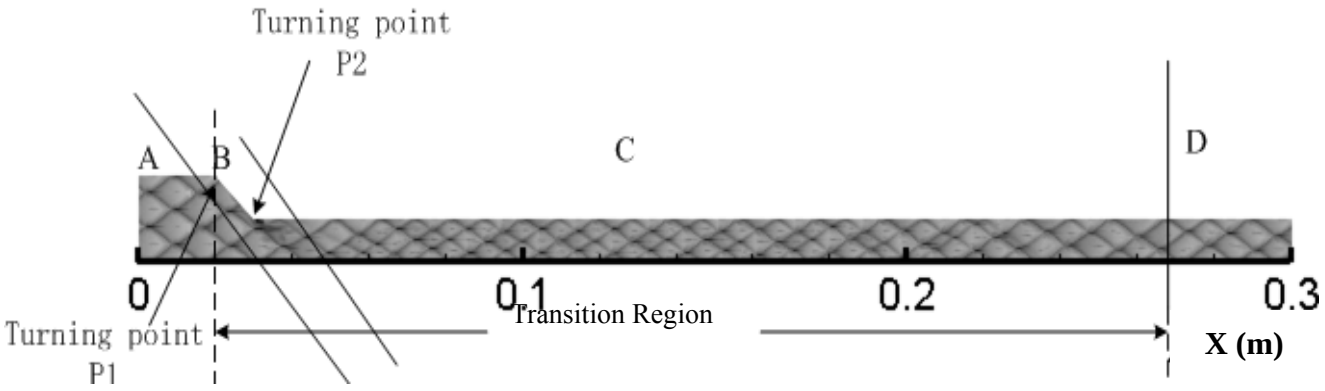

(a) $\theta = 46°$

(b) $\theta = 14°$

(c) $\theta = 25°$

(d) $\theta = 30°$

Figure 6.9 Detonation cells pattern at various converging angles

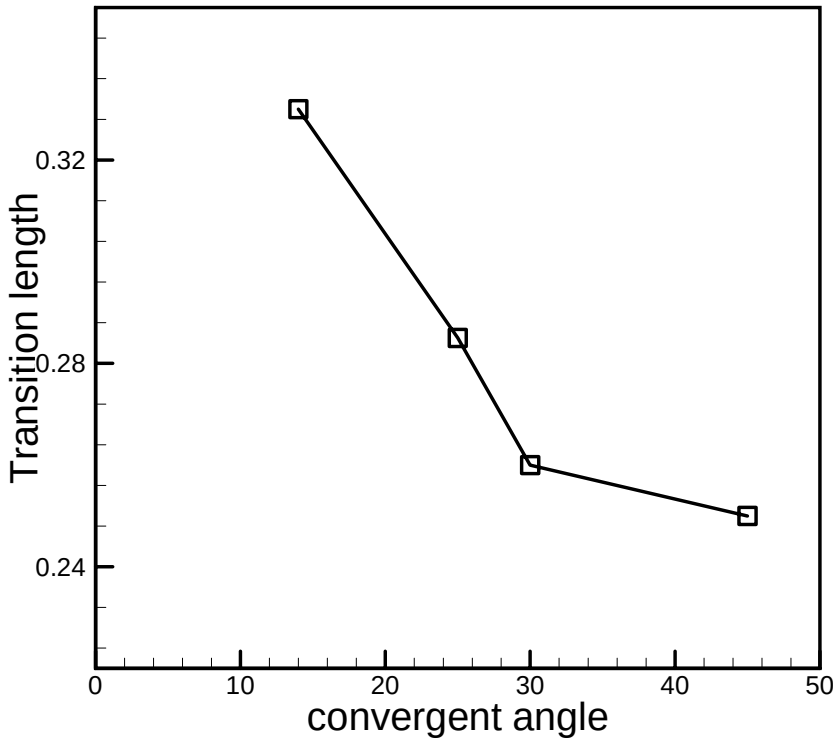

Figure 6.10 Transition length versus the converging angle

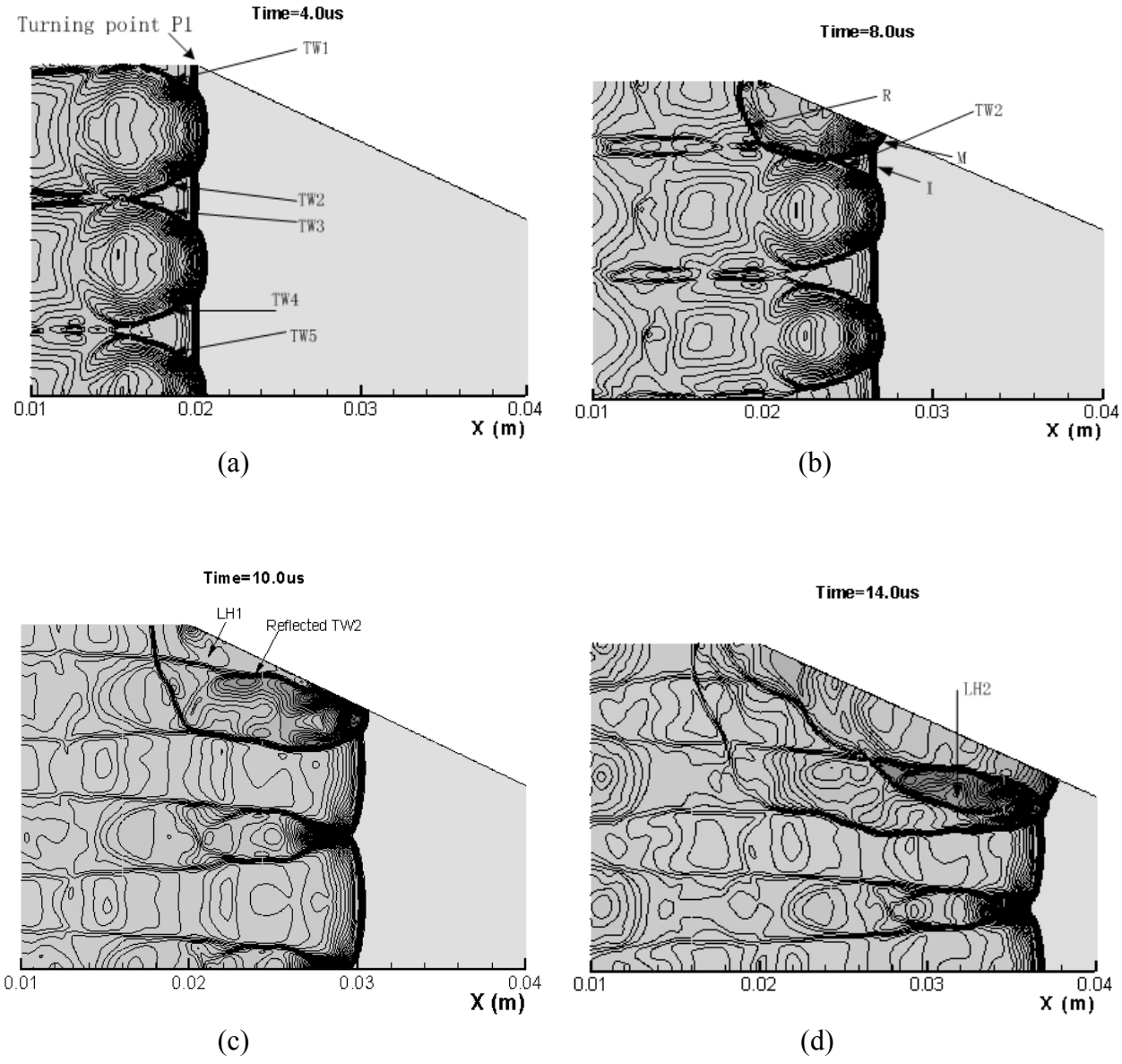

Figure 6.11 Pressure contours around the turning point P1

for configuration of converging angle 25°

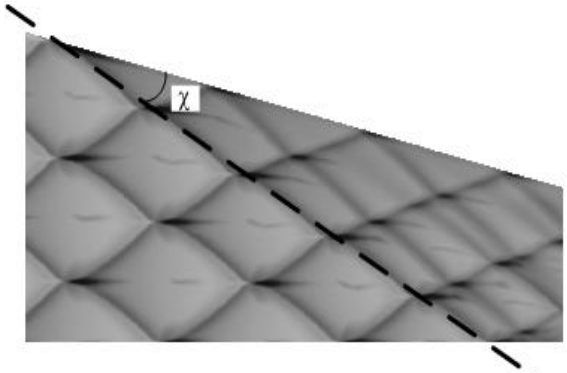

(a) $\theta = 14^{o}$

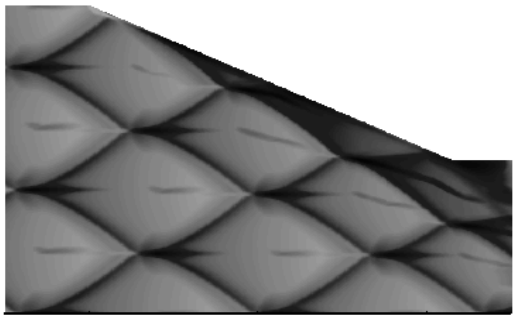

(b) $\theta = 25^{o}$

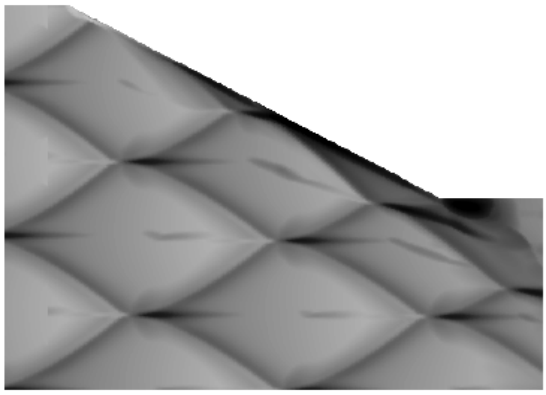

(c) $\theta = 30^{o}$

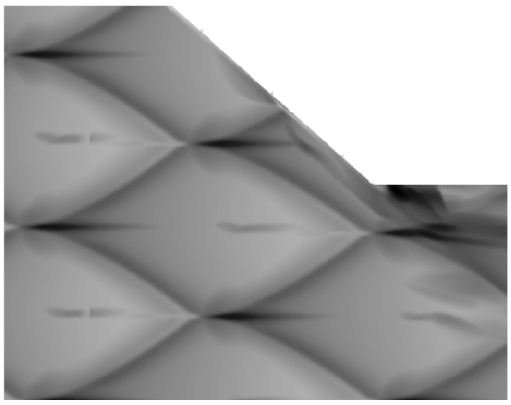

(d) $\theta = 46^{o}$

Figure 6.12 Detonation cells at various converging angles

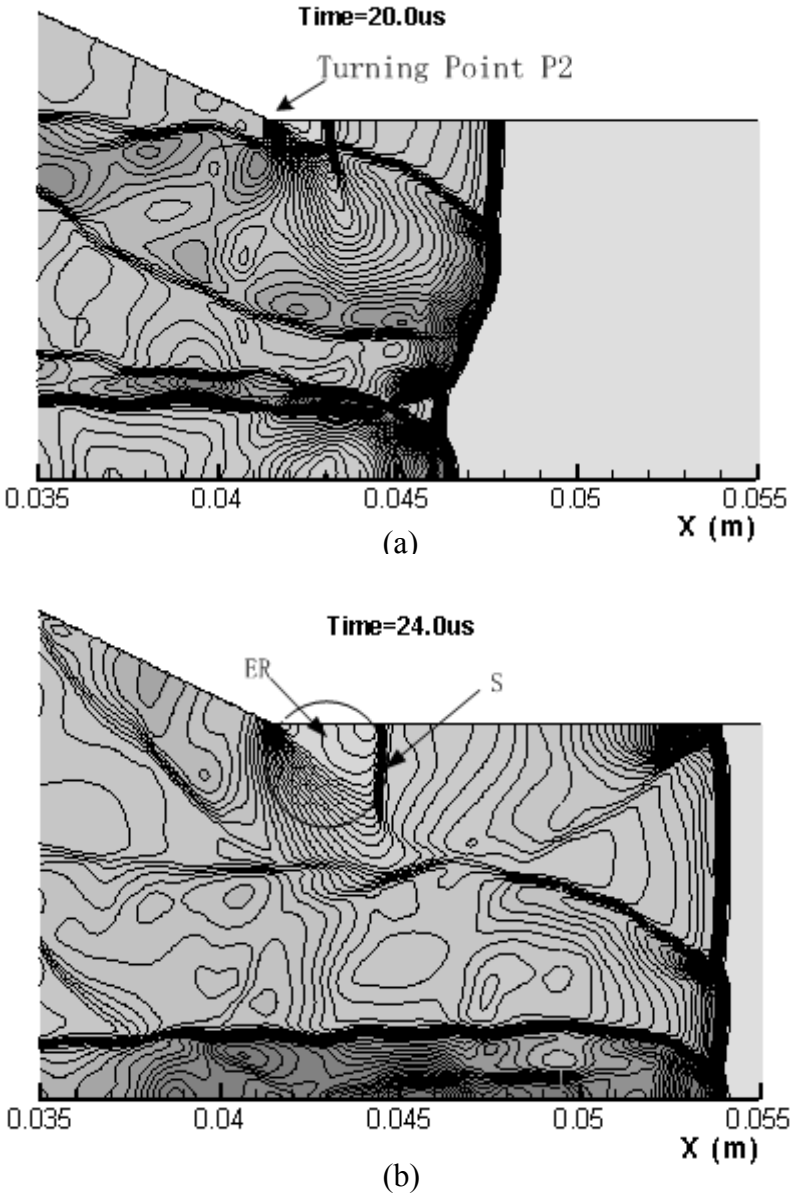

Figure 6.13 Pressure contours around the turning point P2

for configuration of converging angle 25°

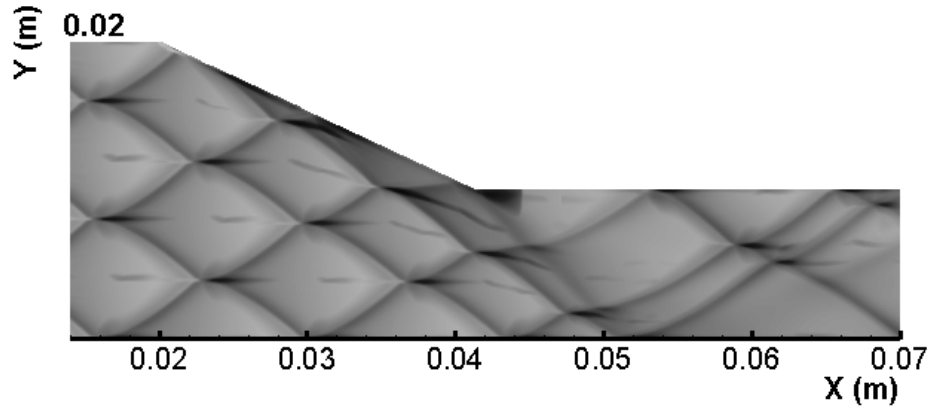

(a) Mesh size $\Delta x = \Delta y = 0.1mm$

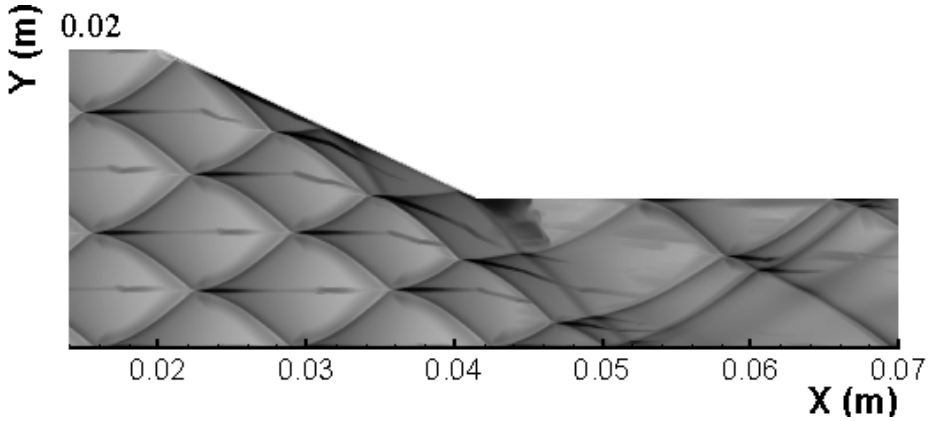

(b) Mesh size $\Delta x = \Delta y = 0.05mm$

Figure 6.14 Detonation cells pattern in the converging chamber around the two corners with different resolutions

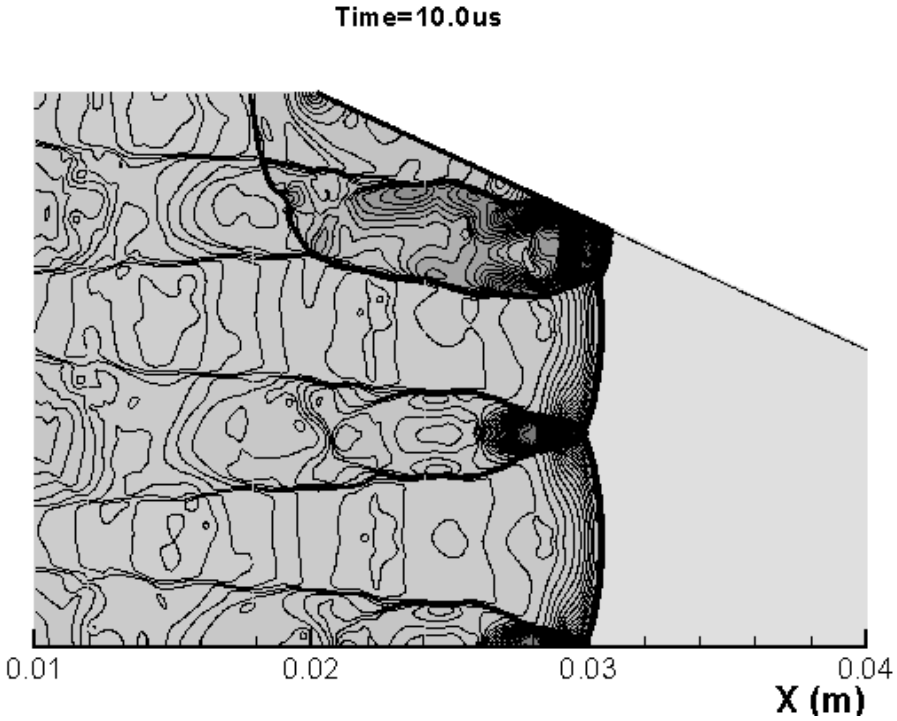

Figure 6.15 Pressure contours around the turning point P1 with the mesh size of 0.05mm

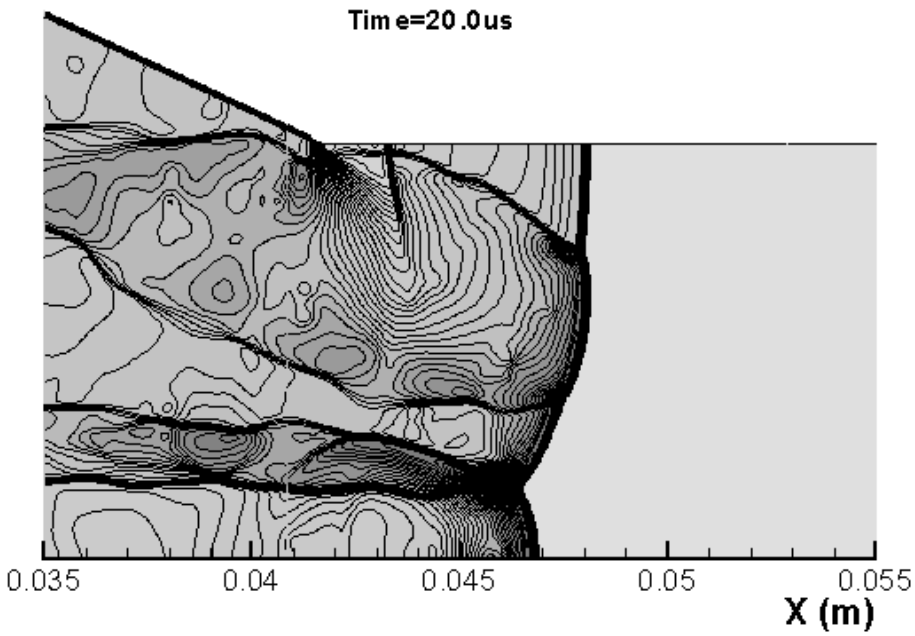

Figure 6.16 Pressure contours around the turning point P2 with the mesh size of 0.05mm

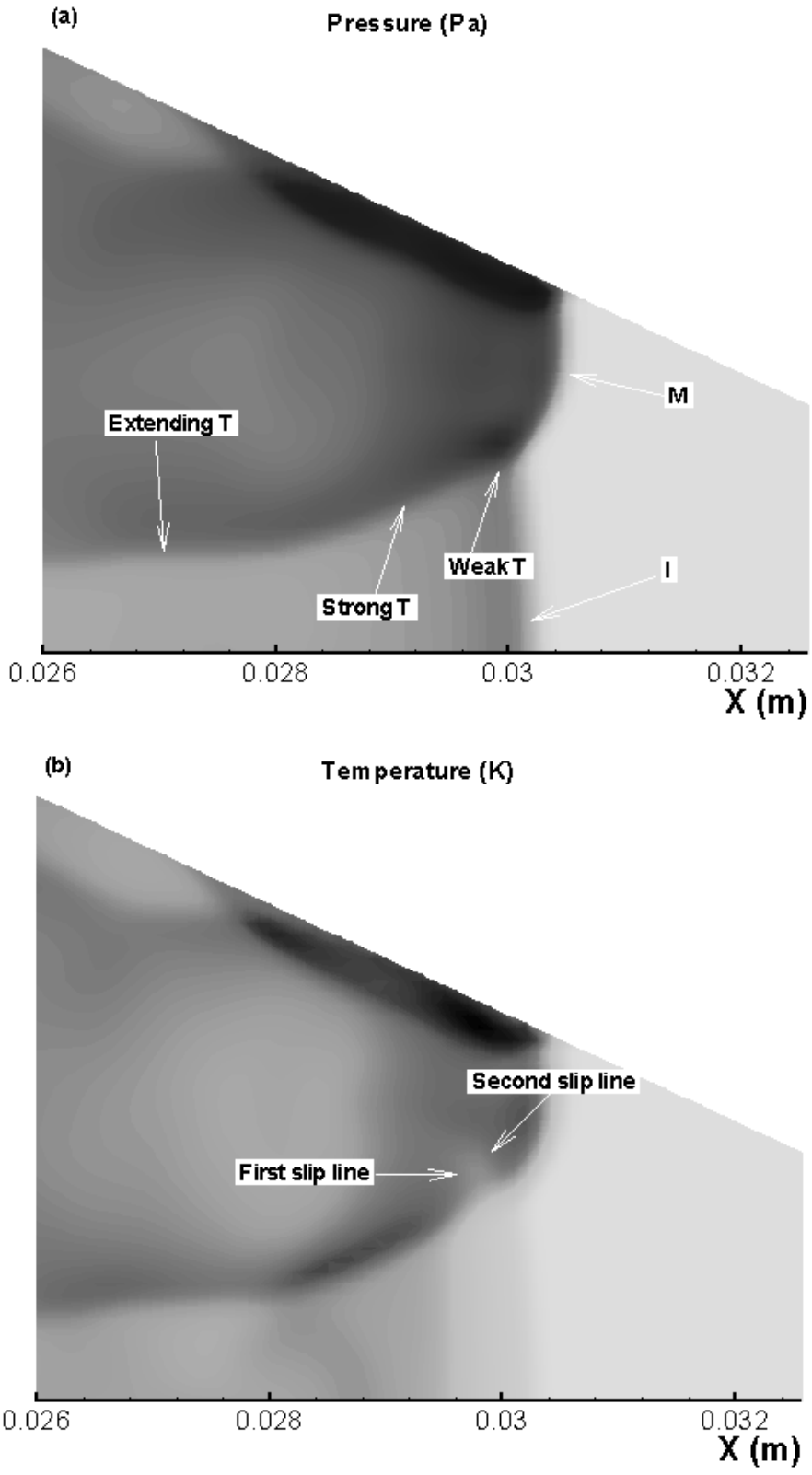

Figure 6.17 Structure near the sloping wall with the mesh size of 0.1mm at time=10.0us

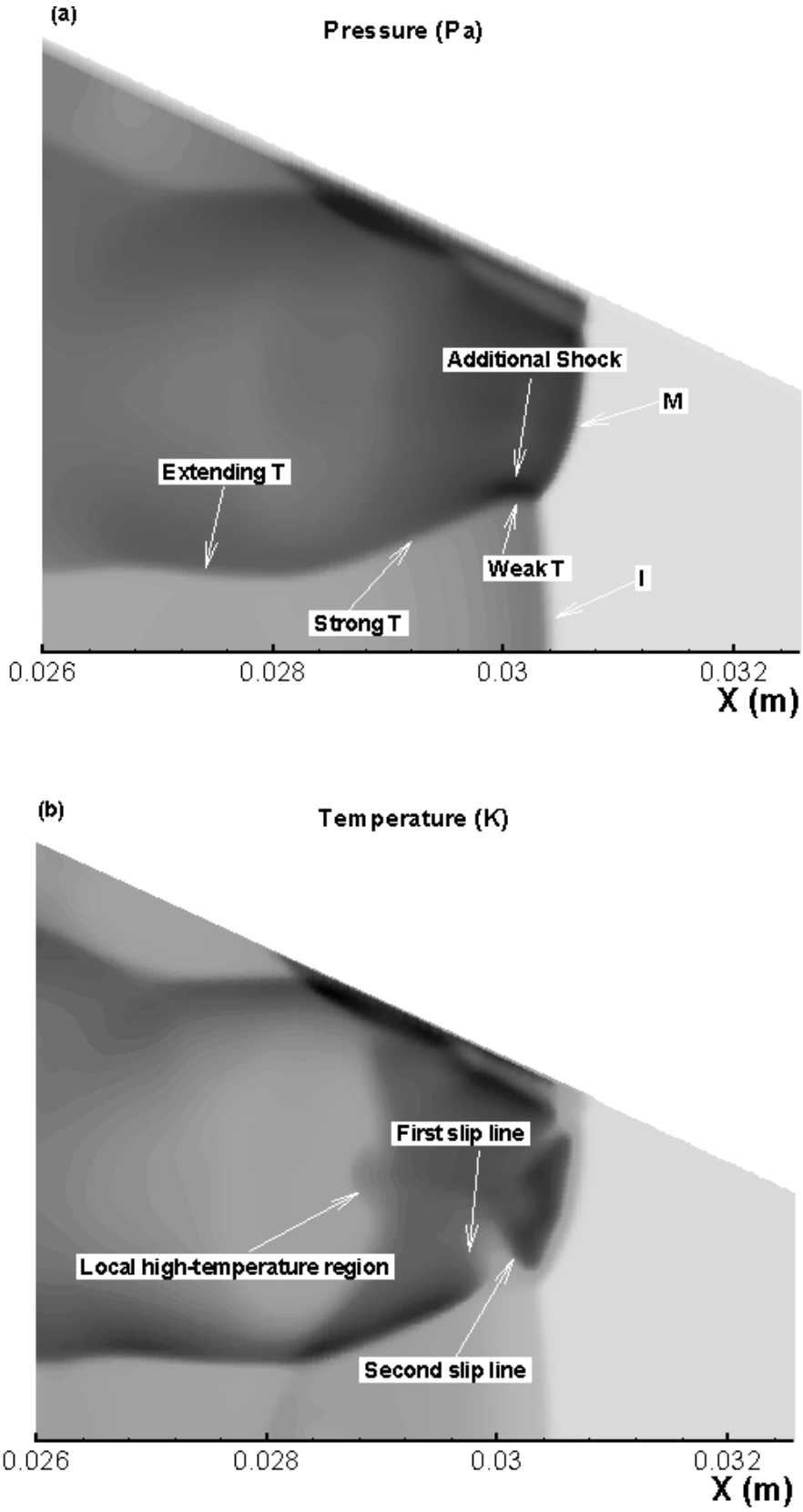

Figure 6.18 Structure near the sloping wall with the mesh size of 0.05mm at time = 10.0us

Chapter 7 Detonation Wave in an Axisymmetric Converging /Diverging Chamber

7.1 Computational Setup

In this chapter, the numerical simulation models a detonation propagating from left to right in an axisymmetric converging/diverging chamber with a stoichiometric H_2/O_2 mixture diluted with 70% argon at an initial pressure and temperature of 6.67kPa and 298K, respectively. Figure 7.1 (a, b) shows the schematic of the two chambers considered for the present computation for the converging and diverging cases. Each case consists of a short axisymmetric straight duct, followed by an axisymmetric converging/diverging duct with a wedge angle θ. The wedge angle θ is varied from 14 to 46 degree while the rest of the dimensions are provided in the figure. As mentioned in Chapter 2, for the axisymmetric computational domain, the governing equations of the gaseous detonation can be modified as,

$$U_t + [F(U)]_x + [G(U)]_r = S$$

$$U = \begin{pmatrix} \rho \\ \rho u \\ \rho v \\ E \\ \rho Y_1 \\ \vdots \\ \rho Y_{N-1} \end{pmatrix}, F(U) = \begin{pmatrix} \rho u \\ \rho u^2 + p \\ \rho uv \\ (E+p)u \\ \rho u Y_1 \\ \vdots \\ \rho u Y_{N-1} \end{pmatrix}, G(U) = \begin{pmatrix} \rho v \\ \rho uv \\ \rho v^2 + p \\ (E+p)v \\ \rho v Y_1 \\ \vdots \\ \rho v Y_{N-1} \end{pmatrix}, S = \begin{pmatrix} 0 \\ 0 \\ 0 \\ 0 \\ \dot{\omega}_1 \\ \vdots \\ \dot{\omega}_{N-1} \end{pmatrix} - \frac{1}{r} \begin{pmatrix} \rho v \\ \rho uv \\ \rho v^2 \\ (E+p)v \\ \rho v Y_1 \\ \vdots \\ \rho v Y_{N-1} \end{pmatrix}$$

$$E = -p + \frac{\rho(u^2+v^2)}{2} + \rho h$$

As mentioned in Chapter 7, in our present numerical computations, the source term at the central line of the axisymmetric chamber (i.e. $r = 0$) is modified as,

$$S = \begin{pmatrix} 0 \\ 0 \\ 0 \\ 0 \\ \dot{\omega}_1 \\ \vdots \\ \dot{\omega}_{N-1} \end{pmatrix}$$

In order to solve the governing equations above, an axisymmetric coordinate system is employed in the present work. The mesh size is fixed at 0.1mm, i.e. $\Delta x = \Delta r = 0.1mm$. The number of grids in the r direction is defined as below,

$$Diverging\ \ Case: \begin{cases} N_r = 200, & if\ \ x <= 0.02m; \\ N_r = \text{int}((x - 0.02)\tan\theta / \Delta r) + 200, & if\ \ x > 0.02m; \end{cases}$$

$$Converging\ \ Case: \begin{cases} N_r = 200, & if\ \ x <= 0.02m; \\ N_r = 200 - \text{int}((x - 0.02)\tan\theta / \Delta r), & if\ \ x > 0.02m; \end{cases}$$

7.2 Initial and Boundary Conditions

Similar to the case of 2-D converging/diverging detonation presented in Chapter 6, the 1-D Chapman-Jouguet (CJ) detonation wave obtained in Chapter 4 is placed on a two-dimensional straight-duct domain and some artificial disturbances are imposed on the computational domain. The initial CJ detonation wave will evolve into a stable triple-shock structure eventually. Then this stable 2-D detonation wave is placed in the straight-duct section of the axisymmetric converging/diverging geometry, serving as the initial condition of the present axisymmetric computation, and let it propagate through the axisymmetric converging or diverging channel, that is, the governing equations described above are solved with an initial distribution of a stable 2-D detonation triple-shock structure. The initial pressure distributions are shown in Figure 7.2 for both the converging and

diverging duct.

In the present axisymmetric converging/diverging computations, we use the same boundary conditions as the 2-D converging/diverging case in the last Chapter 6. These are: extrapolation is used for the outlet boundary condition, specified initial inflow conditions are imposed on the right end, and the upper and lower walls use the reflected boundary conditions. The extrapolation inflow boundary can be expressed as (defined for all the variables),

$$B_b(B = \rho, u, v, \rho e, P, Y_i) = B_1(1-\gamma) + B_N\gamma$$

The unreacted inflow condition is given as,

$(U_k)_{N_x+i} = (U_k)_{t=0}$, $i = 1,2,3,4$; $k = 1,2,..,12$

The reflected boundary for the upper wall is same as the the 2-D converging/diverging case in Chapter 6 . The details are shown in Figure 6.1 (c).

Similarly, the reflected boundary condition for the central line is given as,

$(U_k)_j = (U_k)_4$, $(U_3)_j = -(U_3)_4$, $j = 0,1,2,3$; $k = 1,2,4,5..,12$,

where $(U_k) = (\rho, \rho u, \rho v, \rho e, \rho Y_1, ..., \rho Y_8)$, and N_x is the last non-boundary cell on the right side;.

7.3 Results and Discussions

7.3.1 Converging Chamber

The evolution of the detonation in the converging chamber is illustrated in Figure 7.3 in the form of the grey-scale contours of the maximum velocity, $|v|_{\max}$, reached at each point in space. Same as the converging case in Chapter 6, the contours of the

maximum flow velocity is employed as analogue of the smoke foil tracks used widely in experiments. Figure 7.3(a) shows the detonation cells pattern as the detonation wave propagates through the converging chamber of 14°. From left to right, four regions are identified, marked by regions A, B, C and D. The detonation cells in region A have good regularity as they are not yet affected by the converging oblique wall. The detonation cells formed by the Mach stem are shown in region B. Region A is separated from region B by a triple-point trajectory line, which involves incident wave, reflection wave and Mach stem. Those cells in B lose their regularity and they are much smaller than those in A, which results from the effect of the compression wave. As the detonation wave moves to region C, the cells become bigger and they vary in size at the initial stage. After some triple-point collisions and interactions, these cells tend to be uniform in size and finally they re-obtain their regularity in region D. The division or demarcation between region B and C is to some extent qualitative with the reiteration that region B is dominated by contracting cell structure while region C is characterized by expanding/growing cell structure. Physically, in the region B, due to the reduction of the surface area of the front, the detonation cell becomes smaller in width while the number of triple points on the front still remains constant. The compression effect of shock causes the pressure to rise, thus possibly allowing the detonation cells to shrink, which is observed for the typical cellular structure in the corresponding regions as depicted in Fig. 7.3. The qualitative analysis above is same as that in the converging case shown in Chapter 6.

However, the measurements of the present cellular structure and its development in

the axisymmetric chamber are different from those in the converging case shown in Chapter 6. Table 7.1 shows the length of transition region (defined as the combination of regions B and C), the ultimate cell size and the width/length ratio at various oblique angles, as well as the comparisons with the 2-D converging case in Chapter 6. It is found that as the converging angle increases, the length of transition region gets shorter and the ultimate cell size in region D becomes bigger and also increasingly closer to the initial cell size found in region A. In other words, a larger oblique angle actually shortens the transition process. Thus, in order to re-obtain a regular cellular structure after the converging wall, one will need a shorter straight tube. Although the ultimate cell size is considerably affected by the converging angle, the width/length ratio tends to be constant approximately. In another word, when a steady detonation wave propagates through a converging surface to a straight tube, the detonation cells become distorted and irregular before they re-obtain their regularity. The ultimate regular cell size and the length of the transition region are noticeably affected by the oblique angle of the converging surface, while the width/length ratio of the cells is nearly independent of it, which is similar to that found for the 2-D converging case in Chapter 6. However, it is also found that the length of the transition region in the axisymmetric converging chamber is shorter than its counterpart in the 2-D converging chamber. The ultimate cell size is slightly smaller, while the shape of the detonation cells is nearly same as that found in the 2-D converging chamber. Figure 7.4 shows the change of the transition length with the converging angle, as well as the comparison with the 2-D converging case graphically.

Figure 7.5 shows the close-up of detonation cells near the converging surface at various angles. As we can see in Figure 7.5, there exists a line that separates the undisturbed area (i.e. the area behind the incident detonation wave) from the Mach reflection area (i.e. the area behind the Mach reflection). As we mentioned in Chapter 6, this line is usually referred to as the trajectory of the triple point caused by Mach reflection. It is easily found that as the converging angle increases, the trajectory angle χ decreases. When the converging angle reaches at about 46°, the trajectory angle tends towards to 0°, i.e. no Mach reflection occurs. This changing trend is same as that found in the 2-D converging case. Table 7.2 lists the details of the triple-point trajectory, as well as the comparison with the 2-D converging case discussed in Chapter 6. Figure 7.6 shows the change of the trajectory angle with the converging angle graphically. It is found that the trajectory angle captured in the axisymmetric converging chamber is close to the trajectory angle in the 2-D converging chamber within measurement uncertainty. Similar to the 2-D converging case in Chapter 6, due to the interaction between the transverse waves and the converging wall, the triple-point trajectory is not straight. The trajectory of the triple point is affected by both Mach reflection and the transverse waves. However, for inert shock waves, the triple point trajectory is only a function of the incident Mach number and the wedge angle, and therefore it is a straight line. In order to measure the trajectory angle of the Mach-reflected detonation waves, one has therefore to make a best linear fit to the irregular line to measure the trajectory angle. The dashed line in Figure 7.5(a) is the linearly-fitted trajectory.

As mentioned in the 2-D converging case in Chapter 6, both the size and the shape of the detonation cells have changed after Mach reflection. The cell size behind the Mach stem is smaller, which conforms to the fact that Mach stem is overdriven detonation. The cellular structure behind Mach stem is not as clear as that behind the incident detonation wave, and the deflection caused by the colliding of transverse waves is smaller. This suggests that the cellular structures behind Mach stem are weaker. As the converging angle increases, the cellular structures behind Mach stem are even more difficult to distinguish. When the converging angle is 25° or above, the cellular structures behind Mach stem disappear for a while before they show up again. When the converging angle is larger than 30°, the cellular structures behind Mach stem disappear completely.

In order to find out the reason why the Mach reflection of detonation has the characteristics described above, we take the present numerical result of 14º converging case for example to investigate the detailed process of a Mach reflection around the apex of a wedge. When a detonation wave moves toward the wedge, the leading shock of the upper half cell collides with the wedge first, and a reflection wave is generated. The reflection wave interacts with the detonation cellular structure, thus bringing about various reflection modes. Figure 7.7 shows the related reflection process at the converging chamber of 14º. It is seen that a reflection wave and a Mach stem are generated at the wedge apex, but no sensible tracks are formed. The possible reason is that the wedge angle is small, and the triple-point trajectory angle χ is larger than half of the exit angle φ after the colliding of the triple-wave

configurations. The reflection wave is weaker than the transverse waves, therefore no sensible tracks are found. The reflection wave then collides with the transverse wave of the half cell. Because the reflection wave is much weaker than the transverse wave, the consequence of the collision is a large deflection of the reflection wave. The triple-point trajectory angle changes much, but the cellular structures hardly change. After reflected at the wedge surface, the transverse wave catches up with the weak reflection wave and 'absorbs' it. Thus, the triple-point trajectory χ is incorporated into the cellular structures. Because the track of the reflection wave cannot be observed, the cellular structure that collides with the reflection wave and overwhelms or overshadows it is usually referred to as the triple-point trajectory. Obviously, the trajectory does not originate from the wedge apex, but somewhere behind the wedge apex. When the wedge apex is at a different position in the half cell, the specific reflection process varies, and the point of origin of the triple-point trajectory may be located in a different position on the wedge surface. Further analysis suggests that, no matter where the wedge apex is, the reflection wave generated at the apex will be absorbed by the transverse wave in the cellular structures quickly. At the same time, the triple-point trajectory is incorporated into the cellular structures.

When the wedge angle θ is small (say a few degrees only), the experimental result by Strehlow et al. (1972) showed that the impact on the leading shock caused by the wedge presence is much less significant than the colliding of the transverse waves. Therefore, after passing through the wedge apex, the cellular structures would adapt to their original status in a short while. As the wedge angle increases the reflection

wave generated at the wedge apex becomes stronger, which can be observed in our present numerical simulations. If the wedge angle is larger than a certain critical angle θ_{crit} where the reflection wave starts to become stronger than the transverse wave, the collision between them will make the transverse wave deflect dramatically. When the wedge angle continues to increase, the reflection wave becomes even stronger. After colliding with the reflection wave, the transverse wave will be absorbed by the reflection wave. This is why the cellular structures behind Mach stem is less distinct and even disappear when the wedge angle is larger than say about 30°. The value of θ_{crit} can be evaluated through the geometrical relationship of the detonation cellular structure, which is essentially the wedge angle where the reflection wave starts to become stronger than the transverse wave. The collision between the transverse waves in the cellular structures is approximately equivalent to the Mach reflection of the leading shock on a wedge given by the oblique angle Δ. The angle Δ is also the acute angle between the incident wave and the Mach stem in the leading shock. If the triple-point trajectory angle χ is smaller than half of the exit angle φ in the cellular structure, then the reflection wave is stronger than the transverse wave. Therefore, we have, $\theta_{crit} \cong \frac{1}{2}\Delta$. Our present numerical computation shows that Δ is approximately equal to the difference between the exit angle and the entrance angle. The mean entrance angle, based on our computations, is about 38° and the exit angle is around 8° (see Table 5.1 in Chapter 5). Therefore, the critical angle θ_{crit}, as evaluated, is about 15°, which agrees well with the present numerical result: when the converging angle is larger than 14°, the triple-point trajectory is very clear and the

cellular structures behind the Mach stem are smaller and less distinct.

Figures 7.8 and 7.9 show the pressure contours around the first turning point P1 and the second turning point P2 at the converging oblique angle of 25°, respectively. Similar to the 2-D converging case discussed in Chapter 6, some local high-pressure regions, the Mach reflection, as well as the collisions of the transverse waves around P1, and the expansion region around P2 can be easily observed.

In summary, when passing through the turning points P1 and P2, the detonation wave is compressed and expanded, respectively. Due to the compression effect around P1, the detonation cells shrink. However, after the turning point P2, the size of the detonation cells is enlarged again, which results from the expansion waves arising around P2. Ultimately, these detonation cells tend to become smaller than their original size shown in the typical region A or the corresponding regions of Fig. 7.3. The width/length ratio of the ultimate cells keeps constant and it is hardly affected by the oblique angle, while the transition length and the ultimate cell size have dependence on the converging angle. As the converging angle increases, the length of the transition region decreases, and the ultimate cell size increases. However, they are all smaller than their counterparts in the 2-D converging case discussed in Chapter 6.

7.3.2 Diverging Chamber

Same as the diverging case in Chapter 6, we use the grey-scale contours of the maximum pressure, $P_{\max}$, reached at each point in space to record the traces of the cellular structures, which is similar to the smoke foil technique used in experiments.

Herein, we use the maximum pressure $P_{\max}$, instead of the maximum flow velocity $|v|_{\max}$. This is because the expansion effect caused at the diverging corner will accelerate the present supersonic flow, thus affecting the recording of the original cellular structure. Figure 7.10 shows the evolution of the present detonation cellular structures as the detonation wave propagates through the diverging chamber of different sloping angles. At the oblique angle of 14° as shown in Figure 7.10(a), the evolution of the detonation cells through the diverging section can be clearly observed. The initial detonation cells have good regularity and they have not been affected by the diverging oblique wall yet. As the detonation wave passes through the diverging wall, the regular cells becomes bigger and irregular by distorting upwards, until one of the cells nearly takes up the entire height of the tube. Due to the expansion effect in the diverging section, the detonation wave becomes weaker and weaker. However, the detonation is still sustained before it enters the subsequent straight duct. Then these big cells begin to split into small cells. These cells are in different size, which is shown in Figure 7.10(a)-II for $x \geq 0.15m$. After complex triple-point collisions and interactions, these cells tend to re-obtain their regularity and become uniform in size. As mentioned in Chapter 6, the transition region, defined as the region from the turning point P1 to the location where the ultimate regular detonation structure is formed, is made up of two parts. Part 1 is dominated by expanding/growing cell structure while part 2 is characterized by contracting cell structure, which are counterparts of region B and C in the 2-D diverging case in Chapter 6. In addition, it is found that, the length of the transition region is about 0.648, shorter than its

counterpart (0.752) in the 2-D diverging case, and the ultimate cell size is about 11.53 mm long (x-direction), 6.39 mm wide (y-direction), which is slightly bigger than that found in Chapter 6 (11.11 mm long, 6.15 mm wide).

Figures 7.10(b)-(d) show the other three cases with various diverging angles. As we can see, as the diverging angle increases from 25° to 45°, the detonation cells disappear somewhere in the diverging section, which means that the detonation fails to sustain in these diverging chambers. The possible reason is that, due to the expansion effect caused by the large area change in the diverging section, the pressure in the flow field becomes too low for the detonation to sustain.

Figure 7.11 shows the pressure contours plots in the diverging section at the diverging angle of 30°. Detonation diffraction occurs as the front enters the diverging section. An expansion region can be clearly identified, marked by ER in Fig. 7.11(a), in which the pressure is decreased due to a series of expansion waves. As time progresses, the expansion region grows by spreading downstream. Additionally, there exists a shock wave, marked by S, at the edge of the expansion region, which can be found in the diffraction of a non-reactive shock wave as well. The possible reason is that, as the detonation front moves downstream, the gases expand freely into the diverging tube at a higher rate than can be accommodated by the pressure and density drops behind the detonation wave. Inward facing compression waves hence coalesce and form inward facing shocks. As the pressure in the flow field continues to drop, the leading shock of the detonation wave is decoupled from the following reaction zone and therefore the

detonation dies out, which is shown in Figure 7.10(c). The reason why the detonation can be sustained in the 2-D diverging case, but fails to sustain in the present axisymmetric diverging chamber is related to the area expansion ratio of the diverging configuration (The area expansion ratio is defined as the ratio of the cross-sectional area of the straight tube before the diverging section to the the cross-sectional area of the straight tube after the diverging section). In the 2-D diverging case discussed in Chapter 6, the area expansion ratio is 0.5. However, in the present axisymmetric diverging configuration, the area expansion ratio is 0.25. This means that the pressure drop in the axisymmetric diverging chamber is much bigger than that in the 2-D diverging case. In other words, the big pressure drop leads to the decay of the detonation. In addition, the rate of the pressure drop is also important. That is why the detonation in the diverging chamber of 14° sustains, but dies out in the diverging chamber of 25° or above, although the diverging chamber of 14° has the same area expansion ratio as that of 25° or above.

Shown in Figures 7.12-7.14 are a series of pressure contours with time for the diverging angle of 14°, 25°, and 45°. By comparison with the case of 30° discussed above, it is found that in the diverging chamber of 14° or 25°, the expansion effect around the first turning point P1 is weaker, and the expansion region “ER” is smaller than that in the diverging chamber of 30°. On the contrary, the expansion effect in the diverging chamber of 45° is stronger, and the expansion region “ER” is larger, which agrees with our analysis above.

Figure 7.15 shows the location of the leading front on the central line with time for the diverging chamber of 14°. The trajectory line is a curved line, and there exist small periodic fluctuations. By making linear fit to the curved line, one may find that the line is made up of essentially three segments with different slope (AB, BC and CD). The slope theoretically stands for the mean speed of the leading front. These three segments therefore correspond to the three sections in the present diverging configuration, respectively. The instantaneous speed of the leading front on the central line can be obtained from the location of the leading front with time. The speed of the leading front in the diverging section (BC) is observed to be slower because of the expansion effect, which agrees with our analysis. The instantaneous speed of the leading front on the central line can also be obtained from the location of the leading front with time. Figure 7.16 shows the ratio of the instantaneous detonation speed over the C-J speed as time progresses, which depicts the fluctuation and its relation to the cellular structure. Similar to the straight-duct case in Chapter 5, each fluctuation cycle consists of two stages: acceleration stage and deceleration stage. The acceleration stage involves the process where sub-driven detonation accelerates to overdriven detonation. The peak velocity of the overdriven detonation is reached after the acceleration stage. The deceleration stage involves the process where overdriven detonation decelerates to sub-driven. As we can see in Figure 7.16, when the detonation wave passes through the diverging section, the front speed slows down because of the expansion waves. Herein, the detonation is sub-driven. After the diverging section, the front speed goes up and the detonation is back to over-driven

again.

Figures 7.17 to 7.19 show the ratio of the instantaneous speed of the leading front over the C-J speed the diverging chamber of 25°, 30° and 45°, respectively. Similar to the diverging case of 14° shown in Figure 7.16, when passing through the diverging section, the detonation becomes sub-driven, and the front speed for these cases drops below the C-J speed. However, the difference is that, unlike the case of 14°, the detonation dies out completely and the speed of the leading shock does not come up to C-J speed again

7.4 Concluding Summary for Chapter 7

Numerical simulations of the reflection and diffraction processes of gaseous detonation waves in the axisymmetric diverging and converging chambers have been performed by using weighted essentially non-oscillatory (WENO) scheme, coupled with a detailed chemical reaction model and the numerical package of CHEMEQ. The following conclusions are drawn:

1. As a detonation wave propagates through the converging surface to a straight duct, there exists a transition region. In the transition region, the detonation cells become irregular and distorted at the initial stage, but they will finally re-gain their regularity. The length of the transition region and the ultimate regular cell size are affected by the converging angle. A larger oblique angle can shorten the transition process. However, the width/length ratio of the ultimate cells tends to be constant and it is hardly affected by the oblique angle. The findings above are similar to the 2-D

converging case in Chapter 6. However, the length of the transition region, and the ultimate cell size are smaller than those in the 2-D converging cases, while the width/length ratio of the ultimate regular cells (i.e. the shape of the cells) is nearly the same.

2. For Mach reflection occurring in the axisymmetric converging chambers, the triple-point trajectory is not a straight line. As the oblique angle in the converging chamber configuration increases, the trajectory angle χ decreases, which is similar to that found in the 2-D converging case in Chapter 6. The value of the trajectory angle χ is also very comparable with its counterpart in the 2-D converging case.

3. For the axisymmetric diverging chamber of 14°, the evolution of the detonation cellular structure is similar to the 2-D diverging case in Chapter 6. The difference is that the length of the transition region is shorter and the ultimate cell size is slightly larger than its counterpart in the 2-D diverging case.

4. For the axisymmetric diverging chamber of 25° and above, the small area expansion ratio and a large diverging angle lead to a considerable pressure drop, which in turn makes the detonation die out.

Table 7.1 Transition region and ultimate cell size in the axisymmetric converging chamber vs in the 2-D converging chamber

Converging Oblique Angle	Length of Transition Region		Ultimate Cell Size (Width, length)		width/length ratio	
	2-D Chamber	Axisymmetric Chamber	2-D Chamber	Axisymmetric Chamber	2-D Chamber	Axisymmetric Chamber
14º	0.330 m	0.21m	4.1mm, 7.4mm	4.0mm, 7.2mm	1.806	1.80
25º	0.285 m	0.17 m	5.6mm, 10.12mm	5.2mm, 9.37mm	1.807	1.802
30º	0.260 m	0.166 m	5.7mm, 10.3mm	5.4mm, 9.72mm	1.807	1.80
46º	0.250 m	0.16 m	6.4mm, 11.56mm	6.0mm, 10.8mm	1.806	1.80

Table 7.2 Details of the triple-point trajectory in the axisymmetric converging chamber vs in the 2-D converging chamber

Converging Angle, θ		10º	14º	20º	25º	30º	35º	46º
Trajectory Angle, χ	2-D Chamber	20º	18º	14º	10º	6º	5º	0º
	Axisymmetric Chamber	20º	18º	12º	9º	6º	3º	0º

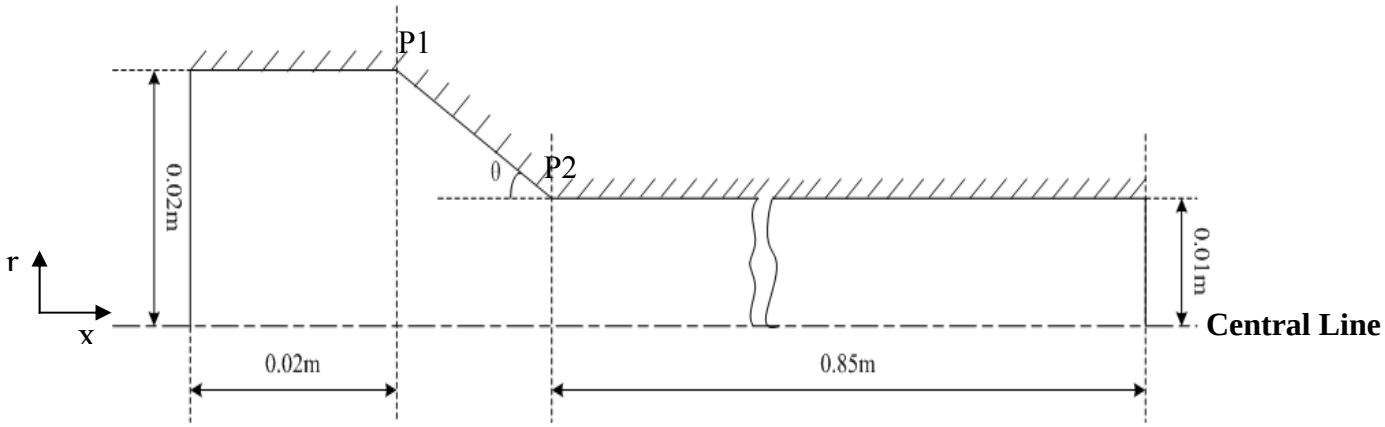

(a)

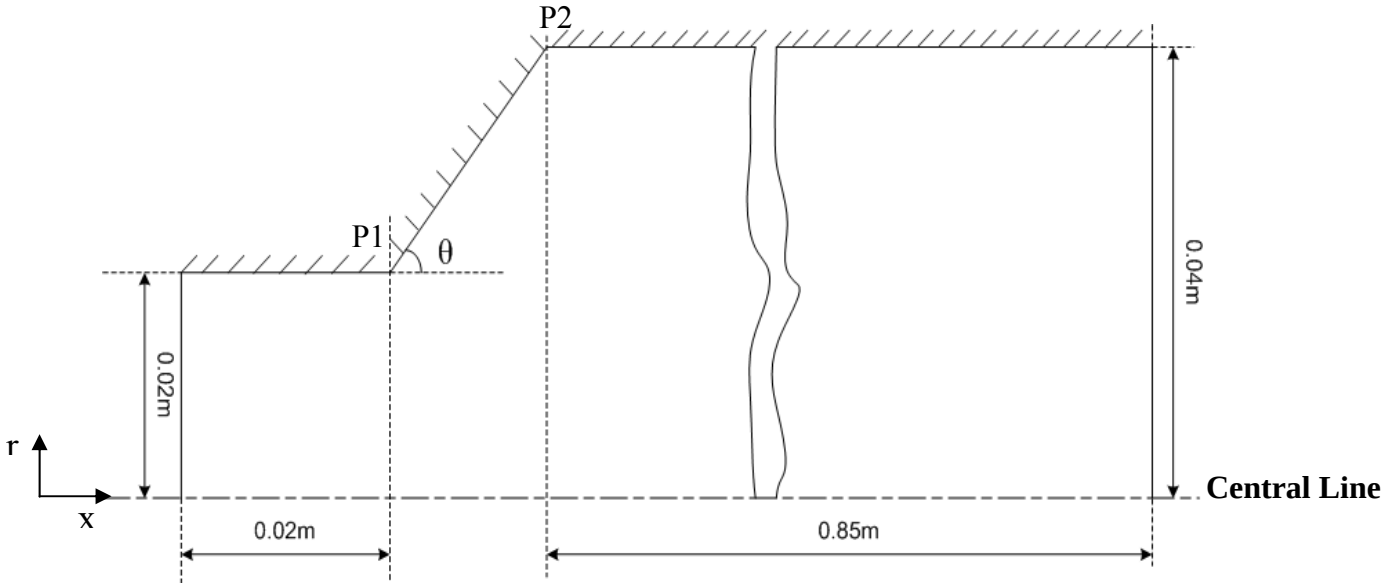

(b)

Figure 7.1 Computational domains for the axisymmetric chambers (not to scale)

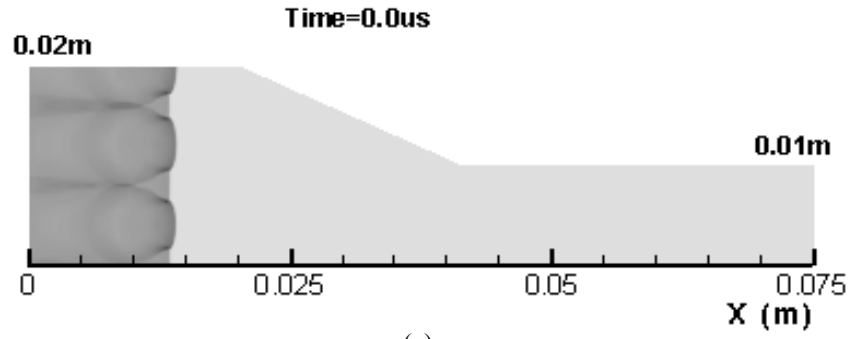

(a)

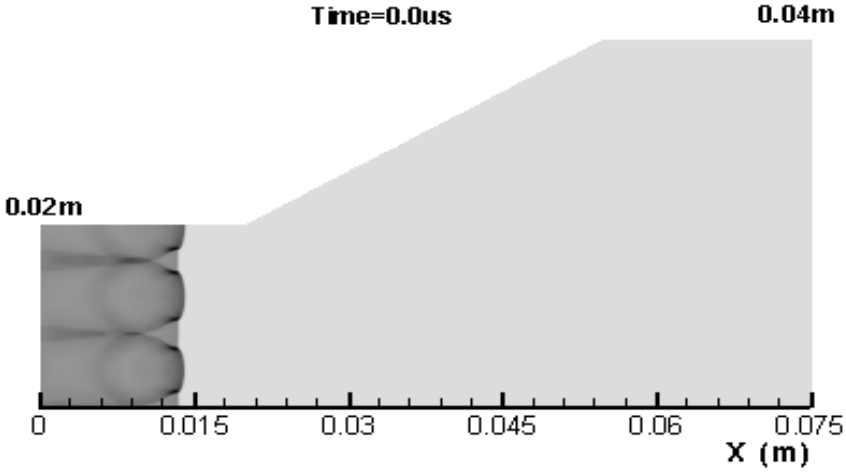

(b)

Figure 7.2 Initial pressure distributions for

the axisymmetric cases

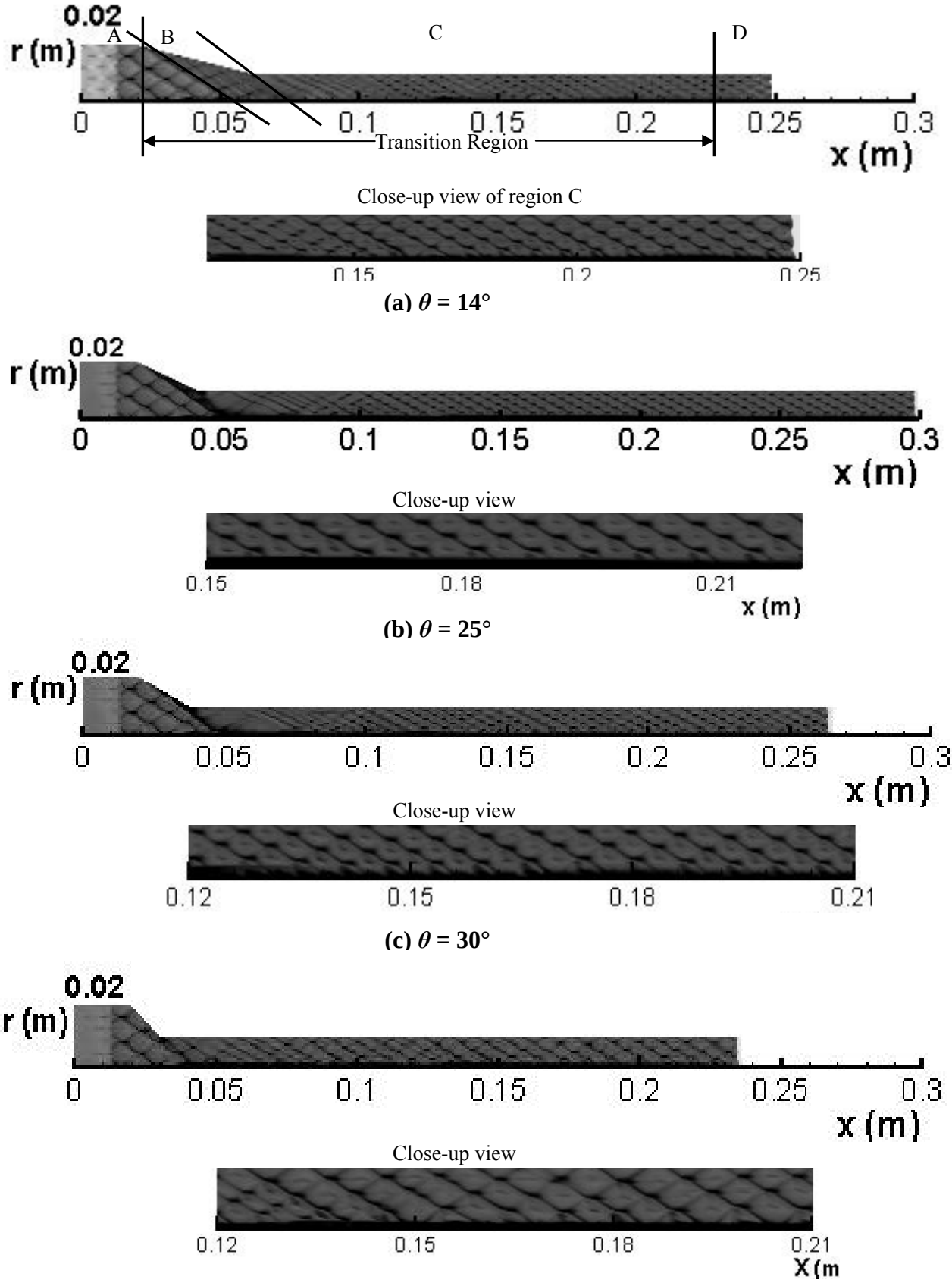

Figure 7.3 Evolution of the detonation cellular structures in the converging chamber of different sloping angles

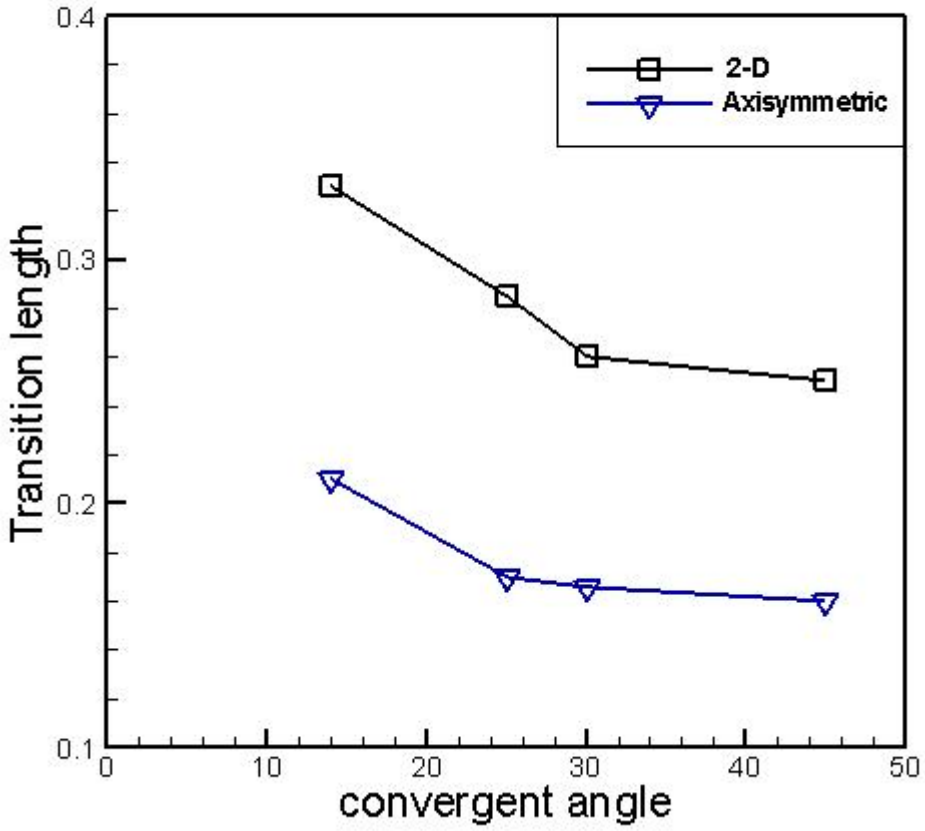

Figure 7.4 Transition length versus the converging angle

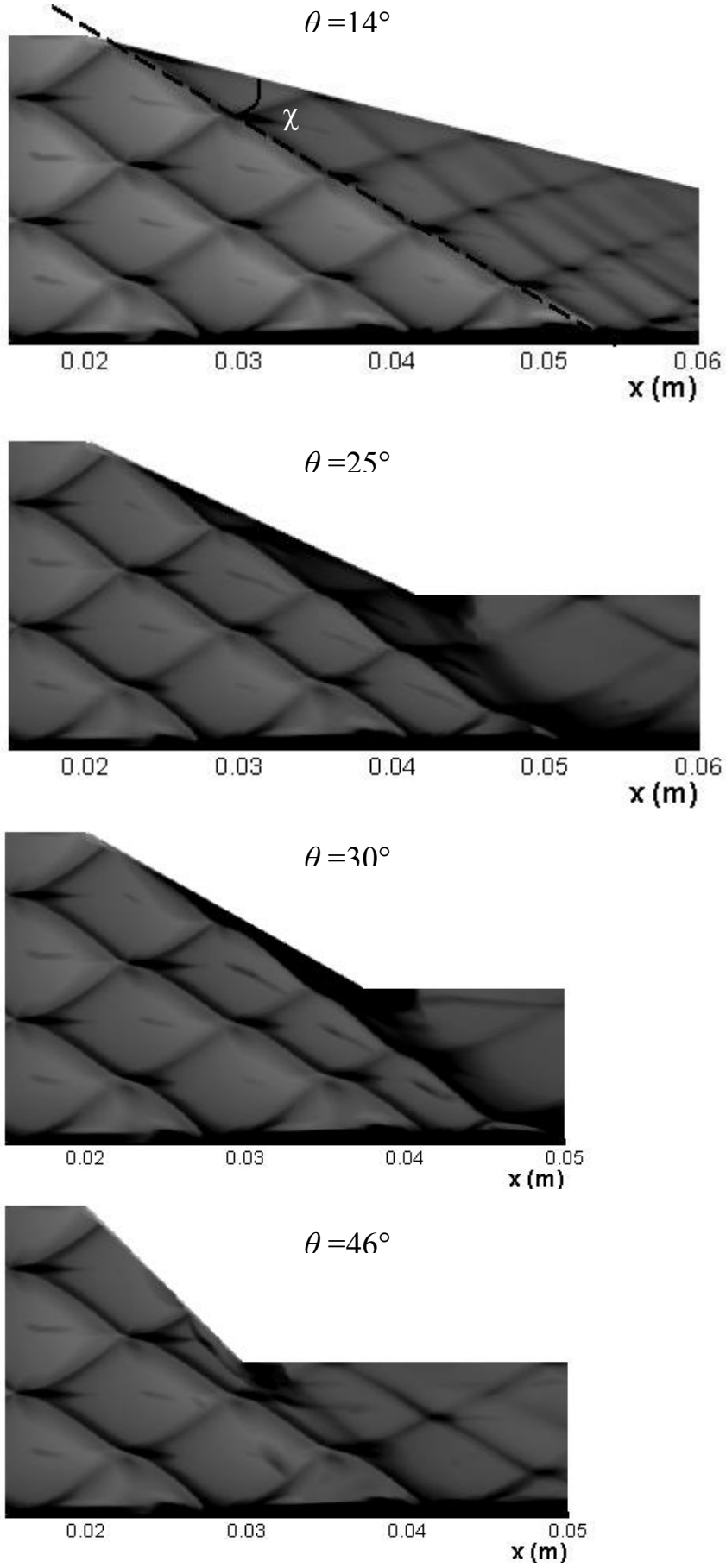

Figure 7.5 Detonation cells and the trajectory angles at various converging angles

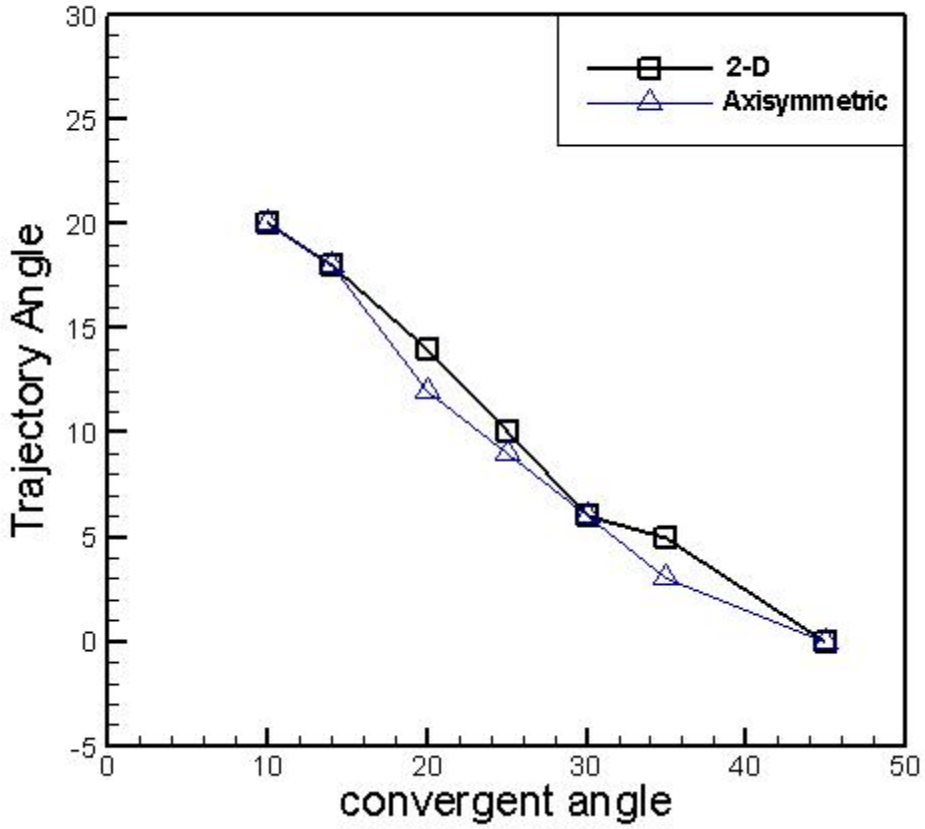

Figure 7.6 Trajectory angle versus the converging angle

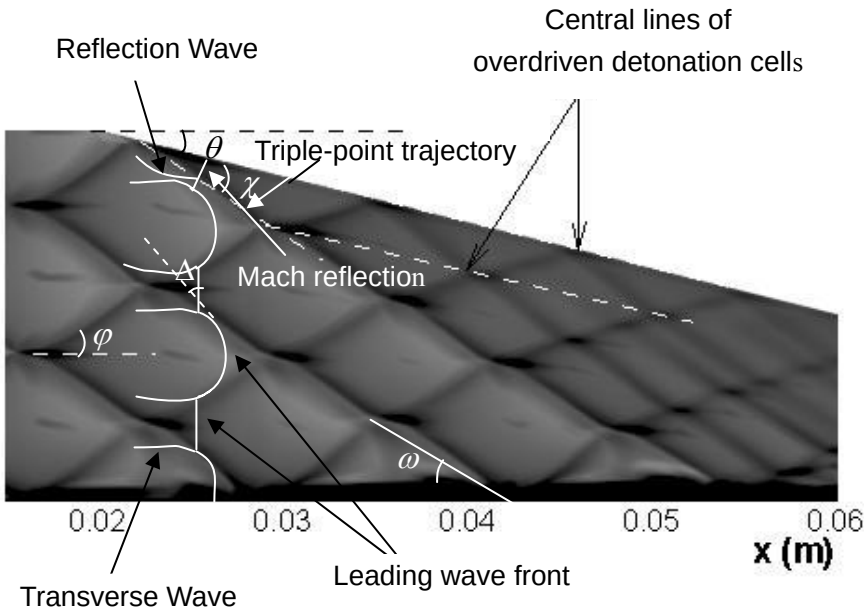

Figure 7.7 The process of a Mach reflection around the wedge apex

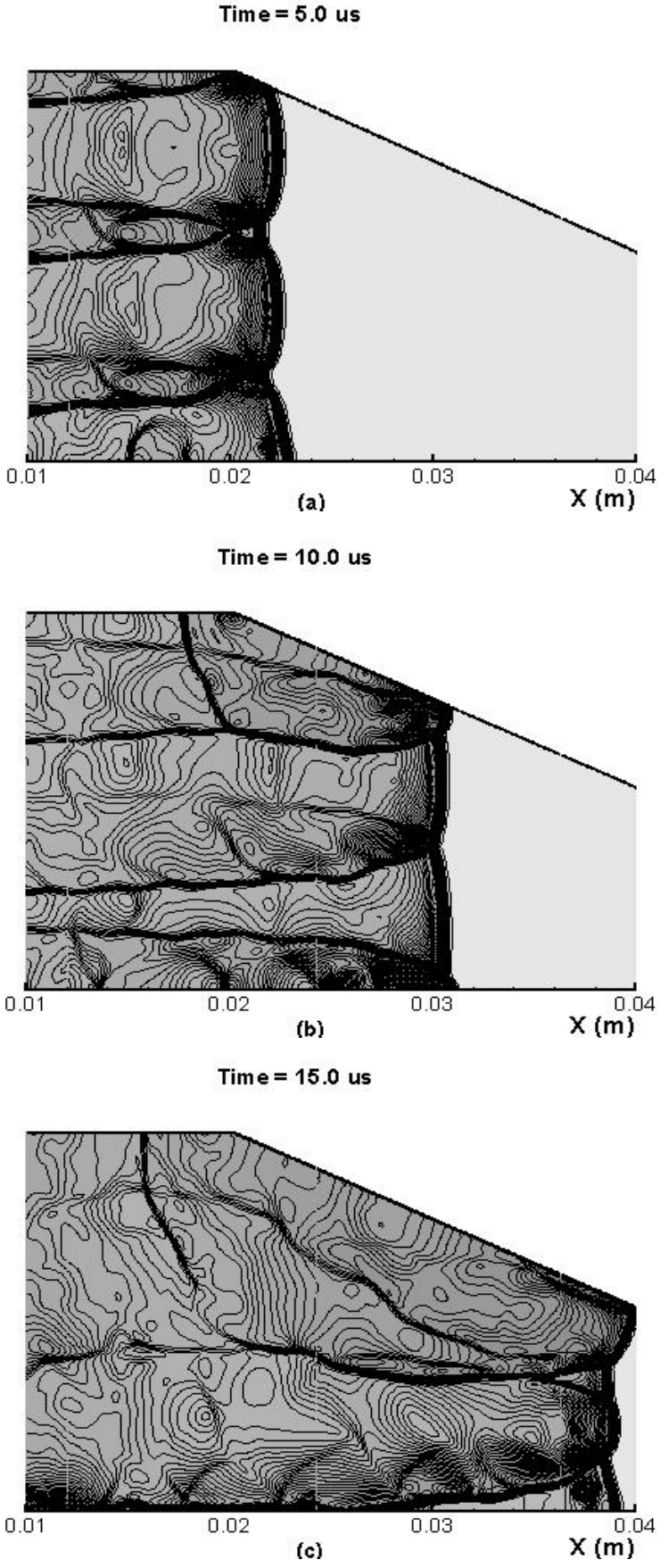

Figure 7.8 Pressure contours around the turning point P1 for configuration of converging angle 25°

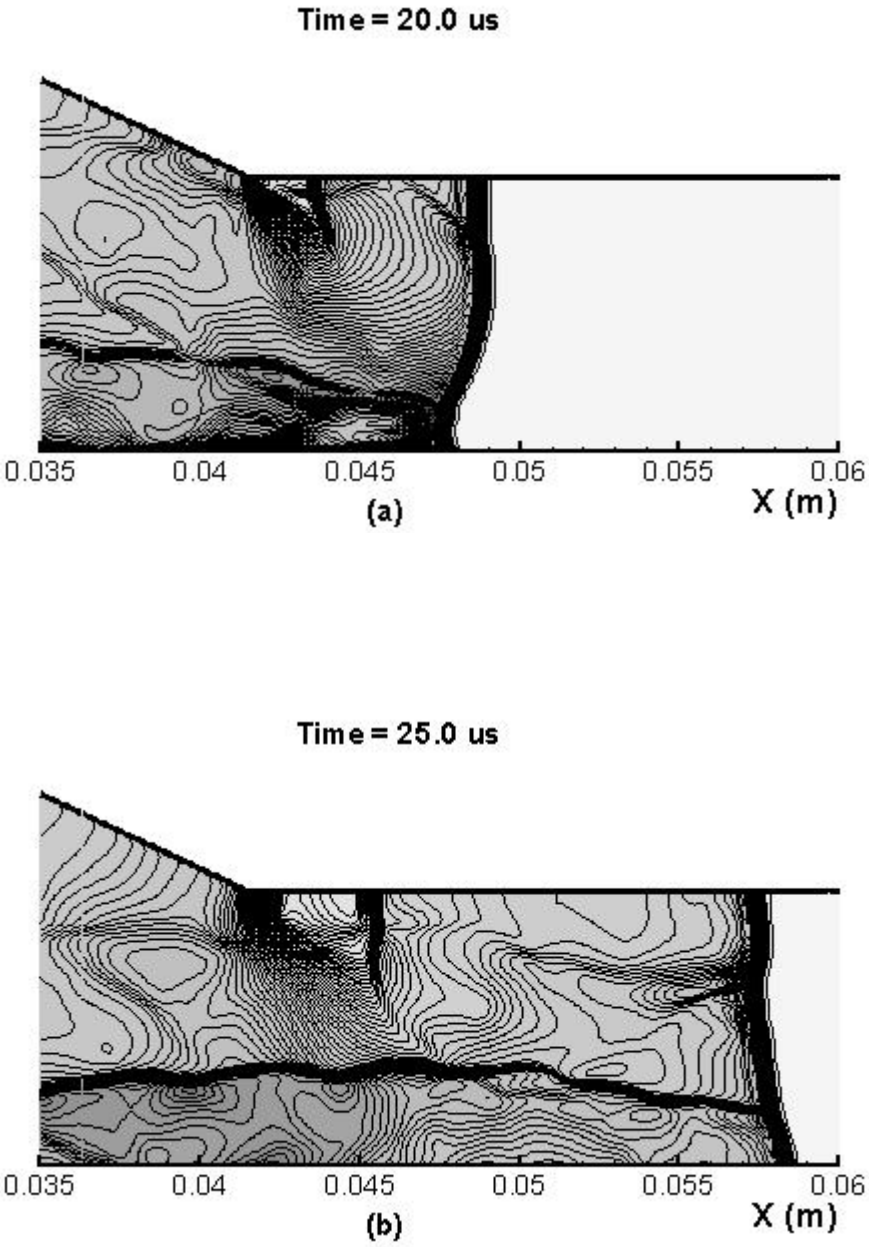

Figure 7.9 Pressure contours around the turning point P2

for configuration of converging angle 25°

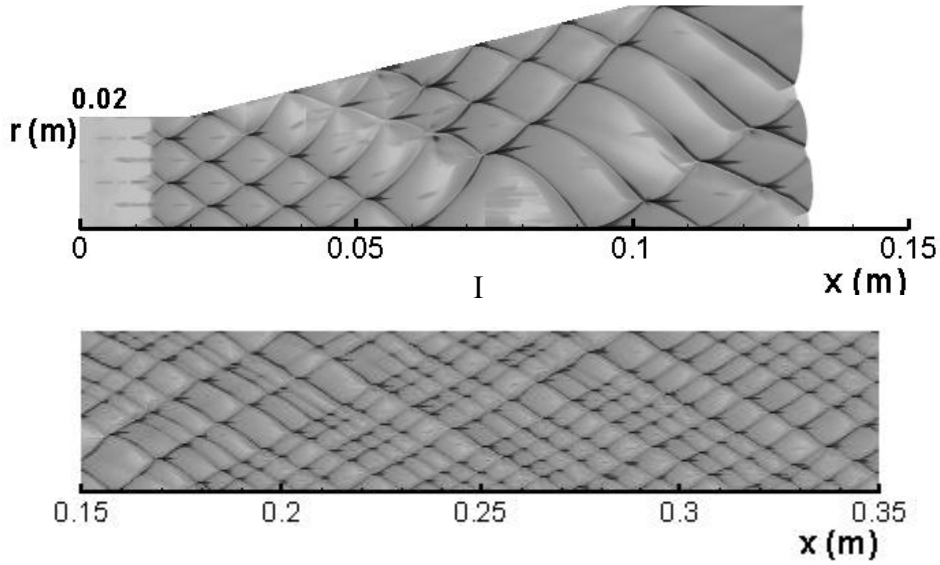

(a) $\theta = 14°$

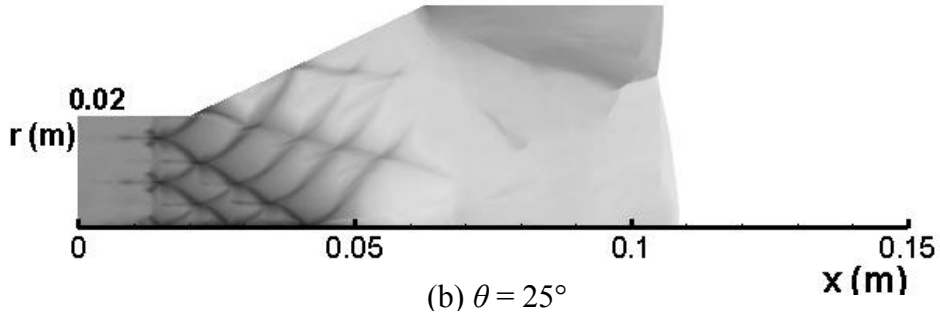

(b) $\theta = 25°$

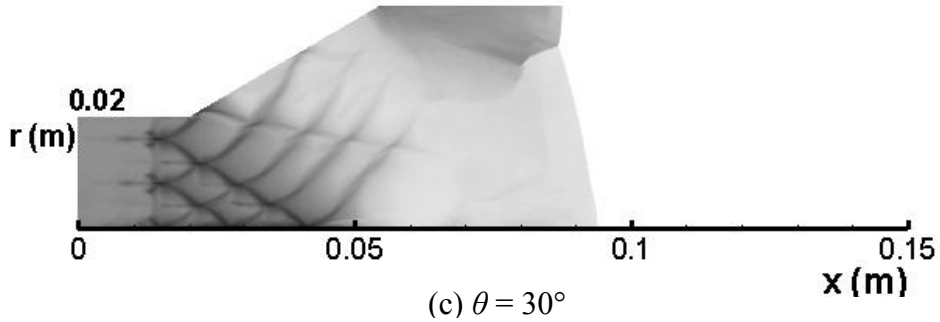

(c) $\theta = 30°$

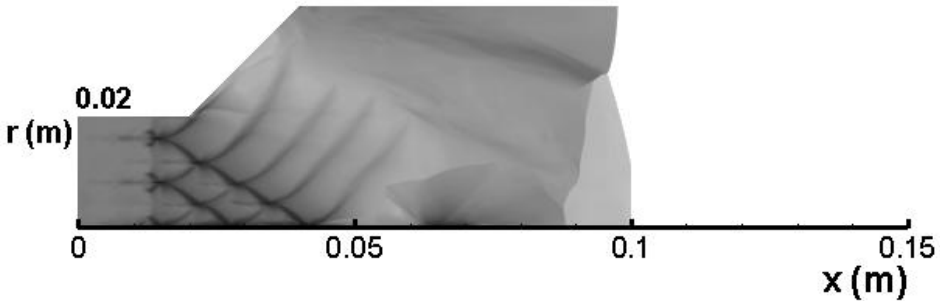

(d) $\theta = 45°$

Figure 7.10 Evolution of the detonation cellular structures in the diverging chamber of different sloping angles

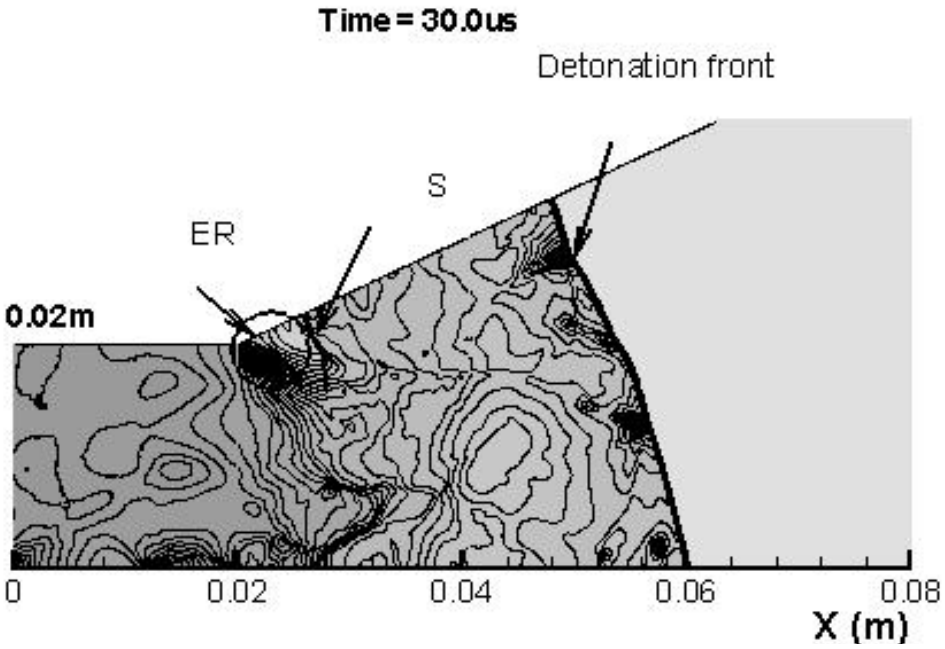

(a)

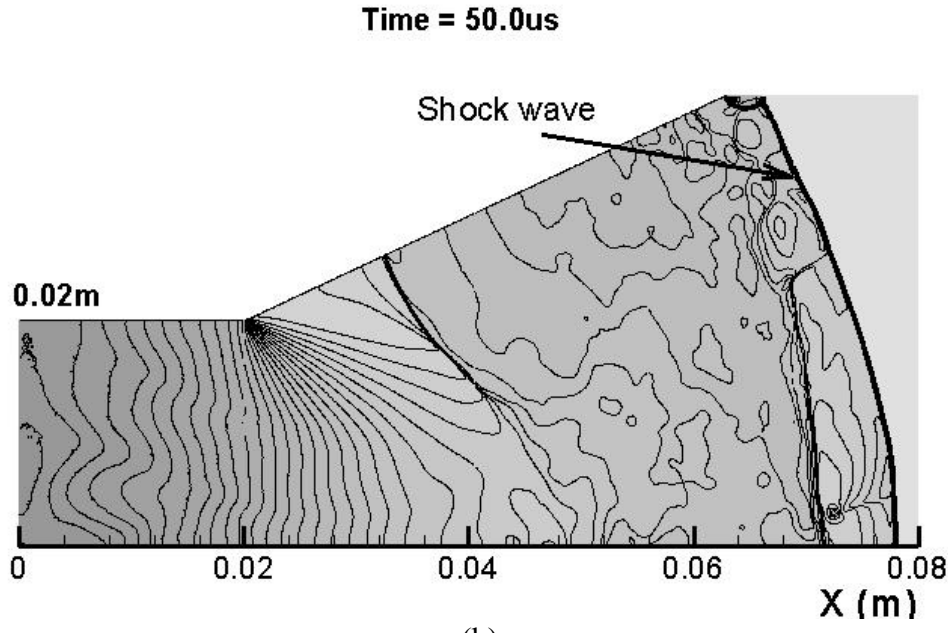

(b)

Figure 7.11 Pressure contours in the diverging section

for the diverging configuration of 30°

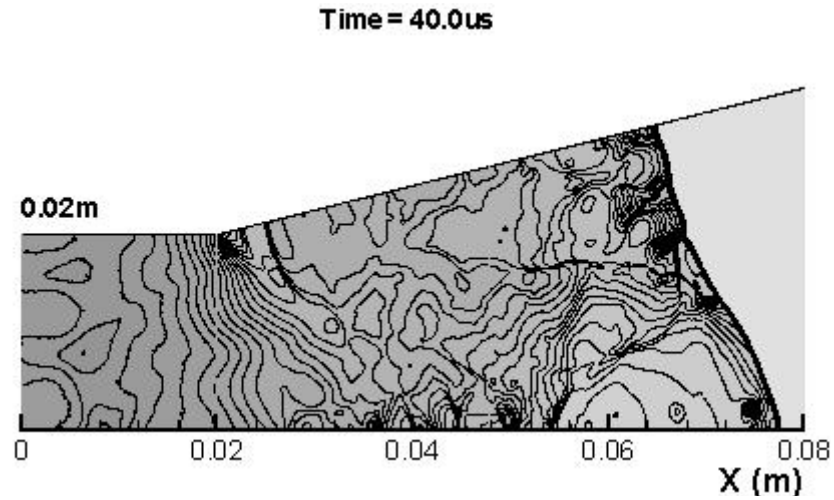

(a)

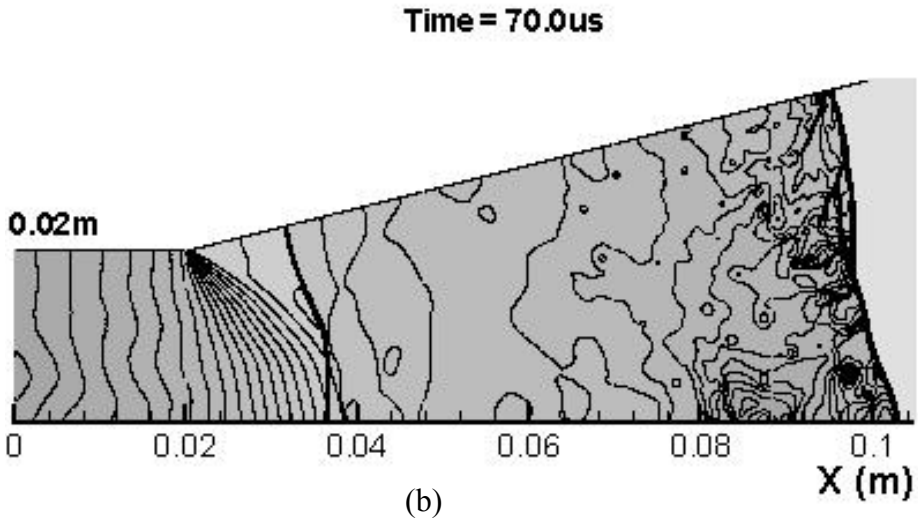

(b)

Figure 7.12 Pressure contours in the diverging section

for the diverging configuration of 14°

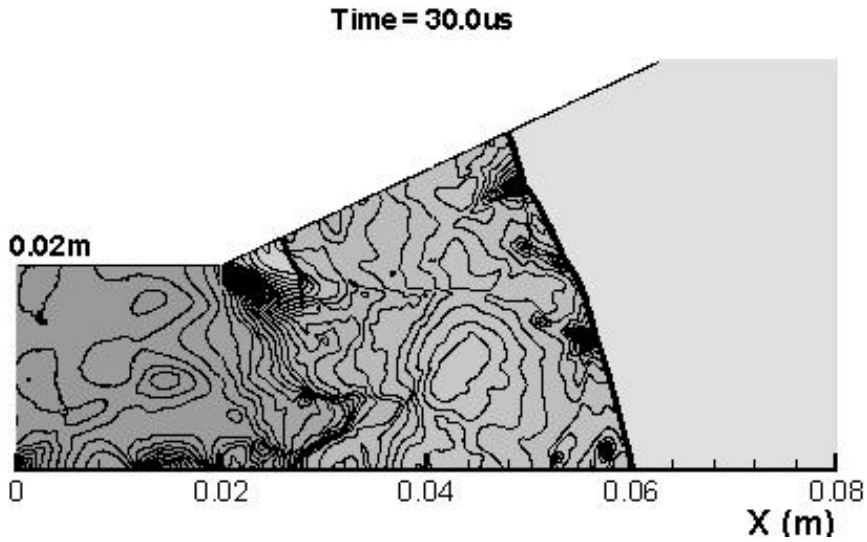

(a)

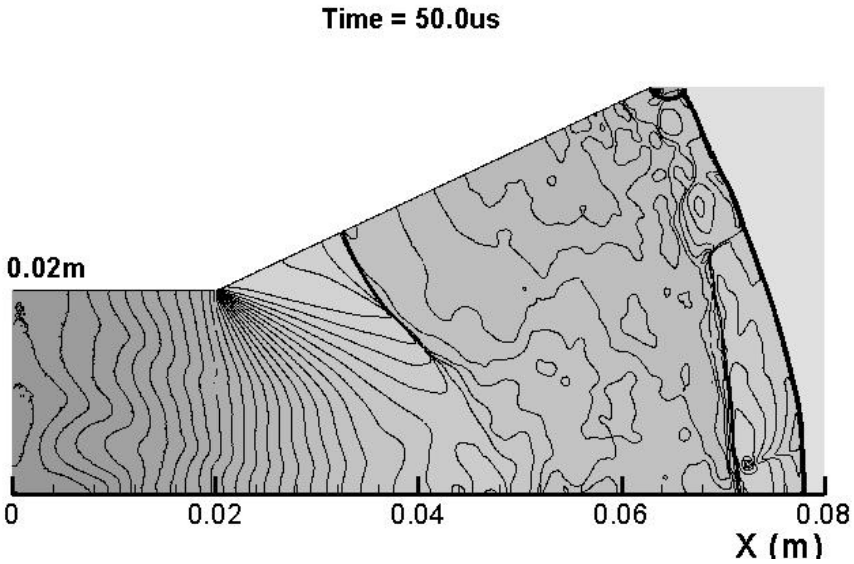

(b)

Figure 7.13 Pressure contours in the diverging section

for the diverging configuration of 25°

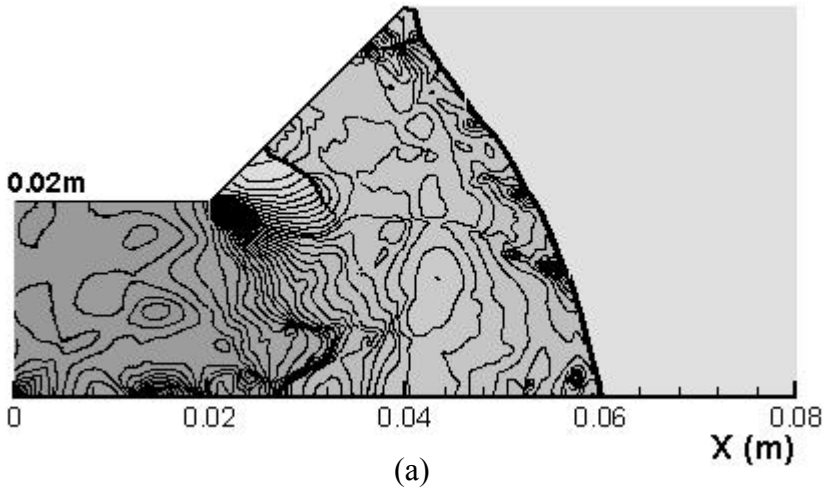

(a)

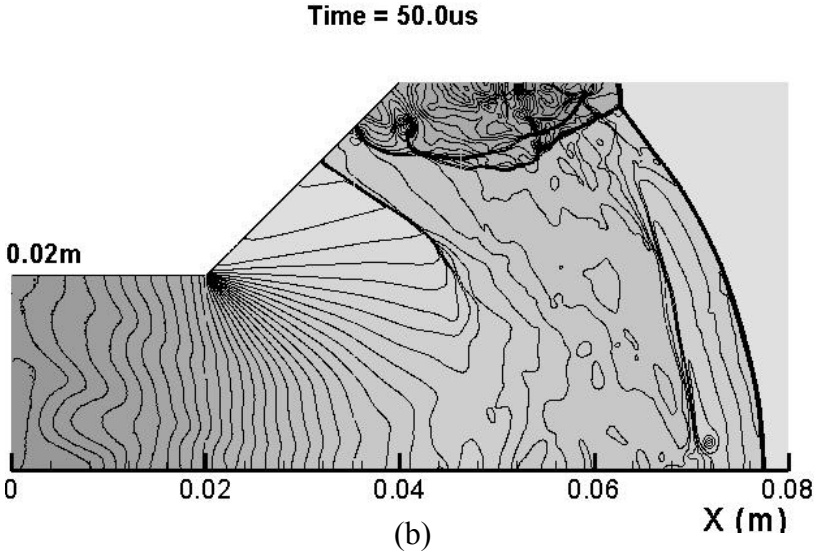

(b)

Figure 7.14 Pressure contours in the diverging section

for the diverging configuration of 45°

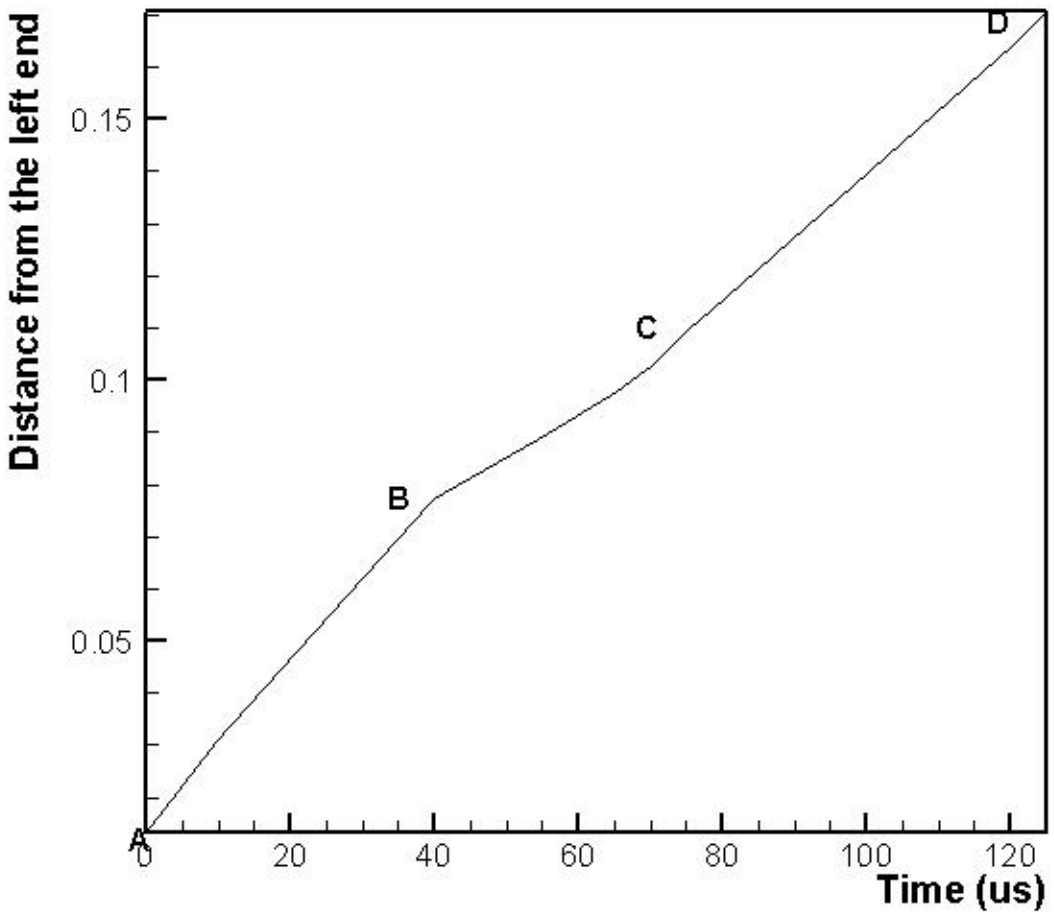

Figure 7.15 Location of the leading front on the central line versus time in the diverging chamber of 14°

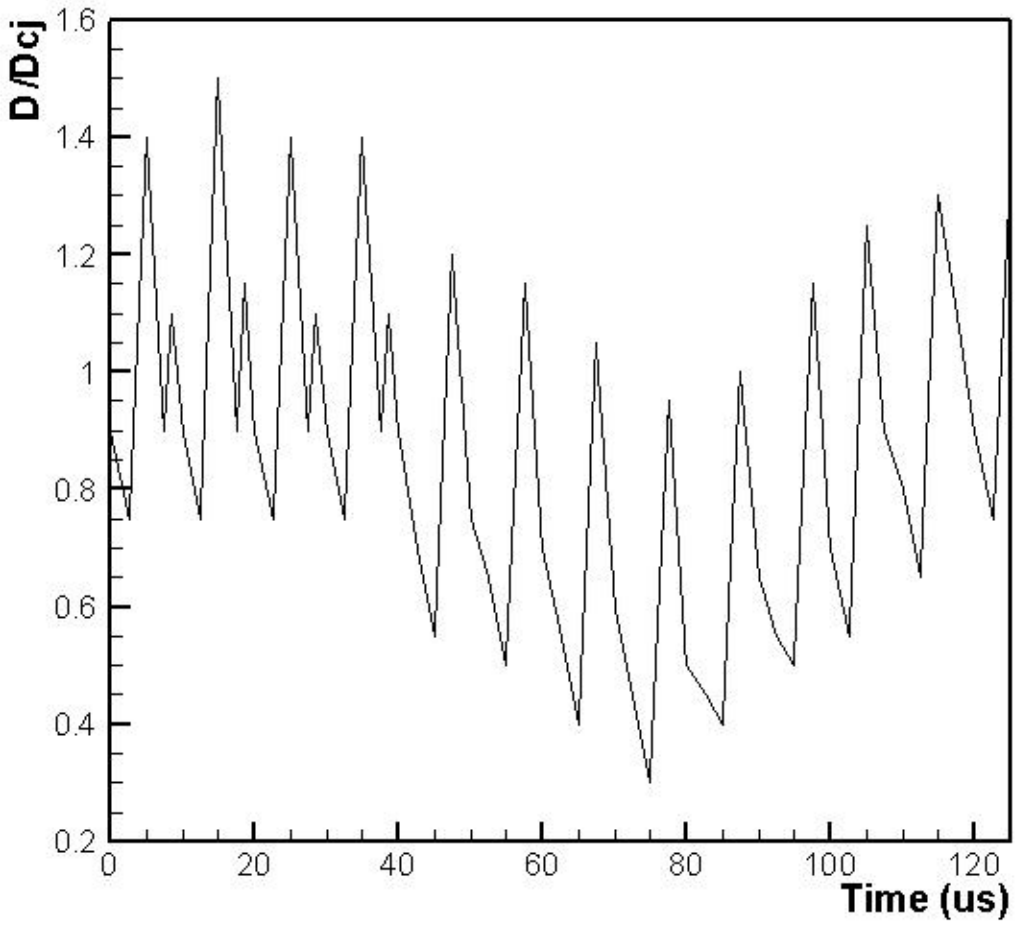

Figure 7.16 Instantaneous speed of the leading front versus time in the diverging configuration of 14°

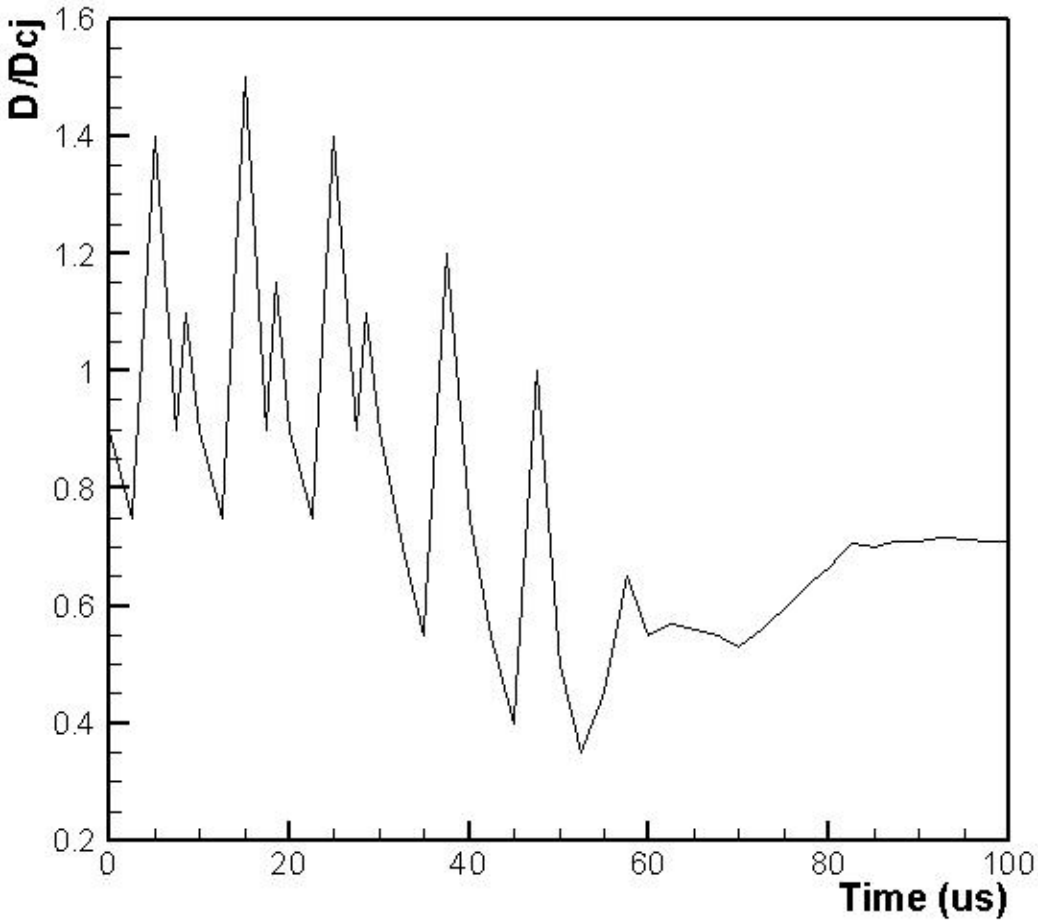

Figure 7.17 Instantaneous speed of the leading front versus time in the diverging chamber of 25°

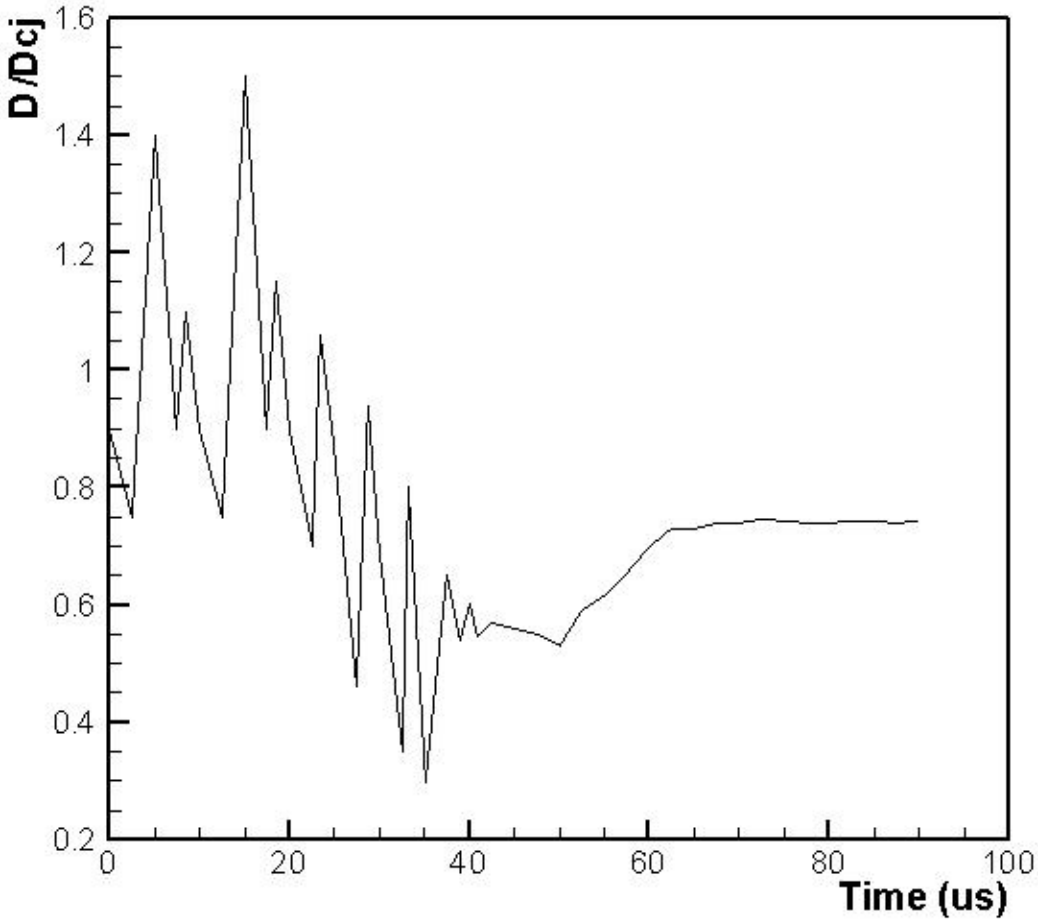

Figure 7.18 Instantaneous speed of the leading front versus time in the diverging chamber of 30°

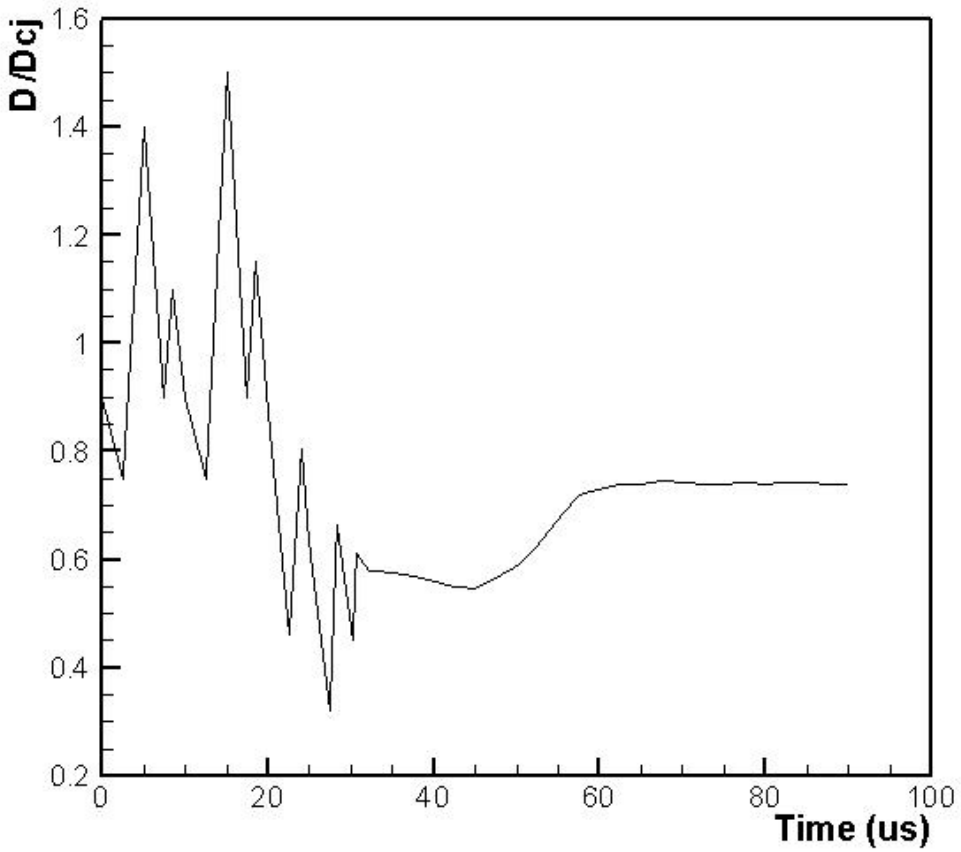

Figure 7.19 Instantaneous speed of the leading front versus time in the diverging chamber of 45°

Chapter 8 Conclusions and Recommendations

8.1 Concluding Summary

A detailed elementary chemical reaction model with 9 species and 19 elementary reactions was used for a stoichiometric H_2/O_2 mixture diluted with argon. The 3rd order TVD Runge-Kutta method and the weighted essentially non-oscillatory (WENO) numerical scheme with fairly good resolution were employed to solve the multi-species flow without chemical reactions, while the chemical reactions were solved by the numerical package of CHEMEQ.

The one-dimensional Chapman-Jouguet (C-J) detonation wave was simulated. The structure of the detonation front, detonation velocity at the front, concentration profile of each species and the effect of mesh size on the result were investigated as well. The one-dimensional results were then mapped to two-dimensional grids as the initial condition of the two-dimensional numerical computation in a straight duct. By introducing some artificial perturbation, the cellular structure of the two-dimensional detonation wave was successfully simulated. The detailed triple-wave configuration, as well as the formation, evolution and the dynamic characteristics of the cellular structure, were investigated. Furthermore, in order to study the influence of the diverging/converging walls on the detonation wave and its cellular structure, we placed the obtained two-dimensional detonation wave in two-dimensional diverging/converging chambers and let the detonation wave propagate through the varying cross-sectional chambers. For further understanding and quantitative analysis

of these influences, axisymmetric diverging/converging chambers were also configured to substitute for the above-mentioned two-dimensional diverging / converging chambers. A comparison on the simulation results between them was presented.

8.1.1 One-dimensional Detonation Wave

The present numerical computation of one-dimensional detonation shows that the detonation front is made up of the leading shock wave and the subsequent chemical reaction zone, followed by the rarefaction wave zone. The flow velocity decreases gradually in the rarefaction wave zone till the steady zone is reached at about 1/2 of the detonation distance. In addition, the mean detonation velocity obtained from the profile of the detonation wave is about 1625m/s, which is quite close to the calculated C-J value (1618m/s) by Gordon and McBride (1971). The C-J pressure p_{cj}, as calculated, is 93600 Pa comparable to the experimental result (94000 Pa) by Lefebvre (1995). The calculated von-Neumann peak pressure of the leading shock is about 1.79 p_{cj}, which is slightly smaller than the analytical value from the ZND model (1.86 p_{cj}). The length of the reaction zone obtained in the present numerical simulation is about 0.011m, which agrees well with the calculated value (0.012m) through the steady solution by Oran et al (1998).

Based on the order of concentration change, the species involved can be classified into three groups. H_2, O_2 and H_2O belong to the first group, and their concentrations change is in the order of $10^{-1} mol/m^3$. The second group includes OH, O and H,

whose concentrations change is a in the order of $10^{-2} mol/m^3$, followed by the last group: H_2O_2 and HO_2, which exhibits the least change of $O(10^{-4})$ or $(10^{-5} mol/m^3)$.

The mesh study shows that the mesh size has negligible influence on some detonation parameters, but sensible influence on others. The integrated variables like detonation velocity, C-J pressure and wall pressure are fairly insensitive to mesh size. Reaction zone length varies when the mesh size is larger than 0.1mm, i.e. reaction zone length is convergent at mesh size = 0.1mm. On the contrary, the von-Neumann pressure and the induction zone length, show some variations as the mesh size reduces to 0.025mm. The variations between the two smallest mesh sizes are, however, fairly limited. At the mesh size $\Delta x \geq 0.5\,\text{mm}$, the induction zone cannot be resolved. At the mesh size $\Delta x \leq 0.2\,\text{mm}$, the calculated induction zone length reduces with the mesh size. The minimum induction zone length obtained in our present computations is 0.16 cm, which is slightly larger than the result (0.147cm) by Joseph et al. (2005).

8.1.2 Two-dimensional Detonation in a Straight Duct

The numerical simulation shows that the formation of cellular structures can be divided into two stages. Stage 1 is the formation of the triple wave configuration, while Stage 2 is the formation of the regular cellular structures with a constant number of transverse waves. The second stage requires much longer time than the first stage. The regular cellular structures formed at the beginning of Stage 2 are not stable. The numerical smoke foil technique was widely used to study the tracks of the cellular structure. In the present work, the maximum flow velocity, $|v|_{\max}$, on all grid

nodes in the time history are recorded as an analogue of smoke foil tracks. The shape of the cellular structure from the present numerical result agrees well with that from experimental results, but the cell size in our present computation is smaller than experimental results.

A typical cellular structure is made up of multiple triple-wave configurations, each of which is the combination of Mach stem (M), incident wave (I) and transverse wave (T). When the detonation wave propagates along the duct, on the leading front, the incident wave keeps exchanging its role with the Mach stem, accompanying with the collision between two adjacent triple-wave configurations. The detonation at Mach stem is overdriven, while that at incident wave is sub-driven detonation. The present numerical computation shows that before the two triple-wave configurations collide, they tend to evolve into a more complex structure, called "Strong Structure". Compared to purely shock waves, the colliding between two triple-wave configurations in a detonation cellular structure is much more complicated. The converging effect plays an important role in the colliding of the triple-wave configurations. The converging effect enhances the energy at the converging point dramatically, which can be considered as a blast wave. The blast wave gives birth to a new Mach stem by interacting with the incident wave. The transverse segments of the blast wave develop into new transverse waves. The chemical reaction front is located behind the leading shock. The reaction front behind the incident wave is further back than that behind the Mach stem. The reaction induction zone behind the incident wave is wider. One functional role of transverse waves is to secondarily compress and ignite

the mixture in the induction zone behind the incident wave, thus shortening the reaction induction zone.

When a detonation wave propagates through the cellular structure, the variation of the detonation velocity presents two stages: acceleration stage and deceleration stage. The acceleration stage involves the process where sub-driven detonation accelerates to overdriven detonation, while the deceleration stage involves the process where overdriven detonation decelerates to sub-driven. The detonation state, when far away from C-J detonation, is not stable. In a cellular structure, sub-driven detonation state occupies more space than the overdriven detonation state.

The study on the grid convergence for the two-dimensional detonation simulations shows that mesh size has fair influence on the numerical simulation of the cellular structure. For the result with mesh size 0.2mm, the triple-wave configuration is only shown or detected roughly. The detailed features around the triple point, however, are not at all resolved. The position of the triple point is not precisely defined. More importantly, till at time t=3ms, the number of the transverse waves is still about 10, which is believed to be yet unstable. The results with mesh size 0.1mm, 0.05mm and 0.025 show similar resolution of the basic cellular structure. The mesh size of 0.05mm and 0.025mm can resolve more and finer features of the structure, such as more slip lines and additional shock wave, which was the focus of Hu et al. (2004), but not the intent of the present work. In addition, using finer mesh size like 0.05mm or 0.025mm requires much more CPU resources. That is the reason why the mesh size of 0.1mm is

used as the standard resolution for computation and analysis in the present work.

8.1.3 Two-dimensional Detonation in a Diverging /Converging Chamber

Numerical simulations of the reflection and diffraction processes of gaseous detonation waves in the diverging and converging chambers were performed. The following conclusions were derived:

1. Due to the change in the surface area of the front while the number of triple points on the front remains constant, detonation diffraction tends to increase the detonation cell size and detonation reflection decreases the detonation cell size.

2. By diffraction, a detonation wave is expanded and decayed by a series of expansion waves and an expansion region is formed, which is opposite to the compression effect by detonation reflection. For Mach reflection detonation, the triple-point trajectory is not a straight line; as the oblique angle in the converging chamber configuration increases, the trajectory angle χ decreases.

3. As a detonation wave propagates through a diverging or converging surface to a straight tube, there exists a transition region, in which the detonation cells become irregular and distorted at the initial stage, but they will finally re-gain their regularity. The length of the transition region and the ultimate regular cell size are relevant to the diverging/converging angle. A larger oblique angle can shorten the transition process. However, the width/length ratio of the ultimate cells tends to be constant and it is hardly affected by the oblique angle.

4. By the collision of transverse waves and reflected transverse waves as in a diverging chamber configuration, a blast wave from a strong localized explosion

occurs, which is similar to the localized explosion observed in the work of Khokhlov et al (2004).

8.1.4 Detonation Wave in an Axisymmetric Diverging /Converging Chamber

Numerical simulations of detonation reflection and diffraction processes in the axisymmetric diverging and converging chambers show that:

1. As a detonation wave propagates through the converging surface to a straight duct, there exists a transition region. In the transition region, the detonation cells become irregular and distorted at the initial stage, but they will finally re-gain their regularity. The length of the transition region and the ultimate regular cell size are relevant to the converging angle. A larger oblique angle can shorten the transition process. However, the width/length ratio of the ultimate cells tends to be constant and it is hardly affected by the oblique angle. The findings mentioned are the same as the 2-D converging case in Chapter 6. However, the length of the transition region, and the ultimate cell size are smaller than those in the 2-D converging cases, while the width/length ratio of the ultimate regular cells (i.e. the shape of the cells) is nearly same.

2. For Mach reflection occurred in the axisymmetric converging chambers, the triple-point trajectory is not a straight line; as the oblique angle in the converging chamber configuration increases, the trajectory angle χ decreases, which is similar to that found in the 2-D converging case in Chapter 6. The value of the trajectory angle χ is also very comparable with its counterpart in the 2-D converging case.

3. For the axisymmetric diverging chamber of 14°, the evolution of the detonation

cellular structure is similar to the 2-D diverging case in Chapter 6. The difference is that the length of the transition region is shorter and the ultimate cell size is slightly larger than its counterpart in the 2-D diverging case.

4. For the axisymmetric diverging chamber of 25° or above, the small area expansion ratio and a large diverging angle lead to a considerable pressure drop and a high rate of the pressure drop, which in turn makes the detonation die out.

8.2 Recommendations for Future Work

Gaseous detonation has a very complicated cellular structure. The mode and details of the cellular structure depends on many factors. The underlying mechanisms are still not well known. Therefore, both the present numerical simulations and the theoretical analysis have room for improvements. The future work can be carried out on the following aspects:

1) Work on three-dimensional numerical simulation

In the current study, for simplicity, only the two-dimensional or axisymmetrical chambers were considered. In fact, the assumption that the computational domain is two-dimensional or axisymmetrical is not often justified because the chambers in the actual engineering design are usually irregular in shape. Furthermore, in the case of a complex geometry, detonation decay or re-ignition, and the detailed cellular structures are interesting topics, which need to be examined closely. So a three-dimensional calculation, including complex geometries, should be made for the further research work.

2) Work on the fluid with viscosity considered

In the current study, the flow model was assumed to be inviscid, and the governing equations used were the Euler equations, instead of the compressible Navier-Stokes equations. However, the actual fluid is viscous. For a fluid with high Reynolds number, the effect of viscosity is very limited and it could be neglected except for the near wall region. For the fluid with lower Reynolds number, the effect of viscosity is not negligible. Therefore, for the fluid with low Reynolds number, the fluid viscosity should be taken into account by solving the Navier-Stokes equations in future work although this will increase the complexity of the problem significantly.

3) Work on finer mesh size

As discussed in this work, the mesh size is very important to a proper resolution of the detailed features around the triple-wave configuration. The mesh size employed in the present study is 0.1mm, which shows faithfully the evolution of the transverse waves and main features of the detonation cell structures in response to the different sloping chamber wall imposed, but it is not fine enough to resolve the very fine and detailed structures/sub-structures around the detonation triple-wave configurations. Thus, a finer mesh size, like 0.025mm, should be considered to study the detailed detonation structures/sub-structures, and eliminate the effect of mesh size.

4) Study of DDT (Deflagration to Detonation Transition)

In the current numerical simulations, the detonation is initiated directly by a small spark region. However, in most experiments, the detonation is initiated through a

deflagration-to-detonation-transition (DDT) process. It might be useful to incorporate this DDT process into numerical simulations so that more detailed comparisons with experiments could be made. In addition, it has been found experimentally that, a Shchelkin spiral configuration can shorten the DDT time. The numerical simulation of the DDT process will be very helpful for us to understand the specific mechanism for that.

5) Work on simplified chemical reaction models

The present elementary chemical reaction model is very complicated, which involves solving 19 elementary chemical reactions. The stiffness of the source terms in the governing equations relating to the elementary chemical reactions requires huge computer resources. Therefore, it is worth spending some time in simplifying the present chemical reaction model.

Bibliography

Akbar, R., 1997, Ph.D. thesis, Dept of Aeronautical Engineering, Rensselaer Polytechnic Institute, Troy, NY

Arienti, M. and Shepherd, J.E., 2005, A numerical study of detonation diffraction. Journal of Fluid Mechanics 529: 117-146

Benedick, W.B., Guirao, C.M., Knystautas, R. and Lee, J.H., 1986, Critical charge for the direct initiation of detonation in gaseous fuel-air mixtures, Progress in Astronautics and Aeronautics, 106:181-202

Berthelot, M. and Vieille, P., 1882, Compt Rend Acad Sci, Paris 94:101–8. 822–823

Chapman, D.L. and Philos, Mag, 1899, 5th Ser 47: 90-104

Broda, J.C., Conrad, C., Pal, S., Woodward, R.D. and Santoro, R.J., 1999, Experimental Results on Air-Breathing Pulse Detonation Studies, Proceedings of 11th Annual Symposium on Propulsion

Brophy, C.M., Werner, L.S. and Sinibaldi, J.O., 2003, Performance Characterization of a Valveless Pulse Detonation Engine, AIAA Paper 2003-1344

Cambier, J.L. and Adelman, H.G., 1988, Preliminary Numerical Simulations of a Pulsed Detonation Wave Engine, AIAA Paper 1988-2960

Cambier, J.L., and Tegner, J.K.,1998, Strategies for pulsed detonation engine performance optimization. Journal of Propulsion and Power, 14(4):489-498

Cooper, M., Jackson, S., Austin, J., Wintenberger, E. and Shepherd, J.E., 2002, Direct Experimental Impulse Measurements for Detonations and Deflagrations, Journal of Propulsion and Power, 18-5: 1033–1041

Daniel E.P., 2003, Optimal area profiles for ideal single nozzle air-breathing pulse detonation engines *AIAA*–2003-4512

Desbordes, D., 1988, Transmission of overdriven plane detonations: critical diameter as a function of cell regularity and size, Progress in Astronautics and Aeronautics, 114:170-185

Doering, W., 1943, On Detonation Processes in Gases, Annals of Physics, 43 (5): 421-436

Ebrahimi, H.B., Mohanraj, R. and Merkle, C.L., 2002, Multilevel Analysis of Pulsed Detonation Engines, Journal of Propulsion and Power, 18-2:225–232

Edwards, D.H. and Jones, A.T., 1978, The Variation in Strength of Transverse Shocks in Detonation Waves, Journal of Physics D: Applied Physics, 11:155-166

Fedkiw, R.P., 1996, A survey of Chemically Reacting Compressible Flows, Thesis, UCLA

Fedkiw, R.P., Merriman, B. and Osher, S., 1997, High accuracy numerical methods for thermal perfect gas flows with chemistry. *Journal of Computational Physics* 132:175-190

Fickett, W. and Davis, W.C., 1979, Detonation, University of California Press, Berkeley

Fusina, G., Sislian, J.P. and Parent B., 2005, “Formation and stability of near Chapman-Jouguet standing oblique detonation waves”, AIAA Journal, 43: 1591-1604.

Gamezo, V.N., Desbordes, D. and Oran, E.S., 1999, Formation and evolution of

two-dimensional cellular detonations. Combustion and Flame 116:154–165

Glassman, I., 1996, Combustion, Academic Press, 3rd Edition

Gordon, S., McBride, B.J., 1971, Computer Program for Calculation of Complex Chemical Equilibrium Compositions, Rocket performance, Incident and Reflected Shocks, and Chapman-Jouguet Detonation, NASA SP273

Guo, C.M., Zhang, D.L. and Xie, W., 2001, The Mach reflection of a detonation based on soot track measurements. Combustion and Flame 127:2051-2058

Hanana, M., Lefebvre, M.H. and Van Tiggelen, P.J., 2000, Preliminary Experimental Investigation of Pressure Evolution in Detonation Cells, Experimental Thermal and Fluid Science, 21:64-70

Harten, A., 1983, High resolution schemes for hyperbolic conservation laws. Journal of Computational Physics 49: 357-393

Helman, D., Shreeve, R.P. and Eidelman, S., 1986, Detonation Pulse Engine, AIAA Paper 86-1683

Henrick, A.K., Aslam, T.D. and Powers, J.M., 2005, Mapped weighted essentially non-oscillatory schemes: achieving optimal order near critical points. Journal of Computational Physics 207: 542-567

Hinkey, J.B., Busing, T.R.A. and Kaye, L., 1995, Shock Tube Experiments for the Development of a Hydrogen- Fueled Pulse Detonation Engine, AIAA paper 95:2578

Hu, X.Y., Khoo, B.C., Zhang, D.L. and Jiang, Z.L., 2004, The cellular structure of a two-dimensional H2/O2/Ar detonation wave. Combustion Theory and Modelling

8: 339-359

Hu, X.Y., Zhang, D.L., Khoo, B.C. and Jiang, Z.L., 2005, The structure and evolution of a two-dimensional H2/O2/Ar cellular detonation. Shock Waves 14: 37-44

Jackson, S. I. and Shepherd, J. E., 2002, The Development of a Pulse Detonation Engine Simulator Facility, Technical Report, California Institute of Technology

Jiang, G.S. and Shu, C.W., 1996, Efficient Implementation of Weighted ENO Scheme. Journal of Computational Physics 126:202-228

Joseph, M.P. and Samuel, P., 2005, Accurate Spatial Resolution Estimates for Reactive Supersonic Flow with Detailed Chemistry. AIAA Journal 43 (5): 1088-1099

Jouguet, E.J., 1905, Math Pures Appl., 6e Series 1:347-425

Kailasanath, K. and Patnaik, G., 1999, Pulsed Detonation Engines – What is its Performance, Proceedings, JANNAF Combustion Meeting

Kailasanath, K., 2000, Review of propulsion applications of detonation waves. AIAA-38:9-1698

Kee, R.J., Miller, J.A., et al, 1980, "CHEMKIN: a general-purpose, Problem-independent, transportable, FORTRAN chemical kinetics code package". Sandia Laboratories Report SAND80-8003

Khasainov, B., Presles, H.N., Desbordes, D., Demontis, P. and Vidal, P., 2005, Detonation diffraction from circular tubes to cones. Shock Waves 14(3): 187-192

Khokhlov, A.M., Austin, J.M., Pintgen, F. and Shepherd, J.E., 2004, Numerical study of the detonation wave structure in ethylene-oxygen mixtures, AIAA 2004-0792

Knystautas, R., Lee, J.H., Moen, I.O. and Wagner, H.G., 1979, Direct initiation of spherical detonation by a hot turbulent gas jet, Proceedings of 16th International Symposium on Combustion, 1235-1245

Krzycki, L.J., 1982, US Naval Ordnance Test Station, China Lake, CA, NavWeps Report 7655, ASTIA 284-312

Kuo, K.K., 1986, Principles of Combustion, John Wiley & Sons, New York

Lax, P.D., 1954, Weak solutions of nonlinear hyperbolic equations and their numerical computation. Communications on Pure and Applied Mathematics, 7: 159-193

Lee, J.H.S., 1984, Dynamic parameters of gaseous detonations, Annual Review of Fluid Mechanics, 16:311-336

Lee, J.H.S. and Moen, I.O., 1980, Progress in Energy and Combustion Science, 6:359–389

Lefebvre M.H. and Oran E.S., 1995, Analysis of shock structures in regular detonation Shock Waves 4:277-283

Li, C.P., Kailasanath, L. and Oran, E.S., 1994, Detonation structures behind oblique shocks. Physics of Fluids 6: 1600-1611

Lieberman, D.H. and Shepherd, J.E., 2002, Detonation Initiation by Hot Turbulent Jet for use in Pulse Detonation Engines, 38th AIAA/ASME/SAE/ASEE Joint Propulsion Conference and Exhibit

Liu, Y. and Vinokur, M., 1989, Upwind Algorithms for Genreral Thermo-Chemical Nonequilibrium Flows, AIAA-89-0201

Mallard, E. and Le Chatelier, H., 1881, Compt Rend Acad Sci, Paris 93:145–148

Meyer, T.R., Hoke, J.L., Brown, M.S., Gord, J.R. and Schauer, F.R., 2002, Experimental Study of Deflagration Enhancement Techniques in a H2/Air Pulsed-Detonation Engine, AIAA Paper 2002-3720

New, T.H., Panicker, P.K., Lu, F.K. and H. M. Tsai, H.M., 2006, Experimental Investigations on DDT Enhancements by Schelkin Spirals in a PDE, AIAA 2006-552

Nicholls, J.A., Wilkinson, H.R. and Morrison, R.B., 1957, Jet propulsion, 27-5: 534-541

Ohyagi, S., Obara, T., Nakata, F. and Hoshi, S., 2000, A numerical simulation of reflection processes of a detonation wave on a wedge. Shock Waves 10: 185-190

Oppenheim, A.K., Laderman, A.J. and Urtiew, P.A., 1962, Combustion and Flame, 6:193–197

Oppenheim, A.E., Smolen, J.J., Kwak, D. and Urtiew, P.A., 1972, On the Dynamics of Shock Intersections, 5th Symposium (International) on Detonation, ONR, Department of Navy, Arlington, Virginia

Oppenheim, A.K. and Soloukhin, R.I., 1973, Experiments in Gasdynamics of Explosions. Annual Review of Fluid Mechanics 5:31-58

Oran, E.S. and Boris, J.P., 1987, Numerical Simulation of Reactive Flow (New York: Elsevier)

Oran, E.S., Boris, J.P. and Kailasannath, K., 1991, Studies of detonation initiation, propagation and quenching. Progress in Astronautics and Aeronautics 135:421–445

Oran, E.S., Weber, J.E., Stefaniw, E.I, Lefebvre, M.H. and Aderson, J.D., 1998, A numerical study of two-dimensional H2-O2-Ar detonation using a detailed chemical reaction model. Combustion and Flame 113:147-163

Osher S., 1984, Riemann Solvers, the Entropy Condition, and Difference. SIAM Journal on Numerical Analysis 21: 217-235

Papalexandris, M.V., 2000, A numerical study of wedge-induced detonation. Combustion and Flame 120: 526-538

Quirk, J.J., 1993, Godunov-type schemes applied to detonation flows AD-A265482

Sanders, S.T., Jenkins, T.P. and Hanson, R.K., 2000, Diode Laser Sensor System for Multi-Parameter Measurements in Pulse Detonation Engine Flows, AIAA Paper 2000-3593

Santoro, R.J., 2003, Thrust Augmentation Measurements for a Pulse Detonation Engine Driven Ejector, 40th AIAA/ASME/SAE/ASEE Joint Propulsion Conference and Exhibit, July 2004

Sharpe, G.J., 2001, Transverse waves in numerical simulations of cellular detonations. Journal of Fluid Mechanics 447: 31-51

Shchelkin, K.I., 1940, Journal of Experimental and Theoretical physics, 10: 823–827

Shu, C.W. and Osher, S., 1988, Efficient implementation of essentially non-oscillatory shock-capturing schemes. Journal of Computational Physics 77: 439-471

Sinibaldi, J.O., Brophy, C.M., and Robinson, J.P., 2000, Ignition Effects on Deflagration to Detonation Transition Distance in Gaseous Mixtures, AIAA Paper 2000-3590

Sinibaldi, J.O., Brophy, C.M., Li, C. and Kailasanath, K., 2001, Initiator Detonation Diffraction Studies in Pulsed Detonation engines, AIAA Paper 2001-3466

Sterling, J., Ghorbanian, K., Humphrey, J. and Sobota, T., 1995, Numerical investigations of Pulse Detonation Wave Engines, AIAA Paper 95–2479

Strehlow, R.A., 1968, Gas phase detonations: recent developments, Combustion and Flame, 12: 81–101

Strehlow, R.A., Admaczyk, A.A. and Stiles, R.J., 1972, Transient Studies of Detonation Waves, Astronautica Acta, 17: 509-527

Strehlow, R.A., 1978, Fundamentals of Combustion, Kreiger, 287-329

Stull, D.R., 1971, JANAF Thermochemical Tables, National Standard Reference Data Series. U. S. National, Bureau of Standards No. 37. 2nd Ed. Gaithersberg, Maryland

Taki, S. and Fujiwara, T., 1978, Numerical analysis of two-dimensional nonsteady detonations. AIAA Journal 16:73-77

Thomas, G.O. and Williams, R.L., 2002, Detonation interaction with wedges and bends. Shock Waves 11:481-492

Von Neumann, 1942, Theory of Detonation Waves, J. OSRD Report: 549

Wada, Y., Ogawa, S., Ishiguro, T. and Kubota, H., 1989, A Generalized Roe s Approximate Riemann Solver for Chemically Reaction Flows, AIAA-89-0202

Walter, M.A. and da Silva, L.F.F., 2006, “Numerical study of detonation stabilization by finite length wedges”, AIAA Journal, 44: 353-361

Wescott, B.L., Stewart, D.S. and Bdzil, J.B., 2004, On self-similarity of detonation

diffraction. Physics of Fluids 16: 373-384

Wilson, G.J. and MacCormack, R.W., 1990, Modelling supersonic combustion using a full-implicit numerical method. AIAA-90-2307

Wintenberger, E. and Shepherd, J.E.,2003, A model for the performance of air-breathing pulse detonation engines, 39th AIAA/ASME/SAE/ASEE Joint Propulsion Conference and Exhibit, Huntsville, AL. AIAA2003-4511

Young, T.R., 1979, CHEMEQ-Subroutine for solving stiff ordinary differential equations AD-A0835545

Yu, Q.,1996, Ph.D. thesis, Dept. of Mechanical Engineering, Aachen Polytechnic Institute, Aachen, Germany

Yu, Q., Ishii, K. and Gr¨onig, H.,1996, On the Mach Reflection of Detonation Waves. Presented at Mach Reflection Symposium, Johanesburg

Yu, Q. and Gr¨onig, H.,1995, Numerical Simulation on the Reflection of Detonation Waves, In: Sturtvant B, Shepherd JE, Hornung HG (eds) Proceedings of the 20th International Symposium on Shock Waves, Pasadena, USA, pp 1143–1148

Zeldovich, Ya B., 1940, Journal of Experiment and Theory in Physics, 10: 542-568

Filename: Complete Thesis v1.7.doc
Directory: F:
Template: C:\Documents and Settings\sbeacham\Application Data\Microsoft\Templates\Normal.dot
Title: Group: 6
Subject:
Author: Qu Qing
Keywords:
Comments:
Creation Date: 2009-10-26 20:55:00
Change Number: 73
Last Saved On: 2009-12-21 3:11:00
Last Saved By: QQ
Total Editing Time: 4,905 Minutes
Last Printed On: 2009-12-21 10:54:00
As of Last Complete Printing
Number of Pages: 239
Number of Words: 35,146 (approx.)
Number of Characters: 200,334 (approx.)